Characterisation of ScN and ScGaN alloys grown by Molecular Beam Epitaxy

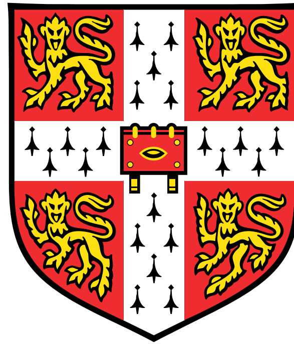

Stephan Manuel Knoll
Department of Materials Science and Metallurgy
University of Cambridge

This dissertation is submitted for the degree of
Doctor of Philosophy

Churchill College | July 2014

Abstract

The wurtzite III-nitrides AlN, GaN and InN are currently widely used in optoelectronic applications such as light-emitting diodes and this success is owed in large part to the possibility of band gap engineering by alloying between the constituent nitrides. Unfortunately, the restricted material properties currently limit the performance of such devices, and efficiencies of emitters in the green and ultraviolet spectral regions remain low. These challenges have motivated the search for alloying additions offering greater degrees of freedom for tuning the material properties.

ScN is of particular interest in this regard, and ScGaN alloys have been predicted to remain stable in the wurtzite structure with direct band gaps for Sc contents of up to 27%. Of further interest is the predicted deviation from wurtzite symmetry towards a non-polar structure at higher Sc contents, which could lead to additional device functionalities such as ferroelectric switching. However, experimental data regarding the properties of ScGaN alloys are very limited, and further investigations of the growth are required if these materials are to be integrated into the existing III-nitride technology.

This thesis is an in-depth characterisation of ScN and dilute ScGaN films grown by molecular beam epitaxy (MBE), with special emphasis on the microstructure, surface topography and local bonding environment of Sc in these materials. The results are based on a broad range of characterisation techniques including transmission electron microscopy, scanning probe microscopy, high-resolution X-ray diffraction and X-ray absorption spectroscopy (XAS).

The effects of varying growth conditions on the properties of ScN and ScGaN films are discussed, including observed growth rates and defect densities. The introduction of Sc into the GaN system was found to decrease growth rates due to the likely presence of a 'floating layer', as has also been observed for other transition metal doped nitrides. Microstructural investigations found that at low Sc contents the formation of I_1-type basal-plane stacking faults is promoted, while at higher contents lamellar inclusions of the cubic phase of up to 4 stacking repeats were observed. The local flattening of the wurtzite unit cell around substitutional Sc atoms was directly observed by XAS measurements, confirming theoretical predictions and giving confidence that related predictions for higher Sc content films are also correct.

Declaration

I hereby declare that except where specific reference is made to the work of others, the contents of this dissertation are original and have not been submitted in whole or in part for consideration for any other degree or qualification in this, or any other University. It is an account of the research that I have undertaken under the supervision of Dr. M. A. Moram in the Department of Materials Science and Metallurgy at the University of Cambridge between October 2010 and July 2014. This dissertation is the result of my own work and includes nothing which is the outcome of work done in collaboration, except where specifically indicated in the text and Acknowledgements. This dissertation contains less than 60,000 words including appendices, bibliography, footnotes, tables and equations.

STEPHAN MANUEL KNOLL
JULY 2014

Acknowledgements

I am grateful to everyone who has helped me in my research during my PhD, and my friends and family for supporting me during these four years. Although I cannot name all of them, I would like to single out individuals who deserve a special thanks.

Above all I thank my supervisor Dr. Michelle Moram, for her continuous encouragement, support and guidance during my studies and numerous discussions of my ideas and results. I am also grateful to both Michelle and Dr. Harvey Beere for providing me interesting samples to investigate, and Prof. Sir Colin Humphreys for giving me the opportunity to work in the GaN group.

I would like to extend my thanks to Dr. Suman-Lata Sahonta and Dr. Jon Barnard for their training in TEM, Dr. Rachel Oliver for providing AFM training and both Dr. Fabrice Oehler and Mary Vickers for their help in all matters of XRD. I am greatly indebted to Dr. Mauro Rovezzi, for both setting up the XAS measurements and for his time and patience in helping me with the data analysis. I am also incredibly thankful to Dr. Siyuan (Spark) Zhang, for providing me with theoretical simulations of the ScGaN system and also for the invaluable discussions of my work, and Dr. Wai Yuen (Gordon) Fu for proofreading my thesis. I would like to thank everyone else in the GaN group that has made these three years such a pleasant experience for me, both in and out of the lab.

Last but not least, I would like to thank my parents and my beautiful girlfriend Ayla for their endless love and support, without whom none of this would have been possible.

Contents

Contents i

Publications v

Nomenclature xiii

1 Background and literature review 1
- 1.1 III-nitrides . . . 1
  - 1.1.1 Crystal structure . . . 2
    - 1.1.1.1 Substrates . . . 3
  - 1.1.2 Defects in III-nitride epilayers . . . 4
    - 1.1.2.1 Dislocations . . . 4
    - 1.1.2.2 Stacking faults . . . 5
  - 1.1.3 Current challenges . . . 7
- 1.2 Transition metal III-N alloys . . . 10
  - 1.2.1 Dilute magnetic semiconductors . . . 11
    - 1.2.1.1 MBE growth of TMNs . . . 12
  - 1.2.2 General trends . . . 13
- 1.3 Scandium nitride . . . 14
  - 1.3.1 Band gap . . . 14
  - 1.3.2 Growth . . . 17
  - 1.3.3 Metastable phases . . . 17
- 1.4 ScGaN and ScAlN alloys . . . 18
  - 1.4.1 Electronic structure . . . 20
  - 1.4.2 Growth and defects . . . 21

2 Epitaxial growth techniques 23
- 2.1 Introduction . . . 23

2.2 Metal-organic vapour phase epitaxy . . . 24
2.3 Molecular beam epitaxy . . . 26

3 Characterisation techniques **31**
3.1 Hall measurements . . . 31
3.2 Ultraviolet-visible spectroscopy . . . 32
3.3 Photoluminescence spectroscopy . . . 33
3.4 Atomic force microscopy . . . 34
3.5 High-resolution X-ray diffraction . . . 36
3.5.1 HRXRD equipment . . . 38
3.5.2 Thickness measurement . . . 39
3.5.3 Composition determination . . . 39
3.5.4 Strain determination . . . 40
3.5.5 Limitations . . . 42
3.6 Transmission electron microscopy . . . 42
3.6.1 TEM apparatus . . . 43
3.6.2 Diffraction in the TEM . . . 45
3.6.3 Diffraction contrast . . . 45
3.6.4 Weak-beam dark-field imaging . . . 49
3.6.5 Scanning transmission electron microscopy . . . 50
3.6.5.1 Z-contrast imaging . . . 51
3.6.5.2 Energy dispersive X-ray spectroscopy . . . 54
3.7 X-ray absorption spectroscopy . . . 55
3.7.1 Data reduction and fitting . . . 56
3.7.2 Experimental setup . . . 59

4 Scandium nitride **61**
4.1 Introduction . . . 61
4.2 Structural investigation . . . 63
4.2.1 HRXRD analysis . . . 63
4.2.2 Microstructure . . . 65
4.2.2.1 Ammonia MBE . . . 65
4.2.2.2 PA-MBE . . . 67
4.2.2.3 Magnetron sputtering . . . 72
4.2.3 Surface morphology . . . 73
4.2.3.1 Ammonia MBE . . . 73

4.2.3.2 PA-MBE . . . 73
4.3 Optical and electrical measurements . . . 76
4.4 XAS studies . . . 78
4.4.1 Local bonding geometry . . . 78
4.4.2 Electronic structure . . . 79
4.4.3 Dichroism . . . 81
4.5 Synopsis . . . 82

5 ScGaN: Microstructure **85**
5.1 Introduction . . . 85
5.2 Determination of Sc content . . . 86
5.2.1 Energy dispersive X-ray analysis . . . 86
5.2.2 HRXRD analysis using $\omega - 2\theta$ scans . . . 87
5.2.3 X-ray absorption spectroscopy analysis . . . 89
5.3 Growth rates . . . 91
5.3.1 Substrate temperature . . . 91
5.3.2 Nitrogen flux . . . 92
5.3.3 Gallium flux . . . 92
5.3.4 Scandium flux . . . 94
5.4 Surface morphology . . . 95
5.4.1 Substrate temperature . . . 96
5.4.2 Scandium flux . . . 99
5.4.3 Gallium flux . . . 101
5.5 Strain analysis . . . 103
5.5.1 Relation between Sc content and strain . . . 103
5.5.2 Poisson ratio . . . 103
5.6 Microstructure . . . 107
5.6.1 Conventional TEM results . . . 108
5.6.1.1 Dislocations . . . 110
5.6.1.2 Stacking faults . . . 110
5.6.1.3 Additional planar defects . . . 113
5.6.2 High-resolution (HR) STEM . . . 113
5.6.2.1 Stacking mismatch boundary . . . 114
5.6.2.2 Cubic inclusions . . . 117
5.7 Synopsis . . . 118

6 ScGaN: X-ray absorption spectroscopy 121
6.1 Introduction 121
6.2 EXAFS 123
6.2.1 Data extraction 124
6.2.2 EXAFS fits 125
6.2.2.1 Fitting parameters 126
6.2.3 Results and discussion 126
6.2.4 EXAFS simulations 128
6.3 XANES 129
6.3.1 Discussion 131
6.3.2 X-ray linear dichroism 133

7 Conclusions and suggestions for future work 137
7.1 Conclusions 137
7.2 Suggestions for future work 139

A Analysis and TEM sample preparation techniques 143
A.1 Statistical analysis in the AFM 143
A.2 TEM specimen preparation 145
A.2.1 Cross-sectional specimens 145
A.2.2 Plan-view specimens 146
A.3 Monte Carlo simulation 147
A.4 X-ray analysis 147
A.4.1 Symmetric $\omega - 2\theta$ diffractogram simulations 147
A.4.2 RSM calculations 149
A.4.2.1 Method 149
A.5 Broadening of spectral lines 151
A.6 XAS pre-edge peak quantification 152

B Growth parameters 155
B.1 Ammonia MBE growth 155
B.2 Plasma-assisted MBE growth 156

C Preliminary PL data 161

References 167

Publications

Journals

"The electronic structure of scandium nitride: effects of disorder and oxygen incorporation"
S. M. Knoll, M. Rovezzi, S. Zhang, T. B. Joyce, and M. A. Moram
Applied Physics Letters (in preparation);

"Electronic structure and local distortions in epitaxial ScGaN films"
S. M. Knoll, M. Rovezzi, S. Zhang, T. B. Joyce, and M. A. Moram
Journal of Physics: Condensed Matter **26**, 225801 (2014);

"Defects in epitaxial ScGaN: Dislocations, stacking faults, and cubic inclusions"
S. M. Knoll, S. K. Rhode, S. Zhang, T. B. Joyce, and M. A. Moram
Applied Physics Letters **104**, 101906 (2014);

"Growth, microstructure and morphology of epitaxial ScGaN films"
S. M. Knoll, S. Zhang, T. B. Joyce, M. J. Kappers, C. J. Humphreys, and M. A. Moram
Phys. Status Solidi A **209:1**, 33–40 (2012);

Conferences

"Planar faults in epitaxial ScGaN films"
S. M. Knoll, S. K. Rhode, S. Zhang, T. B. Joyce, and M. A. Moram
International Conference on Nitride Semiconductors, Washington (2013)

"Electronic structure and local bonding of Sc in epitaxial ScGaN"
S. M. Knoll, M. Rovezzi, S. Zhang, T. B. Joyce, and M. A. Moram
International Conference on Nitride Semiconductors, Washington (2013)

"Morphology and microstructure of Epitaxial ScAlN Films grown on GaN by MBE"
S. M. Knoll, H. E. Beere, M. J. Kappers, D. A. Ritchie, and M. A. Moram
International Workshop on Nitride Semiconductors, Sapporo (2012)

"Structure, morphology and growth of epitaxial ScGaN films"
S. M. Knoll, T. B. Joyce, M. J. Kappers, C. J. Humphreys, and M. A. Moram
International Conference on Nitride Semiconductors, Glasgow (2011)

Nomenclature

Roman Symbols

C_s	Spherical aberration
O_h	Octahedral
R_{Ga}	Radius of Ga bonding shell
R_N	Radius of N bonding shell
Sc_{Ga}	Sc substituting on a Ga site
S_0	Amplitude reduction factor used in EXAFS fits
T_d	Tetrahedral
V_H	Hall voltage
$\mathbf{g}$	Diffraction vector
rs-ScN	Rock-salt ScN
wz-ScN	Wurtzite ScN
ABF	Annular bright-field
AFM	Atomic force microscopy
AlN	Aluminium nitride
B_k-ScN	Hexagonal BN-like ScN
BF	Bright-field
BSF	Basal plane stacking fault

CCD	Charge coupled device
CCS	Close-coupled showerhead
DF	Dark-field
DFT	Density functional theory
DMS	Dilute magnetic semiconductor
DPB	Double positioning boundary
E_g	Band gap
ECR	Electron cyclotron radiation
EDX	Energy dispersive X-ray spectroscopy
EELS	Electron energy loss spectroscopy
ELOG	Epitaxial lateral over-growth
ESRF	European Synchrotron Radiation Facility
eV	Electron volt
EXAFS	Extended X-ray absorption fine-structure spectroscopy
fcc	Face-centred cubic
FEG	Field emission gun
FOLZ	First-order Laue zone
FWHM	Full-width at half-maximum
GaN	Gallium nitride
GPA	Geometric phase analysis
HAADF	High-angle annular dark-field
hcp	Hexagonal close packed
HRTEM	High-resolution transmission electron microscopy

InN	Indium nitride
IQE	Internal quantum efficiency
IR	Infra red
J	Atomic or molecular flux
LD	Laser diode
LED	Light-emitting diode
MBE	Molecular beam epitaxy
MC	Monte Carlo
MD	Misfit dislocation
MOVPE	Metal-organic vapour phase epitaxy
O_N	Oxygen atom substituted on a nitrogen site
OTF	Optical transfer function
PA-MBE	Plasma-assisted molecular beam epitaxy
PDOS	Projected density of states
PIPS	Precision ion polishing system
PL	Photoluminescence
ppm	Parts per million
PSF	Prismatic stacking fault
PV	Plan-view
QCSE	Quantum confined Stark effect
QW	Quantum well
RBS	Rutherford backscattering
RDF	Radial distribution function

RF	Radio frequency
RHEED	Reflection high-energy electron diffraction
rlu	Reciprocal lattice unit
rpm	Revolutions per minute
RSM	Reciprocal space map
SAD	Selected area diffraction
SADP	Selected area diffraction pattern
sccm	Standard cubic centimeters per minute
ScN	Scandium nitride
SF	Stacking fault
SMB	Stacking mismatch boundary
STEM	Scanning transmission electron microscopy
TEM	Transmission electron microscopy
TM	Transition metal
TMG	Trimethylgallium
TMI	Trimethylindium
TMN	Transition metal nitride
UV	Ultraviolet
UV-Vis	Ultraviolet-visible
V_N	Vacancy on a nitrogen site
WBDF	Weak-beam dark-field
XANES	X-ray absorption near-edge spectroscopy
XAS	X-ray absorption spectroscopy

XLD	X-ray natural linear dichroism
XRD	X-ray diffraction
XS	Cross-sectional

Chapter 1

Background and literature review

"Education is a progressive discovery of our own ignorance."

- Will Durant

Contents

1.1 III-nitrides 1
1.2 Transition metal III-N alloys 10
1.3 Scandium nitride 14
1.4 ScGaN and ScAlN alloys 18

1.1 III-nitrides

Optoelectronic devices based on the III-nitrides AlN, GaN and InN have become commercially successful in the last two decades, and continue to be of both scientific and technological interest. This success is due in large part to the possibility of tailoring the band gaps (E_g) of alloys between the three constituent nitrides, which range from 0.78 eV for InN [1, 2] to 6.2 eV for AlN [3]. This covers a wide range of emission energies spanning from far infrared (IR) across the entire visible spectrum into the deep ultraviolet (UV). The band gaps of these III-nitrides and their alloys are all direct [4], such that electron-hole recombination can occur without the need of momentum transfer, leading to high recombination rates in the resulting optoelectronic devices. In conjunction with their high breakdown voltages, this makes the III-nitrides ideal materials for optoelectronic applications such as light emitting diodes (LEDs) and laser diodes (LDs) [5].

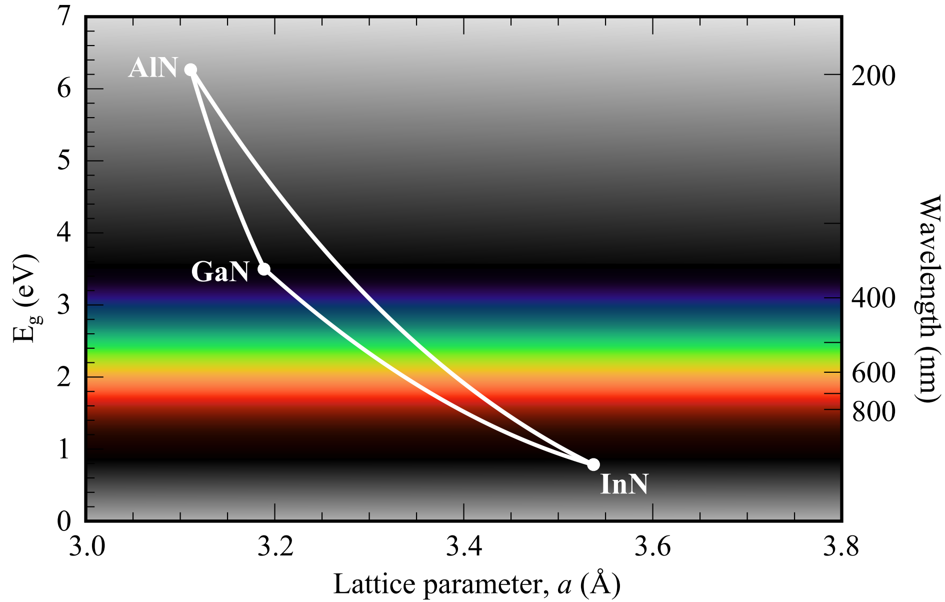

Figure 1.1: Band gap against lattice parameter for the conventional III-nitrides AlN, GaN and InN.

The band gaps of the wurtzite III-nitrides versus their lattice parameters are plotted in figure 1.1, with GaN shown to have a band gap of 3.4 eV [6], corresponding to emission in the near-UV. For UV applications AlGaN alloys are used, whereas InGaN-based materials are used in blue and green LEDs. The band gap for a ternary alloy is assumed to follow the quadratic equation given by equation 1.1, where b is the bowing parameter that accounts for the deviation from a linear relationship [3].

$$E_g(A_x B_{1-x}) = xE_g(A) + (1-x)E_g(B) - x(1-x)b \tag{1.1}$$

1.1.1 Crystal structure

GaN preferentially crystallises in the wurtzite phase [7] with lattice parameters $a = 3.189$ Å and $c = 5.185$ Å [6], although it is also possible to stabilise the zinc-blende phase under the appropriate growth conditions [8]. Most academic and industrial research has been conducted on materials in the wurtzite phase, with the structure of GaN depicted in figure 1.2. The wurtzite structure consists of two interpenetrating hexagonal close packed (hcp) sub-lattices of Ga and N, offset along [0001]. Along this direction, the arrangement can be described as alternating layers of Ga and N in the $A\alpha B\beta A\alpha B\beta$ configuration, where capital letters correspond to layers in the (0001) plane containing the metal atoms and Greek letters to the layers in the (0001) plane

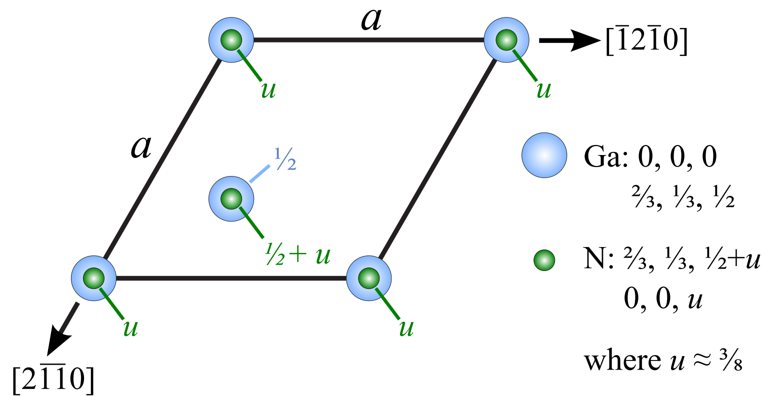

Figure 1.2: Plan view of wurtzite GaN unit cell. *wz*-GaN has a hexagonal lattice with a motif as indicated in the figure.

containing nitrogen atoms. The dimensionless internal parameter u describes the fractional offset in the [0001]-direction between the Ga and N atoms, where a value of $u = 0.375$ would correspond to ideal tetrahedral coordination of both Ga by N and *vice versa* (at room temperature, this value is closer to $u = 0.377$ for GaN).

The wurtzite phase is non-centrosymmetric with a space group of $P6_3mc$ and a *Strukturbericht* designation of B4. The deviation from ideal tetrahedral bonding around the Ga and N atoms also gives the structure an internal polarisation. Compared to competing material systems such as the III-arsenides or III-phosphides, the relatively small size of the nitrogen atom leads to a smaller lattice constant and larger band gaps. The strong metal-nitrogen bond is also responsible for extreme hardness and high chemical stability of the III-nitrides, although it does pose challenges for thin film and device growth.

1.1.1.1 Substrates

Due to the lack of cost-effective lattice-matched native substrates, the III-nitrides are conventionally grown heteroepitaxially on foreign substrates, using layer-by-layer growth techniques such as metal-organic vapour phase epitaxy (MOVPE) or molecular beam epitaxy (MBE) (see Chapter 2). The most commonly used substrate is (0001)-oriented sapphire (Al_2O_3), although Si, SiC and MgO have also been used [8]. Despite the large lattice mismatch between GaN and sapphire (16% after a 30° in-plane relative rotation of the unit cells), it is still the most widely used substrate for the growth of GaN, having the advantage of being optically transparent, stable at high temperatures and relatively inexpensive (compared to bulk GaN).

1.1.2 Defects in III-nitride epilayers

To study the effects of introducing scandium to the GaN structure, it is necessary to first understand commonly occurring structural defects in 'pure' III-nitrides themselves. These defects are classified according to their physical dimension:

Point defects Examples include foreign impurity atoms (which may be interstitial or substitutional) and native point defects, such as vacancies and/or self-interstitial atoms.

Line defects Known as dislocations, these are among the most commonly observed defect in GaN epilayers. In wurtzite crystals, three types are distinguished: *a*-type ($\mathbf{b} = 1/3\,\langle 11\bar{2}0 \rangle$), *c*-type ($\mathbf{b} = \langle 0001 \rangle$) and mixed-type ($\mathbf{b} = 1/3\,\langle 11\bar{2}3 \rangle$).

Planar defects These include stacking faults, grain boundaries in polycrystalline materials, twin boundaries and inversion domain boundaries.

1.1.2.1 Dislocations

Dislocations in epitaxial films are divided into two types, depending on their location with respect to the film and their line orientation with respect to their Burgers vector.

Misfit dislocations (MD) MDs originate at heteroepitaxial interfaces in order to accommodate lattice mismatch strains. For instance, at the InGaN/GaN interface, a pseudomorphic layer is formed in the InGaN where the in-plane lattice parameter compressively strained to match that of GaN. As the InGaN film thickness and corresponding strain energy increase, this pseudomorphic relationship can eventually no longer be maintained, resulting in the formation of misfit dislocations (line vector $\parallel$ interface) to accommodate the strain. The film thickness above which MDs are expected to form is known as the 'critical thickness' and can be predicted theoretically [9–11].

Threading dislocations (TD) TDs are introduced during the early stages of film growth and propagate throughout the thickness of the epilayers into the device active regions (line vector $\perp$ interface) [12, 13]. Heteroepitaxial GaN grown on Al_2O_3 will typically have TD densities ranging between 10^8 - 10^{10} cm^{-2}. High densities of TDs are deleterious to device performance, although their exact role is still under debate. It is argued that TDs act as non-radiative recombination centres for electrons and

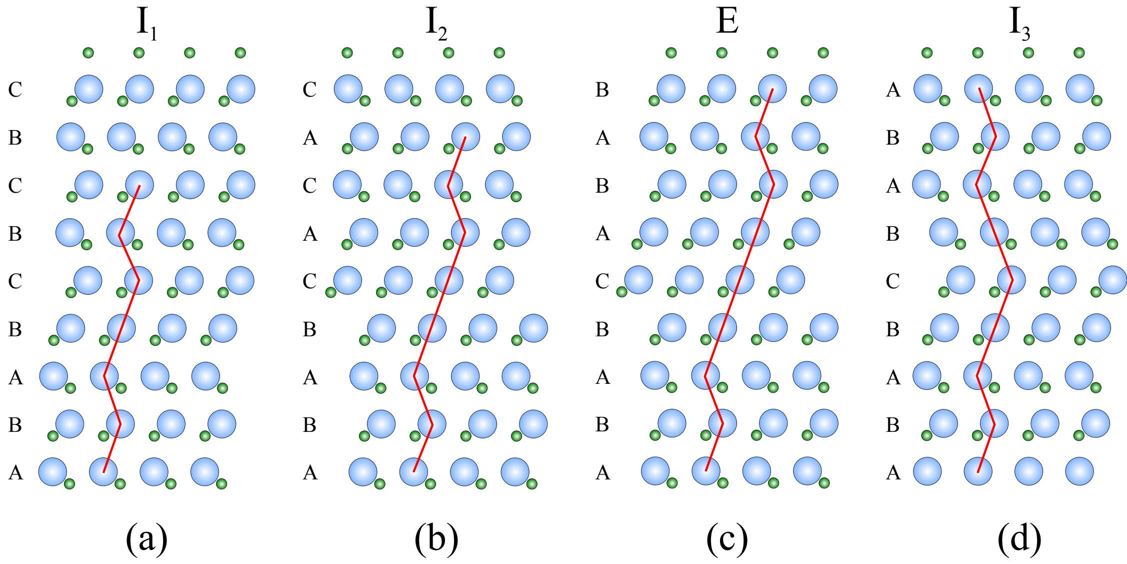

Figure 1.3: Illustration of intrinsic and extrinsic stacking faults in wurtzite crystals projected onto the $(11\bar{2}0)$ plane: (a) I_1-type, (b) I_2-type, (c) E-type and (d) I_3-type BSF.

holes by introducing localised electronic states in the band gap, thereby reducing the overall device efficiency [14]. Other studies suggest current leakage or impurity segregation to the dislocation cores as mechanisms for the observed efficiency losses [15]. Dislocation reduction methods include the use of interlayers (*e.g.* SiN_x [16] or ScN [17]) and epitaxial lateral overgrowth (ELOG) techniques [18].

1.1.2.2 Stacking faults

As introduced in section 1.1.1, the wurtzite lattice can be visualised as two interpenetrating hexagonal close packed lattices. Using GaN as an example, the (0001) basal planes are stacked in an ...*ABAB*... configuration along the *c*-axis, where each letter represents a Ga-N atomic bilayer. Stacking faults (SFs) can be treated as planar defects in which this ideal hexagonal stacking sequence is disrupted. In wurtzite III-nitride crystals, three types of basal-plane stacking faults (BSF) are encountered, which can be classified according to their displacement vector, **R**. These consist of two intrinsic (I_1 and I_2) and one extrinsic (E) BSF. A third type of intrinsic BSF (I_3) is sometimes distinguished, consisting of two adjacent I_1 faults after which the original stacking sequence is restored. A schematic of these is shown in figure 1.3.

I_1-type Intrinsic BSFs denoted I_1 are formed by the removal of a basal plane and subsequent shear by $1/3\,\langle 10\bar{1}0\rangle$, resulting in a stacking order described as ...*ABABCBCB*...

This corresponds to a single violation of the stacking sequence, with an associated displacement vector of $\mathbf{R} = 1/6\,\langle 20\bar{2}3\rangle$. I_1-type BSFs cannot form from shear alone and are therefore likely to be formed during growth [19, 20].

I_2-type The second type of intrinsic BSFs (I_2-type) consist of two violations of the stacking sequence, or the introduction of two rows of zinc-blende into the wurtzite structure. The corresponding displacement vector is $\mathbf{R} = 1/3\,\langle 1\bar{1}00\rangle$, and can be represented as ...$ABABCACA$... I_2-type BSFs can form after growth by shear or by dissociation of a perfect dislocation into two partials separated by the BSF [20].

E-type Extrinsic BSFs are obtained by inserting a complete sequence of zinc-blende stacking into the wurtzite crystal, *i.e.* three violations of the stacking sequence. The resultant stacking is ...$ABABCABA$... with a displacement vector of $\mathbf{R} = 1/2\,\langle 0001\rangle$.

The formation energies of these BSFs is proportional to the number of layers of 'cubic' (...$ABCABC$...) stacking in the fault. The relative formation energies of these various types of BSFs was investigated by Stampfl and Van de Walle [21]. I_1-type BSFs were found to have the lowest formation energies, as they correspond to only a single violation of the stacking sequence [21]. In non-polar GaN films, they constitute about 90% of the total number of observed BSFs, with the remaining 10% corresponding to I_2-type BSFs [20]. E-type BSFs have the highest formation energies and are not commonly observed [21].

Stacking faults can also occur on the prismatic $\{11\bar{2}0\}$ planes in wurtzite crystals. Various models have been proposed regarding their atomic structure, and have been referred to as prismatic stacking faults (PSFs) [22] and stacking mismatch boundaries (SMBs) [23, 24] and double-positioning boundaries (DPBs) [25]. Basal plane stacking faults cannot simply terminate inside a crystal, and must be bounded either by partial dislocations or PSFs [20, 23].

Twin boundaries can be considered a special type of stacking fault, where one part of the crystal is a mirror image of the other. The twin boundary acts as the mirror plane, and can be formed during growth (usually a result of a disruption in the growth conditions) or by mechanical stress after the crystal has formed (deformation twins) [26].

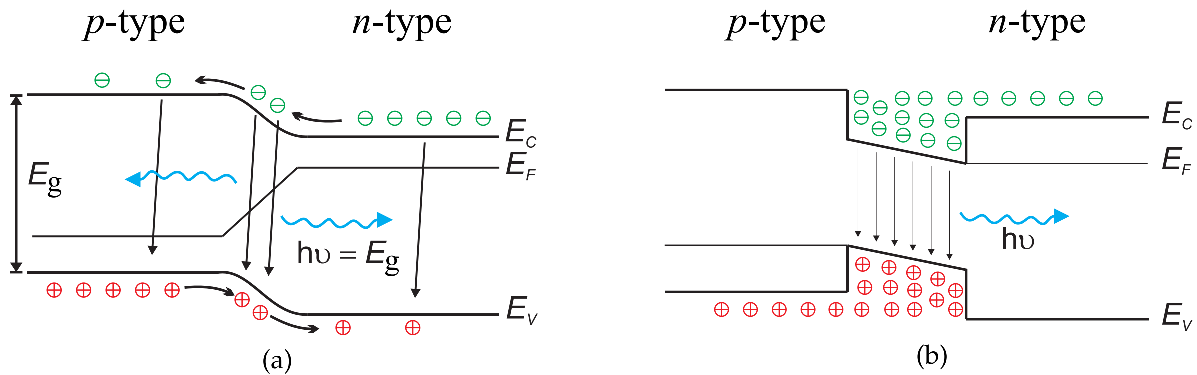

Figure 1.4: Schematic of two LED designs: (a) shows a *p-n* junction LED under forward bias and (b) shows a forward-biased quantum well LED. Reproduced from [28].

1.1.3 Current challenges

The simplest LED structure consists of a simple *p-n* junction, with a characteristic depletion layer at the interface (figure 1.4a). The first blue GaN LED produced by Nakamura in 1991 worked according to this principle [27]. By applying a forward bias to the device, recombination of electrons and holes across the junction result in the emission of photons corresponding to the exciton binding energy. Recombination rates are determined by the degree of electron and hole wavefunction overlap, and although the efficiency of the first GaN LED was very low ($< 0.1\%$) it showed enough promise to pave the way for all current III-nitride technology.

Radiative recombination rates can be improved by using a quantum-well (QW) device design, in which a material with a desired band gap (*e.g.* $In_xGa_{1-x}N$ with E_g = 2.8 eV, the 'well') is bounded by high band gap material (*e.g.* GaN with E_g = 3.4 eV, the 'barrier'). A schematic representation is given in figure 1.4b. Injected carriers will migrate to the region where they can achieve the lowest potential energy, *i.e.* the quantum well. This produces spatial confinement of the carriers and thus leads to enhanced recombination rates. Complex device designs require the use of epitaxial growth techniques such as MOVPE and MBE which can provide precise control of the growth rates (see Chapter 2).

However, although high internal quantum efficiencies (IQE) are routinely achieved for low In content InGaN devices, the IQE drops considerably for the higher In contents required to produce green light [29–32]. Although over the past 20 years researchers have been able to successfully fabricate efficient blue and red LEDs[1], the

[1]Red LEDs are produced using a different materials system based on the III-phosphides

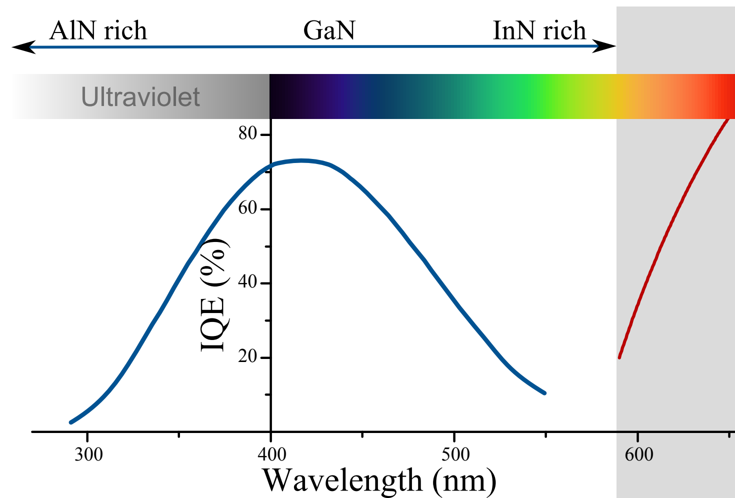

Figure 1.5: Plot of internal quantum efficiencies versus wavelength for quantum-well LED structures, showing the decrease in efficiencies in the ultraviolet and green parts of the spectrum. The blue curve represents IQE obtained by III-nitride structures, the red curve represents the III-phosphides. Replotted from [32].

efficiency of green emitters has lagged behind substantially, a problem commonly referred to as the 'green gap' (see figure 1.5). Although the origin of the green gap is not fully understood, the higher native point defect and impurity concentrations linked with the growth of high In-content InGaN may be responsible. The large lattice mismatch between GaN and high In-content InGaN also leads to the formation of misfit dislocations at the heteroepitaxial interface, which act as non-radiative recombination centres and contribute further to reductions in device performance and lifetimes [33].

The low efficiencies in the green spectral regions are somewhat compensated for by the visual responsivity curve of the human eye, which peaks at around 550 nm [32]. As ideally white light should be generated by the combination of blue, green and red LEDs, bridging the green gap is currently one of the greatest hurdles for the commercialisation of solid state lighting [29]. On the other side of the spectrum, AlGaN based UV-emitters are receiving increasing interest for energy efficient water purification, UV diagnostics and disinfection of medical tools [34]. However, a similar drop in efficiency is also observed here for high Al content AlGaN devices, with maximum current external quantum efficiencies of 10% for LEDs emitting in the $200 - 300$ nm range [35].

One of the fundamental limitations to III-nitride device performance arises due to the quantum confined Stark effect (QCSE), which describes the effect an external electric field has on the emission properties of a QW device. The internal polarisation

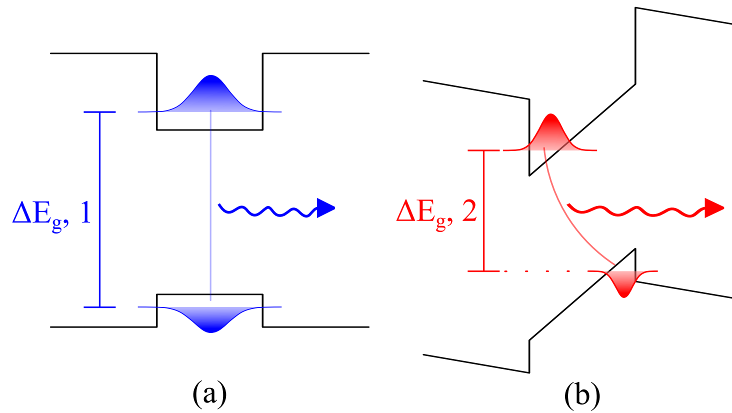

Figure 1.6: Illustration of the quantum confined Stark effect on a single quantum well, without (a) and with (b) an external electric field. The QCSE leads to bending of the band structure and redshift of emitted photons.

of the III-nitrides is increased with strain due to the piezoelectric effect and there is a significant polarisation mismatch at the interfaces between the QW and the barrier layers separating the QWs, leading to a bending of the electronic band structure as shown in figure 1.6. The result is a spatial separation of carriers across the QW and a lowering of the emitted photon energy. The decreased wavefunction overlap leads to increased carrier lifetimes and thus lower IQEs. Three broad directions are being investigated with the aim of overcoming the QCSE:

1. Narrow QWs One approach to tackle the QCSE problem is to use a greater number of narrower QWs, such that the physical separation of electrons and holes is minimised.

2. Eliminate internal fields Another approach is to minimise the internal polarisation. There is ongoing research into using non *c*-plane, higher Miller index planes on which reduced components of the polarisation vector are directed perpendicular to the QW, such as the semipolar *t*-plane $\{11\bar{2}2\}$ and nonpolar *a*-planes $\{1\bar{1}20\}$ and *m*-planes $\{1\bar{1}00\}$. Growth of GaN with these surfaces can be achieved by using substrates oriented parallel to suitable planes, for instance *a*-plane GaN has been successfully grown on *r*-plane sapphire $(1\bar{1}02)$ [36] and on *a*-plane SiC [20]. However, in addition to the difficulty in obtaining suitable substrates, problems with the incorporation of indium and high defect densities are hindering progress in this field [37].[2]

[2]Common methods rely on using expensive bulk GaN substrates cleaved in the appropriate direction, or patterned templates.

3. Novel material systems The QCSE could also be eliminated by designing a device in which there is no polarisation discontinuity across the active region. This might be achieved by using ternary or quaternary alloys in which both the polarisation and the lattice parameter of the QW and the quantum barriers can be tuned. Currently, this is impossible for most wavelengths, due to the limited degrees of freedom provided by alloys consisting of only the three available III-nitrides AlN, GaN and InN. Additional flexibility in the design of lattice-matched heterostructures could be obtained by introducing a fourth alloy end member to the conventional III-nitride system. To overcome these challenges, researchers have looked to replace either the metal cation or the nitrogen anion. Depending on the properties of the new materials, it may also be possible to expand the functionality and applications of these materials.

The remaining group III-elements boron and thallium would be considered obvious candidates but their solubilities in GaN and AlN are far too low for them to be of practical use, primarily due to the large atomic size mismatch. For instance, at common epitaxial growth temperatures of 1000 K, spinodal decomposition occurs for BGaN and BAlN alloys for boron contents above about 5%, and thallium is expected to show a similarly low solubility [38, 39]. Instead, the focus is shifted to transition metals (TM) with a 3+ oxidation state, which could be used to substitute for the metal cation. In fact, transition metal nitrides (TMNs) are a well studied material system in their own regard, and some alloys between TMNs and group III-nitrides are also known, such as rock-salt TiAlN and CrAlN [40]. The following section will give a brief overview of the current research into TM doped III-nitrides.

1.2 Transition metal III-N alloys

Rock-salt transition metal nitrides are of technological interest due to their excellent physical properties, such as high hardness, stiffness, and chemical and thermal stability. As such, they are commonly used as hard wear-resistant coatings, thermoelectric barriers and diffusion barriers. The most extensively studied TMN is TiN, which is currently being used in all the aforementioned applications [41]. The electronic properties of TMNs are similar across the *d*-block elements, with most displaying a metallic character. This has been explained by the delocalisation of *d*-shell electrons, which are not involved in the bonding to nitrogen and thus occupy antibonding states. These 'surplus' electrons push the Fermi energy into the conduction band,

leading to metallic conductivity [42–44].

1.2.1 Dilute magnetic semiconductors

Extensive research has been devoted to TM-doped GaN in recent years, albeit not for optoelectronic but for spintronic applications. The field of spintronics aims to exploit both the spin and the charge of the electron simultaneously, and could lead to increased storage densities, higher processing speeds and lower power consumption [45]. TM-doped GaN has attracted a lot of interest for the development of a dilute magnetic semiconductor (DMS), which as the name suggests, are semiconductors in which a fraction of the host cations have been replaced by magnetic ions.

Since Dietl *et al.* [46] predicted ferromagnetic behaviour in GaN doped with at least 5% Mn, there has been extensive research into experimentally producing a GaN-based DMS. It should be noted that his prediction also required a hole density of above 10^{20} cm^{-3}, which is so large that it may in fact never be obtainable in practice.[3] Although Mn-doped GaN has received most of the attention to date, some work has been published on other TM-doped and rare-earth doped nitrides. The focus has been on the first row of *d*-block transition metals, as these have the smallest size mismatch with Ga. Several reviews exist on the search for a room temperature DMS [47–50].

Unfortunately the literature on TM-doped GaN is very broad and often contradictory, and it can be challenging to identify general trends. Nevertheless, one consistent obstacle is the low solubility level of the transition metal in GaN, ranging from about 0.4% for Fe [51] to a maximum of about 4% for Mn [52], depending on the fabrication method used. Above the solubility limit, nucleation of metal-rich precipitates occurs (see figure 1.7), although spinodal decomposition has also been suggested [53]. Considering the low solubility limit, the size and volume fraction of the precipitates will be very small, and detection remains a challenge, as conventional X-ray diffraction will not necessarily reveal the presence of small volumes of other phases. Instead, advanced characterisation tools such as high-resolution transmission electron microscopy (HRTEM) coupled with energy-dispersive X-ray spectroscopy (EDX) [51], or synchrotron radiation techniques such as EXAFS [54, 55] are required.

[3] Dietl's original publication also suggested room-temperature ferromagnetism should be achievable in Mn-doped ZnO; there is parallel research into doping ZnO with transition metals [47].

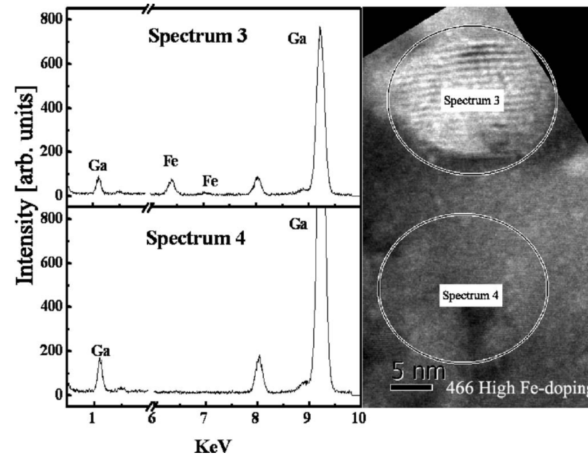

Figure 1.7: HRTEM image of a MOVPE grown (Ga,Fe)N nanocrystal showing Moiré fringe contrast. The EDX spectra on the left-hand side indicate that the nanocrystal is Fe-rich. Reproduced from [51].

To suppress the formation of secondary phases, a wide range of non-equilibrium growth techniques have been investigated, including MOVPE, MBE, pulsed-laser deposition and ion-implantation (see the review by Bonanni [48] and the references therein). As the magnetic properties are strongly dependent on the growth technique and crystalline quality, there is considerable variation in the results published in the literature for work done on the same material system, making it difficult to identify trends and key results. For instance, for the (Ga,Mn)N system, the reported magnetic properties range from paramagnetic, ferromagnetic, antiferromagnetic to spin-glass behaviour. A wide variation also exists in the measured Curie temperatures for the reportedly ferromagnetic materials, with values ranging from 10 K [56] to as high as 940 K [57]. However, many of these investigations acknowledge the likely presence of a secondary magnetic phase which, depending on the method of fabrication, may in fact be the main contributor to the observed ferromagnetic response.

1.2.1.1 MBE growth of TMNs

As mentioned above, considering the low solubilities of TMs in GaN, non-equilibrium epitaxial growth techniques such as MBE are frequently employed. As the crystal properties, including surface quality, stoichiometry, electronic and magnetic properties are all dependent on the specific growth conditions used, considerable effort is dedicated to the understanding and optimisation of the MBE growth process.

Surface morphology and reconstruction The smoothest surface morphologies for binary GaN are achieved in the Ga-rich regime [26, 58]. For ternary alloys, the smoothest surface morphologies were found at the transition between metal-rich and Ga-rich regimes [26].

Several studies report on a distinct change in the reflection high-energy electron diffraction (RHEED) pattern during growth when in the metal-rich regime, indicating a different surface reconstruction. However, *ex-situ* analysis after growth revealed no differences in the surface reconstruction. This is attributed to the presence of a metal 'floating layer' during growth, consisting of a 1-2 atom thick layer of metal which has diffused to the surface [59–61].

Suppression of precipitation by co-doping Various studies reported a suppression of the formation of secondary phases by co-doping with Si or Mg (both shallow impurities), thus effectively increasing the solubility limit of the TM [62]. In the case of (Ga,Fe)N, it was suggested that co-doping changes the oxidation state of the Fe ions, leading to a reduction in ion aggregation due to magnetic interactions. In the case of (Ga,Mn)N, effective co-doping was achieved using H, with solubility levels increasing from undoped values of 3-4%, to single crystal films with Mn contents of up to 7% [63, 64]. It appeared that the presence of hydrogen during growth inhibited phase segregation for higher levels of Mn, although the mechanism for this suppression is yet unknown.

1.2.2 General trends

Identifying general trends within the TM-III-nitride system is difficult due to the wide range of growth techniques employed and also due to the wide range of results reported within a single material system. In particular, problems such as the aforementioned solubility limit have not necessarily been considered by all experimenters and their presence would have significant impact on the interpretation of the experimental results. However, from the literature certain trends can be distinguished which are common to all *d*-block TM-III-nitride alloys.

1. At dopant concentrations the TM form localised states within the band gap [26, 44]

2. At higher concentrations the Fermi energy lies in the conduction band leading to metallic behaviour [42–44]

3. The low solubility limit arises due to excess *d*-shell electrons occupying antibonding states [43, 48, 62]

4. The formation of a metal 'floating' layer at the surface during growth [59–61]

5. An increased solubility limit by appropriate co-doping [62–64]

6. The smoothest surface morphologies are obtained by growth in slightly metal-rich conditions [26]

1.3 Scandium nitride

Scandium possesses only a single *d*-shell electron, and almost always assumes the 3+ oxidation state, by giving up its $4s^2$ and $3d^1$ electrons. This is in contrast to other transition metals, where multiple oxidation states are common. As a result, the chemical properties of ScN lie somewhat in between those of the III-nitrides and TM-nitrides (figure 1.8a).

Like other TMN, ScN crystallises in the rock-salt structure[4], and has a lattice parameter of $a = 4.5057 \pm 0.0005$ Å [65] (figure 1.8b). However, while other TMNs are metallic in character, ScN is semiconducting, with an indirect band gap of E_g = 0.9 eV and a direct band gap at 2.1 eV [66–68]. Due to its small lattice mismatch with GaN in the (111) plane (0.1%) and the much lower band gap, ScN attracted a lot of technological interest for band gap engineering with GaN (see § 1.1.3 on page 10). Additionally, ScN interlayers have been shown to successfully reduce threading dislocation densities in MOVPE grown GaN epilayers [17, 69].

1.3.1 Band gap

Early experimental and theoretical studies were divided on the true nature of the band structure of ScN. Some early reports suggested that ScN was a semimetal [70–72], attributed to a slight band overlap between the conduction and valence bands. However, these findings relied on either poor-quality samples and/or on early uncorrected density functional theory (DFT) calculations, which are well-known to underestimate the magnitude of the band gap [73].

[4]The rock-salt structure is denoted B1 in the *Strukturbericht* designation.

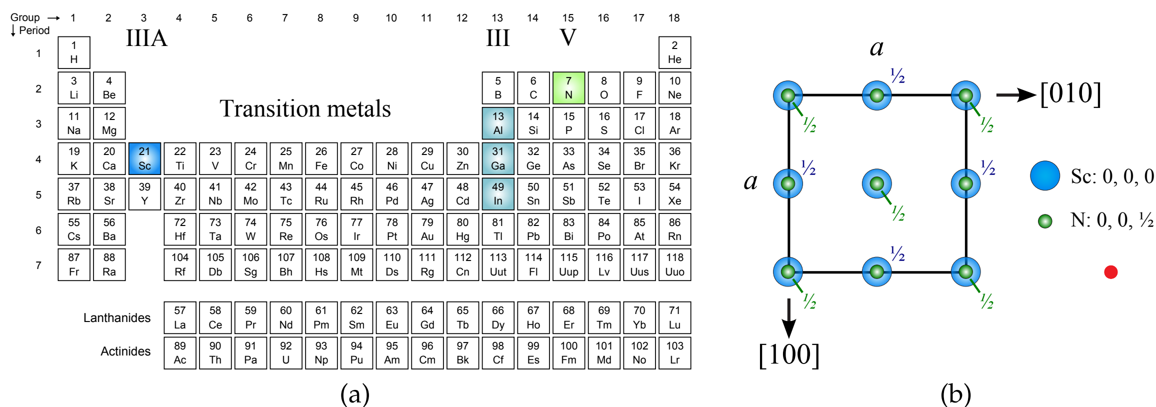

Figure 1.8: (a) Periodic table showing the elements of interest for the III-nitride family. Sc sits in the IIIA transition metal group and preferentially displays a 3+ oxidation state.
(b) Plan-view unit cell of rock-salt ScN, with a lattice parameter of $a = 4.5057 \pm 0.0005$ Å [65]. *rs*-ScN has a face-centred cubic lattice, with a motif as indicated in the figure.

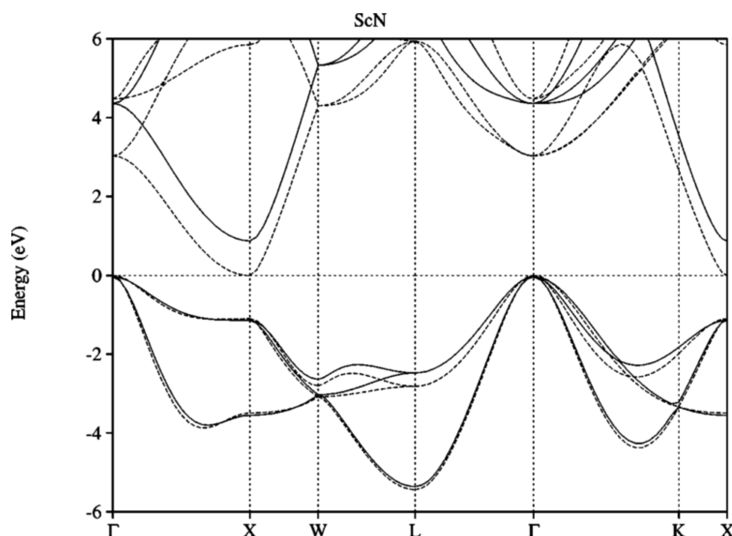

Figure 1.9: Uncorrected (dashed lines) and corrected (solid lines) DFT calculation of the band structure of *rs*-ScN, showing the indirect band gap from $\Gamma \rightarrow X$ [74]. Calculations using quasiparticle [74] and exact exchange interaction calculations yield indirect band gaps of $0.9 - 1.3$ eV and a direct band gap of $2.0 - 2.4$ eV [68].

III-nitride	a (Å)	c (Å)		E_g(eV)	Ref.
AlN	3.112	4.982	6.23	direct at Γ	[6]
GaN	3.189	5.185	3.50	direct at Γ	[6]
InN	3.545	5.703	0.78	direct at Γ	[1]
rs-ScN	4.506	-	0.9 2.1	indirect at $\Gamma \rightarrow X$ direct at X	[74]
wz-ScN	3.49	5.58	$\sim$4	indirect at $M \rightarrow \Sigma$	[72]
B_k-ScN	3.66	4.42	1.55	indirect at $\Gamma \rightarrow K$	[76]

Table 1.1: Important parameters of the III-nitrides including lattice parameter at room temperature and magnitude of band gaps.

It has since been established that ScN is indeed semiconducting, with a small, indirect band gap at $\Gamma \rightarrow X$[5] of between 0.9 - 1.3 eV and a direct band gap of 2.0 - 2.4 eV [66–68]. These findings are supported by theoretical studies using DFT calculations with quasiparticle corrections [74] (figure 1.9) and exact exchange interactions [68]. A summary of the lattice parameters and band gaps of the III-nitrides including ScN is given in table 1.1. Unlike other TMNs, the electronic configuration of Sc means that both the 3*d* and 4*s* electrons are involved in the bonding with nitrogen. This pushes the Fermi level into the band gap between the nitrogen and scandium orbitals, giving ScN the unusual semiconducting behaviour otherwise not observed in TMNs.

The electronic properties were found to be sensitive to the relative concentration of nitrogen and scandium vacancies, which can vary depending on the growth method used. The evolution of the density of states with stoichiometry was investigated by Moreno-Armenta *et al.* [77]. The study shows that for nitrogen-deficient materials (ScN_x, with $x < 1$) the Fermi energy lies inside the conduction band and metallic properties are expected, whereas for $x \geq 1$ the material is expected to display semiconducting properties. This can be qualitatively understood by considering the available nitrogen *p*-states the Sc *d*-electrons can occupy [42]. Similar trends have also been observed for non-stoichiometric TiN_x compounds [78]. These calculations may in part account for the discrepancies in reported values for the band gap of ScN, although experimentally it has been difficult to synthesize pure sub-stoichiometric ScN [42]. High concentrations of electrically active impurities may also affect the mea-

[5]The capital letters in band structure calculations correspond to different high symmetry points in the Brillouin zone. More information can be found in any good physics textbook, such as [75].

sured band gap by the Moss-Burstein shift and/or by alloying effects [42, 79, 80]. The Moss-Burstein shift is an apparent increase in the measured band gap due to the filling of all electronic states close to the conduction band edge. Electrons from the top of the valence band can only be excited into unoccupied states in the conduction band, leading to an observed increase in the apparent band gap.

1.3.2 Growth

ScN in its rock-salt structure (*rs*-ScN) has been synthesized by a range of techniques, including direct nitridation of Sc metal [81], decomposition of nitride intermetallic phases [82], sublimation-recondensation [83], sputter deposition [79, 84–86], MOVPE [87] and MBE [88–90]. From a devices perspective, epitaxial growth techniques are preferred (§ 2.3 on page 26), although recently atomically-smooth single-crystal ScN films have also been grown using reactive magnetron sputtering [86]. Well-oriented epitaxial ScN films have also been grown by MBE on MgO by Al-Brithen *et al.* [88] and on Si (111) by Moram *et al.* [89]. Vapour phase epitaxial growth of ScN was achieved by Dismukes *et al.* [66] on sapphire and later by Edgar *et al.* [91] on 6H-SiC (0001). The use of MOVPE for growth of ScN would be advantageous not only due to the high quality films obtainable by this technique but also for the ease of integration with GaN growth technologies. However, currently available scandium-based organometallics have vapour pressures too low to be integrated into existing GaN reactors. Although there is active research in the field of TM and rare-earth organometallic precursors for MOVPE [87, 92], there is still no chemical precursor available for Sc which has a suitably high vapour pressure and purity.

1.3.3 Metastable phases

Pioneering theoretical work by Takeuchi [72] predicted a metastable wurtzite phase for ScN (*wz*-ScN) using first-principles calculations. The energy of the wurtzite phase was found to be only moderately higher than that of the rock-salt phase (0.34 eV/formula unit), and it was suggested that the wurtzite phase could be stabilised by appropriate alloying, such as with GaN. The predicted band gap of *wz*-ScN was in the region of $4 - 5$ eV, with lattice parameters a = 3.49 Å and c = 5.58 Å [72]. However, Farrer and Bellaiche refuted this study, claiming that the wurtzite structure is unstable in ScN [76]. Instead, they predicted a different metastable structure for ScN (B_k-ScN), with an energy of just 0.316 eV/formula unit higher than the rock-salt phase, and an

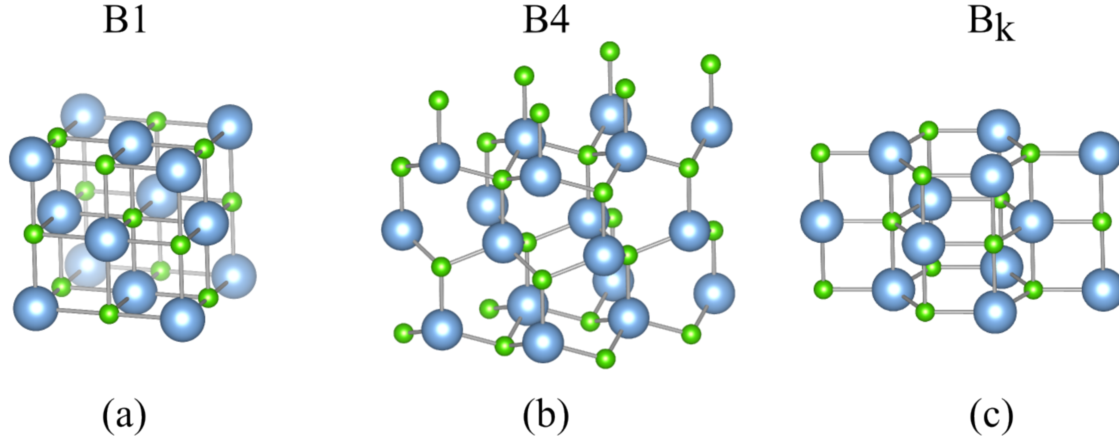

Figure 1.10: Schematic representations of the predicted crystal structures of ScN. (a) *rs*-ScN, (b) *wz*-ScN predicted by Takeuchi [72] and (c) B_k structure first predicted by Farrer and Bellaiche [76].

indirect band gap of 1.5 eV [93]. This structure is also hexagonal (predicted lattice parameters of a = 3.66 Å and c = 4.42 Å), but unlike wurtzite has an internal parameter of $u = 0.5$, such that the Sc and N atoms both lie in the same basal plane (figure 1.10).

In this configuration, ScN exhibits five-fold coordination, which can be viewed as a 'flattening' of the wurtzite unit cell. Because of its 6/mmm point group symmetry, B_k-ScN is a non-polar structure, compared to the wurtzite III-nitrides which show electrical polarisation (§ 1.1.1 on page 2). This non-polar phase is of huge technological interest for the fabrication of multifunctional materials, which simultaneously exhibit semiconducting and ferroelectric properties.

1.4 ScGaN and ScAlN alloys

Motivated by the exotic B_k-structure predictions for ScN, subsequent research went into identifying methods that could stabilise this phase. Farrer and Bellaiche suggested that this could be achieved by alloying with a wurtzite material such as GaN [76, 93, 94]. Recent theoretical studies have predicted that $Sc_xGa_{1-x}N$ and $Sc_xAl_{1-x}N$ alloys retain the wurtzite structure with direct band gaps for Sc mole fraction of up to x = 0.66 and x = 0.56, respectively [95]. For higher compositions the structures are expected to assume the rock-salt configuration of binary ScN. As the Sc content is increased while in the wurtzite regime, a gradual evolution in the c/a ratio is observed from 1.6 to 1.2 (corresponding to the B4 $\rightarrow$ B_k transition), accompanied by a local flattening of the wurtzite structure in the vicinity of the Sc atoms. By stabilising

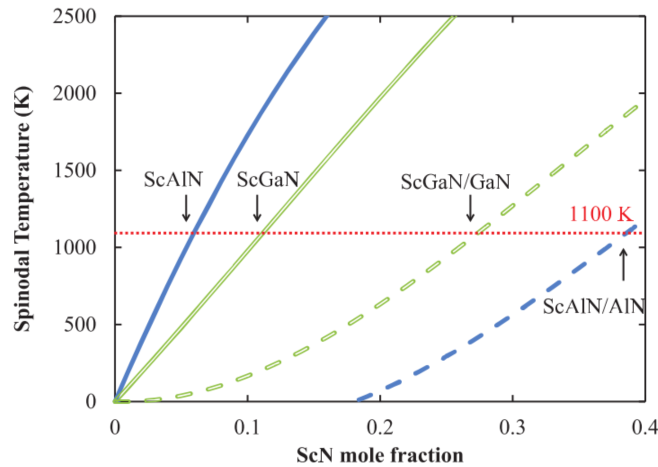

Figure 1.11: Variation of spinodal decomposition temperatures with Sc mole fraction for strained and unstrained ScGaN and ScAlN alloys. Reproduced from [95].

a ScGaN alloy in the wurtzite phase just before the B4 $\rightarrow$ B_k transition, it could be possible to fabricate devices which simultaneously exploit semiconducting and ferroelectric properties [95]. Ranjan *et al.* [93] found that close to the transition region, B_k-ScN films should experience large variations in the piezoelectric coefficient with increasing compressive strain. This has led to a lot of research activity in the synthesis of ScAlN alloys with increased piezoelectric coefficients, driven by potential applications in energy harvesting devices [96–99].

The relative stability of the wurtzite and rock-salt phases is dependent on both the composition and the temperature of the alloy system, and thus in real systems a phase separation into low Sc-content wurtzite phase and high Sc-content rock-salt phase is expected. Phase separation is likely to occur via spinodal decomposition rather than nucleation and growth, due to kinetic constraints in the latter. For unstrained materials, the onset of spinodal decomposition at a common epitaxial growth temperature of 1100 K has been predicted to be x = 0.11 for ScGaN and x = 0.06 for ScAlN [95] (figure 1.11). However, experimental studies on ScAlN films grown by sputter deposition show that single-phase wurtzite films have been obtained for compositions of up to x = 0.43 [96]. The onset of spinodal decomposition was found to be strongly affected by in-plane epitaxial strains. By straining the ScGaN films compressively on GaN substrates, the compositional stability of the wurtzite phase was found to increase to up x = 0.27 (x = 0.40 for ScAlN) [95]. Epitaxial single-crystal wurtzite films have also been grown by MBE for compositions of up to x = 0.17, above which the crystal quality deteriorated and mixed-phase films were obtained [100, 101]. In order

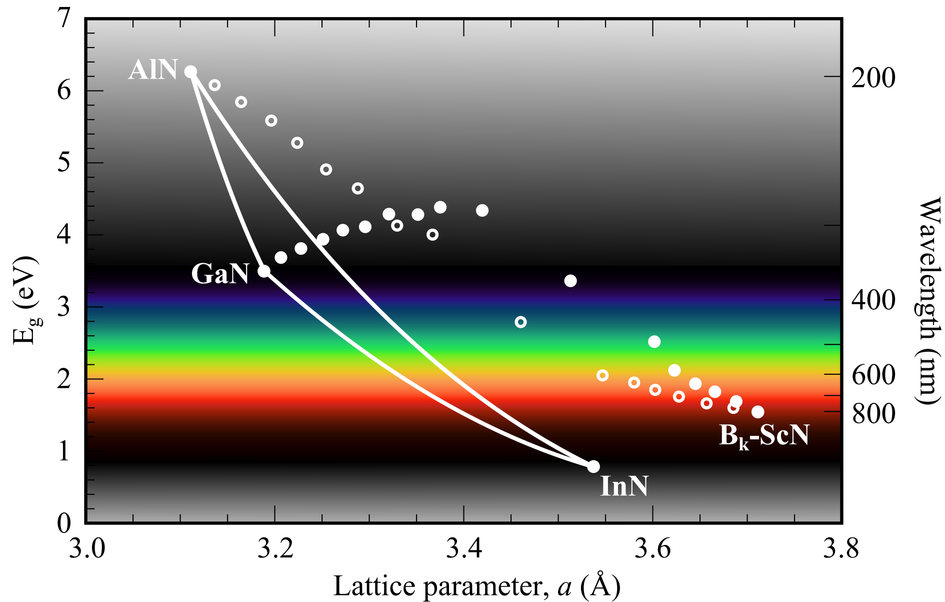

Figure 1.12: Band gap against lattice parameter for the conventional III-nitrides (solid lines) and the calculated values for ScGaN (filled circles) and ScAlN (empty circles) included in the plot. The discrete points correspond to the calculated lattice parameters and band gaps by [95]. A description of the B_k crystal structure can be found in § 1.3.3 on page 17.

to achieve device-quality single-phase ScGaN and ScAlN films, epitaxial growth on III-nitride materials is a necessity.

1.4.1 Electronic structure

Both ScGaN and ScAlN films are expected to remain semiconducting while in the wurtzite structure. Although accurate predictions of the absolute magnitude of the band gap are difficult with DFT, by using suitable band gap corrections realistic predictions of variations with composition can be made. A general decrease of the band gap of ScAlN alloys with increasing Sc content was predicted [95] and observed experimentally [102]. Recent theoretical investigations predicted that the band gap of ScGaN films should increase with Sc content [95]. For these films, the band gaps are expected to remain direct for compositions of up to $x = 0.5$ (figure 1.12).

However, experimental results differed from these predictions: an early investigation of sputtered polycrystalline ScGaN films found the band gap to decrease monotonically with Sc content [103], and a similar trend was also observed for wurtzite MBE-grown films of compositions up to $x = 0.17$ [100]. While the sputtered films were

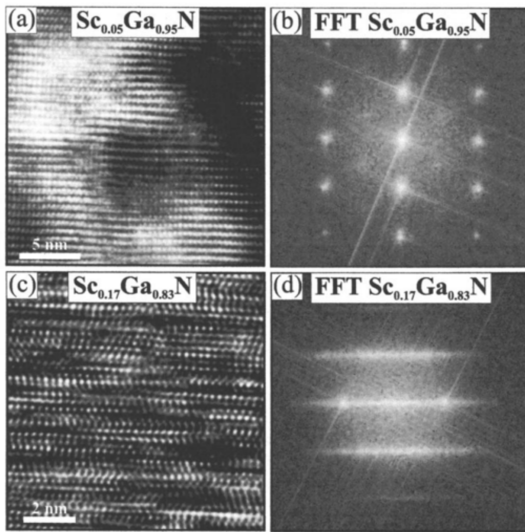

Figure 1.13: High resolution TEM images of epitaxial ScGaN films with (a) x = 0.05 and (c) x = 0.17 and their respective Fast Fourier Transforms (b) and (d). Both films showed significant densities of stacking faults and the in-plane long-range crystalline order appears to be completely lost for the higher Sc content film. Reproduced from [101].

most likely mixed-phase, it is more difficult to explain the result from the higher-quality MBE-grown films. It is possible that sub-band gap recombination occurred due to high density of planar defects (*e.g.* stacking faults and/or potentially nanoscale inclusions of the zinc-blende phase) or due to a large degree of band gap bowing.

1.4.2 Growth and defects

In order to realise Sc-based III-nitride devices, it is essential to achieve low-defect density epitaxial film growth. Although epitaxial ScGaN films have already been grown by PA-MBE, even the best films are significantly far from device-quality. The surface morphology was very rough (peak-to-valley heights of up to 875 Å), indicative of a 3D growth mode [101]. For increasing Sc content, large contrast variations in successive basal planes were observed by HRTEM, and diffraction analysis showed that in-plane long-range crystalline order is lost for compositions of $x = 0.17$ (figure 1.13).

A decrease in the c/a ratio was also observed for increasing Sc mole fractions, in accord with the theoretical predictions made for ScGaN films by Farrer and Bellaiche [76]. Although the variation in c/a has been claimed as evidence of a flattening of the wurtzite bilayer [100, 101], no direct observations of this nature have yet been made. Other experimental studies of MBE grown ScGaN films also report on high densities of stacking faults, although again no detailed study on their nature has been attempted [100, 101, 104]. Epitaxial, wurtzite ScGaN films approaching device quality have also been grown by Moram *et al.* [105] using ammonia MBE. Using this method, no evidence of stacking faults was observed for compositions of up to $x = 0.02$.

Chapter 2

Epitaxial growth techniques

"Perseverance, secret of all triumphs."

-Victor Hugo

Contents

2.1 Introduction 23

2.2 Metal-organic vapour phase epitaxy 24

2.3 Molecular beam epitaxy 26

2.1 Introduction

This chapter will give a brief description of the two most widely used epitaxial growth techniques for III-nitrides: metal-organic vapour phase epitaxy (MOVPE) and molecular beam epitaxy (MBE), both used in the fabrication of samples investigated in this thesis. Although MBE began purely as a tool for academic research, significant improvements in the development of MBE components have transformed it into a commercial device used for production of advanced semiconductor structures. However, most of the III-nitride material produced commercially is grown by MOVPE, due to the higher growth rates and lower dislocation densities than can be obtained. The Sc-based III-nitride epilayers investigated in this work were grown by MBE on GaN (0001) templates, themselves grown heteroepitaxially on Al_2O_3 (0001) substrates by MOVPE. These GaN template films will be referred to as GaN-on-sapphire 'pseudo-substrates' throughout this thesis (figure 2.1).

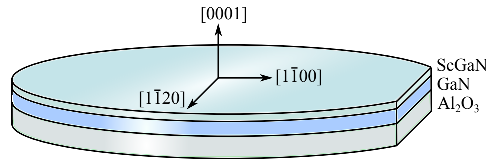

Figure 2.1: Schematic of ScGaN epilayer grown by MBE on GaN-on-sapphire pseudosubstrate. The GaN was grown by MOVPE.

2.2 Metal-organic vapour phase epitaxy

MOVPE has become the principal technique for the epitaxial growth of nitride semiconductors, both in research and for commercial mass-production of optoelectronic devices such as LEDs and LDs. Its relatively high throughput (up to a maximum capacity of 7 $\times$ 6-inch wafers per run for an industrial reactor [106]), high growth rates (up to 5 µm/hour), high uniformity ($<$ 1% thickness variations across the wafer) and high system up-times make it economically advantageous compared to MBE.

In MOVPE, crystal growth occurs by the chemical reaction of compound precursors at the substrate surface. For the III-nitrides, the metallic precursors are organometallic compounds such as trimethylgallium (TMG) or trimethylindium (TMI). These precursors are liquid at room temperature. However, their high vapour pressure at this temperature means that the vapour can be transported by means of an inert carrier gas, usually H_2, Ar or N_2, which is bubbled through the liquid. Ammonia gas (NH_3) provides the source of nitrogen. A simple description of the growth process is as follows [107]:

1. A gas mixture containing the precursor molecules is passed over a heated substrate
2. The precursor molecules pyrolyse leaving the metal atoms on the surface
3. Surface diffusion and chemical reaction between metal atoms and NH_3-derived species form the new crystal

The precursors react at the substrate surface according to the following reaction [107]:

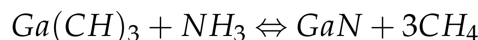

$$Ga(CH)_3 + NH_3 \Leftrightarrow GaN + 3CH_4$$

It should be noted that the above reaction is a considerable simplification of the actual mechanisms involved during growth. There are many designs of MOVPE reactors, such as the close-coupled showerhead (CCS) reactor design (an illustration is shown in figure 2.2). The CCS reactor design minimises parasitic reactions and improves the compositional and thickness uniformity of the resulting films by injection

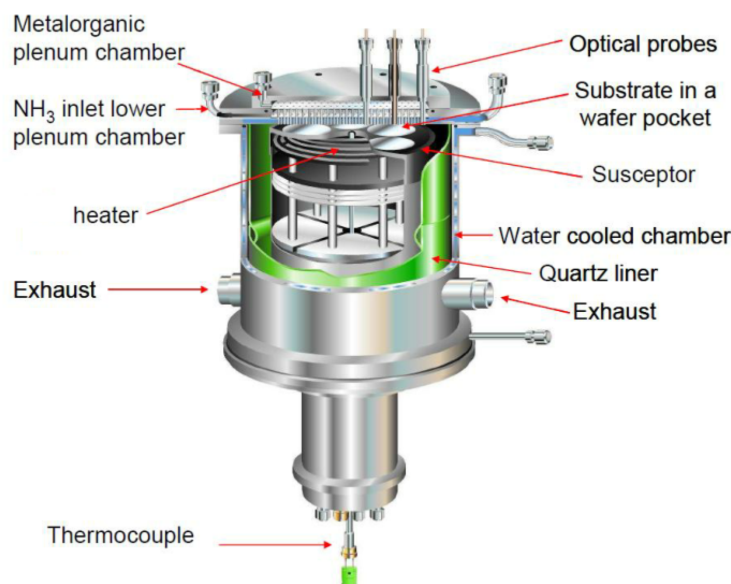

Figure 2.2: Illustration of a *Thomas Swan* close-coupled showerhead MOVPE reactor. The showerhead design minimises unwanted parasitic reactions by physically separating the precursors until they are close to the substrate. Adapted from [109].

of the precursors through an array of closely spaced tubes, resembling a showerhead. The showerhead sits only a few millimetres above the substrate surface. Additionally, the substrate is continuously rotated to increase uniformity further.

The substrate temperature, V/III ratio and reactor pressure can be controlled during the MOVPE process to control the film properties. High substrate temperatures are commonly used for the growth of GaN, commonly $1000 - 1100$ °C [108]. This allows both significant amounts of surface diffusion, improving the surface morphology, as well as an increased cracking efficiency of the ammonia gas. Growth is also commonly performed at very high V/III ratios ($10^4 - 10^5$), to stabilise the GaN (0001) surface and prevent the desorption of nitrogen.

A series of 500 nm *c*-plane GaN films used as pseudosubstrates in this work were grown by MOVPE on *c*-plane sapphire wafers using a *Thomas Swan Scientific Equipment* 6×2-inch CCS reactor. Growth was performed by Dr. Menno Kappers at the Department of Materials Science and Metallurgy in the University of Cambridge. The GaN films were grown at a substrate temperature of 1020 °C, after growth of an initial low-temperature nucleation layer at 540 °C. The dislocation density of the GaN film as measured by TEM was $(6 \pm 1) \times 10^9$ cm^{-2}, where $80 \pm 2\%$ were edge dislocations and the remaining $20 \pm 2\%$ were mixed type. Less than 1% of the dislocations

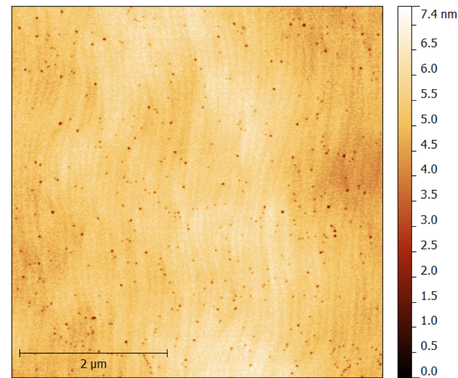

Figure 2.3: Linearly flattened atomic force microscopy height scan of a 500 nm GaN-on-sapphire pseudosubstrate. The high dislocation density and step-flow growth is clearly visible in the image.

were pure screw (*c*-type) [110]. Further details on the growth procedure and characterisation of the GaN epilayers can be found in references [111]. High dislocation density templates were deliberately chosen because (a) they are comparatively thin and thus relatively fast to grow, (b) relaxation in thicker GaN templates would further influence the properties of the overgrown ScN and ScGaN and (c) a sufficiently high density of dislocations allows for easier characterisation of the defect microstructure in the ScN and ScGaN films by TEM. Atomic force microscopy of the GaN templates showed a very smooth step-flow morphology, with an RMS roughness of R_q= 0.3 nm (figure 2.3).

2.3 Molecular beam epitaxy

MBE is an epitaxial growth technique in which a thin film is grown on a substrate surface by reactions between molecular beams of the constituent species. Despite many practical challenges, the lower growth rates compared to MOVPE (*e.g.* 0.5 µm/hour) and rapid elemental source switching capability lead to precise control of layer thicknesses and interfacial abruptness, while *in-situ* reflection high-energy electron diffraction (RHEED) monitoring and the ability to use a wide range of elemental precursors make MBE an extremely versatile technique for the preparation of semiconductor films [58, 112].

The film composition is determined by the arrival rates and the sticking coefficients of the primary elements and dopants at the growth temperature. A schematic representation of a typical MBE system is shown in figure 2.4. Molecular beams are produced by thermally evaporating precursor materials in effusion cells. The gas molecules will not be scattered if their mean free path is larger than the chamber di-

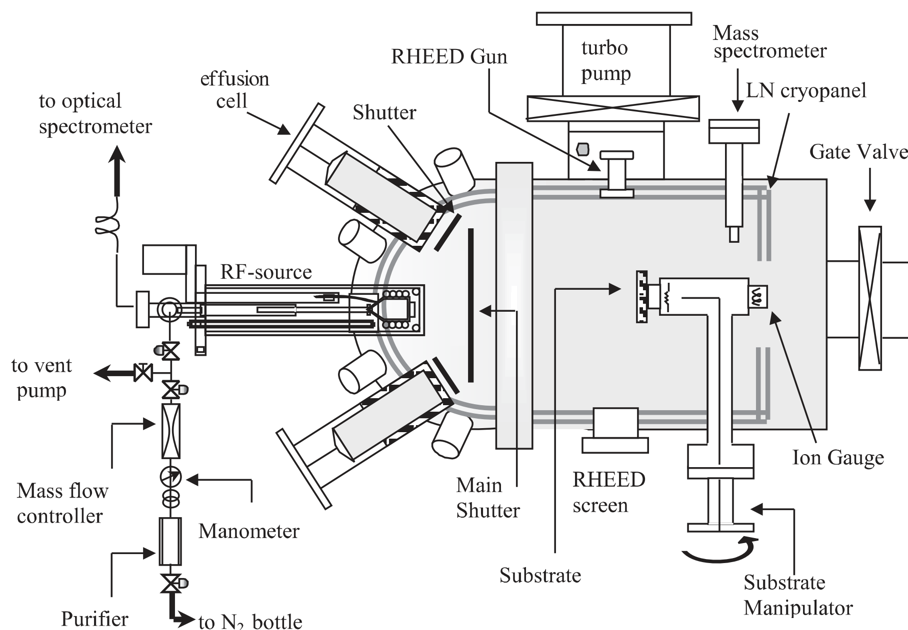

Figure 2.4: Schematic of a typical MBE system fitted with RHEED. Adapted from [58].

mensions, and are hence termed 'molecular beams'. This criterion is easily fulfilled if the total pressure inside the chamber does not exceed 10^{-6} Pa.

Elemental precursors There are several different methods to grow GaN by MBE, depending on the nitrogen precursor. While the source of Ga is usually provided by an effusion cell, obtaining atomic nitrogen is more complicated. It is not possible to use diatomic nitrogen gas (N_2) in itself because typical growth temperatures (600 – 800 °C) are not high enough to break the nitrogen triple bond. In plasma-assisted MBE (PA-MBE), a plasma is used to dissociate the nitrogen molecule. Common ways to create nitrogen plasmas include radio-frequency (RF) [113–115] and electron cyclotron radiation (ECR) sources [116]. The fraction of excited species in the nitrogen plasma is an important factor affecting the surface film quality [117] as high-energy ions can create crystallographic damage.

Epitaxial, single-crystal films have also been produced using ammonia MBE (also known as *reactive* MBE), using ammonia gas (NH_3) as a nitrogen source (NH_3 dissociates more readily than N_2) [118]. NH_3-MBE has the advantage of providing a highly reducing atmosphere in the MBE chamber, which effectively reduces oxygen incorporation in the film (previously identified to be a problem for the growth of ScN, due to the high oxygen affinity of Sc [79]). On the other hand, films grown by ammonia MBE are likely to suffer from a higher degree of hydrogen incorporation, due to the

formation of hydrogen upon dissociation of the ammonia. Additionally, *in-situ* characterisation techniques such as RHEED cannot be employed due to the high partial pressure of ammonia [26, 58, 112]. Furthermore, growth conditions are inherently nitrogen-rich, due to the excess residual ammonia which is invariably present in the growth chamber.

The effusion cells in MBE use thermal evaporation of very high purity condensed material to produce a molecular or atomic flux (designated J). Electronic shutters in front of the orifices are used to abruptly shut the atomic flux on or off. The cell temperature is a key parameter which can be controlled to adjust the amount of flux and therefore the film growth rates and composition. As with MOVPE, the film surface morphology obtained is strongly dependent on the III/V ratio [113–115].

Substrate temperature The substrate is heated from behind by an infrared source, and continuously rotated to improve lateral thermal homogeneity across the wafer. It provides the impinging species with enough thermal energy to overcome the energy barrier to diffuse to a favourable site. High surface adatom diffusion is required to obtain atomically smooth films. Although higher substrate temperatures facilitate surface diffusion, thermal decomposition of the film and adatom desorption are also increased, leading to surface roughening and slower growth [58]. The optimum growth temperature for compound semiconductors generally lies in the range of 1/2 to 2/3 of the predicted melting temperature. Common growth temperatures for GaN (T_m = 2500 °C) are usually in the range of 600 − 800 °C, due to the decomposition of the GaN (0001) surface into Ga and N_2 at higher temperatures [118]. The surface morphology can be monitored *in-situ* by RHEED [114, 119].

From a practical perspective, uniformity in both composition and layer thickness is crucial to device performance, requiring precise control over the growth rates. For InGaN, temperature variations of only ±5 °C can lead to significant changes in both the growth rate and composition [26].

Growth regimes The atomic composition of the growing film is dependent on the surface concentrations of the reactive species. This ratio is not simply dependent on the ratio of atomic fluxes, because the sticking coefficients of the different species themselves vary depending on the structure and composition of the growth surface. Therefore it is not simple to predict the film composition solely from the flux ratios. In the purely binary GaN system there are only two growth regimes: nitrogen-rich

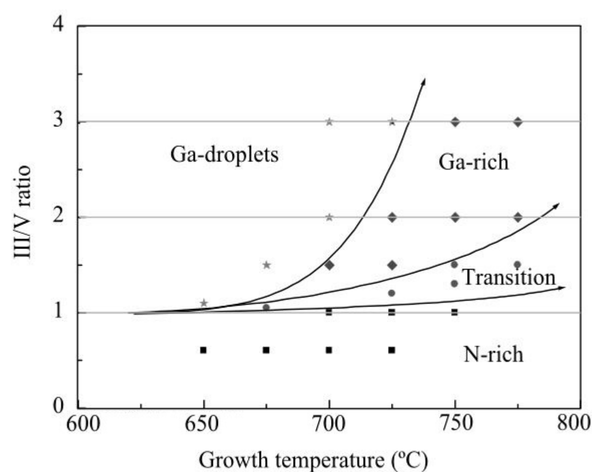

Figure 2.5: Growth regimes for MBE growth of GaN for varying III/V ratio. The smoothest films are typically grown in the transition region between Ga-rich and N-rich conditions. From [26].

and gallium-rich. The best quality films are obtained at the transition point between the two regimes (see figure 2.5). However, for a three-component system such as ScGaN one would expect to find three growth regimes: nitrogen-rich, metal-rich (Ga-predominant) and metal-rich (Sc-predominant).

Chapter 3

Characterisation techniques

"I hear and I forget,
I see and I remember,
I do and I understand."

-Confuzius

Contents

3.1 **Hall measurements** 31
3.2 **Ultraviolet-visible spectroscopy** 32
3.3 **Photoluminescence spectroscopy** 33
3.4 **Atomic force microscopy** 34
3.5 **High-resolution X-ray diffraction** 36
3.6 **Transmission electron microscopy** 42
3.7 **X-ray absorption spectroscopy** 55

3.1 Hall measurements

Room-temperature Hall measurements were performed in the van der Pauw geometry using a custom-built machine. The advantage of the van der Pauw technique is that is was developed to work well on arbitrarily shaped thin films, provided they are simply connected and are not islanded [75]. Samples were cleaved into 10×10 mm

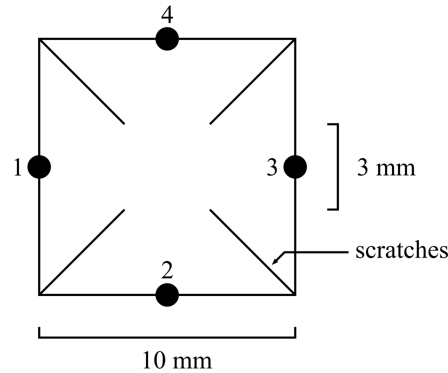

Figure 3.1: Van der Pauw contact placement for Hall measurements.

squares, with diagonal scratches applied preserving a 3×3 mm area in the centre (figure 3.1). Electrical contacts to the surface were made using indium solder, positioned on the centre of the specimen edges. The carrier density (N) is given by:

$$N = \frac{IB}{q|V_H| \cdot t}$$

where I is the current applied through the sample (through contacts 1 and 3); B is the magnetic field applied perpendicular to the plane of the sample; q is the electronic charge of the carriers, V_H is the Hall voltage (measured across opposing pair of contacts 2 and 4) and t is the film thickness.

3.2 Ultraviolet-visible spectroscopy

Ultraviolet-visible (UV-Vis) spectroscopy in materials science is routinely used to establish the band gaps of semiconductors. Here, measurements were performed using an *Agilent* Cary 5000 UV-Vis spectrophotometer capable of operating in the $175 - 3300$ nm range, with a maximum achievable wavelength resolution of < 0.05 nm in the UV-Vis spectral region [120]. In UV-Vis spectroscopy, monochromated light from either a tungsten-halogen or deuterium lamp (depending on the wavelength used) is passed through the sample onto a photo-diode (figure 3.2).

Quantities such as transmittance, reflectance and absorbance can be determined with respect to a blank reference sample. The optical absorption is displayed on a Tauc plot [122], which typically shows energy on the abscissa and the quantity $(\alpha E)^2$ on the ordinate. Tauc plots of this nature typically display a linear portion in the

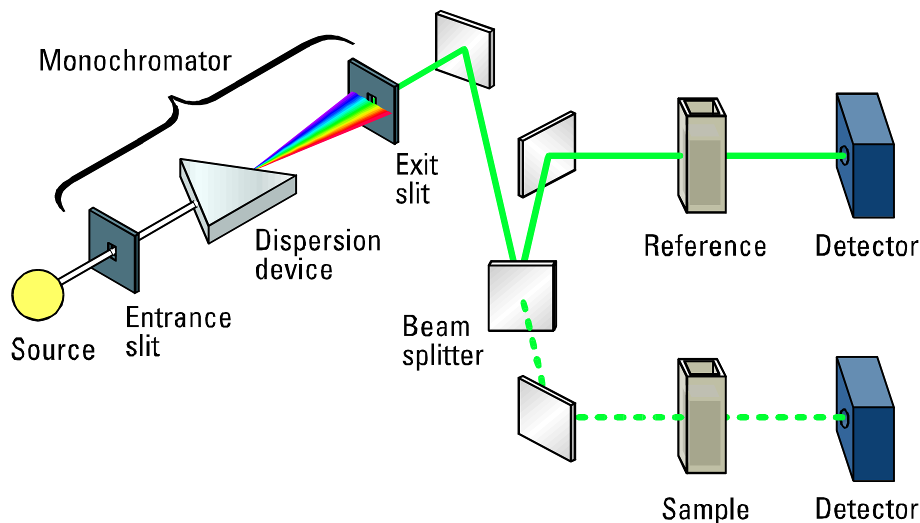

Figure 3.2: Schematic of a split-beam UV-Vis spectrophotometer system [121].

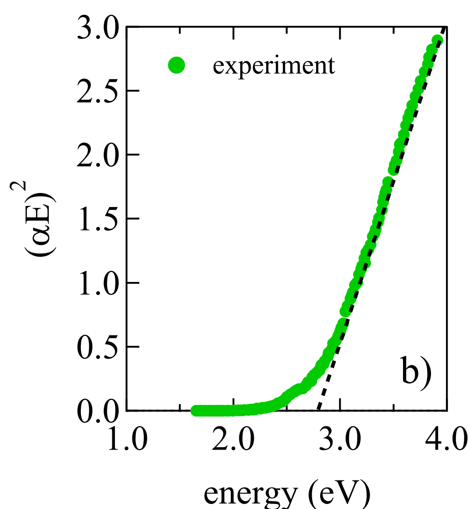

Figure 3.3: Typical example of a Tauc plot, in this case a NiFeO thin film. The intercept of the straight line segment with the abscissa indicates the optical band gap. Adapted from [123].

spectrum denoting the onset of optical absorption. The energy of the optical band gap can be determined by extrapolating this linear portion to the abscissa (figure 3.3).

3.3 Photoluminescence spectroscopy

Photoluminescence (PL) spectroscopy is one of the most common techniques used to study the optical properties of semiconductors, and is frequently used as one of the first characterisation tools to give rapid feedback to the growers. In PL spectroscopy, a laser light source with an energy higher than the band gap of the material measured is used to produce electron-hole pairs in the crystal, which may be bound together as

an exciton, if the exciton binding energy is greater than the thermal energy available at the measurement temperature.

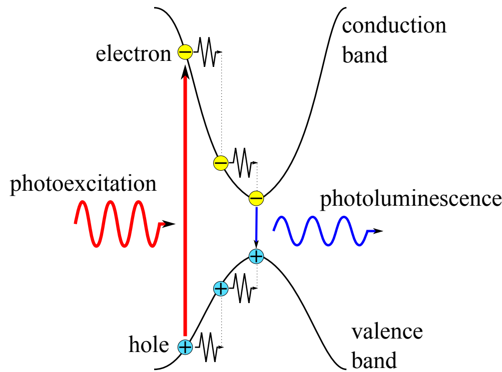

Figure 3.4: Schematic illustration of the photoluminescence process.

The electrons and holes thermalise by emitting phonons, reaching the conduction band minimum or the valence band maximum, respectively. Recombination of the electron and hole pair results in the emission of a photon (figure 3.4). The PL emission spectrum of direct band gap semiconductors contains useful information on the band gap at the measurement temperature, and relative defect or impurity concentrations (due to characteristic emission peaks associated with the levels introduced by the defects into the band gap) [124–126].

PL measurements were conducted at room-temperature using an *Accent* RPM 2000 spectrometer. A λ = 266 nm laser source (operating at an average power between $1-3$ mW) was used with a 600 g/mm diffraction grating, slit width of 0.1 mm and 300 nm focal length monochromator, giving a wavelength resolution of 0.50 nm. The laser power was decreased by inserting neutral density filters in the incident beam path, allowing data to be collected using varying excitation powers. The PL can also be used in mapping mode, which is used to analyse the PL emission uniformity across the wafer. Here, the wafer is rotated rapidly with a spectrum taken at each point on the surface.

3.4 Atomic force microscopy

Atomic force microscopy (AFM) is a non-destructive technique used to study surface topography, in which a very sharp tip is rastered across a surface to produce an image. The scanning probe consists of a sharp tip located at the end of a cantilever. The cantilever is flexible enough to be deflected by interactions between the tip and the surface, such as Coulomb or Van der Waals forces (see figure 3.5).

In its simplest form, the AFM scanning process can be described in a few steps:

- Tip rastered across surface

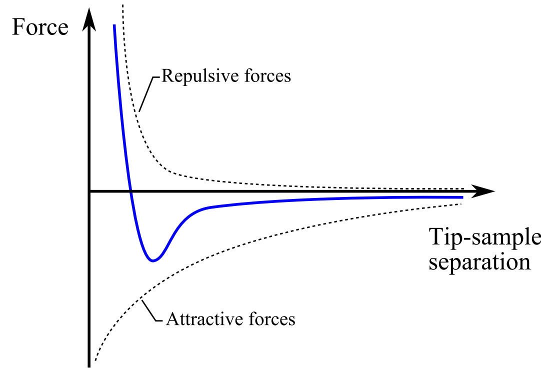

Figure 3.5: Force response curve for AFM tip interacting with sample surface. At large separations the Van der Waals forces lead to attractive tip-sample interaction. When the tip is close to the surface the repulsive Coulombic forces deflect the cantilever.

- Tip deflection detected by reflecting a laser off the cantilever (see figure 3.6)
- Feedback circuit adjusts the cantilever height until deflection returns to zero

The AFM can be operated in several modes, however, all images in this work were acquired in tapping mode using a *Digital Instruments* Dimension 3100 microscope. In tapping mode, the cantilever is oscillated just below its main natural resonant frequency by a piezo-actuator and is maintained at a fixed height above the surface by keeping the tip oscillation amplitude constant using a feedback circuit (by setting a fixed parameter termed the 'amplitude setpoint'). As the tip scans over the surface, the resonant frequency and amplitude of oscillation are affected by changes in the tip-surface separation (equation 3.1). The parameters in the feedback circuit can be adjusted to obtain optimum imaging conditions for each sample.

$$\omega = \omega_0 \sqrt{1 - \frac{1}{k}\frac{dF}{dz}} \tag{3.1}$$

where ω is the resonant frequency, k is the elastic modulus of the cantilever and $\frac{dF}{dz}$ is the force gradient with tip-sample separation [127]. It must be noted that images produced by AFM are a type of convolution between the tip and the sample surface geometry. The best vertical resolution of the AFM is excellent and commonly lies in the sub-Ångstrom regime. Although in principle only limited by the vertical resolution of the piezo scanner, in practice the primary limiting factor is system noise due to mechanical and electric vibrations [127]. However, measured depths are commonly

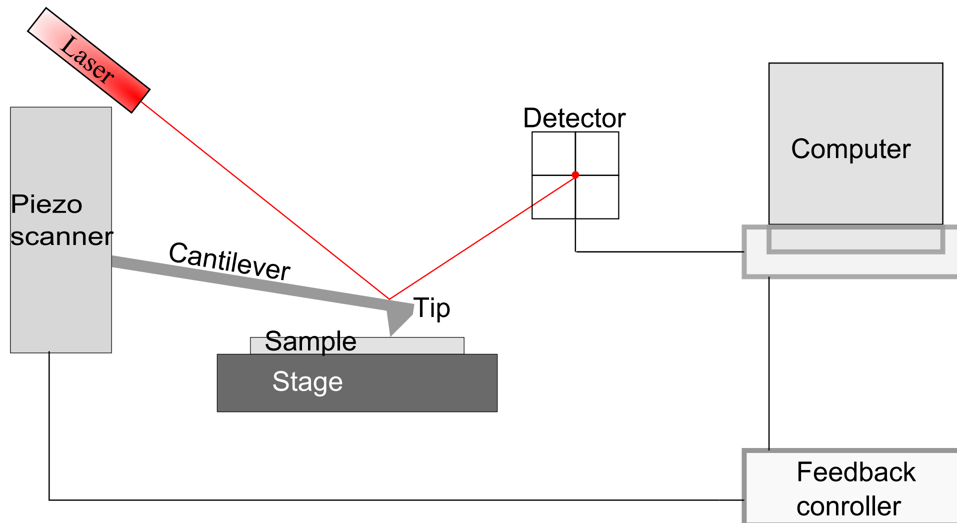

Figure 3.6: Schematic of AFM apparatus. Deflections in the cantilever are picked up by a laser reflected onto a four-piece photodetector. In tapping mode, the feedback circuit adjusts the tip-specimen separation to maintain a set oscillation amplitude.

underestimated for very narrow surface features (such as the pits that frequently appear where dislocations intersect the surface of a thin film), because the tip is not able to fully penetrate to the bottom. The lateral resolution is very strongly dependent on both the tip and the surface, with smaller tip radii necessary to achieve higher resolutions [128]. An illustration of these error sources is given in figure 3.7.

3.5 High-resolution X-ray diffraction

High resolution X-ray diffraction (XRD) is a popular, non-destructive technique for the characterisation of heteroepitaxial thin films that requires no sample preparation. It can be used to determine composition, strain state and thickness of layered structures, all of which are important parameters that affect device performance. The crystal structure is analysed by XRD by measuring the intensity of diffracted X-ray beams as a function of the incident angle. Constructive interference occurs when the path difference between scattered rays is related to the interplanar spacing by Bragg's Law (equation 3.2):

$$n\lambda = 2d_{hkl}\sin(\theta) \tag{3.2}$$

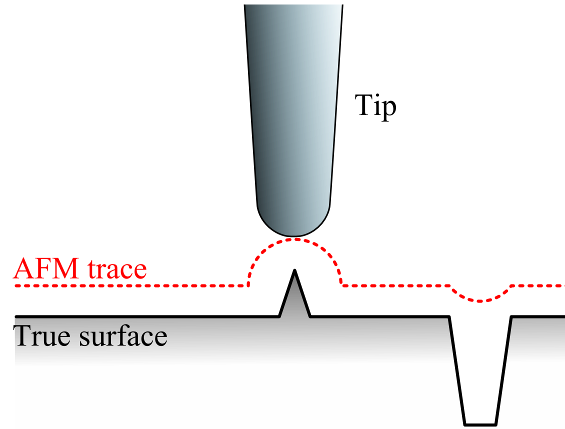

Figure 3.7: Sources of lateral and vertical errors in the AFM trace due to a finite tip size. In this illustration the effects of a hemispherical tip are considered.

where n is an integer, λ is the radiation wavelength, d_{hkl} is the separation of the diffracting planes and θ is the (Bragg) angle at which constructive interference occurs (figure 3.8). Measurement of the Bragg angle gives the interplanar spacing from which the lattice parameters of the crystal can be calculated. In a hexagonal system, the interplanar spacing is related to the Miller indices of the plane by the following relation [129]:

$$\left(\frac{1}{d_{hkl}}\right)^2 = \frac{4}{3}\frac{h^2 + k^2 + hk}{a^2} + \frac{l^2}{c^2} \tag{3.3}$$

where a and c are the in-plane and out-of-plane lattice parameters, respectively. In practice, this requires measurement of at least one symmetric and one asymmetric reflection (as defined in [130]). The c lattice parameter can be obtained directly from any accessible symmetric reflection. For GaN, these correspond to the 0002, 0004 and 0006 reflections. Whilst higher order reflections minimise the error in d_{hkl}, the intensity decreases rapidly with increasing 2θ angle, with the adequate choice of reflection dependent on the sample studied. Then, an asymmetric reflection is measured; the $10\bar{1}5$ and $20\bar{2}1$ reflections are commonly used, with the former being of higher intensity. The value of the in plane lattice parameter, a, is calculated with equation 3.3 using the previously obtained value for c.

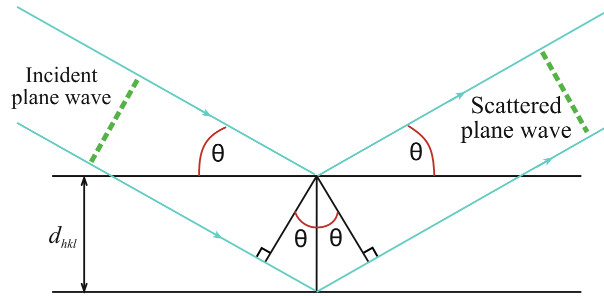

Figure 3.8: The condition for constructive Bragg interference is satisfied when the path difference between the diffracted beams is an integer number of wavelengths, λ. Adapted from [131].

3.5.1 HRXRD equipment

Due to the high crystalline quality of nitride semiconductors (and correspondingly sharp diffraction peaks), a high degree of instrumental precision is required to resolve closely-spaced peaks and to locate peak maxima accurately. Measurements were performed in the 'triple-axis' setup [129] to achieve maximum resolution (see figure 3.9).

The X-ray beam is generated by a copper target giving a wavelength of $\lambda = 1.540597$ Å, corresponding to the Cu $K\alpha_1$ transition [130]. In the incident beam optics, the emitted X-rays are collimated into a bright parallel beam using a graded parabolic mirror, which also removes the Cu Kβ radiation. The beam is then passed through an asymmetric 4-bounce Ge (220) monochromator to restrict the spectral and angular spread of the beam. The sample is mounted on a Eulerian cradle, allowing translation along x, y and z axes as well as rotation along ω, ϕ and ψ. ω is defined as the angle between the incident beam and the sample surface and 2θ is the Bragg angle between the incident beam and the diffracted beam. In the diffracted beam optics, a triple-bounce analyser crystal is placed before the detector to narrow the angular integrated intensity of the diffracted beam. In this work, a *Philips* X'Pert MRD diffractometer was used, with ω and 2θ accurate to $\sim$0.0001°. In the double-axis configuration, the analyser crystal is removed from the diffracted beam optics (sometimes known as an *open detector*). This setup provides increased signal intensity at the cost of a lower resolution. Data analysis was performed using the commercial `X'Pert Epitaxy 4.0` software.

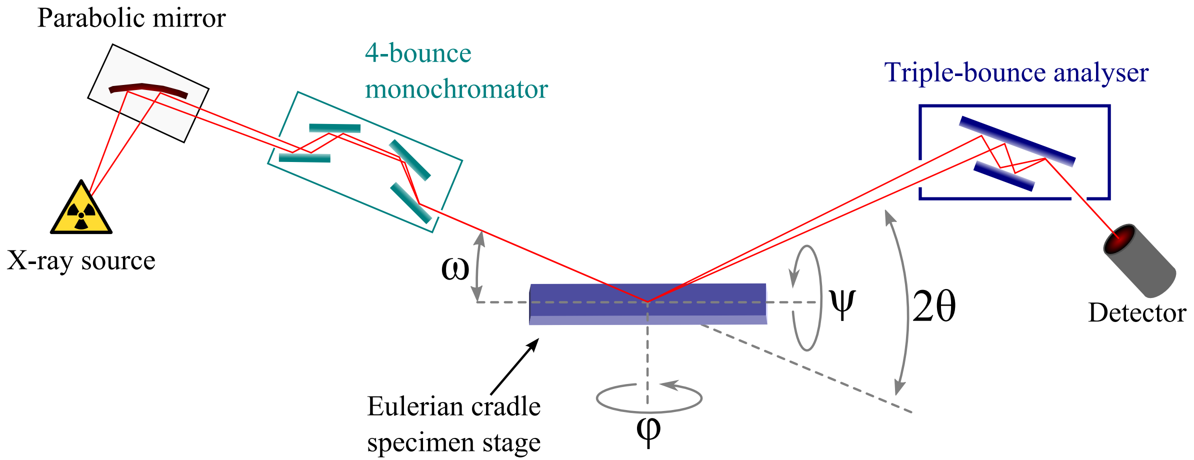

Figure 3.9: Illustration of the HRXRD configuration. X-rays produced at the Cu target pass through an asymmetric 4-bounce Ge (220) monochromator to hit the sample. High angular resolution is achieved by placing a triple-bounce analyser crystal before the detector.

3.5.2 Thickness measurement

Thickness fringes (also known as Kiessig fringes [129]) are sometimes observed at the base of diffraction peaks, resulting from interference in scattering between layers. For symmetrical scans, the angular spacing between these fringes (numbered n_i and n_j) correspond to the inverse of the film thickness, and can often be used to estimate the thickness (t) of epilayer films or superlattice periodicities (see equation 3.4).

$$t = \frac{(n_i - n_j)\lambda}{2(\sin\theta_i - \sin\theta_j)} \approx \frac{\lambda}{2\Delta\theta\cos\theta} \tag{3.4}$$

3.5.3 Composition determination

HRXRD is commonly employed to determine the composition of conventional III-nitride alloy films, such as AlGaN and InGaN. For a fully relaxed alloy film, the lattice parameters are solely affected by composition. To a first approximation, Vegard's law can be used, which assumes a linear variation of the lattice parameters between the alloy end members. It is more likely to be reliable for alloys where the end members have similar lattice spacings. Vegard's law is reliable for AlGaN [129, 130] and low In content InGaN films [130, 132] (see figure 1.1). In its general form, for an alloy

$A_xB_{1-x}C$, the interplanar spacing varies according to equation 3.5.

$$d_{ABC} = xd_{AC} + (1-x)d_{BC} \tag{3.5}$$

It is implicitly assumed that the same crystal structure is shared by both alloy end members, only differing in relative unit cell size. For the analysis of strained epitaxial layers, strain equations need to be combined with Vegard's law. The resulting mathematics can rapidly become very complex and commercial analytical tools are available to calculate compositions for specific crystal orientations and types of measurement. The elasticity coefficients of the alloys are commonly also obtained by a linear interpolation between the end members.

This conventional route for determining the composition cannot be applied to ScGaN alloys, due to the different crystal structures of ScN and GaN. However, ScGaN alloys have been predicted to retain the wurtzite structure for compositions of up to x = 0.11 in the bulk and up to x = 0.27 when strained to GaN [95]. Unfortunately, neither the lattice parameters nor the elasticity coefficients are expected to vary linearly even in the wurtzite-like phase. An alternative method used to determine the composition of ScGaN alloys has been investigated in § 5.2 on page 86.

3.5.4 Strain determination

If the film is only partially strained to the substrate, the lattice parameters are dependent both on the composition and on the strain state. Strain gradients in a film can arise due to 'composition pulling' during growth (*i.e.* the strain state of the growing epilayer influences the composition of the layers grown subsequently in a way which reduces the total elastic strain energy of the epilayer), formation of microcracks and climb of threading dislocations. The strain state of a film can be assessed using an asymmetric reciprocal space map (RSM). Reciprocal space maps are 2-dimensional projections of reciprocal space around diffraction spots, collected by a series of successive $\omega - 2\theta$ scans at different ω values. RSMs are commonly taken of the asymmetric $10\bar{1}5$ reflection to obtain information on both the in and out-of-plane lattice parameters. In practice, diffraction spots are broadened by limits to the instrumental resolution and crystalline defects (such as dislocations and wafer curvature) [130]. RSMs are commonly presented in map form, where the instrument scanning axes ω

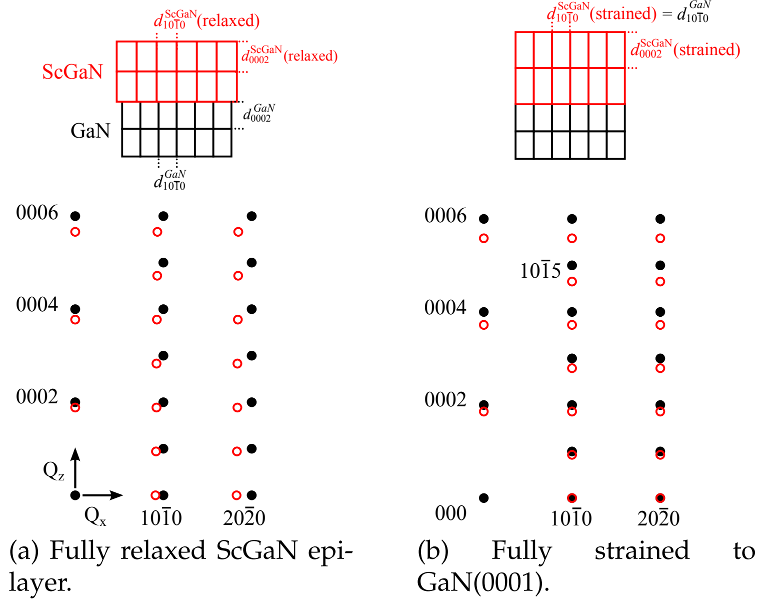

(a) Fully relaxed ScGaN epilayer.

(b) Fully strained to GaN(0001).

Figure 3.10: Schematic illustration of a section through reciprocal space of epitaxial ScGaN on GaN. Adapted from [133].

and $\omega - 2\theta$ are converted to reciprocal lattice units by the following relations:

$$Q_x = \frac{2\pi}{\lambda} \{\cos\omega - \cos(2\theta - \omega)\} \tag{3.6}$$

$$Q_z = \frac{2\pi}{\lambda} \{\sin\omega + \sin(2\theta - \omega)\} \tag{3.7}$$

The reciprocal space directions Q_x and Q_z correspond to the inverse of the x and z real-space directions, respectively, where the x and y real-space axes lie in the (0001) crystallographic plane. Thus for fully strained films, the film and substrate reflections will align vertically at the same Q_x coordinates (corresponding to the same a parameter). Any misalignment will correspond to partial relaxation of the film (see figure 3.10). Often, reciprocal lattice units (rlu) are used, where 1 rlu = 10^4 Å^{-1}.

By measuring the position of the film reflection relative to the substrate, an estimate of the composition and strain relaxation can be obtained, assuming the film lattice parameters and elastic constants are known. A description of this method applied to *wz*-ScGaN films is outlined in § A.4.2 on page 149.

3.5.5 Limitations

Despite many advantages, standard X-ray diffraction techniques are not sufficiently sensitive to detect the presence of nanoscale precipitates. In this regard, HRXRD is unsuitable to assess the solubility limit of transition metals in GaN, for a number of reasons:

1. If the structure of the secondary phase is unknown, the position of diffraction peaks may be far from substrate peak positions and thus not included in the scan range.

2. The overall volume of precipitates may be below the detection limit for reasonable scan times and resolutions.

3. The relative crystallographic orientation of the precipitates with respect to the crystal may differ, thus further reducing the signal at any given angle.

4. Due to the reciprocity theorem, nanoscale precipitates should result in significant broadening of the diffraction peak, raising the detection limit further.

For more accurate determination of the solubility limit, specialised techniques involving synchrotron radiation, or Rutherford backscattering spectroscopy (RBS) need to be used [48]. Other techniques include HRTEM, which can detect the presence of nanoscale precipitates directly, and 3D atom probe tomography, which could be used to detect a non-random Sc/Ga distribution before precipitation.

3.6 Transmission electron microscopy

Transmission electron microscopy (TEM) is an immensely powerful technique for studying materials at the atomic scale with unprecedented precision. TEM allows imaging of dislocations and other defects, also revealing information about the lattice structure and internal strain fields. From a device perspective, understanding the role of dislocations and strain in a structure is a crucial aspect, making TEM an indispensable tool for the study of GaN and its alloys. The TEM work in this study was conducted using several microscopes listed in table 3.1.

	Acc. voltage	Source	Resolution	used for
Philips CM30	300 kV	LaB_6	~2-3 nm	BF/DF, WBDF, SAD
FEI Tecnai G^2 F20	200 kV	FEG	<1 nm	STEM-HAADF, EDX
FEI Titan^3 80-300	300 kV	FEG	<0.10 nm	probe-corrected HR STEM

Table 3.1: List of TEMs used in this project. See Nomenclature on page xiii.

3.6.1 TEM apparatus

A TEM is similar to an optical transmission microscope in basic design, consisting of three main parts. A schematic illustration can be seen in figure 3.11.

Illumination system An electron beam is produced at the top of the microscope tower by the electron gun (either thermionic (LaB_6) or field emission (FEG)) and accelerated to very high energies (typically 100 - 400 keV). The emitted electrons are then condensed into a narrow beam and directed onto the sample surface by a set of condenser lenses and apertures. Depending on the type of experiment, the beam can be focused at the sample surface or set up to produce parallel illumination.

Objective lens and stage The sample is inserted into the microscope using one of several different types of specimen holders. The objective lens focuses the electrons emerging from the sample to produce a diffraction pattern in the back-focal plane of the lens and an image in the image-plane. Due to its strength, the objective lens actually sits around the specimen itself. The objective aperture sits in the back-focal plane of the objective lens and is used to selectively produce either bright-field or dark-field imaging conditions (§ 3.6.3 on page 45).

Projection system The post-specimen projection system consists of a selected area diffraction (SAD) aperture and an intermediate and projector lens. This combination is used to selectively produce either an image or a selected area diffraction pattern (SADP) on the viewing screen. The ability to rapidly switch between image and diffraction pattern is one of the features that makes TEM such a powerful technique. Several types of detectors are commonly used, such as phosphor screens, photographic film (older TEMs) or charge-coupled device (CCD) cameras (modern machines).

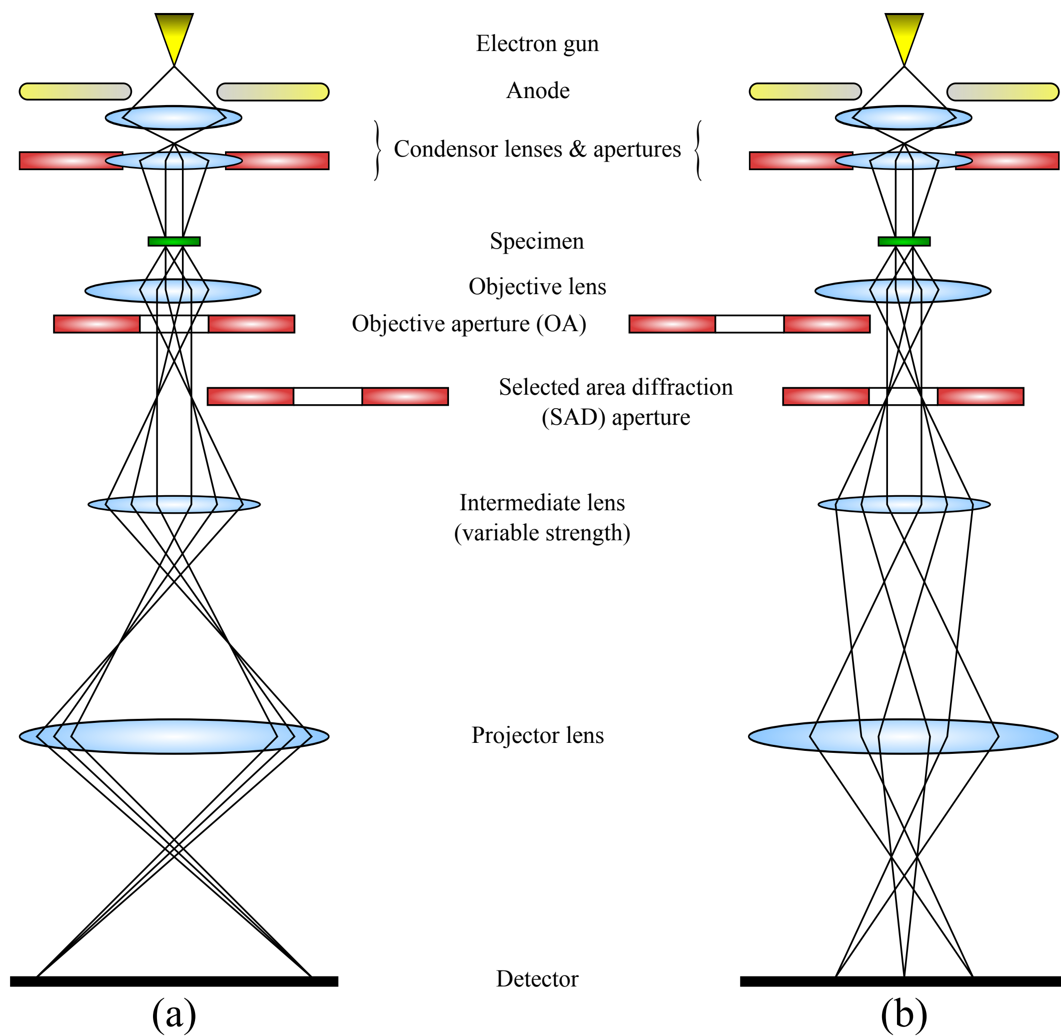

Figure 3.11: Schematic illustration of a basic TEM design. By varying the strength of the intermediate lenses one can choose to view either (a) the magnified image or (b) the diffraction pattern of the specimen.

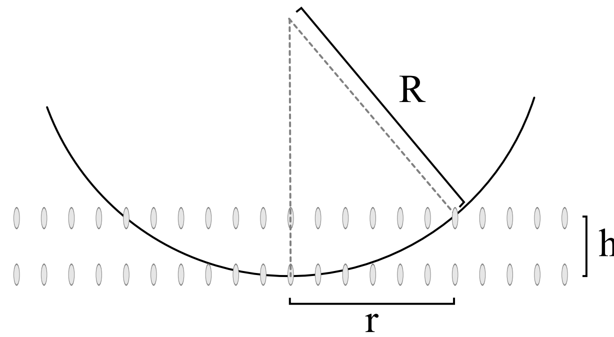

Figure 3.12: Section through reciprocal space showing part of the Ewald sphere and two rows of reciprocal lattice rods (*relrods*). Calculating out-of-plane lattice spacings using first order Laue zone (FOLZ).

3.6.2 Diffraction in the TEM

The magnification of a diffraction pattern is dependent on the camera length, L, defined as the separation between the specimen and photographic film. The measured spacing, x, between spots on the diffraction pattern can be related to the interplanar spacing, d, by relation 3.8, where λ is the de Broglie wavelength of the accelerated electrons.

$$d = \frac{\lambda L}{x} \tag{3.8}$$

The out-of-plane planar spacing can also be determined given the appropriate diffraction conditions. Consider the Ewald sphere intersecting the first order Laue zone (FOLZ) as illustrated in figure 3.12.

By Pythagoras,

$$R^2 = r^2 + (R - h)^2$$

$$\therefore h = R - \sqrt{R^2 - r^2}$$

where all elements have reciprocal space units (*e.g.* Å^{-1}).

3.6.3 Diffraction contrast

Imaging techniques in the TEM can be classified according to the mechanisms that produce contrast in the resulting image. In conventional TEM imaging, parallel illumination is used, and the observed contrast stems from spatial variations in the elastic scattering of electrons in the crystal (hence often called *diffraction contrast*). Im-

ages are formed either using only forward scattered electrons (bright-field, BF) or only electrons scattered to $\mathbf{g}$ (dark-field, DF). The scattering vector $\mathbf{g}$ corresponds to Bragg scattering in the crystal. In practice, this is done by placing the objective aperture in the back focal plane of the objective lens and selecting certain diffraction spots to form the final image. In a diffraction pattern, the central bright spot corresponds primarily to the direct, unscattered electrons and the surrounding diffraction spots correspond to elastically scattered electrons. By placing the objective aperture only around the direct beam (figure 3.13a) a BF image is formed. DF imaging is obtained by either displacing the objective aperture (figure 3.13b) or tilting the incident beam such that the desired diffracted beam lies on the optical axis of the microscope (figure 3.13c). On-axis DF is generally considered superior to off-axis DF as the electron beam passes closer to the optic axis, resulting in fewer lens aberrations and improved resolution [131, 134].

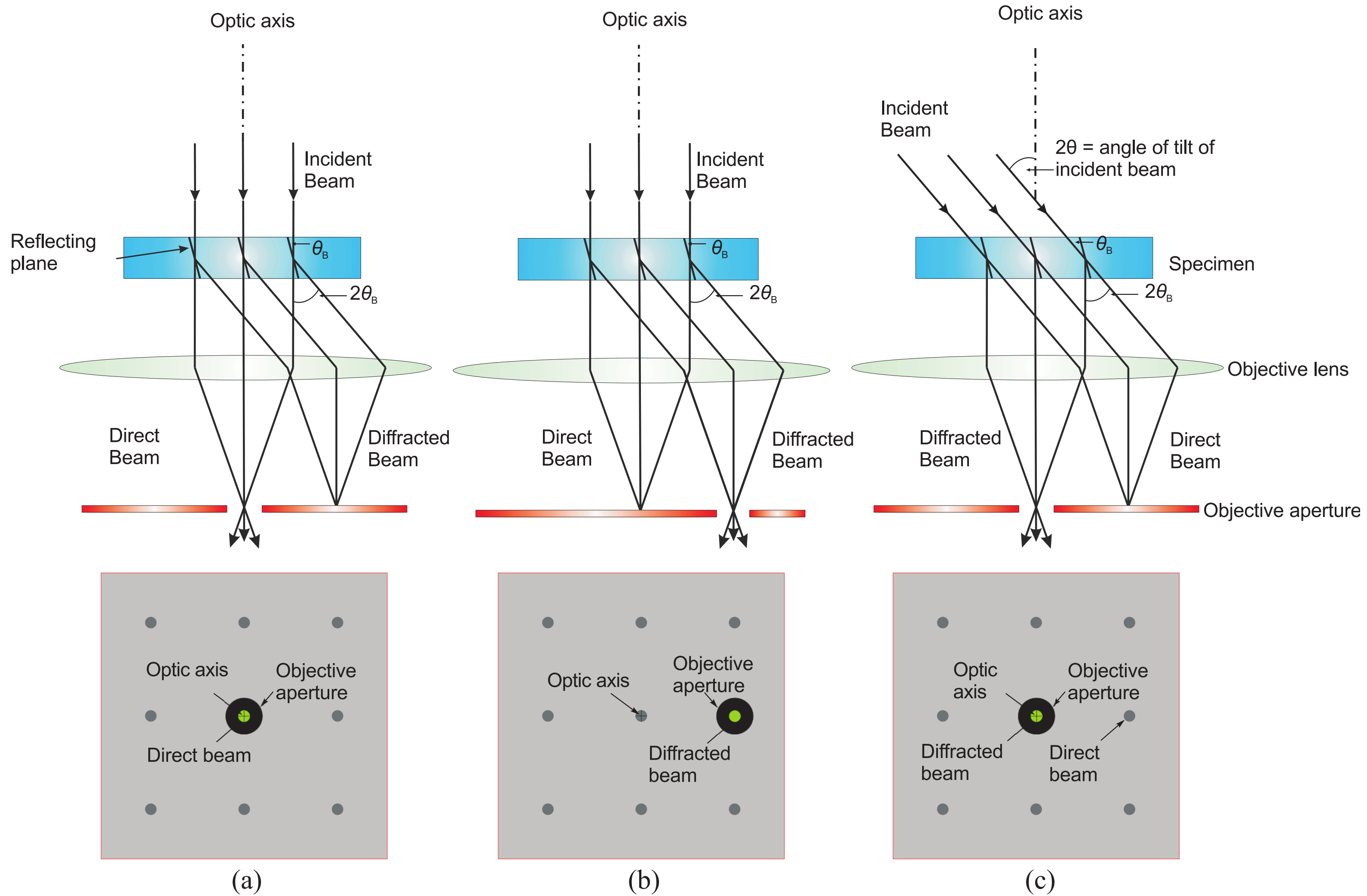

Figure 3.13: Ray diagram illustrating different forms of diffraction contrast (a) BF, (b) on-axis DF, and (c) off-axis DF. On-axis DF generally achieves a higher resolution as lens aberrations are minimised [135].

$\mathbf{g} \cdot \mathbf{b}$ rule for null contrast

Dislocations and other structural defects can be visualised in diffraction contrast TEM because of differences in the scattering geometry in the strained regions of the specimen. Dislocations are visible because the diffracting planes near the dislocation core sufficiently scatter the incident beam to produce contrast in BF/DF images. The diffraction contrast produced by structural defects such as dislocations can be understood by considering the displacement vector, **R**, around the defect. For a general dislocation (edge, screw or mixed) with a Burgers vector **b** in an isotropic medium, the relation by Hirth [136] applies:

$$\mathbf{R} = \frac{1}{2\pi}\left(\mathbf{b}\phi + \frac{1}{4(1-\nu)}\left[\mathbf{b}_e + \mathbf{b}\times\mathbf{u}\left\{2(1-2\nu)\ln r + \cos 2\phi\right\}\right]\right) \tag{3.9}$$

where **R** is given in the polar coordinates r, ϕ; $\mathbf{b_e}$ is the edge component of the Burgers vector and **u** is the line vector of the dislocation; the isotropic Poisson ratio is given by ν. No contrast is observed when $\mathbf{g}\cdot\mathbf{R} = 0$. For pure screw dislocations there is no edge component to the Burgers vector, hence both $\mathbf{b_e} = 0$ and $\mathbf{b}\times\mathbf{u} = 0$. Thus screw type dislocations are expected to be invisible when $\mathbf{g}\cdot\mathbf{b} = 0$, whereas pure edge type dislocations disappear when both $\mathbf{g}\cdot\mathbf{b} = 0$ and $\mathbf{g}\cdot\mathbf{b}\times\mathbf{u} = 0$.[1] This difference allows diffraction contrast to be used to identify dislocation types. The Burgers vectors and visibility conditions for dislocations in wurtzite materials are given in table 3.2.

The same principle can be used to differentiate between stacking faults (SF). SFs are invisible when the product $\mathbf{g}\cdot\mathbf{b} = 0$ or any integer value. In these cases the phase shift introduced by the stacking fault is exactly out by λ so no contrast will be seen. Table 3.3 summarises the invisibility criteria used for imaging different stacking faults.

[1]**Four-index notation**
The four-index system can be thought of as a projection of four dimensional space onto three dimensions. To account for the different c/a ratios, a correction factor of $\lambda = c/a\,(2/3)^{1/2}$ needs to be introduced to the fourth Miller index. Hence a four-index vector $[u\,v\,t\,w]$ in conventional notation becomes $[u\,v\,t\,\lambda w]$ in Cartesian coordinates, and a four-index plane $(h\,k\,i\,l)$ becomes the Cartesian plane normal $\left(h\,k\,i\,\frac{l}{\lambda}\right)$. The angles between two directions is given as convention using the scalar product. Thus the scalar product between two directions is $uu' + vv' + tt' + \lambda^2 ww'$, and the scalar product between the normals of two planes is $hh' + kk' + ii' + \frac{ll'}{\lambda^2}$. The scalar product $\mathbf{g}\cdot\mathbf{b}$ is the scalar product between the vector **b** and the normal of the set of planes **g**, thus in the dot product the terms cancel each other out: $hu + kv + it + \frac{l}{\lambda}\lambda w = hu + kv + it + lw$. Care must be taken to use the magnitudes of the Cartesian vectors.

g	*a*-type (edge) $\frac{1}{3}\langle 11\bar{2}0\rangle$	*c*-type (screw) [0001]	mixed $\frac{1}{3}\langle 11\bar{2}3\rangle$
$11\bar{2}0$	✓	✗	✓
$1\bar{1}00$	✓	✗	✓
0002	✗	✓	✓

Table 3.2: Burgers vectors and invisibility criteria for threading dislocations ($\mathbf{u} = [0001]$) in wurtzite crystals with edge, screw and mixed character.

g	I_1 $\frac{1}{6}\langle 20\bar{2}3\rangle$	I_2 $\frac{1}{3}\langle 1\bar{1}00\rangle$	E $\frac{1}{2}\langle 0001\rangle$	PSF $\frac{1}{2}\langle 10\bar{1}1\rangle$
$11\bar{2}0$	✗	✗	✗	✓
$1\bar{1}00$	✓	✓	✗	✓
0002	✗	✗	✗	✗

Table 3.3: Invisibility criteria for different types of stacking faults. ✓ indicates the stacking fault is visible and ✗ denotes it is invisible.

3.6.4 Weak-beam dark-field imaging

The contrast can be improved upon further by using the weak-beam dark-field (WBDF) technique. The observed dislocation line widths are much narrower (∼1.5 nm) than in conventional BF or DF imaging, and their position is well-defined with respect to the dislocation core. This makes WBDF imaging a particularly useful technique to study high dislocation density films, allowing pairs of closely spaced dislocations or stacking faults to be resolved. The principle behind WBDF imaging is to tilt the specimen to imaging conditions where most diffraction is weak and the image appears very dark. However, around dislocation cores, the lattice planes are sufficiently strained to be bent back into the Bragg condition, resulting in a strong increase in intensity along the dislocation line (figure 3.14).

WBDF imaging conditions are achieved by setting up conventional on-axis DF conditions and subsequently tilting the specimen to select a weak diffracted beam (denoted **g**). In reciprocal space, this corresponds to selecting a reflection which lies slightly off the Ewald sphere, *i.e.* with a large excitation error, *s*. Instead, a higher-order reflection will be close to the Bragg condition, and thus appear as a bright spot on the diffraction pattern (figure 3.15). The most commonly used WBDF imaging

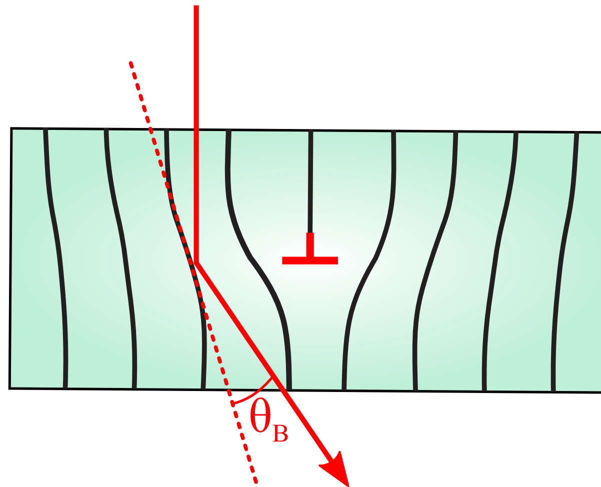

Figure 3.14: Weak-beam dark-field images from strained regions only show strong intensity where diffracting planes are bent back into the Bragg condition (θ_B). This schematic represents the region surrounding an edge dislocation.

setup is the **g**-3**g** condition, resulting as a compromise between a high resolution at high values of **g** and good contrast at low values of **g**. Here, the **g** beam is used to form the image and the 3**g** reflection is at the Bragg condition. The procedure for setting up the **g**-3**g** condition is listed below:

1. Tilt the specimen away from the zone axis to obtain a row of diffraction spots
2. Set up two beam conditions by tilting the specimen in the perpendicular direction, activating the desired **g** reflection
3. Using the diffraction coils, tilt the incident beam onto the optical axis. **g** will become very weak as the excitation error increases.
4. Form a DF image by positioning the objective aperture around the diffracted beam, **g**.

3.6.5 Scanning transmission electron microscopy

In contrast to the parallel illumination used in conventional TEM, scanning TEM (STEM) involves rastering a narrow, convergent beam across the specimen surface. The beam is focused into a small electron probe by the set of condenser lenses, and using a set of double-deflection scan coils the probe can be moved across the surface.

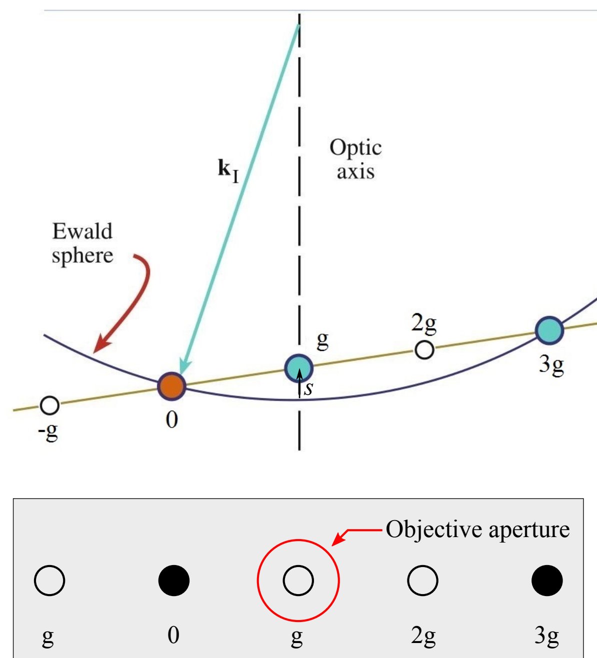

Figure 3.15: Illustration of the Ewald sphere construction in reciprocal space for the **g**-3**g** condition. The objective aperture is placed on the optical axis, allowing only the weakly excited beam through. Adapted from [131].

Unscattered electrons can be collected by a bright-field detector or an electron energy-loss spectrometer (EELS) positioned below the specimen along the optical axis of the microscope. Electrons scattered to higher angles are collected by a high-angle annular dark-field detector (HAADF), positioned in the back-focal plane. A schematic illustration of a typical STEM column is shown in figure 3.16.

3.6.5.1 Z-contrast imaging

As the scattering angle increases, incoherent (Rutherford) scattering tends to dominate over the coherent (Bragg) scattering considered previously [131]. In this limit the scattered electrons bear no phase relationship between them, and the scattered intensity is solely a function of the atomic mass, Z. When sufficiently large collection angles have been used (>50 mrad), the STEM contrast is found to vary as a function of Z^2, in accordance with the Rutherford scattering cross section for an unscreened nucleus (equation 3.10). The equation describes the variation of the scattering cross section, σ_R, as electrons are scattered through an angle θ into a solid angle Ω. E_0 is

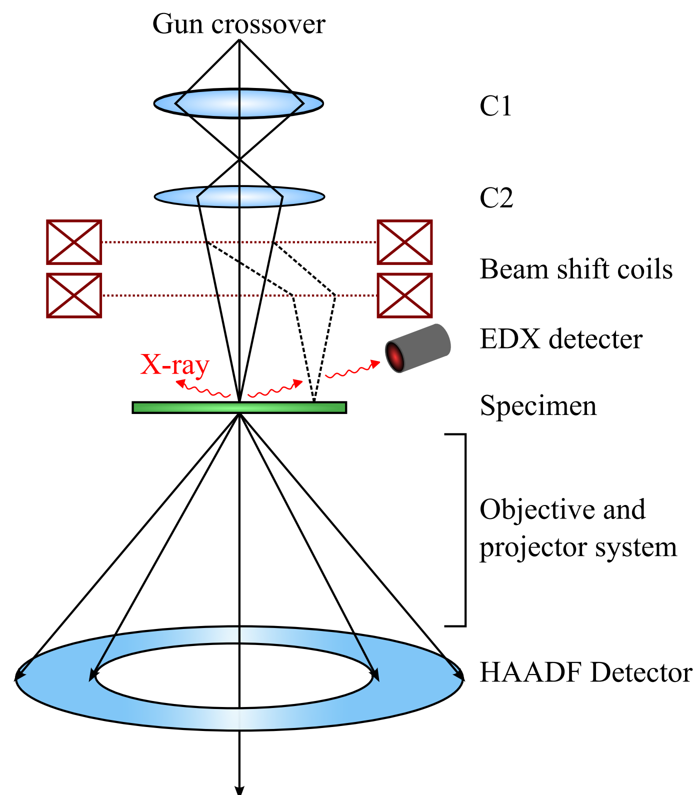

Figure 3.16: Schematic diagram of the STEM column.

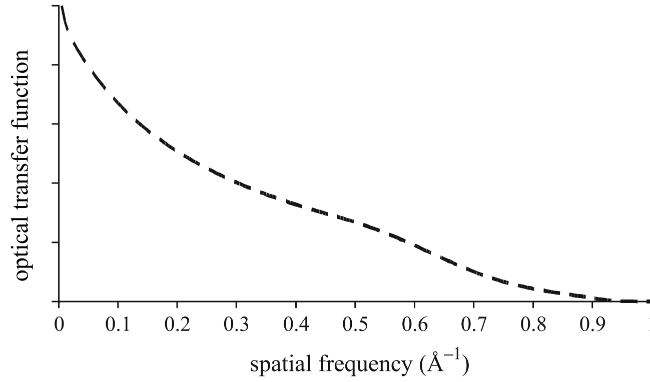

Figure 3.17: Typical optical transfer function for incoherent imaging in STEM, calculated for 300 kV with a spherical aberration of C_s = 1 mm. The optical transfer function decreases monotonically with spatial frequency and displays no contrast reversals [137].

the electron energy defined by the acceleration voltage [131].

$$\sigma_R = \frac{e^4 Z^2}{16\left(4\pi\epsilon_0 E_0\right)^2} \frac{d\Omega}{\sin^4 \theta/2} \tag{3.10}$$

Because of the absence of post-specimen projection lenses, STEM imaging does not suffer from the same lens aberrations which commonly limit the resolution of conventional TEMs. Instead, the fundamental resolution limit in STEM is determined by the size of the electron probe itself. In order to obtain high probe currents for narrow probe diameters, a high gun brightness is required. Most STEM systems, such as the *FEI* Tecnai G^2 F20 microscope used in this work, are equipped with a Schottky FEG, which have brightnesses up to 3 orders of magnitude larger than the LaB_6 source used in the *Philips* CM30 [131]. To achieve atomic resolution, the requirement in STEM is to use a probe size which is smaller than the interatomic spacing. In the absence of stigmatism, the aberrations in the condenser lens (in particular the spherical aberration) will broaden the probe size. Modern high-resolution STEM microscopes (such as the *FEI* Titan^3 80-300) are equipped with aberration correctors (C_s-correctors) which can correct spherical aberrations in the probe, allowing resolutions of below 1 Å.

A significant advantage of high resolution STEM imaging is the fact that the optical transfer function (OTF) decreases monotonically with spatial frequency [137], and unlike conventional high resolution TEM, there are no contrast reversals (figure 3.17). This allows high-resolution STEM images to be interpreted intuitively, and does not require additional image simulation in order to understand the results [131].

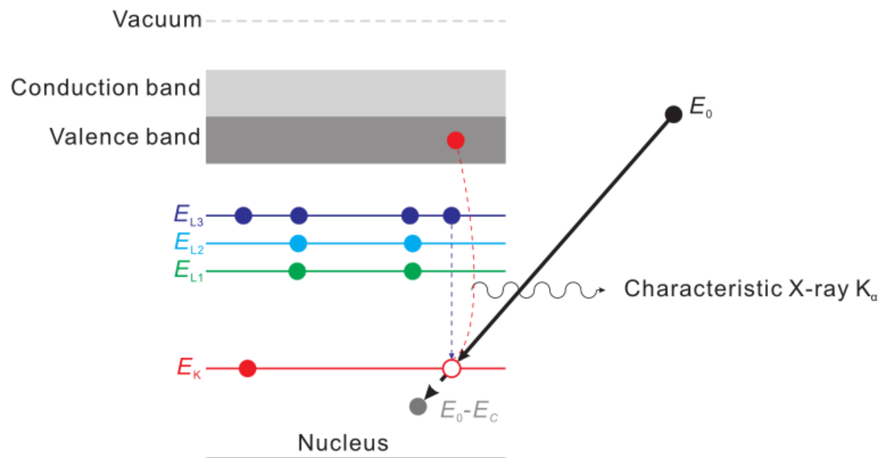

Figure 3.18: The generation of a characteristic X-ray due to the excitation and de-excitation of an inner core electron. From [135].

3.6.5.2 Energy dispersive X-ray spectroscopy

Another advantage of using STEM is the ability to perform chemical analysis. Energy dispersive X-ray (EDX) analysis uses the characteristic elemental X-ray emission lines to analyse a material composition. The X-ray emission lines are dependent on the electronic configuration around the nucleus and will thus be different for each element. A selection of characteristic X-ray emission lines can be found in table 3.4. Characteristic X-rays are generated in a two-step process, illustrated in figure 3.18:

1. Core-level atomic electron is excited to a higher energy level by a passing high-energy electron

2. De-excitation of electron results in the emission of an X-ray

In practice, spectroscopy is performed by positioning an EDX detector close to the specimen inside the TEM column (figure 3.16). Because of the thin specimen thickness and limited collection angle, the X-ray count rate can be very low and the specimen is usually tilted towards the detector to enhance the collection rate.

Z	Element	$K_{\alpha1}$	$K_{\alpha2}$	$K_{\beta1}$	$L_{\alpha1}$	$L_{\alpha2}$	$L_{\beta1}$	$L_{\beta2}$	$L_{\gamma1}$
7	N	0.3924							
13	Al	1.48670	1.48627	1.55745					
21	Sc	4.0906	4.0861	4.4605	0.3954	0.3954	0.3996		
31	Ga	9.25174	9.22482	10.2642	1.09792	1.09792	1.1248		
49	In	24.2097	24.0020	27.2759	3.28694	3.27929	3.48721	3.71381	3.92081

Table 3.4: Characteristic X-ray emission lines for selected elements.

3.7 X-ray absorption spectroscopy

X-ray absorption spectroscopy (XAS) is a unique tool for investigating the local structure of materials at the atomic scale, and can be applied to a range of materials, including crystals, amorphous materials, liquids and even molecular gases. This versatility allows XAS to be used in a wide range of scientific fields including physics, chemistry, biology, environmental science, engineering and materials science.

The fundamental quantity measured in XAS is the X-ray absorption coefficient, $\mu(E)$, with energy. When X-rays are absorbed by a material, the intensity usually follows an exponential decay dependent on both $\mu(E)$ and the specimen thickness, t, according to Beer's Law [138]:

$$I = I_0 e^{-\mu t} \tag{3.11}$$

Generally there is a smooth decrease of the absorption coefficient μ with energy, roughly varying according to:

$$\mu(E) \approx \frac{\rho Z^4}{AE^3} \tag{3.12}$$

where ρ corresponds to the density of the material, Z is the atomic number and A is the atomic mass. However, when the X-ray energy is equal to the binding energy of a core-electron (*e.g.* 1*s* or 2*s*, 2*p*), a sharp increase in the absorption coefficient is observed - this is the *absorption edge*. Absorption of the X-ray results in the promotion of a core electron to the vacuum by the photoelectric effect. Each element has as unique set of absorption edges giving XAS elemental selectivity. The emitted photoelectron will scatter with the atoms surrounding it, a schematic illustration is shown in figure 3.19.

Self-interference between the forwards and backwards scattered electron waves give an energy-dependent variation in the X-ray absorption coefficient. These measurable variations can give information on the distance, species and coordination

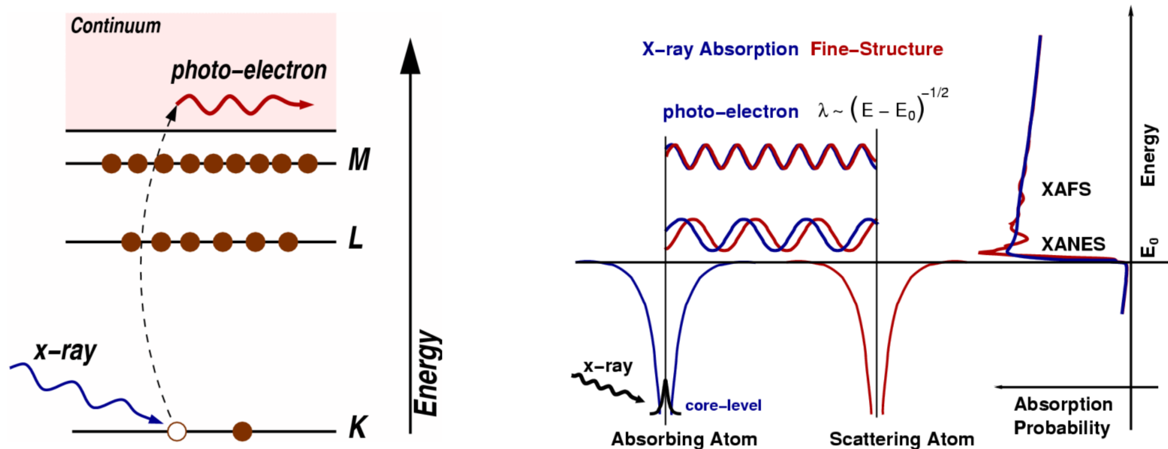

(a) Absorption of an X-ray results in the annihilation of a core-electron and the creation of a photoelectron in the process.

(b) The resultant photo-electron can scatter with a neighbouring atom and interfere with itself. This will cause oscillations in $\mu(E)$ that are the XAS.

Figure 3.19: Illustration of the (a) X-ray absorption and (b) subsequent photo-electron scattering event that are the basis of XAS. Illustrations adapted from [138].

number of the atoms immediately surrounding the observed element. XAS spectra are usually split into two regions: X-ray absorption near-edge spectroscopy (XANES) and extended X-ray absorption fine-structure spectroscopy (EXAFS). XANES covers a range from the absorption edge to several tens of eV (∼50 eV), and arises from scattering path lengths of the emitted photoelectron comparable to the interatomic distances. Although a full theoretical interpretation of XANES is challenging, it permits an understanding of both the oxidation state and geometrical arrangement of the absorbing species. The EXAFS regime extends from about 50 to up to 1000 eV above the absorption edge. An example of an experimental XAS spectrum taken from an epitaxial ScN film at the Sc K-edge is shown in figure 3.20, depicting the different regions of a typical XAS spectrum.

3.7.1 Data reduction and fitting

To extract the EXAFS signal $\chi(k)$ from $\mu(E)$, a background function, $\mu_0(E)$, is removed from the spectrum according to equation 3.13. It is often easier to interpret the EXAFS in terms of the photo-electron wavenumber, k, where $k = \sqrt{\frac{2m(E-E_0)}{\hbar^2}}$. The background function $\mu_0(E)$ corresponds to the absorption of an isolated atom and in practice is usually taken as a smoothing spline. $\Delta\mu_0(E)$ corresponds to the edge-jump intensity at the threshold energy E_0, commonly defined as the position of the maxi-

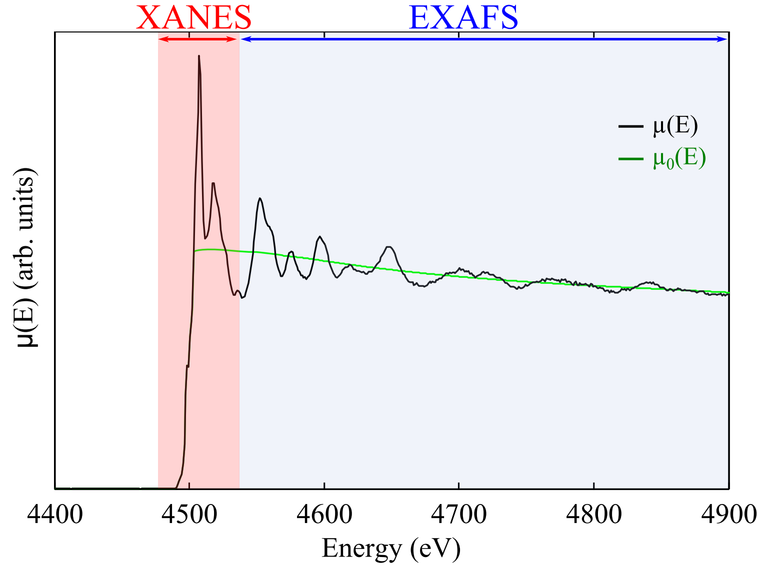

Figure 3.20: Absorption coefficient spectrum $\mu(E)$ of a ScN sample at the Sc K-edge, with the XANES and EXAFS regions identified. The $\chi(k)$ signal extracted from this curve is shown in figure 3.21.

mum derivative, $\frac{\partial \mu(E)}{\partial E}$ [138, 139]. The EXAFS signal $\chi(k)$ is usually weighted by k^2 or k^3 to amplify the oscillations at higher wavenumbers.

$$\chi(E) = \frac{\mu(E) - \mu_0(E)}{\Delta\mu_0(E)} \tag{3.13}$$

The EXAFS signal was extracted using the `Athena` program [140], following the standard approach by Newville [138] and Kelly [141]. Where necessary, removal of glitches in the spectrum was performed using the `Viper` software [142]. An example of the extracted EXAFS signal can be seen in figure 3.21. The $\chi(k)$ signal was extracted from the raw $\mu(E)$ data shown in figure 3.20.

Once the EXAFS data has been extracted from the raw spectrum it is possible to perform quantitative fitting. In its most general form, the fine-structure scattering process is modelled using the EXAFS equation 3.14.

$$\chi(k) = \sum_i \frac{N_i f_i(k) \exp\left\{-2k^2\sigma_i^2\right\}}{kR_i^2} \sin\left[2kR_i + \delta_i(k)\right] \tag{3.14}$$

where $f(k)$ and $\delta(k)$ are the photoelectron scattering properties of the neighbouring atom, representing the scattering amplitude and phase shift, respectively. If these

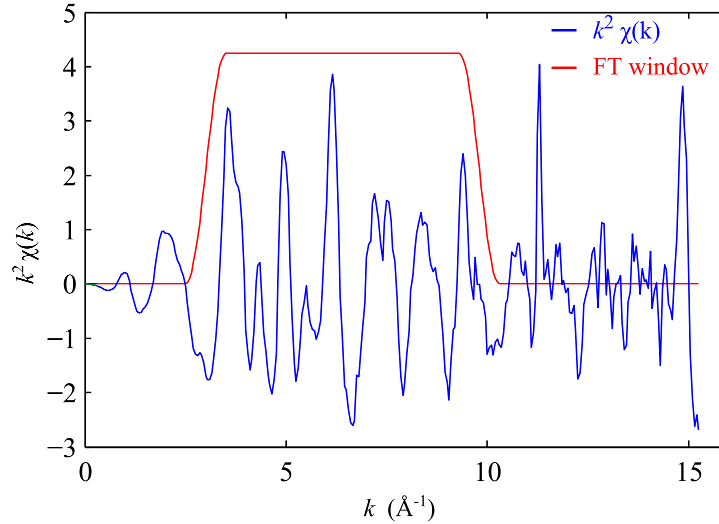

Figure 3.21: Extracted $\chi(k)$ signal of a ScN film, weighted by k^2 for clarity (the raw $\mu(E)$ data is shown in figure 3.20). Subsequent fitting is commonly performed in Fourier-transformed (FT) R-space, using a predefined range in k. The FT-window is shown in red.

factors are known[2] one can determine the following variables:

N_i	The coordination number of the ith shell around the absorbing atom
R_i	The radius of the ith coordination shell
σ_i	The RMS disorder in the ith coordination shell, also called the Debye-Waller factor

Given that both $f(k)$ and $\delta(k)$ are dependent on the atomic number of the absorbing atom, Z, the chemical species of the adjacent atom can also be ascertained.

In fact equation 3.14 is an average over all angles, suitable for powder samples. When analysing single crystals an additional factor of $\chi(k)_{pol} = 3\sum_i cos^2(\theta_i\chi(k))$ needs to be included, where θ_i corresponds to the scattering angle between the X-ray polarisation vector and the scattering path vector [144]. Using a plane-polarised X-ray beam, which is naturally produced by a synchrotron source, a quantitative comparison between the in-plane and out-of-plane bonding can be obtained. This is particularly useful for wurtzite structures such as ScGaN alloys, and allows the study of any local changes in the bonding and c/a ratio around the Sc atom.

[2]The photoelectron scattering properties are conveniently either tabulated or calculated by dedicated XAS analysis programs such as `FEFF9.6` [143].

Signal fitting and quantitative analysis were performed using the `Artemis` software package [140, 145]. Step-by-step instructions to the data fitting procedure in `Artemis` can be found in references [138–141, 146].

3.7.2 Experimental setup

Synchrotron radiation is the preferred X-ray source because high brightnesses can be achieved (*e.g.* 10^{13} photons/s) which allow for excellent monochromation (*e.g.* 0.64 eV in the setup used in this work) and plane-polarised radiation [147]. This allows XAS measurements on elements of very low concentrations (< 1 ppm) and to distinguish any differences between in-plane and out-of-plane bonding [138, 139]. All the experiments were performed at the ID26 beamline [148] of the European Synchrotron Radiation Facility (ESRF) in Grenoble, France with the help of Dr. Mauro Rovezzi. Details of the beam optics and experimental setup geometry can be found in references [54, 55, 147].

Chapter 4

Scandium nitride

"Research is what I'm doing when I don't know what I'm doing."

-Wernher von Braun

Contents

4.1 Introduction 61

4.2 Structural investigation 63

4.3 Optical and electrical measurements 76

4.4 XAS studies 78

4.5 Synopsis 82

4.1 Introduction

ScN has been heralded as a promising candidate in the search for a suitable alloying addition to the existing 'palette' of III-nitrides. ScGaN and ScAlN alloys with low Sc mole fractions have been predicted to retain the wurtzite structure and direct band gaps [76, 95], opening up the possibility of integrating these alloys into existing III-nitride device structures. However, before the synthesis of ScGaN and ScAlN alloys can be attempted, it is necessary to have an understanding of the growth of binary ScN films. ScN crystallises in the rock-salt (B1) structure in its ground state, with an unstrained lattice parameter of $a = 4.5057 \pm 0.0005$ Å [65] (see §1.3). Unlike most transition metal nitrides, ScN is a semiconductor with an indirect band gap of 0.9 eV and a direct band gap near 2.1 eV [66–68].

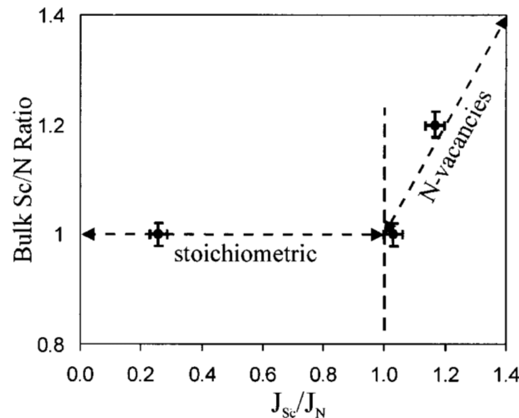

Figure 4.1: Film stoichiometry as a function of elemental flux ratio (J_{Sc}/J_N) [67].

The structural, optical and electrical properties of ScN films are strongly dependent on the growth technique employed. The film stoichiometry has also been identified as having a strong impact on the surface morphology and electronic structure of ScN. Nitrogen vacancies (V_N) are expected to produce states near the conduction band leading to n-type doping, and are expected to form much more readily than Sc vacancies [77]. Previous experimental results have found that PA-MBE grown films under strong Sc-rich conditions can stabilise ScN films with V_N concentrations of up to 20% [149], whereas films grown by reactive sputter deposition showed a phase separation into stoichiometric ScN and Sc metal [42]. For MBE grown films, it was observed that films grown under nitrogen rich conditions ($J_{Sc}/J_N < 1$) resulted in an ideal 1:1 stoichiometry, as observed by Rutherford backscattering spectroscopy [67]. Sc-rich growth conditions led to substoichiometric films by the stabilisation of V_N's in the crystal, with the average stoichiometry roughly proportional to the J_{Sc}/J_N flux ratio (figure 4.1) [67]. The band gaps of substoichiometric ScN_x films have also been predicted to decrease until metallic conductivity is obtained (see 1.3.1 on page 14).

Oxygen contamination was identified as a particular issue in the growth of ScN, leading to a degradation of the crystal quality of sputtered ScN films [79]. Incorporation of oxygen into the ScN films also leads to increases in the optical band gaps of up to 1.1 eV, believed to arise from a Moss-Burstein shift of the Fermi level, rather than the formation of a ScN-Sc_2O_3 alloy. In this explanation, the oxygen substitutes on the nitrogen sites in ScN (O_N) acting as an n-type donor. As the doping level increases, the energy states near the conduction band minimum become populated shifting the Fermi level upwards in energy and leading to an apparent increase in the optical band gap. However, as yet there has been no direct experimental confirmation of the effect

of O_N on the crystal and electronic structure of ScN.

The ScN samples investigated in this work were grown by NH_3-MBE and PA-MBE. The growth details are summarised in B.1. In addition, a ScN sample grown by sputter deposition was used as reference material (see [79] for growth details). It was found that the lowest defect density ScN films were grown by NH_3-MBE under N-rich conditions, consistent with the literature [67, 90], whereas Sc-rich conditions lead to substoichiometric films. Oxygen contamination was found to degrade the film quality, but could be effectively suppressed in highly reducing growth environments, such as by NH_3-MBE.

4.2 Structural investigation

4.2.1 HRXRD analysis

Rock-salt ScN is expected to grow with the (111) plane parallel to the GaN (0001) surface, with an epitaxial relationship of $(111)_{\text{ScN}} \parallel (0001)_{\text{GaN}}$ and $[11\bar{2}]_{\text{ScN}} \parallel [1\bar{1}00]_{\text{GaN}}$. Such an epitaxial relationship would result in only a 0.1% lattice mismatch between the two layers. HRXRD was used to investigate this relationship, and to determine the lattice parameters of ScN.

For unstrained cubic crystals, a symmetric reflection would suffice for lattice parameter determination. However, in-plane biaxial strain is expected for epitaxial film growth of (111)-oriented ScN on GaN, resulting in a rhombohedral distortion of the unit cell [65]. Using the method outlined in this publication, an alternative non-primitive hexagonal unit cell is chosen, which shall be denoted by the subscript 'h' (figure 4.2). The hexagonal unit cell parameters can be related to the conventional cubic notation by:

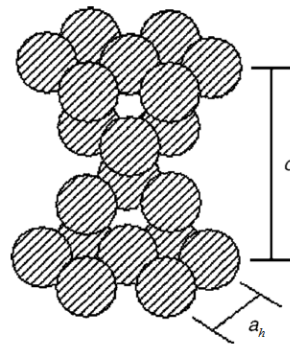

Figure 4.2: Illustration of the nonprimitive hexagonal unit cell parameters as outlined in [65].

$$c_h = 3 \times d_{111}$$
$$a_h = \sin 45^\circ \times d_{100}$$

In this convention, the c_h parameter is perpendicular to the film surface, and corresponds to three face-centred cubic (fcc) stacking repeats and the a_h parameter lies parallel to the film surface, corresponding to the interatomic distance.

The cubic 111 reflection parallel to the growth surface can be probed via a symmetric $\omega - 2\theta$ XRD scan. Figure 4.3a shows the $\omega - 2\theta$ scan for a ScN-on-GaN film grown by NH_3-MBE, with the intense GaN 0002 peak occurring at $2\theta = 34.5484°$ and a ScN 111 reflection at $2\theta = 34.4587°$. The peak positions were determined by fitting Gaussian functions to the diffractogram. Although better accuracy could be obtained at higher diffraction angles, the ScN 222 and 333 peaks could not be distinguished from significantly stronger GaN peaks that occur at very similar 2θ positions. The measured interplanar spacing is $d_{111} = 2.6006$ Å, giving $c_h = 7.8018$ Å. The in-plane lattice parameter was determined by measuring an asymmetric reflection. The cubic 311 reflection is equal to the hexagonal 105 reflection, and using equation 3.3 on page 37, the a_h lattice parameter can be determined. Figure 4.3b shows a reciprocal space map (RSM) of the ScN 311 reflection. The centre of the peak was measured to be at $\omega = 5.09042°$, $2\theta = 69.17941°$, with a d-spacing of $d_{311} = 1.3569$ Å, giving $a_h = 3.1733$ Å. Assuming a strain-free lattice parameter of $a = 4.5057$ Å [65], this distortion corresponds to a biaxial compressive strain of 0.4%.

The presence of a peak in the expected position of the ScN 311 reflection confirmed the epitaxial relationship of ScN-on-GaN, and enables the plotting of sections through reciprocal space, showing the positions of accessible reflections of *rs*-ScN grown on *wz*-GaN (figure 4.4).

The same epitaxial relationship is expected for the PA-MBE grown ScN films, despite the substrate being a (lattice matched) $In_{0.18}Al_{0.82}N$-on-GaN film (see B.1 for full details). However, it was not possible to identify the ScN 111 peak from the intense substrate peak on the HRXRD diffractograms. This is most likely due to overlap between the two peaks, whereby the signal from the ScN is swamped by the strong GaN/InAlN peak. However, it is also possible that the expected epitaxial relationship does not hold, or that the film is polycrystalline with no preferred orientation. To verify the epitaxial relationship between ScN and InAlN for PA-MBE grown films,

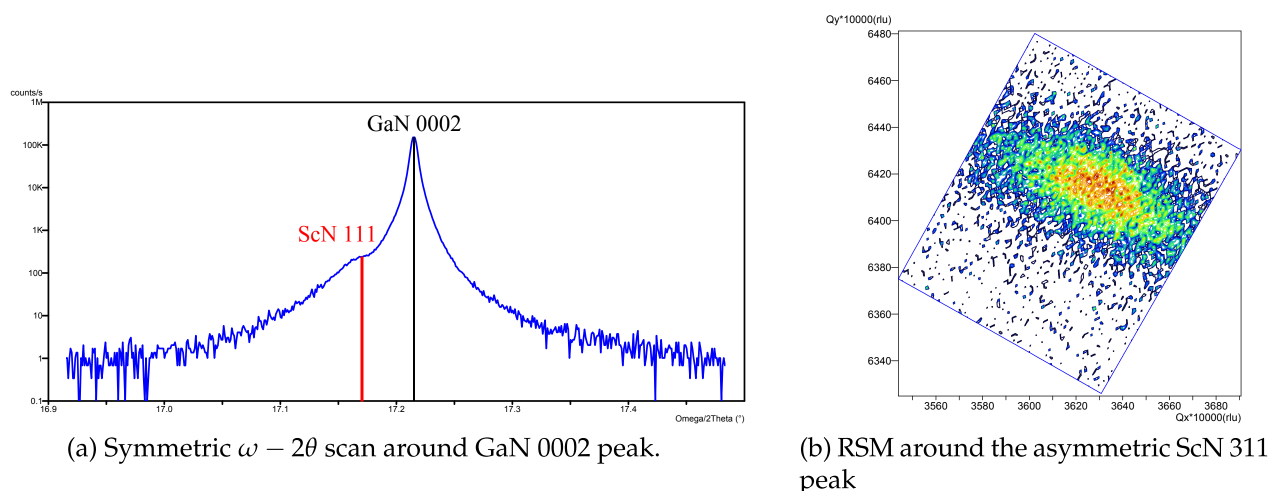

(a) Symmetric $\omega - 2\theta$ scan around GaN 0002 peak.

(b) RSM around the asymmetric ScN 311 peak

Figure 4.3: HR XRD scans of ammonia MBE grown ScN film. The RSM are plotted using iso-intensity contours equally spaced on a logarithmic scale. The scales are in reciprocal lattice units (1 rlu = 10 000 Å^{-1}).

it is necessary to use SAD on the TEM.

Symmetric HRXRD diffractograms can be used to determine film thicknesses using interference fringes between the layers (see § 3.5.2 on page 39), and this method is indeed commonly used in the III-nitride field to provide rapid feedback regarding *e.g.* growth rates. As it was not possible to observe interference fringes in these scans, it is also necessary to resort to TEM to establish accurate thicknesses for determining the growth rate.

4.2.2 Microstructure

The ScN film microstructure was investigated by TEM, using a combination of imaging and diffraction techniques as described in § 3.6 on page 42. The sample preparation method employed is outlined in § A.2 on page 145.

4.2.2.1 Ammonia MBE

The thickness of the ScN film was determined to be 195 ± 5 nm, giving a growth rate of 1.49 ± 0.03 nm/min. Microstructural investigation by TEM reveal a columnar microstructure with sharp facets. Figure 4.5 shows BF and WBDF micrographs taken along the GaN $[1\bar{1}00]$ zone axis. The epitaxial relationship established by XRD was found to be correct. However, the film also showed a high degree of twinning in the (111) plane along $[11\bar{2}]$. A fully indexed diffraction pattern taken along the

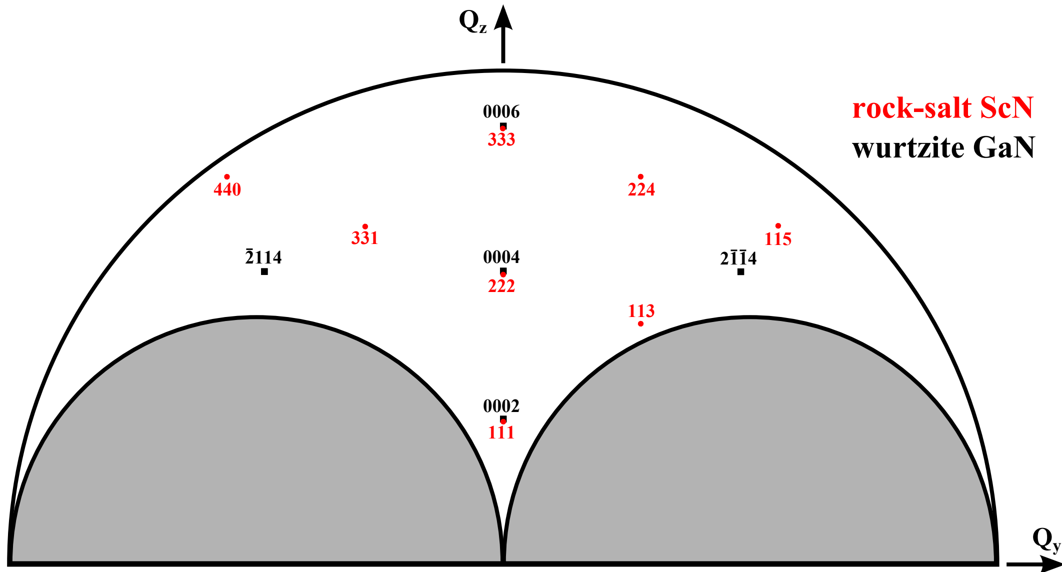

(a) Section through reciprocal space containing the GaN $2\bar{1}\bar{1}4$ and ScN 113 reflections.

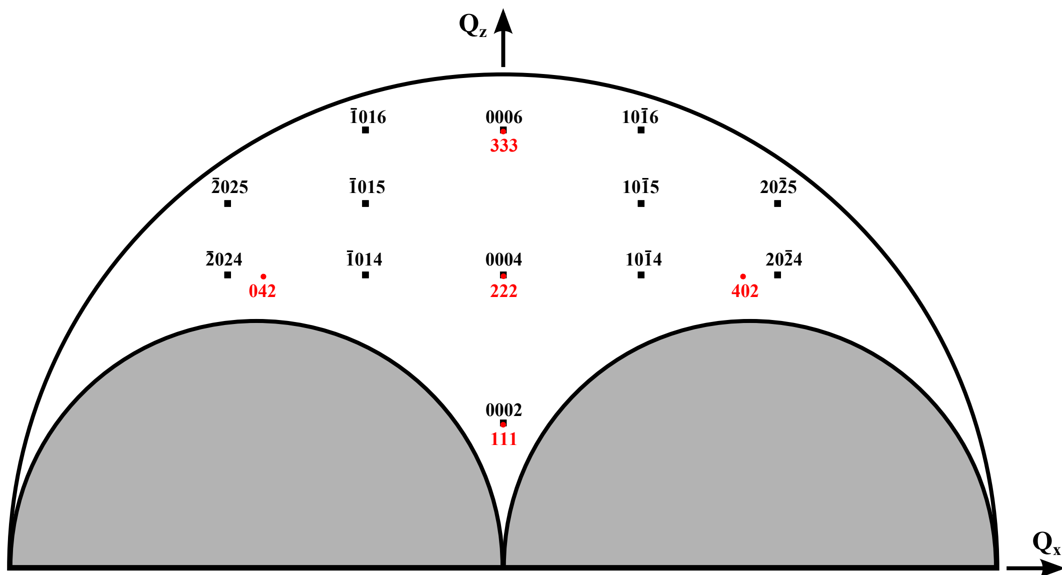

(b) Section through reciprocal space containing the GaN $10\bar{1}5$ and ScN 402 reflections.

Figure 4.4: Sections through reciprocal space showing all accessible GaN (black) and ScN (red) reflections assuming a $(111)_{\mathrm{ScN}} \,||\, (0001)_{\mathrm{GaN}}$ and $\langle 1\bar{1}0\rangle_{\mathrm{ScN}} \,||\, [11\bar{2}0]_{\mathrm{GaN}}$ epitaxial relationship. The grey semicircles correspond to inaccessible regions where either the sample is blocking either the incident or diffracted beam.

GaN $[2\bar{1}\bar{1}0]$ zone axis is shown in figure 4.6, clearly demonstrating the twinning. The complex SADP actually corresponds to three superimposed diffraction patterns, corresponding to the GaN $[2\bar{1}\bar{1}0]$ zone axis (indexed in blue), and two ScN $\langle 1\bar{1}0 \rangle$ patterns (indexed in yellow and red). The ScN diffraction patterns are mirror images of each other, reflected horizontally about a vertical axis in the centre of the diffraction pattern. In real space, this corresponds to diffraction from two volumes which are mirrored about the (111) plane. The fcc stacking sequence can be described as ...$ABCAB\mathbf{C}BACBA$... where the twin boundary is located at plane **C**.

Simulated diffraction patterns for GaN and ScN are shown in figure 4.7, which can be used to identify the zone axis in future experiments. To observe contrast in both film and substrate by WBDF, the objective aperture was placed around $\mathbf{g} = 0002_{\mathrm{GaN}}$, which overlaps with $\mathbf{g} = 111_{\mathrm{ScN}}$.

4.2.2.2 PA-MBE

The film growth rates were determined by relating the thicknesses as measured by cross-sectional TEM to the total growth time. As can be observed from figure 4.8, the growth rate increases monotonically with J_{Sc} over the measured range, from a rate of 2.3 ± 0.1 nm/min at J_{Sc} = 1.6 nA to a maximum growth rate of 6.5 ± 0.5 nm/min at a J_{Sc} = 4.0 nA. The continuous increase of film growth rate with Sc flux is suggestive of N rich growth conditions, as the availability of Sc becomes the rate-limiting factor. Interestingly, the growth rates do not show a linear increase with Sc flux as would be expected for true N-rich growth conditions, but instead show a curved line. This implies that the true growth conditions are more complex than expected and cannot be obtained by purely comparing the film growth rates. In fact, considering the large Sc fluxes used, it is likely that the growth was Sc-rich.

Figure 4.9 shows both WBDF and STEM-HAADF images of PA-MBE grown films grown at low (J_{Sc} = 1.6 nA) and high (J_{Sc} = 4.0 nA) Sc fluxes. The films were found to maintain the same epitaxial relationship to the wurtzite substrate as found in §4.2.2.1. Although both film microstructures are difficult to interpret due to the high defect densities, as evidenced by both WBDF and STEM-HAADF images, closer inspection reveals differences between the two films. At low Sc fluxes the microstructure is dominated by features parallel to the growth direction, whereas the film grown at the higher Sc flux shows a much more complex, disordered defect structure. It

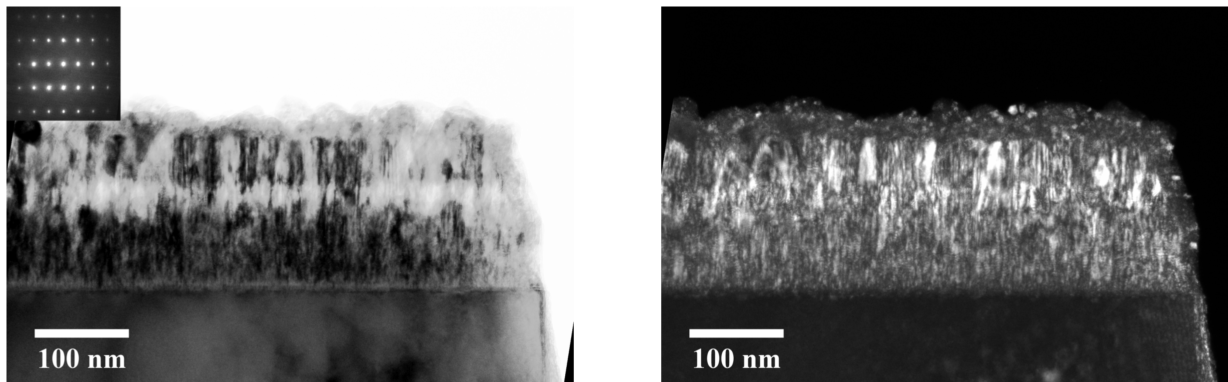

(a) BF image with inset SADP showing the ScN [11$\bar{2}$] zone axis.

(b) WBDF image, **g**-3**g**, **g** = 0002_{GaN}.

Figure 4.5: TEM micrographs of ScN grown by NH_3-MBE on GaN, imaged along the GaN [1$\bar{1}$00] zone axis.

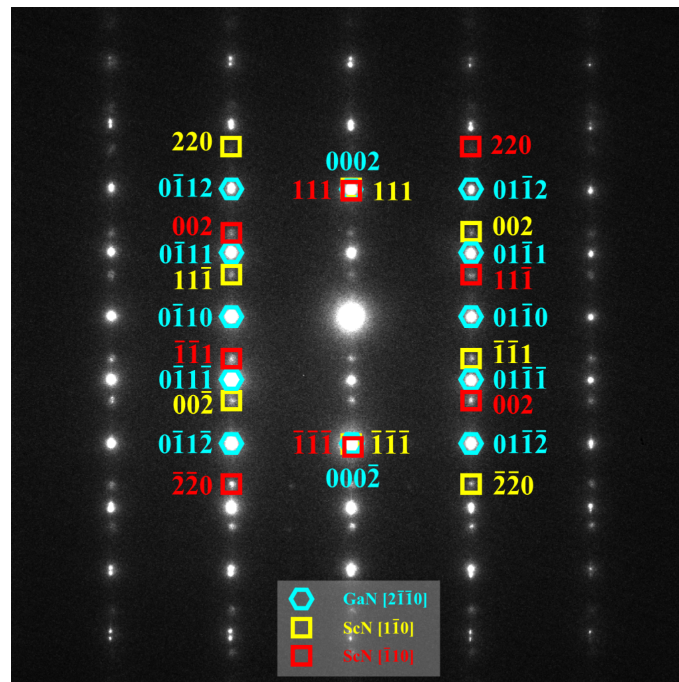

Figure 4.6: Indexed SADP obtained from the GaN/ScN interface, taken along the GaN [2$\bar{1}\bar{1}$0] zone axis. The SADP is a superposition of three separate diffraction patterns: a GaN pattern (indexed in blue) and two twinned ScN patterns (indexed in yellow and red).

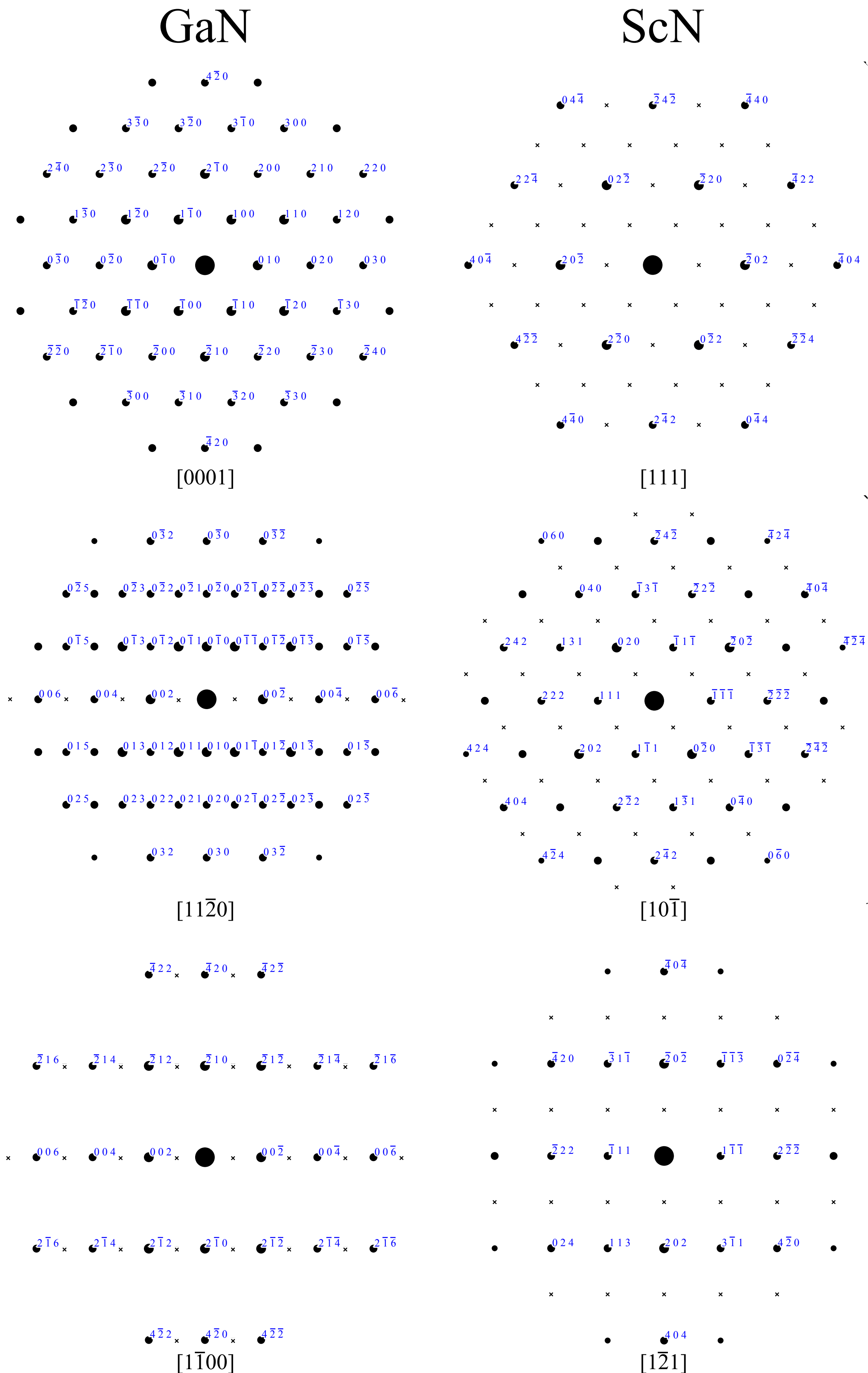

Figure 4.7: Simulated diffraction patterns for GaN and ScN in three perpendicular directions. Systematic absences are noted with a cross.

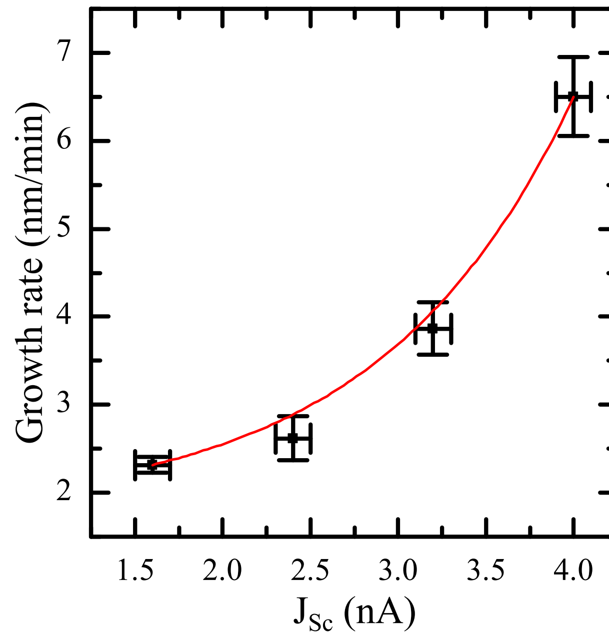

Figure 4.8: Variation of growth rate with Sc flux (J_{Sc}). The red line serves as a guide to the eye.

is interesting to note that both films show amorphous rings in the diffraction patterns, which judging by the ring spacing corresponds to Sc_2O_3 contamination. The strong and well-defined rings in the high Sc flux film suggest a higher degree of contamination, which provides a possible explanation for the observed degradation in the microstructure [79]. However, it is also possible that the Sc_2O_3 formed after the growth process, during the sample preparation process or during the plasma cleaning performed prior to imaging. This step is routinely performed to remove unwanted hydrocarbons from the TEM specimen surface before imaging, by pyrolysing the hydrocarbons in an oxygen-argon plasma. It is possible that this could have led to the oxidation near the surface. It must also be noted that the PA-MBE films were grown on InAlN-on-GaN templates, which may have an effect on the growth conditions and the microstructure. Although any adverse effects arising from the InAlN template are unlikely, given the lattice parameters of the InAlN alloy and GaN are equal, further experiments on GaN-on-sapphire templates need to be performed to exclude this possibility.

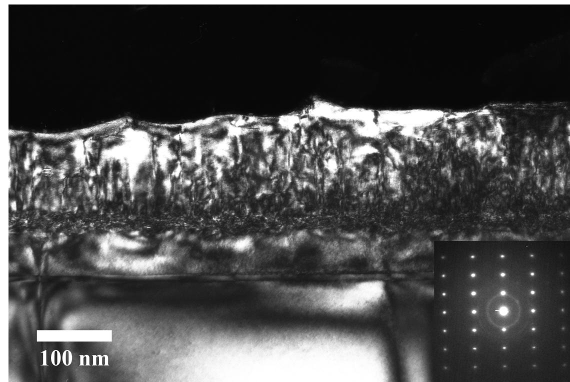

(a) WBDF image of ScN grown at low Sc flux (J_{Sc} = 1.6 nA)

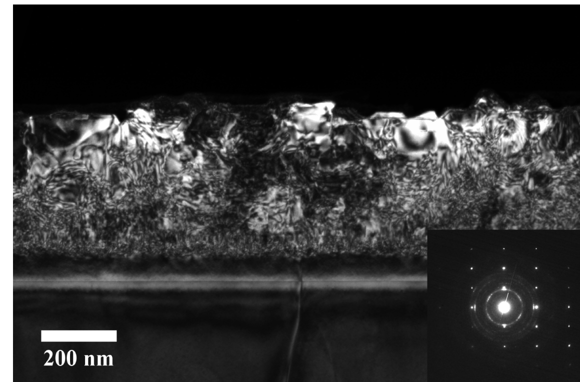

(b) WBDF image of ScN grown at high Sc flux (J_{Sc} = 4.0 nA)

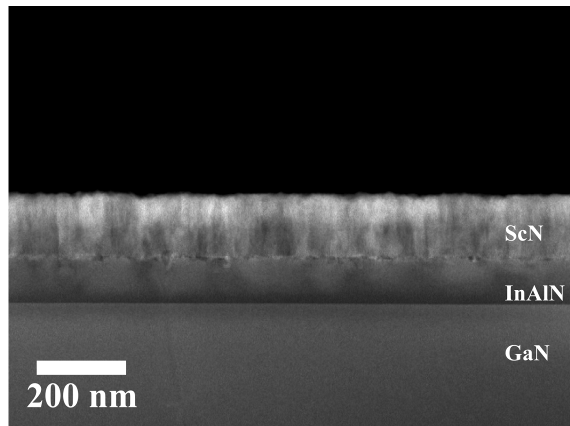

(c) STEM-HAADF, J_{Sc} = 1.6 nA.

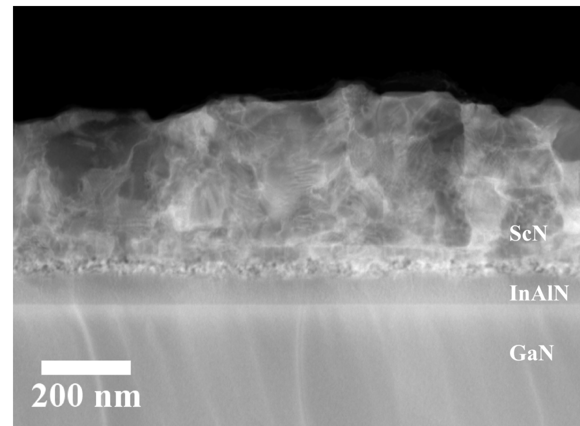

(d) STEM-HAADF, J_{Sc} = 4.0 nA.

Figure 4.9: STEM and WBDF micrographs of ScN grown by PA-MBE on GaN, imaged along the GaN $[1\bar{1}00]$ zone axis. The WBDF images were taken in the **g**-3**g** condition with **g** = 0002_{GaN}.

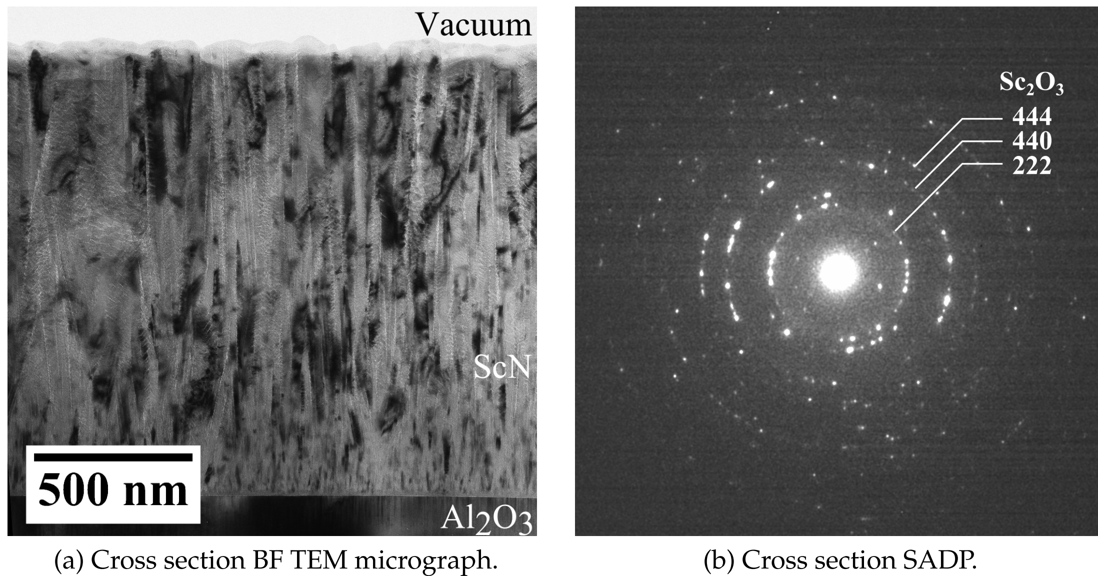

(a) Cross section BF TEM micrograph.

(b) Cross section SADP.

Figure 4.10: ScN film grown by sputter deposition on (0001) Al_2O_3 showing (a) BF TEM micrograph in cross section and (b) the corresponding SADP. The rings were identified to correspond to nanocrystalline or amorphous diffraction of Sc_2O_3 inclusions.

4.2.2.3 Magnetron sputtering

To verify the origin of the amorphous rings, a TEM investigation of a sputtered ScN film was performed. Previous experimental studies of these films have shown that relatively high levels of oxygen contamination are largely responsible for the poor crystal quality of sputtered ScN films [79], thus similar amorphous rings are expected to be found in the diffraction patterns.

The reference ScN film was grown by magnetron sputter deposition on Al_2O_3 substrates to a thickness of 900 ± 5 nm. The cross-sectional TEM micrograph in figure 4.10a shows a columnar microstructure with an average grain size of 100 ± 20 nm. The SAD patterns show the polycrystalline nature of the ScN films, with no evidence of an epitaxial relationship with respect to the sapphire substrate. As expected, the diffraction patterns clearly show concentric rings which correspond to amorphous or nanocrystalline inclusions of the Sc_2O_3 phase. Sc_2O_3 has a cubic crystal structure with space group $Ia\bar{3}$ [150], and the most intense diffraction rings have been indexed in figure 4.10b.

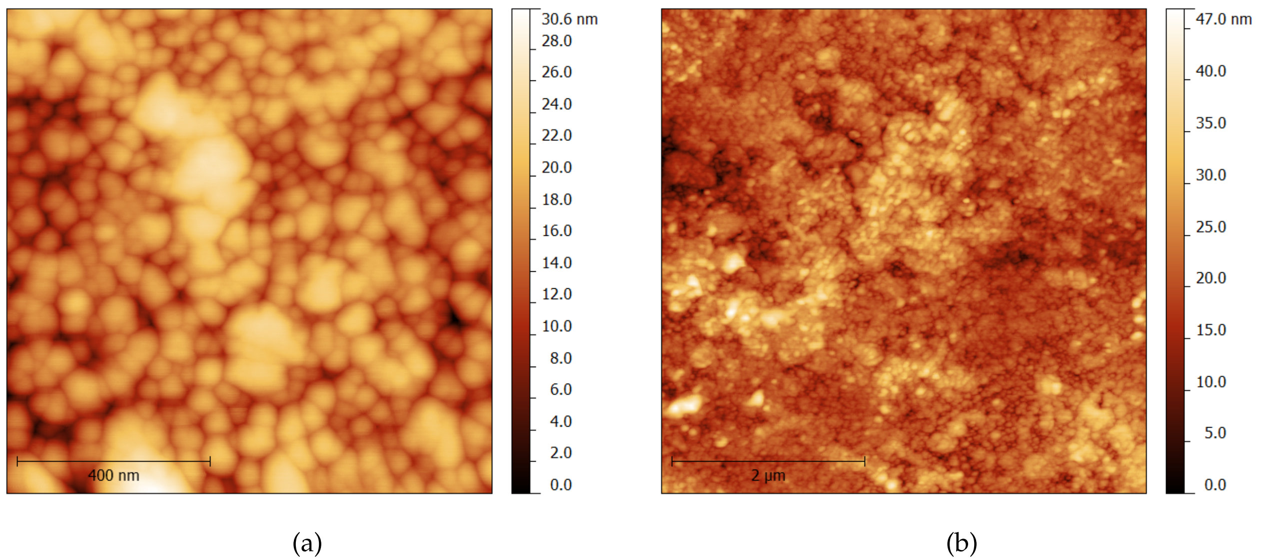

(a) (b)

Figure 4.11: AFM topography scans of ScN film grown by NH_3 MBE on GaN-on-sapphire pseudosubstrates, with lateral sizes of (a) 1 × 1 μm and (b) 5 × 5 μm.

4.2.3 Surface morphology

4.2.3.1 Ammonia MBE

Analysis of the surface topography by AFM showed a rough surface morphology, consisting of rounded mounds between 50 − 100 nm in diameter and 20 nm in height, with an RMS roughness of $R_q = 7.0 \pm 1.5$ nm (figure 4.11). However, plan-view micrographs by STEM reveal a morphology consisting of very small, triangular mounds with a high density of pinholes and gaps (figure 4.12). The average mound size is only about 10 nm, smaller than the typical width of an AFM tip and thus below its lateral resolution limit. However, even though the lateral resolution of an AFM is limited by convolution with the tip radius, the vertical resolution is generally very high (see §Section 3.4), and thus AFM topography scans provide an accurate measure of the film roughness [127].

4.2.3.2 PA-MBE

AFM topography scans showed a range of surface morphologies (figure 4.13 on page 75):

- At low Sc fluxes (J_{Sc} = 1.6 nA) a granular morphology is observed, similar to the ammonia MBE grown sample (figure 4.13a). The average mound is about 40 nm in diameter with a mean height of 15 nm.

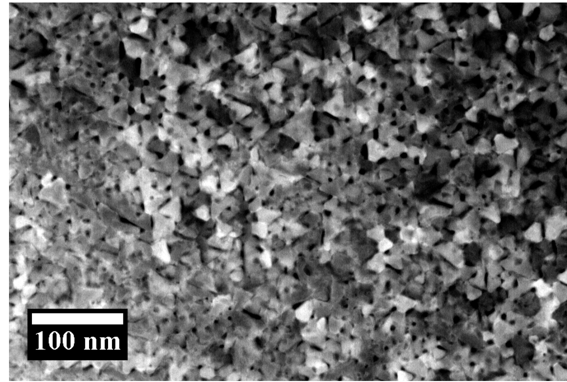

Figure 4.12: PV STEM image.

- As the Sc flux is increased (J_{Sc} = 2.4 nA), a clear morphological transition is seen. The surface consists of many flat-topped mounds or plateaus with six-fold facet symmetry (figure 4.13c). The plateaus have a lateral size of between 200-400 nm and a mean height of 20 nm, with atomically flat surfaces. Slightly smaller, pyramidal mounds are also found, with an average diameter of 50 nm and height of 30 nm. The density of plateaus and pyramidal mounds is about 20 mounds µm^{-2} and 2 mounds µm^{-2}, respectively.

- As seen in figure 4.13e for an increased Sc flux of J_{Sc} = 4.0 nA, a similar morphology consisting of wide plateaus and pyramidal hillocks is observed. Although the plateau size remains the same, a five-fold increase in pyramidal hillock density is observed (increased to about 10 µm^{-2}). A similar increase in pyramid density for increased J_{Sc}/J_N flux ratios was also observed by Smith *et al.* [67]. The formation of pyramidal hillocks has been related to the presence of screw dislocations.

The RMS roughness increases continuously with increasing Sc flux (see figure 4.14), although this effect could also result from the increased film thicknesses. The atomically smooth terraces observed at higher Sc fluxes suggest a considerable amount of surface diffusion, which would be consistent with Sc-rich conditions expected for these films. However, higher substrate temperatures also increase surface diffusion, but the lack of data on the substrate temperature does not allow a closer investigation of these results.

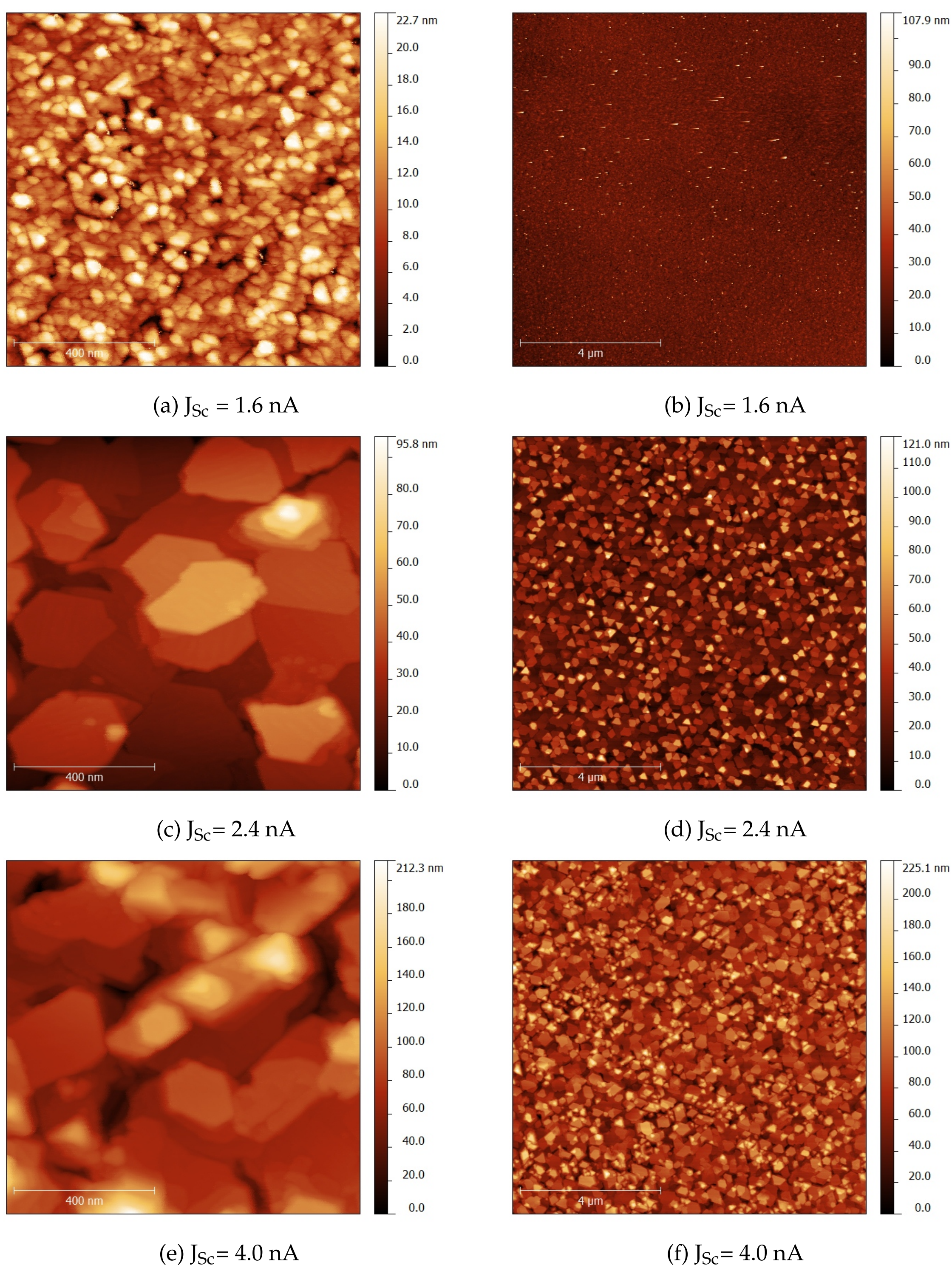

(a) J_{Sc} = 1.6 nA

(b) J_{Sc}= 1.6 nA

(c) J_{Sc}= 2.4 nA

(d) J_{Sc}= 2.4 nA

(e) J_{Sc}= 4.0 nA

(f) J_{Sc}= 4.0 nA

Figure 4.13: 1×1 µm (left) and 10×10 µm (right) AFM topography scans of three ScN films grown by PA-MBE with varying Sc fluxes (J_{Sc}). Top row (a, b): J_{Sc} = 1.6 nA, film thickness = 139 $\pm$ 5 nm; middle row (c, d): J_{Sc} = 2.4 nA, film thickness = 157 $\pm$ 15 nm; bottom row (e, f): J_{Sc} = 4.0 nA, film thickness = 390 $\pm$ 27 nm.

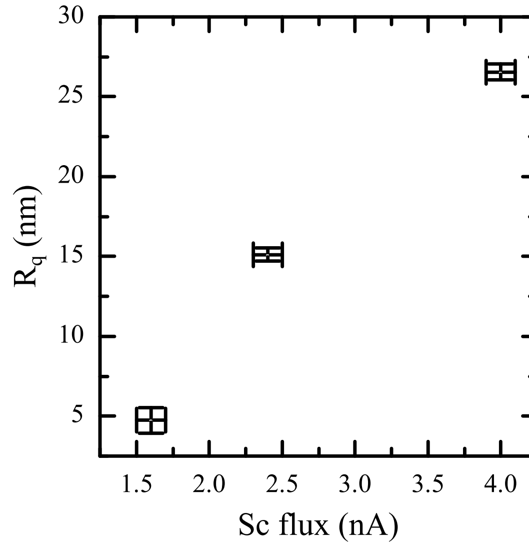

Figure 4.14: RMS roughness for PA-MBE grown ScN samples.

4.3 Optical and electrical measurements

The electrical carrier density was obtained using four-point probe Hall measurements in the van der Pauw geometry. The samples were all found to be intrinsically *n*-type, consistent with both O_N and V_N, with carrier concentrations spanning from $N = 10^{19} - 10^{22}$ cm^{-3} (see table 4.1). These values lie well within the range measured in the literature, which range from $N = 10^{18} - 10^{22}$ cm^{-3} depending on the growth method used [86, 90, 151]. Despite the high oxygen content in the sputtered films [79], the carrier density is relatively low at 10^{19} cm^{-3}. Similar results for sputtered films have also been observed by Gall *et al.* [152] and Ohgaki *et al.* [90], who attributed this to the introduction of deep acceptor states in the band gap due to irradiation damage by the nitrogen plasma. The PA-MBE grown samples showed considerably higher carrier densities at around 10^{21} cm^{-3}, with N increasing with Sc flux. However, both films showed amorphous rings of Sc_2O_3 under the TEM, such that the influence of O_N cannot be discarded. To differentiate between the two effects the optical band gap of these films was investigated: oxygen incorporation is expected to lead to increases in observed E_g, whereas high densities of N-vacancies have been predicted to lower the measured E_g due to subbandgap recombination [67, 153].

The optical band gaps of the ScN films as determined from Tauc plots is shown in figure 4.15. All the ScN films investigated show band gaps higher than the ~ 2.1 eV observed previously for ScN films [66–68], suggesting that at least some degree of oxygen contamination has occurred. The direct band gap of the PA-MBE

	Carrier density, N (cm^{-3})	E_g (eV)
Sputtered	$< 10^{19}$	2.53 ± 0.05
NH_3-MBE	$(1.9 \pm 0.1) \times 10^{20}$	2.25 ± 0.02
PA-MBE, J_{Sc} = 1.6 nA	$(2.4 \pm 0.1) \times 10^{21}$	2.65 ± 0.15
PA-MBE, J_{Sc} = 2.4 nA	$(3.2 \pm 0.3) \times 10^{21}$	2.50 ± 0.03
PA-MBE, J_{Sc} = 4.0 nA	$(3.5 \pm 0.3) \times 10^{21}$	2.24 ± 0.04

Table 4.1: Carrier densities and optical band gaps (direct transitions) of ScN films grown by various techniques.

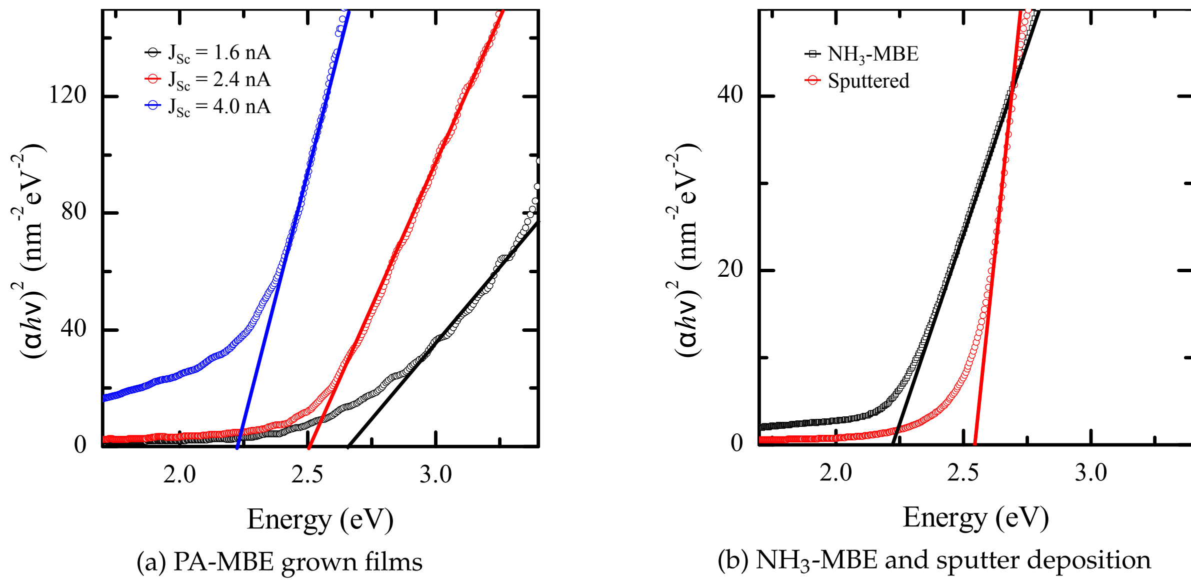

(a) PA-MBE grown films

(b) NH_3-MBE and sputter deposition

Figure 4.15: Tauc plots for ScN films grown by (a) PA-MBE and (b) NH_3-MBE and sputter deposition. The intercept of the tangent with the ordinate corresponds to the magnitude of the direct band gap.

grown films was found to decrease with Sc flux, from a maximum value of 2.65 eV (J_{Sc} = 1.6 nA) to 2.24 eV (J_{Sc} = 4.0 nA), suggesting an increasing deviation from ideal Sc:N stoichiometry towards a nitrogen-deficient material [67, 77, 153]. Indeed, an increase in V_N concentration for higher Sc fluxes would also be consistent with the observed Hall measurements, which show a similar increase in *n*-type carrier concentration. The magnetron sputtered ScN film shows a band gap of 2.55 eV, in agreement with the high degree of oxygen contamination observed by TEM. A detailed investigation of the effect of oxygen contamination on these sputtered ScN films can be found in [79].

4.4 XAS studies

4.4.1 Local bonding geometry

The local coordination environment around the absorbing atom was investigated using EXAFS (see § 3.7 on page 55). The simulations were performed using single and multiple scattering path lengths up to a maximum path length of R = 15 Å using `FEFF9.6` [143]. The observable damping in the experimental signal was accounted for by introducing a Debye-Waller factor (σ) to reproduce the effects of structural disorder [154].

The experimental EXAFS data from the NH_3-MBE grown sample were compared to simulated EXAFS spectra of the ideal rock-salt ScN structure, with a lattice parameter of $a = 4.5057$ Å [65]. The NH_3-MBE sample was chosen as a reference as it displayed the lowest defect density and showed no evidence of oxygen incorporation: the optical band gap was found to be 2.25 ± 0.02 eV. The experimental and simulated EXAFS spectra and respective Fourier-transforms are shown in figure 4.16. It can be seen that the simulated spectra are in very good agreement with the experimental spectrum for the first two coordination shells, corresponding to the Sc-N and Sc-Sc shells. At larger scattering lengths, a slight discrepancy between the two spectra becomes more visible. These data indicate that the NH_3-MBE grown ScN samples are stoichiometric with effectively all the Sc atoms octahedrally (O_h) coordinated by N, with the structural disorder in the sample successfully reproduced by the inclusion of σ.

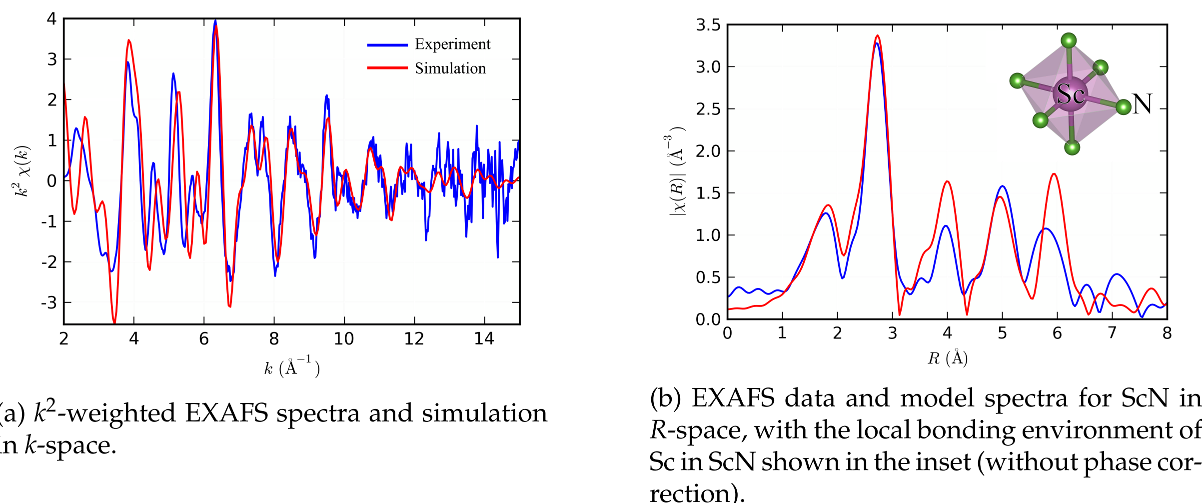

(a) k^2-weighted EXAFS spectra and simulation in k-space.

(b) EXAFS data and model spectra for ScN in R-space, with the local bonding environment of Sc in ScN shown in the inset (without phase correction).

Figure 4.16: Experimental and simulated EXAFS data from ScN films grown by NH_3-MBE.

4.4.2 Electronic structure

The local electronic structure of Sc in ScN was investigated using X-ray absorption near-edge spectroscopy (XANES). XANES spectra can be directly interpreted using projected density of states (PDOS) calculations, and a similar approach was used to interpret the XANES spectra of ScGaN samples (see § 6.3 on page 129). Again, the NH_3-MBE sample was chosen as a reference, and compared to simulated XANES for pure ScN. As can be observed from figure 4.17, the predicted spectrum matches the experimental spectrum well, with all the main spectral features successfully reproduced. The simulated data was fitted to the experiment by a two-step process, whereby it was attempted to match the peak positions by broadening the raw simulated data as outlined in § A.5 on page 151 and subsequently shifting the absolute position in energy.

Comparison of the XANES spectra of epitaxial ScN films grown using different methods reveal similar features for all spectra, indicating that the local electronic structure of Sc remains the same for all investigated growth techniques (figure 4.18). This lends further evidence to the observation that the measured increases in optical band gap from oxidation contamination arise from the Moss-Burstein effect, rather than the formation of a ScN-Sc_2O_3 mixture, as the latter would modify the electronic band structure of the Sc atoms [79, 80].

Interpretation of the XANES spectrum can be separated into two regimes, the pre-absorption edge features (labelled A_1 and A_2) and the fine-structure region. The

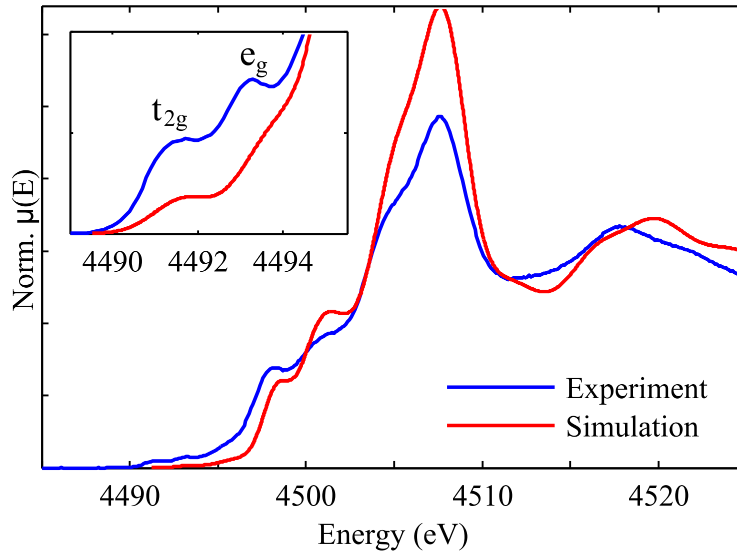

Figure 4.17: XANES spectra collected experimentally ('Experiment') from a typical epitaxial ScN film grown using NH_3-MBE, and simulated by `WIEN2k` for ScN ('Simulation'). The inset shows the pre-edge region more clearly.

fine-structure region corresponds to multiple scattering events around the absorbing atom, and is influenced by the structural quality of the sample [155]. The decreased oscillation amplitude in the fine-structure region observed for both the sputtered and high J_{Sc} PA-MBE films correlates with the greater structural disorder previously observed by HR XRD [89] and cross-sectional TEM (figures 4.10a and 4.9b). Conversely, the NH_3-MBE and low J_{Sc} PA-MBE films with lower defect densities (figures 4.5 and 4.9a) also displayed strong features in the fine-structure.

An inset of the pre-edge region of the XANES spectrum is shown in figure 4.18. The first two peaks in this region, A_1 and A_2, arise from the crystal field splitting of the O_h point group symmetry, however only very weak pre-edge features are expected for the O_h bonding environment [156]. On the other hand, transition metals in tetrahedral coordinations, such as Sc in ScGaN, characteristically display very intense pre-edge absorption peaks, and decreases in these features have been used to identify distortions from the ideal tetrahedral bonding environment [54, 147]. In a similar manner, slight deviations from the ideal O_h bonding environment will result in increases in the pre-edge absorption features. The film grown by NH_3-MBE shows the lowest intensity pre-edge features, as expected for a stoichiometric film with near-ideal O_h coordination symmetry, with slight increases in the A_2 peak intensity observed for the remaining films. Most notably, the PA-MBE film grown under highly

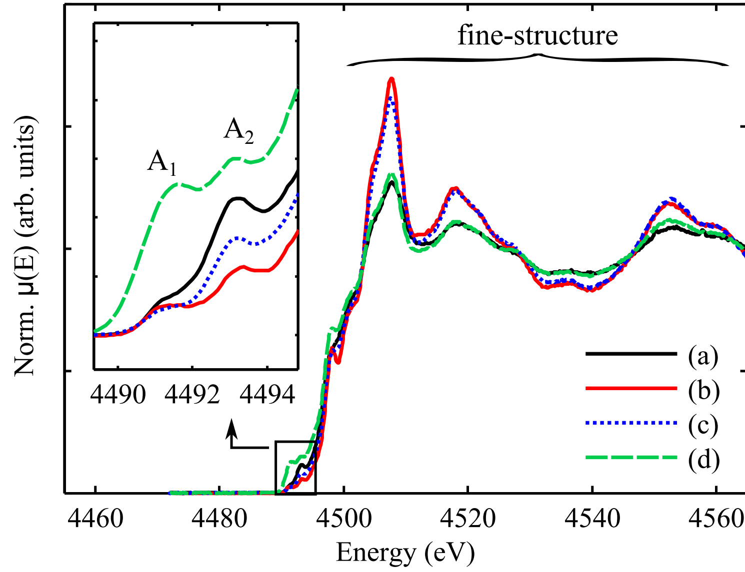

Figure 4.18: XANES spectra of epitaxial ScN grown by (a) magnetron sputter deposition, (b) NH_3-MBE, (c) low J_{Sc} PA-MBE and (d) high J_{Sc} PA-MBE. The inset shows detail in the pre-edge region.

Sc-rich conditions shows a considerable increase in A_1 peak intensity, suggesting a stronger deviation from ideal O_h coordination. This observation may be explained by the high density of nitrogen vacancies expected in this film. The removal of a nitrogen atom from the crystal leads to a relaxation of the surrounding atoms into a non-ideal octahedral configuration, thus leading to the observed increases in pre-edge absorption features.

4.4.3 Dichroism

The six-fold cubic coordination of Sc by N was also verified by measuring the XANES spectrum at different angles relative to the sample. A difference in the in-plane and out-of-plane environment, as is the case in non-centrosymmetric crystal lattices such as wurtzite, would result in measurable differences between the measured spectra. As ScN is cubic with the $Fm\bar{3}m$ space group, no dichroism is expected. This was verified by taking XANES spectra at vertical grazing incidence ($E \parallel c$) and at the magic angle ($E\angle c = 54.7°$ [144]) (see figure 4.19).

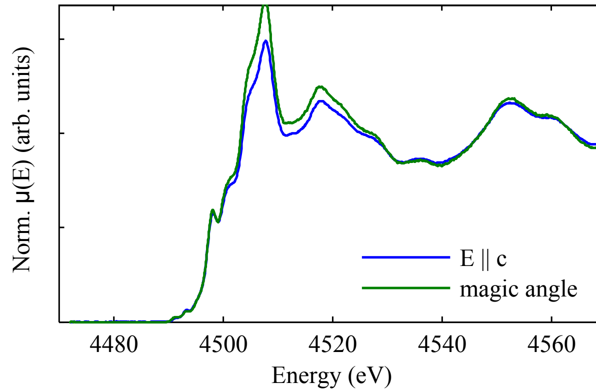

Figure 4.19: XANES spectrum for ScN taken at different angles of polarisation. No qualitative differences in the two spectra are observed, as expected for isotropic crystals.

4.5 Synopsis

This chapter investigated the structural and electronic properties of ScN films grown by MBE. Unlike for growth of conventional III-nitrides [58], the lowest defect density films were grown under N-rich conditions. In particular, the use of NH_3 as a nitrogen source in MBE forms a strongly reducing growth environment, and limits the degree of oxygen contamination. An epitaxial relationship of $(111)_{ScN} \parallel (0001)_{GaN}$ and $[11\bar{2}]_{ScN} \parallel [1\bar{1}00]_{GaN}$ was observed, with in-plane twinning in the (111) plane along $[11\bar{2}]$. Using a procedure developed by Moram *et al.* [65], a biaxial compression of 0.4% was found.

The ScN films grown by PA-MBE were found to be nitrogen deficient, which overall rougher surface morphologies and higher defect densities. The films also suffered from oxygen contamination, already known to deteriorate the crystal quality of ScN films [79], observed in the form of amorphous Sc_2O_3.

Although the majority of Sc atoms remained in octahedral coordination environments, high concentrations of nitrogen vacancies were found to lead to distortions of this ideal bonding environment, leading to increases in the pre-edge peak intensity as observed by XANES.

Chapter 5

ScGaN: Microstructure

"The experimenter who does not know what he is looking for will not understand what he finds."

-Claude Bernard

Contents

5.1 Introduction 85
5.2 Determination of Sc content 86
5.3 Growth rates 91
5.4 Surface morphology 95
5.5 Strain analysis 103
5.6 Microstructure 107
5.7 Synopsis 118

5.1 Introduction

This chapter describes an investigation of the growth conditions and resulting microstructural properties of ScGaN epilayer films, characterised by a range of techniques encompassing AFM, HRXRD, TEM and PL. Growth was performed by MBE using NH_3 as a nitrogen source at the University of Liverpool. A complete description of the samples and growth conditions can be found in § B on page 155.

5.2 Determination of Sc content

It is important to quantify the Sc content accurately before conducting further analysis. Precise control of the alloy composition is an essential requirement for engineering of band gaps and lattice parameters. Three methods have been investigated to determine the film alloy Sc content, *viz.* EDX quantification, HRXRD diffractogram simulation and using the normalised XAS signal intensity.

5.2.1 Energy dispersive X-ray analysis

EDX is a common technique used for obtaining approximate compositions of alloy films, by comparing the relative intensity of characteristic elemental X-ray emission lines (see § 3.6.5.2 on page 54). In the case of ScGaN, the nitrogen $K_{\alpha 1}$ line and the scandium L_{α} line occur at 0.392 keV and 0.395 keV, respectively (see Table 3.4 on page 55) [131]. Unfortunately, the emission lines are too close in energy to be distinguished from each other.

The use of higher energy peaks is complicated by the need to use higher accelerating voltages, which result in larger electron interaction volumes. As a general rule, an acceleration voltage of around three times that of the desired emission line is required [131]. To probe the scandium $K_{\alpha 1}$ line at 4.09 keV, an acceleration voltage of around 12 kV is necessary. In the conventional plan-view SEM-EDX analysis geometry, the larger electron interaction volume (and hence the larger X-ray sampling volume) leads to a higher probability of detecting X-rays from the underlying GaN substrate as well as from the ScGaN film. The interaction volume can be calculated analytically (*e.g.* using the Kanaya & Okayama expression [157]) or using a Monte Carlo (MC) simulation. As an example, a 12 kV MC simulation was performed on a 250 nm thick ScGaN-on-GaN film (figure 5.1) using the `Casino v2` software [158]. Details of the simulation setup are provided in § A.3 on page 147. These simulations show that considerable signal would come from the underlying GaN layer and hence that uncertainty in the film thickness would lead to additional uncertainty in the Sc content obtained.

EDX quantification was also attempted in the TEM, where unintentional sampling of the underlying GaN layer can be avoided using the cross-sectional geometry. However, the small sampling volume and dilute specimens involved resulted in very poor signal-to-noise ratios, such that this method also proved unsuccessful. In addition, the aformentioned problem of emission line overlap remains.

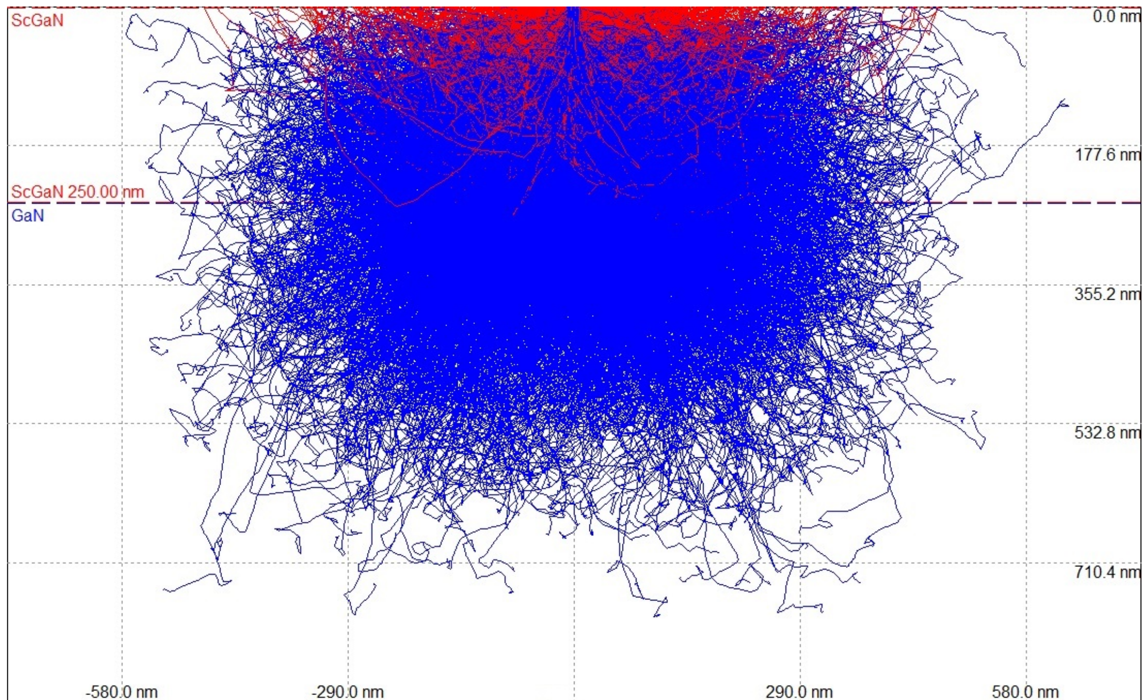

Figure 5.1: Monte Carlo simulation of electron interaction volume for a ScGaN epilayer of 250 nm thickness, using an accelerating voltage of 12 kV. Re-exiting trajectories are marked in red. The electron interaction volume penetrates deeply into the GaN pseudosubstrate.

Additionally, the peak intensities in EDX spectra are affected by the crystal structure of the sample. The significant differences in crystal structure between ScN and GaN, combined with a general lack of calibrated standards, make it difficult to accurately relate the EDX spectra to the Sc content in the film. The lower intensities of the high energy peaks also results in a higher detection limit. Thus it is not possible to accurately quantify the Sc content of ScGaN films using EDX alone.

5.2.2 HRXRD analysis using $\omega - 2\theta$ scans

The composition of conventional III-nitride alloys can be estimated by measuring the position of a symmetric reflection and relating the d-spacing back to the film composition. Vegard's law is assumed, namely that the alloy lattice parameter can be predicted by a linear interpolation between the lattice parameters of the alloy end members (see § 3.5.3 on page 39). As can be seen from figure 5.2, Vegard's law does not apply to ScGaN alloys as the structure changes significantly across the composition range, manifested in abrupt changes in a, c and the internal parameter u. How-

x (ScN)	a	c	u	ν
0	3.1890	5.1865	0.377	0.21
0.0625	3.2090	5.2001	0.378	0.24
0.1250	3.2300	5.2113	0.379	0.26
0.1875	3.2530	5.2147	0.381	0.28
0.2500	3.2740	5.2232	0.382	0.31
0.3125	3.2970	5.2249	0.384	0.33
0.3750	3.3230	5.2168	0.387	0.36
0.4375	3.3530	5.1838	0.391	-
0.5000	3.3770	5.1783	0.394	-
0.5625	3.4220	5.0785	0.404	-
0.6250	3.5150	4.7951	0.449	-
0.6875	3.6040	4.4844	0.498	-
0.7500	3.6240	4.4883	0.497	-
0.8125	3.6460	4.4879	0.500	-
0.8750	3.6680	4.4878	0.500	-
0.9375	3.6900	4.4833	0.500	-
1	3.7120	4.4841	0.500	-

(a)

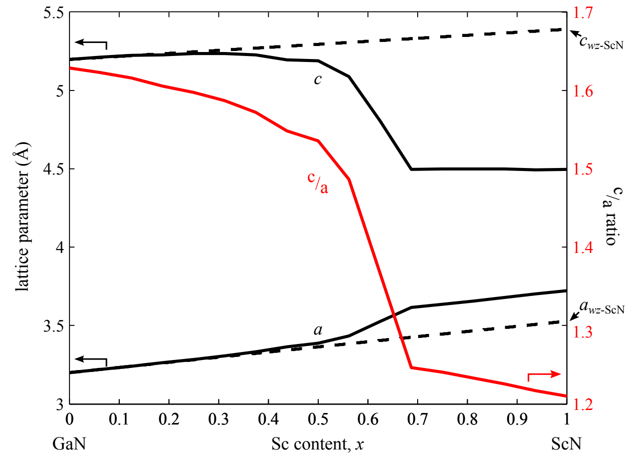

(b)

Figure 5.2:
(a) Table of calculated lattice parameters and Poisson ratio, ν, of $Sc_xGa_{1-x}N$ alloys. The ScN and GaN lattice parameters have been scaled to their experimental values, with the $Sc_xGa_{1-x}N$ parameters scaled by a linear interpolation [95].
(b) Plot of lattice parameters and c/a ratio against Sc content, x.

ever, $Sc_xGa_{1-x}N$ films are expected to retain the wurtzite phase for low Sc contents, at least up to $x = 0.27$ [95], and indeed previous experimental studies of ScGaN films grown by MBE found the wurtzite structure is maintained up to Sc contents of at least $x = 0.17$ [101].

The lattice parameters show a linear increase with increasing Sc content for very low Sc contents ($x < 0.1875$) and a linear regression fitted to the a and c parameters in the low Sc content regime yields goodness-of-fit values of $R^2 = 0.9998$ and $R^2 = 0.9976$, respectively. By extrapolating to a Sc content of $x = 1$, the theoretical lattice parameters of *wz*-ScN were established (see table 5.1). The extrapolated values for this hypothetical *wz*-ScN are noticeably different to those predicted by Takeuchi (a = 3.49 Å, c = 5.58 Å) [72]. Note that *wz*-ScN is an unstable structure and the calculated lattice parameters are only used in relation to low Sc content $Sc_xGa_{1-x}N$ alloys. In this low Sc content region ($x < 0.1875$), the alloy lattice parameters are assumed to vary linearly between those of *wz*-GaN and *wz*-ScN, following Vegard's law (see

	A	B	R^2	*wz*-ScN
a	3.189 Å	0.328 Å	0.9998	3.517 Å
c	5.187 Å	0.192 Å	0.9976	5.379 Å
u	0.377 Å	0.016 Å	1.0000	0.393 Å
ν	0.21	0.400	0.9868	0.610

Table 5.1: Linear regression analysis and theoretical lattice parameters of hypothetical *wz*-ScN structure. The regression parameters are displayed in the format of $y = A + Bx$, together with the goodness-of-fit parameter, R^2.

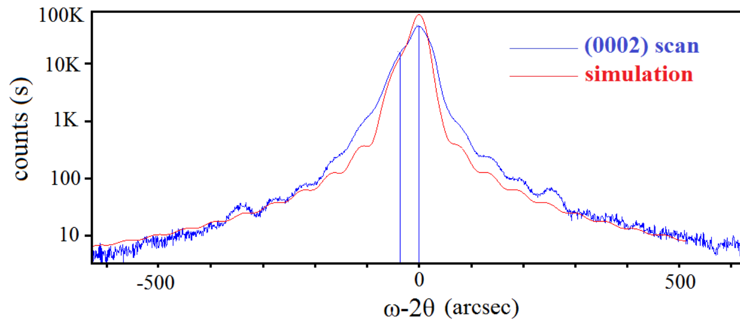

Figure 5.3: Experimental $\omega - 2\theta$ scan and best-fit simulation of the 0002 peak for a strained $Sc_xGa_{1-x}N$ film, with the simulation assuming a Sc content of $0.45 \pm 0.1\%$. From [159].

§ 3.5.3 on page 39). Simulation of $\omega - 2\theta$ X-ray diffractograms was performed using commercial `X'Pert Epitaxy 4.0` software; details of the fitting parameters used can be found in A.4.1 on page 147.

Uncertainties in the film Sc contents were established by attempting to fit the experimental data using a range of Sc contents and elastic constant values, where only the best fits were accepted. The detection limit lies at around 0.1% Sc, and typical uncertainty values were of the same order of magnitude. Some films showed signs of strain relaxation, as evidenced by asymmetric RSMs of the $10\bar{1}5$ reflection. In these cases, best-fit simulations of the $\omega - 2\theta$ scans only provide a lower limit to the possible Sc content. An example of a simulated $\omega - 2\theta$ scan for the 0002 reflection is shown in figure 5.3.

5.2.3 X-ray absorption spectroscopy analysis

As part of the XAS alignment procedure, the intensity of the Sc signal is measured as a function of position across the width of the sample, to ensure that the X-ray beam is

	ScN	$Sc_xGa_{1-x}N$
structure	rock-salt	wurtzite
Sc atoms per unit cell	4	2
lattice parameters	4.5057 Å	a = 3.189 Å c = 5.185 Å
unit cell volume	91.125 Å^3	45.666 Å^3
density of Sc atoms, ρ	4.3896×10^{-2} Å^{-3}	4.3797×10^{-2} Å^{-3}

Table 5.2: List of parameters used to normalise the Sc XAS emission intensity.

correctly aligned on the centre of the sample. Several samples can be mounted on the XAS sample stage in one batch. The Sc content of ScGaN samples was calculated by comparing the signal relative to the NH_3-MBE grown ScN reference sample, which was assumed to be stoichiometric. The XAS intensity (I) is proportional to the total number of Sc atoms sampled, *i.e.* $I \propto t \cdot A \cdot \rho$ where t is the X-ray penetration depth, A is the area illuminated by the X-ray beam and ρ is the density of Sc atoms per unit volume (table 5.2). For the incident angle of 45.9° used during the alignment, the penetration depth is ~ 4 µm, *i.e.* considerably larger than the thickest films investigated. Thus to calculate the Sc content of a $Sc_xGa_{1-x}N$ sample one would need to apply the following conversion factor:

$$x = \left(\frac{I_{ScGaN}}{I_{ScN}} \right) \left(\frac{t_{ScN} \cdot \rho_{ScN}}{t_{ScGaN} \cdot \rho_{ScGaN}} \right)$$

Given an ideal stoichiometric reference sample, the estimated uncertainties in Sc content were between ±0.1% and ±1% Sc. This error was estimated by adding the relative errors of film thickness and XAS intensity in quadrature. The XAS intensity count was assumed to follow a Poisson distribution, giving an error estimate equal to the square-root of the measured intensity. Determination of Sc content using the XAS absorption intensity thus provided the highest relative accuracy of the different methods investigated. The estimated Sc contents of $Sc_xGa_{1-x}N$ alloys reported in this thesis were obtained using this method. Unfortunately, XAS analysis could not be performed on all samples. For these samples, the Sc content was measured using $\omega - 2\theta$ scans and scaled using reference XAS measurements.

5.3 Growth rates

Precise control of the thickness and composition of the III-nitride active region is an essential for obtaining consistent device performance. It is thus necessary to have an accurate understanding of the growth rates as a function of different growth parameters. For example, it is known that only small changes in the substrate temperature (± 5 °C) can significantly affect both the growth rate and alloy composition of InGaN films [160]. Film thicknesses were determined using Kiessig fringes in symmetric X-ray diffraction scans (see § 3.5.2 on page 39), subsequently verified using cross-sectional TEM measurements.

5.3.1 Substrate temperature

To study the effects of substrate temperature on the ScGaN film growth rate, the relative fluxes of Sc, Ga and NH_3 were kept constant. The Sc and Ga cell temperatures were fixed at 1400 °C and 950 °C, respectively, with a constant NH_3 flow rate of 40 sccm. No detectable change in the growth rate of ScGaN films was observed over a temperature range of $650 - 900$ °C (see figure 5.4). The Sc content also increased to a very small extent with increasing temperature, from below the detection limit to $1.0 \pm 0.2\%$. In contrast, InGaN alloys show a *decrease* in both growth rate and In content at elevated temperatures [160]. This is attributed to a reduction in the In adatom sticking coefficient, which is thus less likely to be incorporated into the growing film. The independence of the growth rate with respect to the substrate temperature in the growth of ScGaN is clearly advantageous: potential temperature variations across the wafer should not influence the film properties, leading to increased uniformity and reproducibility.

In the MBE growth of binary compounds such as GaN, growth conditions can be either metal-rich or N-rich, with optimum conditions lying at the crossover between the two regimes (§ 2.3 on page 28). Optimum conditions can be determined by plotting the growth rates versus the Ga and N fluxes. For ternary alloys such as ScGaN, the growth conditions will be affected by a third factor, the Sc flux, and growth rates versus the three elemental fluxes need to be considered to find the optimum growth conditions.

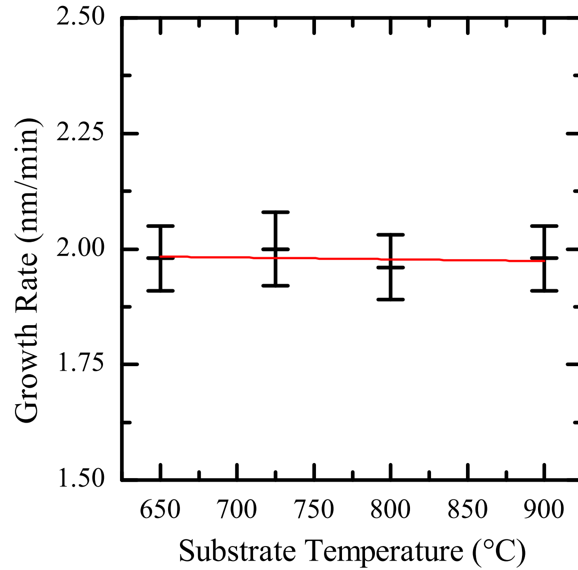

Figure 5.4: A plot of the effect of varying substrate temperature on the growth rate of ScGaN films. Over the temperature range of 650 − 900 °C, no detectable differences were observed.

5.3.2 Nitrogen flux

In MBE systems where the source of nitrogen is NH_3, the relative flux of active nitrogen is not easily quantifiable. One cannot simply control the amount of active nitrogen by changing the NH_3 pressure, as the cracking efficiency of NH_3 is dependent on the sample surface composition itself. As the effect of Sc on the cracking efficiency is unknown, studying the effect of varying nitrogen flux on the growth conditions was not attempted, and all films were grown at the same NH_3 flux of 40 sccm. However, the different growth parameters are intricately linked, so that a change in either of the metallic fluxes will inevitably result in different amounts of active nitrogen, despite the NH_3 flow rate itself remaining constant. Due to the relatively high amount of nitrogen compared to other atomic species, the growth conditions are exclusively in the N-rich (also termed 'metal-limited') regime.

5.3.3 Gallium flux

The effect of Ga flux, J_{Ga}, on the growth rate was studied by maintaining a substrate temperature of 800 °C and a Sc cell temperature of 1400 °C, while increasing the Ga cell temperature from 930 − 1000 °C. The measured growth rates were compared

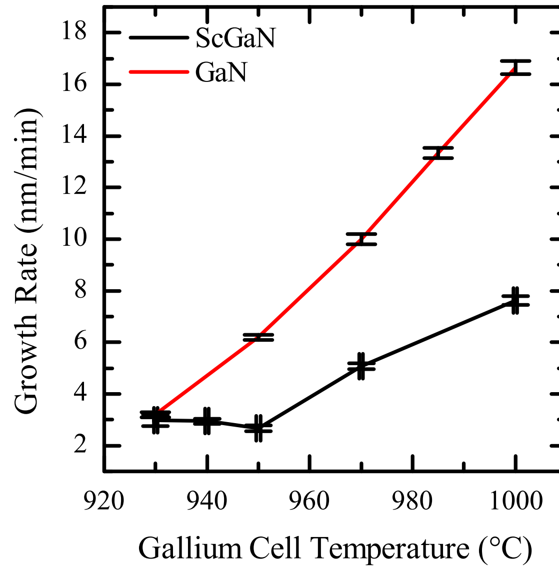

Figure 5.5: Plot of the GaN growth rate versus the Ga cell temperature (red) and a plot of the ScGaN film growth rate versus the Ga cell temperature (black), for a constant Sc cell temperature of 1400 °C. The substrate temperatures for all films was kept constant at 800 °C and the NH_3 flow rate was maintained at 40 sccm.

against binary GaN grown under similar conditions. Note that in both cases the high NH_3 chamber pressure resulted invariably in N-rich conditions. It was found that the ScGaN film growth rate remains relatively constant up to T_{Ga} = 950 °C, after which a monotonic increase with T_{Ga} is observed (figure 5.5). This suggests that before the transition at 950 °C growth was limited by the availability of Sc. After this point, a transition from the Sc-limited to the Ga-limited growth regime is observed.

The apparent paradox in the transition to Ga-limited conditions for higher J_{Ga} may be explained in the light of a Sc-rich surface adlayer. For low J_{Ga}, the growth surface accumulates Sc atoms and growth rate is dependent on the diffusion of Ga adatoms across the Sc-rich layer. For small changes in J_{Ga}, the Sc-rich adlayer persists and growth rates are only marginally affected. However, at sufficiently large J_{Ga}, the high arrival rate of Ga adatoms can prevent the Sc-adlayer from forming and film growth rates increase rapidly with J_{Ga}. The Sc content also increases monotonically in parallel with the growth rates, suggesting that the growth surface advances so rapidly that Sc adatoms are rapidly buried by arriving Ga and N species (figure 5.6). Significantly, the total growth rates of ScGaN films were lower than those of comparable GaN films by about a factor of 2. Similar observations have also been made in the growth of MnGaN films, where presence of Mn was found to decrease film growth rates in

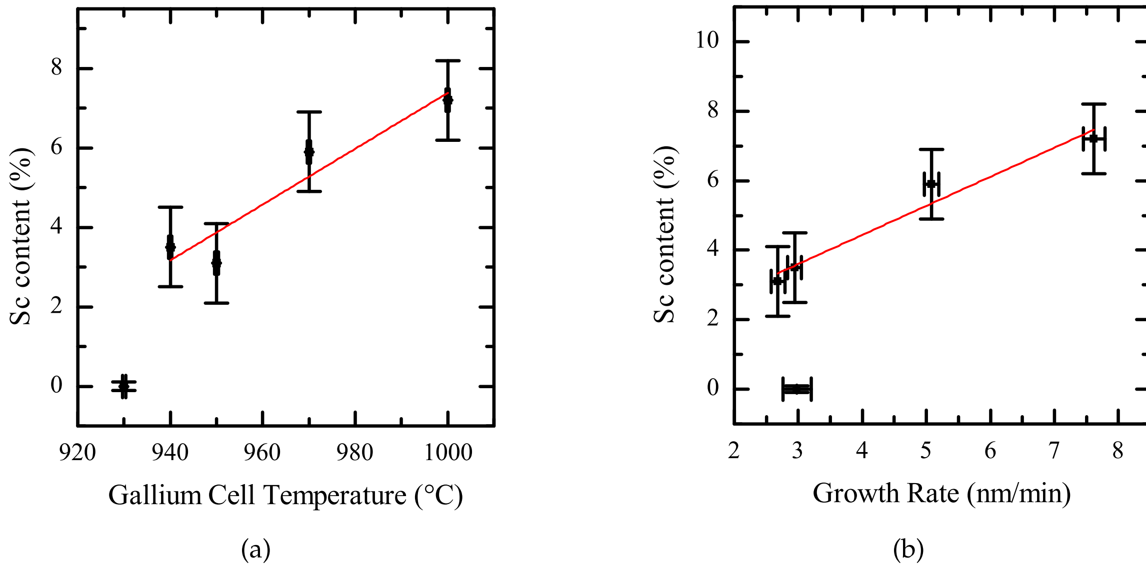

Figure 5.6: Variation of film Sc content plotted against (a) T_{Ga} and (b) film growth rate for a constant Sc flux. The Sc content of the film grown at T_{Ga} = 930 °C was below the detection limit.

stoichiometric and N-rich conditions [161]. In the case of FeGaN, Fe incorporation was found to increase as the V/III ratio increased [61].

5.3.4 Scandium flux

It was found that increasing the Sc cell temperature while keeping all other parameters constant actually *decreased* the growth rates, *i.e.* an increase in J_{Sc} hinders growth of the ScGaN alloy (figure 5.7). In fact, the growth rate for the ternary alloy was found to lie in between the growth rates of the alloy end members, with a growth rate of 5 nm/min for GaN (at a Ga cell temperature of 950 °C) and 1.5 nm/min for binary ScN (with a Sc cell temperature of 1400 °C, see § 4.2.2.1 on page 65). As the Sc cell temperature was increased from 1370 − 1400 °C, the growth rates were found to drop by 40%, while the Sc content increased from near the detection limit to 4% over the same range (figure 5.8a).

These results are also in agreement with the presence of a Sc-rich adlayer on the growth surface. The surface mobilities of Ga and N adatoms are effectively decreased, and for the growth surface to advance diffusion of the adatoms through the Sc adlayer is required. By this interpretation, as J_{Sc} is increased, the Sc adatom density increases, further reducing the film growth rates. Similar metal-rich surface layers have also

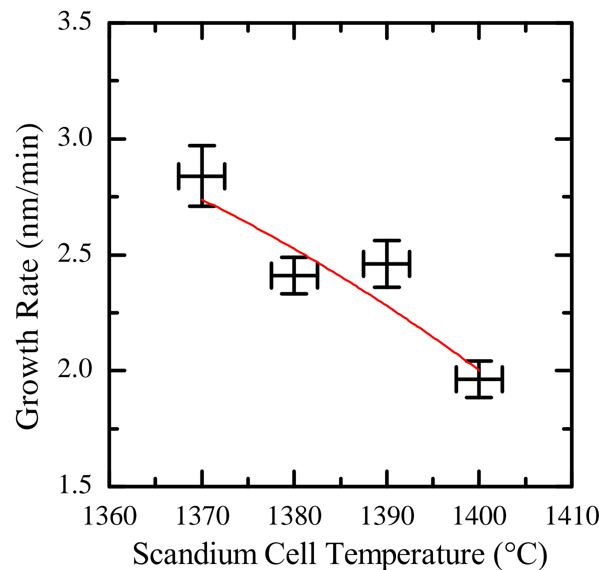

Figure 5.7: Plot of the ScGaN growth rate versus the Sc cell temperature, for a constant Ga cell temperature of 950 °C and a constant NH_3 flow rate of 40 sccm. The red line serves as a guide to the eye.

been observed for the growth of other transition metal doped nitrides, such as FeGaN [60, 61] and MnGaN [59, 161, 162] and CrGaN [163] (see § 1.2.1.1 on page 12 for further details). The presence of such floating layers was inferred from changes to the surface reconstruction during and after growth, as measured *in-situ* by RHEED. Unfortunately, RHEED measurements could not be taken in our setup due to the high NH_3 partial pressures during growth. The Sc content increases was found to decrease with the growth rate, as can be observed in figure 5.8b.

5.4 Surface morphology

AFM analysis showed that the ScGaN films had a relatively rough surface morphology compared to the GaN substrate (figure 5.9), consistent with N-rich film growth conditions [26]. As described in § 2.3 on page 28, layer-by-layer growth of GaN by MBE is achieved in the Ga-rich regime. Indeed, the III/V ratio not only has significant effects on the surface morphology but also on the structural and optical properties of GaN [113]. Ga adatoms are thought to have limited diffusion lengths on the growth surface, after which they are either incorporated into the film or desorb [114]. In the case of N-rich conditions, Ga adatoms rapidly find an N adatom to bond with. In ad-

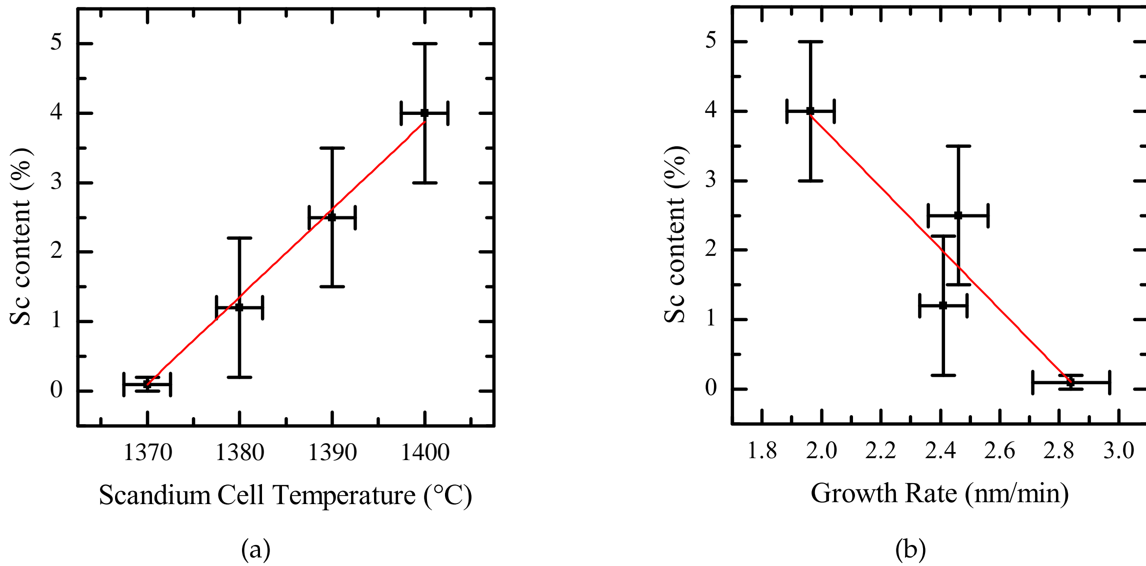

Figure 5.8: Variation of film Sc content plotted against (a) Sc cell temperature and (b) film growth rate for varying J_{Sc} (J_{Ga} constant).

dition to the III/V ratio, the substrate temperature directly affects adatom mobilities and is thus an important growth parameter.

The Sc flux is a further growth parameter. Relative adatom mobilities and ammonia cracking efficiency are all affected by the presence of Sc. It is not possible to use growth conditions established for binary GaN; a separate investigation of all parameters needs to be performed in order to determine the optimum growth conditions for ScGaN films. Here, we investigate the development of the surface morphology with changing substrate temperature, Ga and Sc cell temperatures. As the growth system did not have an ion gauge for flux measurement, the effusion cell temperature was taken to be directly proportional to the flux as a first approximation.

5.4.1 Substrate temperature

The effect of the growth temperature (T_g) on the surface morphology of ScGaN was investigated by varying the substrate temperature from 650 °C to 900 °C while keeping all other parameters constant, where the growth times were adjusted to achieve similar film thicknesses (264 ± 4 nm). The surface morphology of the ScGaN films was found to be very different to the GaN substrate (figure 5.10). Preliminary PL data can be found in Appendix C on page 161.

At the lowest temperature of T_g = 650 °C, the surface shows a heavily pitted mor-

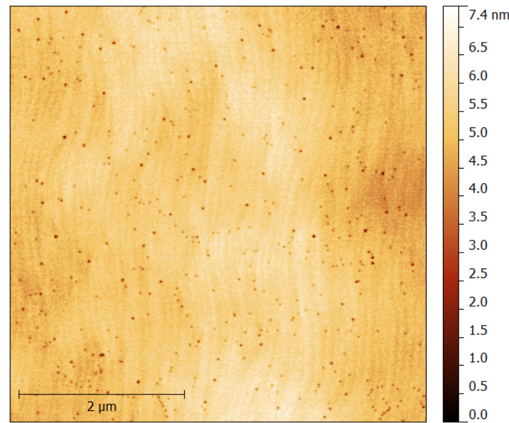

Figure 5.9: 5 × 5 µm AFM topography scan of GaN-on-sapphire pseudosubstrate grown by MOVPE. These samples were used as templates for heteroepitaxial growth of ScGaN by MBE.

phology (figure 5.10a). At these low growth temperatures, reduced surface diffusion commonly leads to uncoalesced film surfaces [115]. The surface morphology is very similar to that of FeGaN films grown in the Fe-rich growth regime [61]. The ammonia cracking efficiency also drops significantly at this temperature, despite the high ammonia flow rate of 40 sccm employed here [164].

As the temperature is increased to T_g = 725 °C, a distinct change in the surface morphology is observed, from an uncoalesced plateau-like surface to a coarse grain-like topography (figure 5.10b). The surface consists of rounded hillocks 40 ± 10 nm high at a density of approximately 100 µm^{-2}. This topography is typical for N-rich conditions, in which the metal adatom surface diffusion lengths tend to be shorter and thus lead to rough surface morphologies. A further increase in T_g increases the NH_3 cracking efficiency and thus the V/III ratio, leading to a finer grain structure (figure 5.10c). Such morphological transitions are commonly observed in the MBE growth of GaN, during the crossover from Ga-rich to N-rich conditions [113] and also in the MBE growth of TM-doped GaN such as FeGaN [61] and MnGaN [162].

At the highest growth temperature of T_g = 900 °C, the surface maintains a grain-like topography, but is markedly smoother (figure 5.10d). The average hillock height is only 4 ± 1 nm at an increased density of roughly 240 µm^{-2}. However, the PL emission intensity is almost entirely quenched for this sample. The GaN evaporation rate in an MBE environment is known to increase rapidly above 850 °C [118]. As a general rule, elemental sticking coefficients, in the same manner as effusion cell evaporation

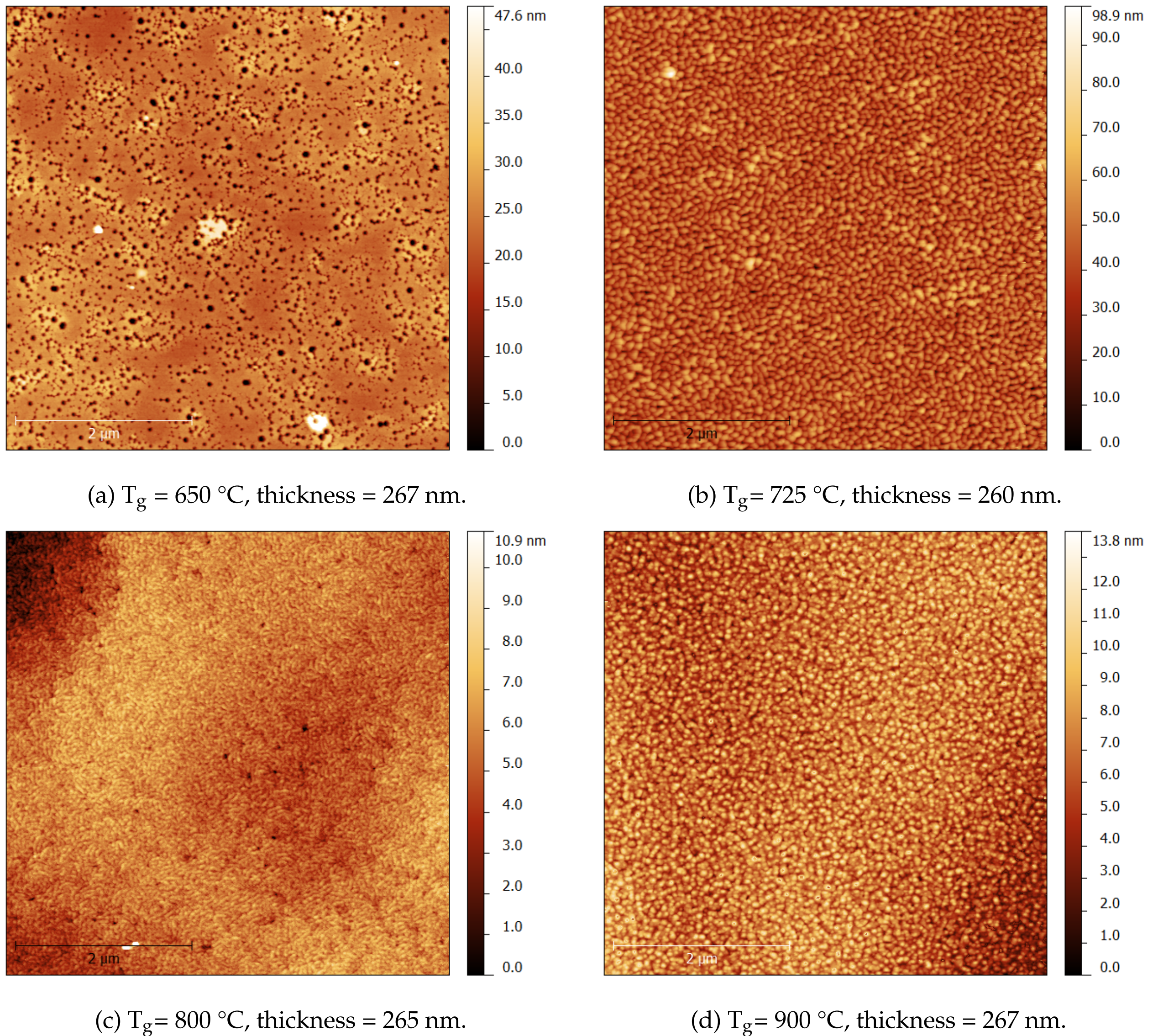

(a) T_g = 650 °C, thickness = 267 nm.

(b) T_g= 725 °C, thickness = 260 nm.

(c) T_g= 800 °C, thickness = 265 nm.

(d) T_g= 900 °C, thickness = 267 nm.

Figure 5.10: 5 × 5 µm AFM height scans of ScGaN films grown on GaN-on-sapphire substrates by NH_3-MBE. The four samples constitute a series with increasing growth temperature, T_g. The errors in T_g and film thickness are ±2.5 °C and ±10 nm, respectively.

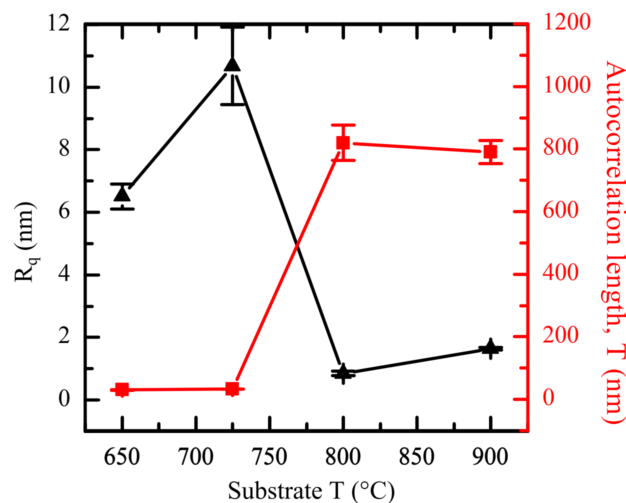

Figure 5.11: Roughness parameters for increasing substrate temperature. The Ga and Sc cell temperatures were kept constant at T_{Ga}= 940 °C and T_{Sc}= 1400 °C, respectively.

rates, related to the vapour pressure of the element. At a growth temperature of 800 °C, the vapour pressure of Sc metal, at 3×10^{-8} Torr, is significantly lower than that of Ga metal at the same temperature (6×10^{-6} Torr) [67]. Thus it can be envisaged that at higher growth temperatures the relative concentration of Sc adatoms increases, as a result of the respectively lower adatom desorption rate compared to Ga or N.

As the substrate temperature increased, increased surface diffusion lengths led to a reduction in the RMS roughness, R_q, with an associated increase in the lateral autocorrelation length, T (figure 5.11).

5.4.2 Scandium flux

A similar change in morphology is observed with increasing Sc cell temperature (figure 5.12). At T_{Sc} = 1370 °C, the ScGaN surface is patchy containing many deep pits, which coalesce as the T_{Sc} is increased forming the grain-like morphology typical of stochastically roughened films [165]. Additional larger hillocks are observed that appear to originate underneath the familiar grain-like morphology (average height and diameter of 5 nm and 300 nm, respectively), which increase in density as the T_{Sc} is increased to 1390 °C. At T_{Sc} = 1400 °C the roughness and scale of the superimposed smaller, grainy features remained the same throughout.

Analysis of the film growth rates (§ 5.3 on page 91) indicated the formation of a Sc-rich adlayer on the growth surface, which was associated with a reduction in growth rates as the Sc flux was increased (T_{Sc} raised). Figure 5.13 shows a sharp

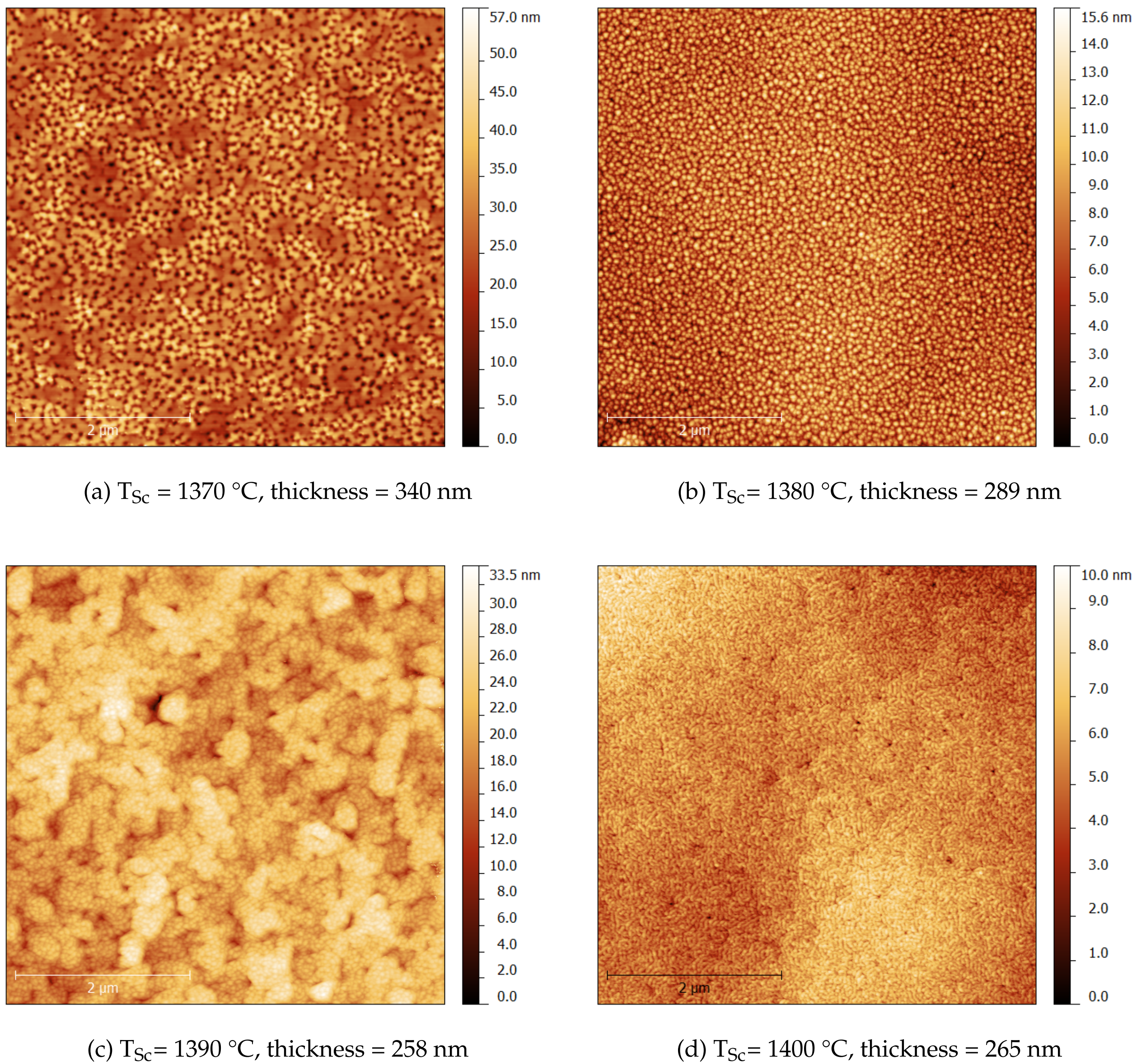

(a) T_{Sc} = 1370 °C, thickness = 340 nm

(b) T_{Sc}= 1380 °C, thickness = 289 nm

(c) T_{Sc}= 1390 °C, thickness = 258 nm

(d) T_{Sc}= 1400 °C, thickness = 265 nm

Figure 5.12: 5 × 5 μm AFM topography scans of ScGaN films grown on GaN-on-sapphire substrates by NH_3-MBE. The four samples represent a series with increasing Sc cell temperature. The errors in T_{Sc} and film thickness are ±2.5 °C and ±10 nm, respectively.

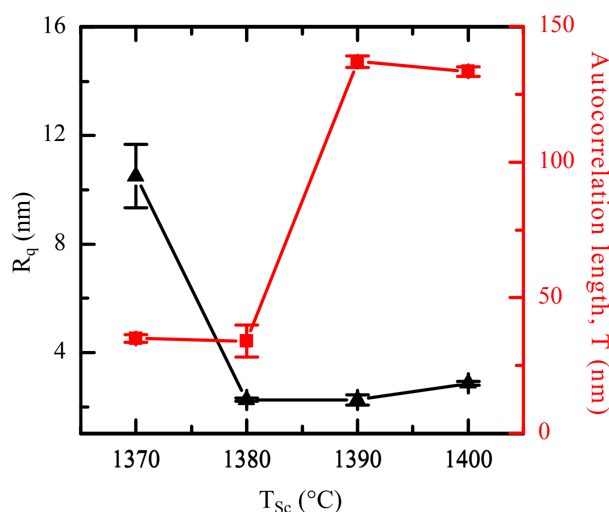

Figure 5.13: Roughness parameters for ScGaN samples with varying Sc cell temperature, T_{Sc}.

decrease in RMS roughness as the surface voids are covered, after which very smooth films of R_q = 2.5 ± 0.1 nm are observed. It is likely that the Sc-rich adlayer, which is not expected to be present for the film grown at T_{Sc} = 1370 °C (Sc content was near detection limit of 0.1%, see figure 5.8b) counteracts stochastic roughening by allowing extensive surface diffusion of the adatoms before they are incorporated into the lattice. Similar observations have been made in the growth of MnGaN films [162].

5.4.3 Gallium flux

To study the effect of varying the Ga flux on the surface morphology, a series of ScGaN films were grown at the same NH_3 fluxes, with both substrate and Sc cell temperatures fixed at 800 °C and 1400 °C, respectively (see Table B.2c on page 158 for full details). However, a direct comparison between the surface morphologies is not possible, as the film thicknesses varied between 133 − 457 nm. Other effects such as stress and compositional induced roughening will affect the surface topography [166].

Figure 5.14 shows the AFM topography scans of a series with increasing Ga cell temperature, T_{Ga}. At T_{Ga} = 935 °C, the surface displays a high density of spiral growth mounds with hexagonal features. Such a morphology is also observed in the MBE growth of GaN, and is attributed to Ga-rich growth conditions [113]. Contrary to the expected trend, as the Ga cell temperature is increased to 940 °C and higher, the morphology changes to a granular morphology, typical of N-rich growth conditions.

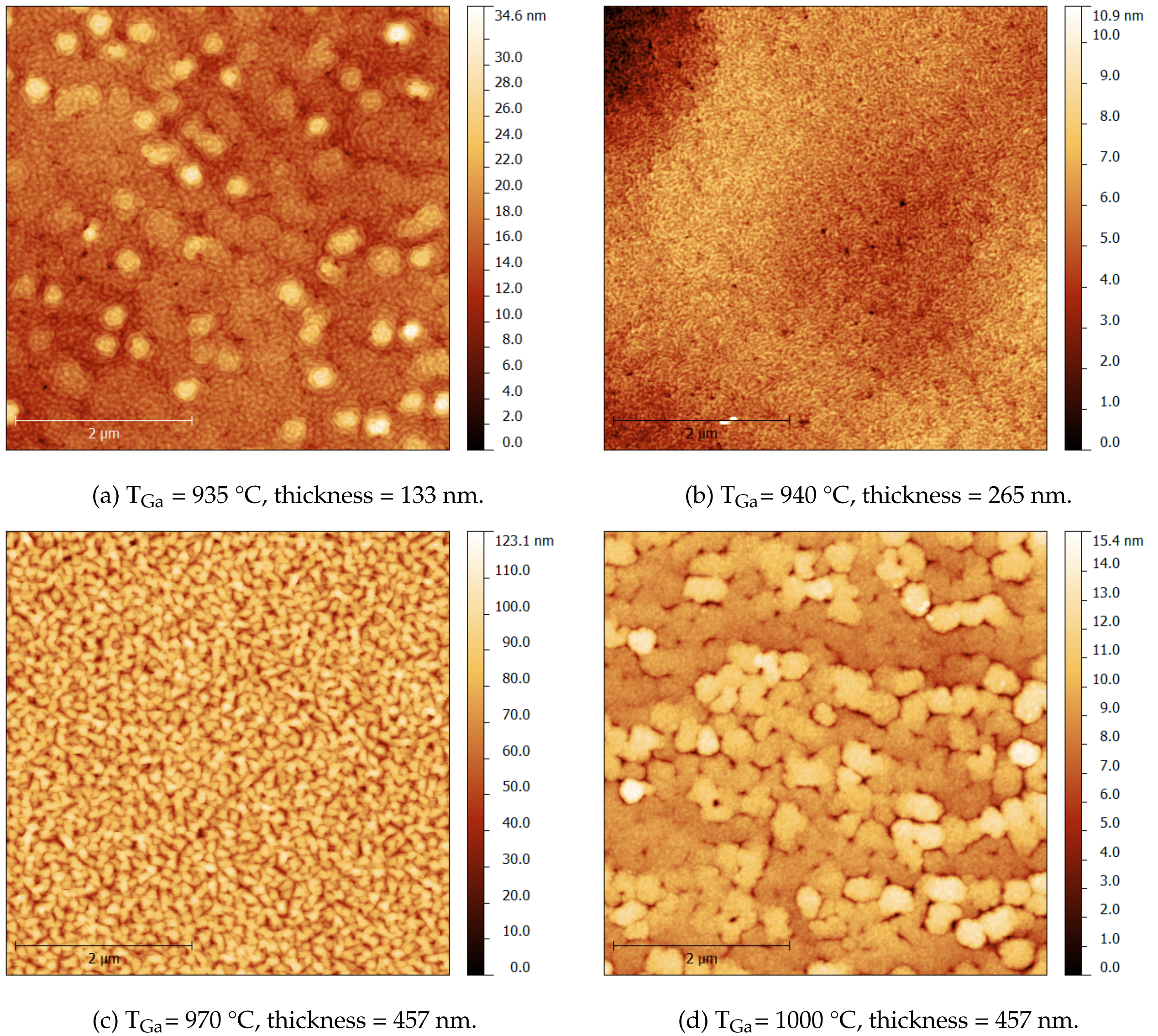

(a) T_{Ga} = 935 °C, thickness = 133 nm.

(b) T_{Ga}= 940 °C, thickness = 265 nm.

(c) T_{Ga}= 970 °C, thickness = 457 nm.

(d) T_{Ga}= 1000 °C, thickness = 457 nm.

Figure 5.14: 5 × 5 µm AFM topography scans of ScGaN films grown on GaN-on-sapphire substrates by NH_3-MBE. The four samples represent a series with increasing Ga cell temperature, T_{Ga}. The errors in T_{Ga} and film thickness are ±0.5 °C and ±10 nm, respectively.

5.5 Strain analysis

5.5.1 Relation between Sc content and strain

The correlation between Sc content and film strain state can be investigated using the series of films grown at increasing Sc cell temperatures. The films have been grown to relatively similar thicknesses allowing a direct comparison between Sc content and strain state to be made. Figure 5.15 shows a series of $Sc_xGa_{1-x}N$ films with increasing Sc content, from below the detection limit ($x < 0.1\%$) to $x = 4 \pm 1\%$. It can be observed that even for low Sc contents, strain relaxation is occurring in the films. This is determined by considering the relative positions of the diffraction peaks in reciprocal space, according to the procedure described in § A.4.2 on page 149. Strain relaxation occurred via the inclination of threading dislotions and the formation of stacking faults and cubic inclusions in the film. The role of these defects is dicussed in further detail in § 5.6 on page 107.

5.5.2 Poisson ratio

Broadening in XRD reciprocal space maps usually arises due to defects such as dislocations; mosaic tilt, twist and size; microstrain, compositional gradients and instrumental resolution [130]. For example, the GaN $10\bar{1}5$ reflection shown in figure 5.17 on page 106 is broadened into an elliptical shape. Broadening can occur in three dimensions of reciprocal space, and each effect will lead to broadening along different directions, typically resulting in the near-horizontal broadening of the GaN peak along $\mathbf{Q_x}$.

However, the broadening of the ScGaN reflection appears to be dominated by a different factor to that of the GaN as the elliptical shape is inclined at an angle to the GaN reflection. It is probable that strain relaxation is occurring in the film, from a near-strained pseudomorphic layer at the ScGaN/GaN interface to a gradually more relaxed layer towards the free surface. Strain relaxation can occur via the formation of misfit dislocations, climb of threading dislocations and formation of microcracks (for tensile strains) [26]. The critical thickness of a material determines the thickness to which the material can be grown before the elastic strain energy (which varies as a function of volume) outweighs the dislocation formation energy [9, 11]. If the critical thickness is large enough, one can consider diffraction to occur from two blocks of material with slightly different lattice parameters: the pseudomorphic, fully-strained

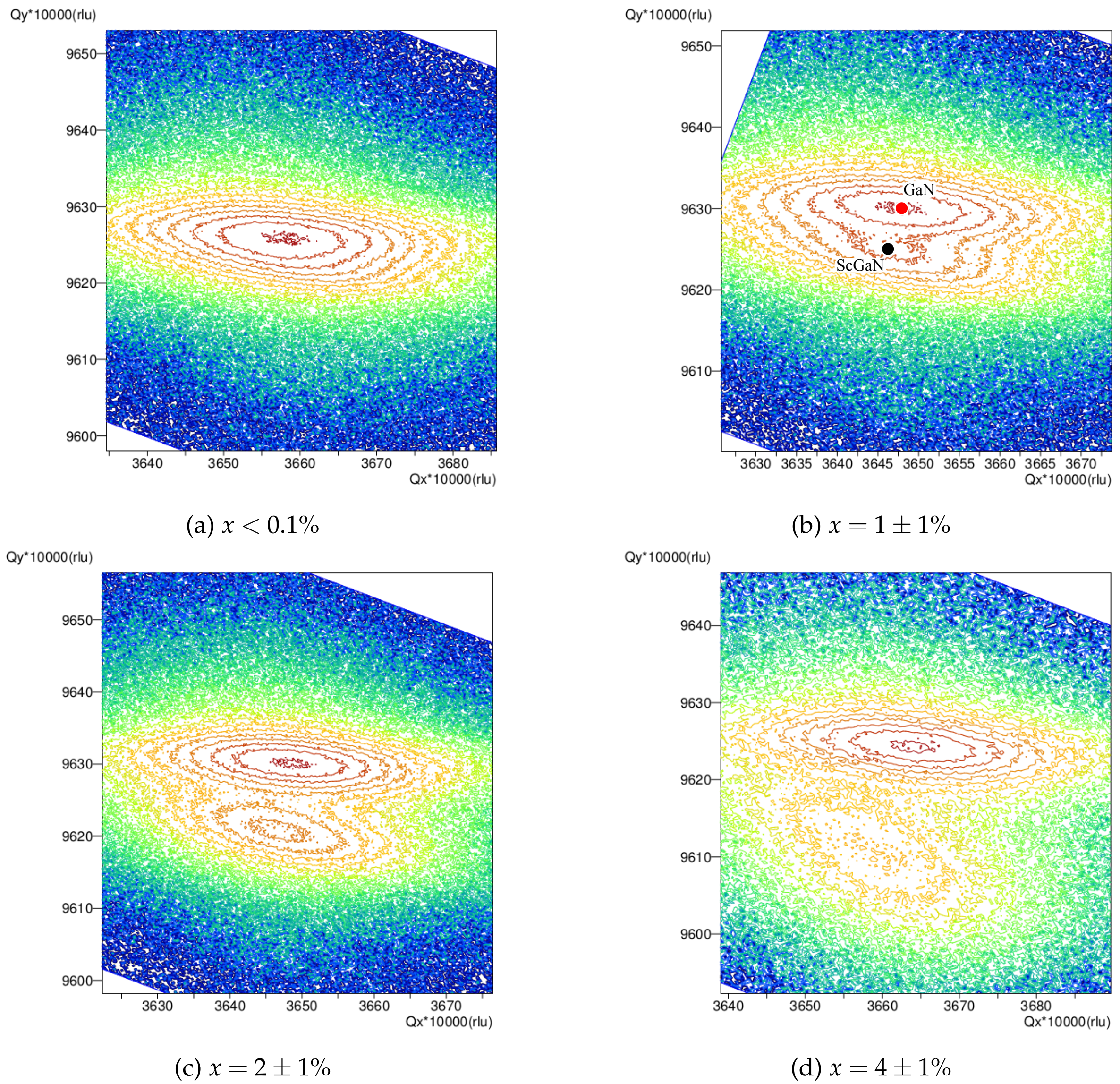

(a) $x < 0.1\%$

(b) $x = 1 \pm 1\%$

(c) $x = 2 \pm 1\%$

(d) $x = 4 \pm 1\%$

Figure 5.15: Reciprocal space maps of the $10\bar{1}5$ reflection of $Sc_xGa_{1\text{-}x}N$ films grown at different Sc cell temperatures, (a) T_{Sc} = 1370 °C, (b) T_{Sc} = 1380 °C, (c) T_{Sc} = 1390 °C and (c) T_{Sc} = 1400 °C. The RSMs are plotted using iso-intensity contours equally spaced on a logarithmic scale.

c_{GaN}	5.187 Å
c_{relax}	5.192 Å
c_{strain}	5.195 Å
ε_z	5.6×10^{-4}

(a) Out-of-plane parameters

a_{GaN}	3.190 Å
a_{relax}	3.198 Å
a_{strain}	3.195 Å
ε_{xy}	-1.0×10^{-3}

(b) In-plane parameters

Table 5.3: Lattice parameters and strains for the GaN substrate and ScGaN epilayer.

film and the relaxed film. This realisation suggests the possibility of determining the Poisson ratio from a single sample without requiring the application of an external force, simply by taking a pair of symmetric and asymmetric RSMs.

Assuming ideal in-plane biaxial strain:

$$\varepsilon_z = \frac{-2\nu}{1-\nu}\varepsilon_{xy} \tag{5.1}$$

where ν is the Poisson ratio; and ε_{xy} and ε_z are the in- and out-of-plane strains, respectively. This can be rearranged for ν:

$$\nu = \frac{X}{X-2} \tag{5.2}$$

where $X = {}^{\varepsilon_z}/_{\varepsilon_{xy}}$. Thus by determining the in- and out-of-plane strains one could obtain an estimate for the Poisson ratio, ν.

The first step is to obtain a value for the strained and relaxed c-lattice parameters of ScGaN, which we shall refer to as c_{strain} and c_{relax}, respectively. These values are obtained from the RSM of a symmetrical reflection such as 0002, as shown in figure 5.16 and listed in table 5.3. The value of ε_z is then obtained using relation 5.3.

$$\begin{aligned} \varepsilon_{xy} &= \tfrac{a_{\text{strain}} - a_{\text{relax}}}{a_{\text{relax}}} \\ \varepsilon_z &= \tfrac{c_{\text{strain}} - c_{\text{relax}}}{c_{\text{relax}}} \end{aligned} \tag{5.3}$$

The measured in-plane lattice parameters for the film measured above are listed in table 5.3.

Thus we obtain a Poisson ratio of $\nu = 0.21$ for a Sc content $x = 0.035$.

However, the obtained value should only be considered a semi-qualitative estimate, as several important assumptions have been made in the analysis:

- The identified ScGaN peaks may not correspond to fully strained and/or fully relaxed material. In particular, as ScGaN of this Sc content has not been grown

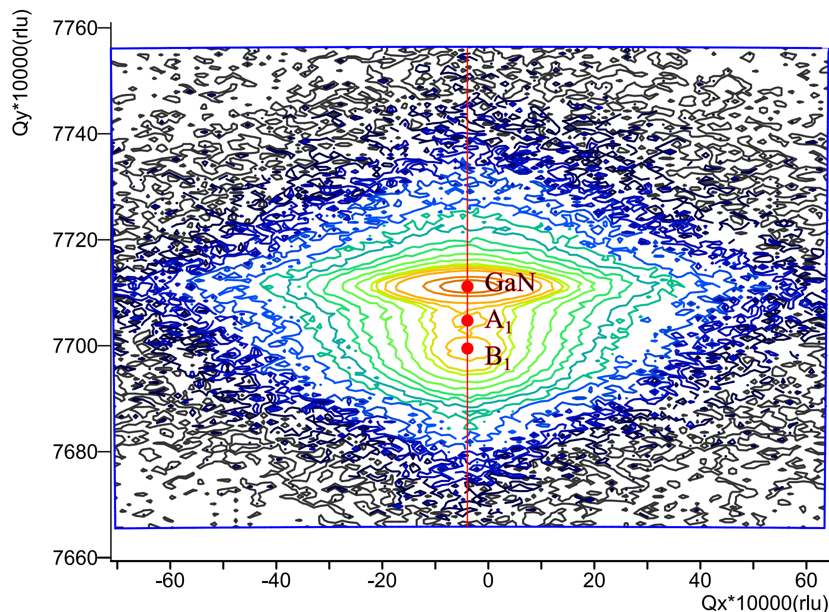

Figure 5.16: Symmetrical RSM of the GaN 0002 reflection, plotted using iso-intensity contours equally spaced on a logarithmic scale. The additional peaks A_1 and B_1 correspond to the relaxed and strained $Sc_xGa_{1-x}N$ films, respectively (x = 0.035).

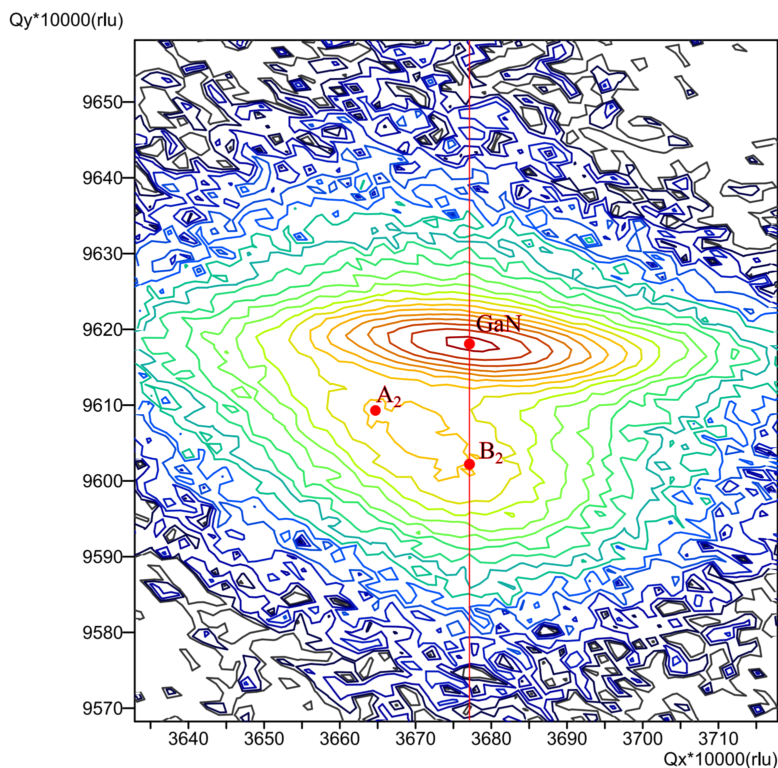

Figure 5.17: Asymmetric RSM of the GaN $10\bar{1}5$ reflection, plotted using iso-intensity contours equally spaced on a logarithmic scale, showing additional peaks A_2 and B_2 corresponding to the relaxed and strained $Sc_xGa_{1-x}N$ films, respectively (x = 0.035).

free-standing it is not known whether the position of the reflection corresponds to that of a fully relaxed film.

- The film may not be in a perfect in-plane biaxial strain state.
- Instrumental inaccuracies and systematic errors in ω and 2θ and chosen peak positions.
- It was assumed that the relaxed and strained layers maintain the same composition. This assumption, for example, is known to be inaccurate in the case of InGaN alloys were variations of In content of up to 20% have been measured between strained and relaxed layers [167].

As a result, it is difficult to assign quantitative error margins to this measurement. However, the obtained value falls within the limits of both experimental and calculated values in the literature, which also show a very wide spread of values. For example, the range of reported Poisson ratios for bulk GaN, with experimental values ranging from $\nu_{\mathrm{GaN}} = 0.146 - 0.23$ and theoretical calculations between $\nu_{\mathrm{GaN}} = 0.119 - 0.248$ [130]. However, using the theoretical Poisson ratios calculated for $Sc_xGa_{1\text{-}x}N$ alloys calculated by DFT [168], a Poisson ratio of $\nu = 0.224$ is expected for a Sc content of $x = 0.035$.

5.6 Microstructure

The ScGaN film microstructure was investigated using a combination of conventional TEM, STEM-HAADF and high-resolution STEM-HAADF imaging. Selected area diffraction patterns confirmed the epitaxial relationship of the ScGaN film to the substrate, with $(0001)_{\mathrm{ScGaN}} \,||\, (0001)_{\mathrm{GaN}}$ and $[11\bar{2}0]_{\mathrm{ScGaN}} \,||\, [11\bar{2}0]_{\mathrm{GaN}}$ (see diffraction patterns in figure 5.18). The films showed a high density of linear and planar defects, including dislocations, basal plane stacking faults (BSF), stacking mismatch boundaries (SMB) and lamellar inclusions of the cubic phase. A close correlation between the density of planar defects and both Sc content and strain relaxation was observed.

The role of Sc on the defect microstructure was investigated by considering a series of $Sc_xGa_{1\text{-}x}N$ epilayers with increasing Sc content. Reciprocal space maps of the $10\bar{1}5$ reflection were used to assess the strain state of the films, taken in the asymmetric scan geometry (see figure 5.19). At the lowest Sc content of $x = 0.012$ the film is fully strained to the underlying GaN. Partial strain relaxation is observed in the

medium Sc content film ($x = 0.035$) and the highest Sc content film ($x = 0.059$) shows significant strain relaxation with respect to the underlying GaN: a strain gradient is also present through the thickness of these films. Strain relaxation was found to occur via inclination of threading dislocations away from the [0001] direction and by the inclusion of stacking faults in the crystal.

5.6.1 Conventional TEM results

Weak-beam dark-field images taken along the $[11\bar{2}0]$ zone axis in the $\mathbf{g}$-$3\mathbf{g}$ condition with $\mathbf{g} = 1\bar{1}00$ are shown in figure 5.18, together with selected area diffraction patterns of the ScGaN film. The imaging conditions reveal basal plane stacking faults and dislocations having a Burgers vector that includes an a-component (*i.e.* mixed and edge dislocations).

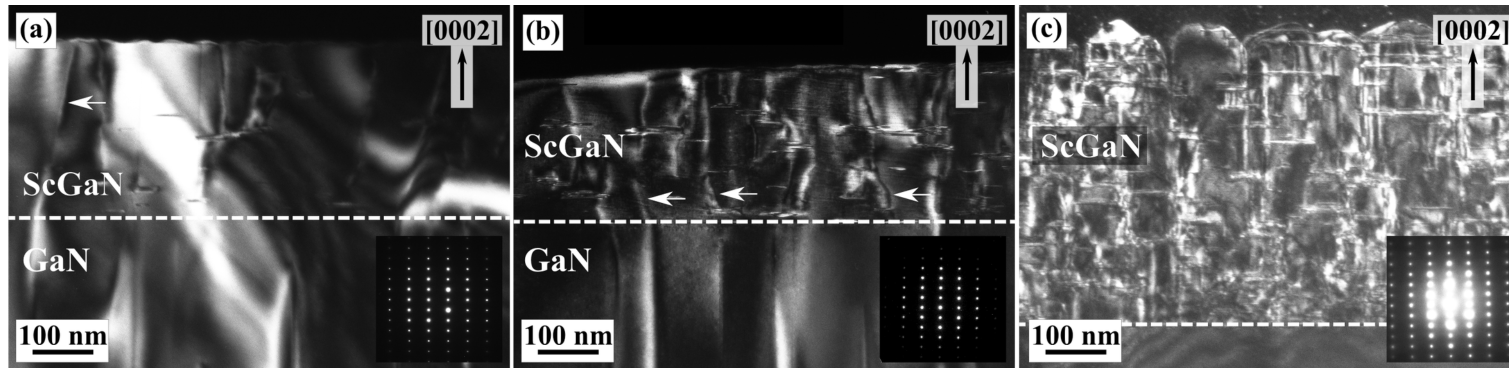

Figure 5.18: Weak-beam dark-field TEM images of $Sc_xGa_{1-x}N$ films with (a) x = 0.017, (b) x = 0.035 and (c) x = 0.059. The white arrows mark positions of inclined dislocations. The BSFs present in the films are observed as horizontal bright streaks in the micrographs. From [159].

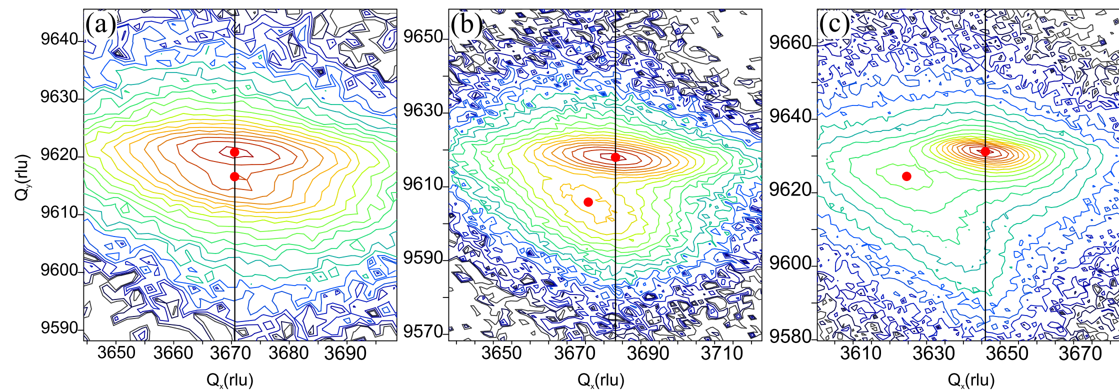

Figure 5.19: Reciprocal space maps of the $10\bar{1}5$ reflection of $Sc_xGa_{1-x}N$ films at (a) x = 0.012, (b) x = 0.035 and (c) x = 0.059. The maps were plotted using equally spaced iso-intensity contours on a logarithmic scale. Peaks on the vertical line are fully strained to the GaN substrate.

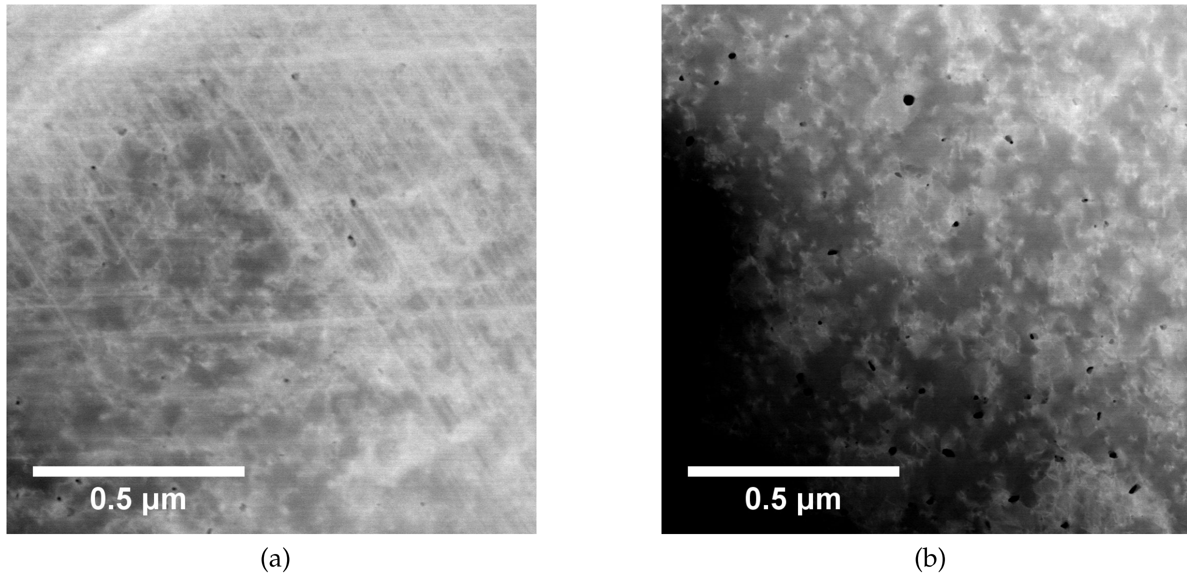

(a) (b)

Figure 5.20: Plan-view STEM-HAADF images of $Sc_xGa_{1-x}N$ sample with x = 0.035. Panel (a) shows an array of misfit dislocations, observed near a large crack in the specimen. However, misfit dislocations are not observed in other regions of the specimen (b), are are likely to have been introduced during the sample preparation.

5.6.1.1 Dislocations

Threading dislocations are oriented close to the [0001] axis in the underlying GaN layer, but incline away from the [0001] axis in the $Sc_xGa_{1-x}N$ film (figure 5.18). This dislocation behaviour has previously been observed in III-nitrides as a mechanism of relief of in-plane stress [111]. Misfit dislocations at the $Sc_xGa_{1-x}N$/GaN interface have only been observed in one of the specimens. However, these appeared to originate from the sample preparation process, as they were only seen in proximity to a crack that developed during ion milling (figure 5.20).

5.6.1.2 Stacking faults

The microstructure of the lowest Sc content $Sc_xGa_{1-x}N$ film (x = 0.012) is similar to that of the underlying MOVPE-grown GaN pseudosubstrate. The intermediate Sc content film (x = 0.035) remains epitaxial but contains a high density (2.4×10^6 cm^{-1}) of intrinsic (I-type) basal plane stacking faults as revealed by $\mathbf{g} \cdot \mathbf{R}$ analysis. The highest Sc content $Sc_xGa_{1-x}N$ film (x = 0.059) also remains epitaxial and contains a very high density (2.9×10^6 cm^{-1}) of I-type BSFs, but in contrast to the lower Sc content films displays a columnar microstructure. A comparison of the microstructures of the two

higher Sc content films is shown in figure 5.21. In agreement with the invisibility criteria for BSFs (see table 3.3), the defects were visible with $\mathbf{g} = 1\bar{1}00$ but invisible in both $\mathbf{g} = 11\bar{2}0$ and $\mathbf{g} = 0002$ conditions.

High densities of BSFs have previously been observed in ScGaN epilayers grown by MBE [101]. These investigations found that at Sc concentrations of $x = 0.17$, almost all long-range periodicity in the basal planes is lost, leading to elongated streaks in the diffraction pattern (see figure 1.13 on page 21).

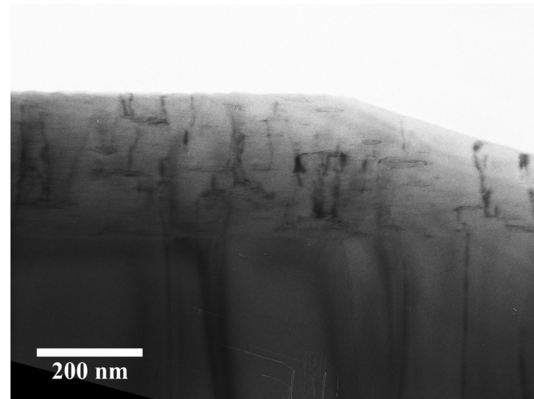

(a) Bright-field, x = 0.035

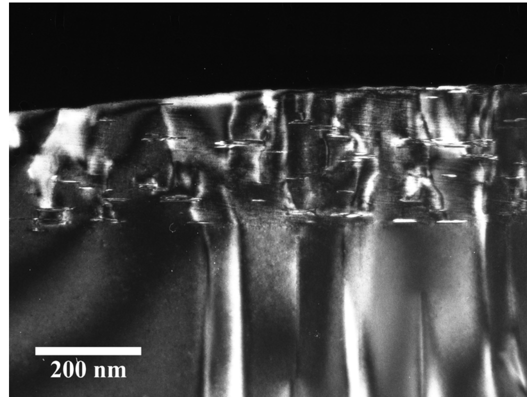

(b) **g**-3**g**, **g** = $1\bar{1}00$

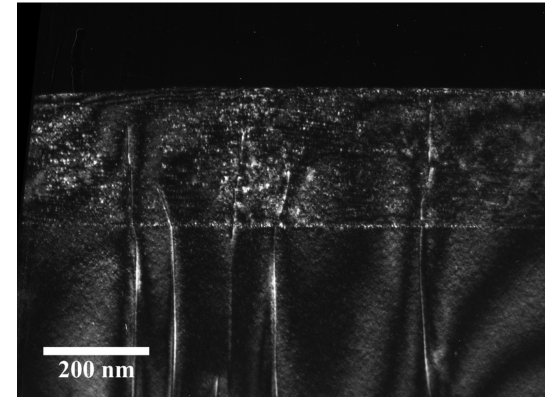

(c) **g**-3**g**, **g** = 0002

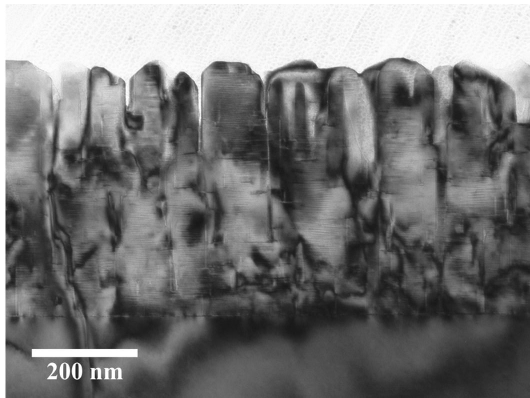

(d) Bright-field, x = 0.059

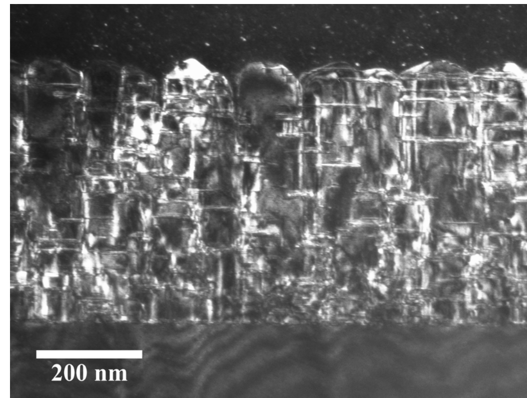

(e) **g**-3**g**, **g** = $1\bar{1}00$

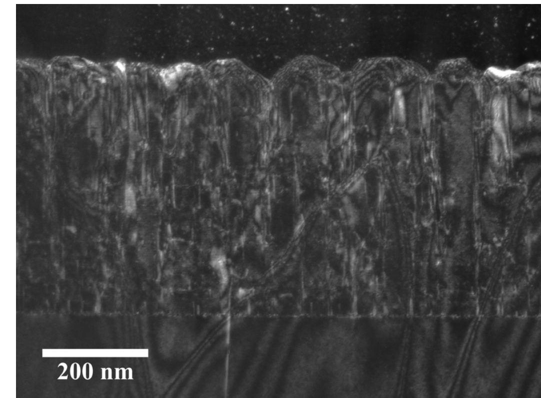

(f) **g**-3**g**, **g** = $11\bar{2}0$

Figure 5.21: Bright-field and WBDF micrographs of $Sc_xGa_{1-x}N$ films with x = 0.035 (top row) and x = 0.059 (bottom row). All images were taken along the GaN $[11\bar{2}0]$ zone axis.

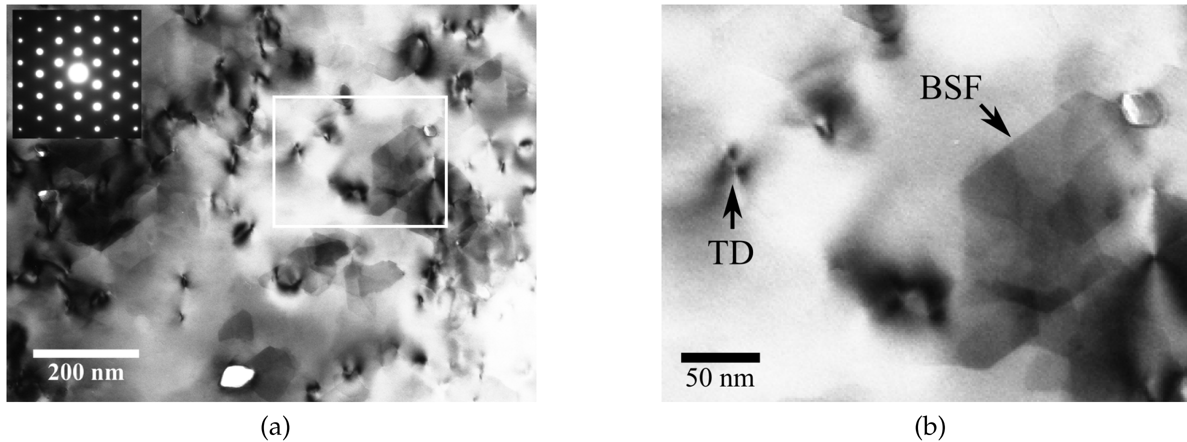

(a) (b)

Figure 5.22: Plan-view BF TEM images of $Sc_xGa_{1-x}N$ sample with $x = 0.035$. Panel (a) shows a large field of view with an inset of the SADP. Panel (b) shows a magnified view of the area shown in (a), indicating positions of threading dislocations (TD) and the outlines of basal plane stacking faults (BSF).

The stacking faults can also be observed in plan-view, as shown in figure 5.22. The micrographs show a high density of threading dislocations and voids in the film. Close inspection reveal the outline of sharp facets corresponding to the stacking faults. STEM-EDX maps (not shown) revealed no detectable variations in the relative elemental intensities over these areas, indicating that contrast does not arise from fluctuations in the Sc content.

5.6.1.3 Additional planar defects

An additional unidentified planar fault showing different contrast also appears in the (0001) plane, with a density of 3.5×10^5 cm^{-1}. As with the I-type BSFs, these defects show no *c*-type component in the displacement vector, and are thus invisible with $\mathbf{g}$ = 0002 (figure 5.23a). However, the defects remain visible with $\mathbf{g} = 3\bar{3}00$, where both I-type BSFs should not be visible, suggesting a displacement vector differing from both the I_1 and I_2 type BSFs displacement vectors (see figure 5.23b).

5.6.2 High-resolution (HR) STEM

Cross-sectional HR STEM images were taken along the $[11\bar{2}0]$ zone axis. Analysis was performed using the Geometric Phase Analysis (GPA) plug-in in `DigitalMicrograph`, as outlined in [169]. This procedure allows quick identification of stacking faults in other images. Conventional WBDF cannot distinguish between I_1 and I_2-type as the

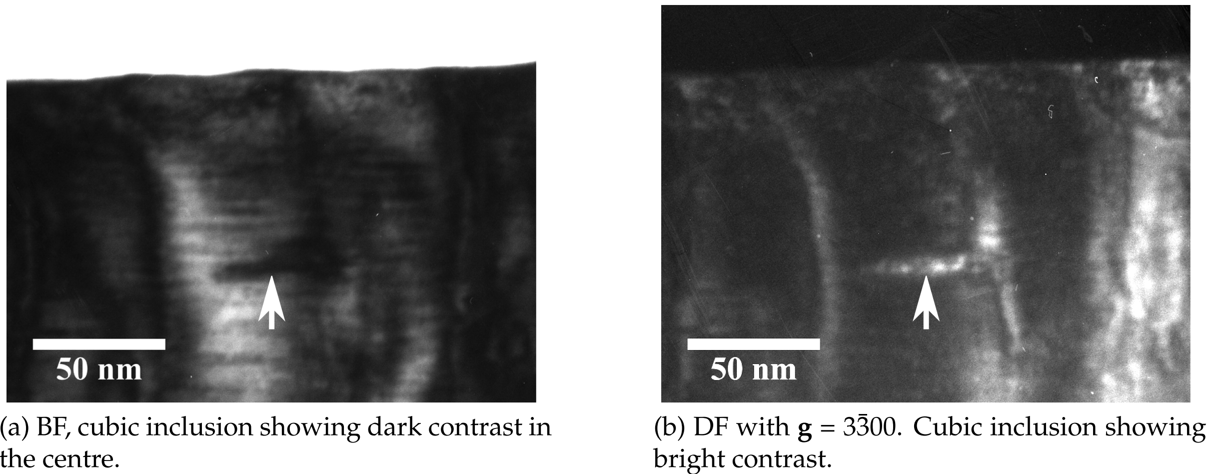

(a) BF, cubic inclusion showing dark contrast in the centre.

(b) DF with $\mathbf{g} = 3\bar{3}00$. Cubic inclusion showing bright contrast.

Figure 5.23: BF and DF TEM micrographs of cubic inclusion (white arrow). Both I_1 and I_2-type BSFs should be invisible in the $\mathbf{g} = 3\bar{3}00$ setup, suggesting the presence of an altogether different kind of planar defect.

same extinction condition applies to both BSFs. However, from HR STEM, the BSFs could be determined to be I_1-type, with a displacement vector of $\mathbf{R} = \frac{1}{6}\langle 20\bar{2}3\rangle$.

The observed phase change in the GPA corresponded to 2.20 ± 0.26 rad. I_1-type BSFs follow the stacking sequence AB***ABC***BC and correspond to one violation of the stacking rule (see § 1.1.2.2 on page 5). They have the lowest formation energy of the three different stacking faults and can be formed during growth [19, 23]. In contrast, I_2-type BSFs correspond to a double violation of the stacking sequence, represented as AB**ABCA**CA. Of over 100 analysed HR STEM images, only occurrences of I_1 BSFs were found (never any I_2 faults), thus it can be concluded that I_1-type BSFs dominate in ScGaN films.

5.6.2.1 Stacking mismatch boundary

I_1-type BSFs frequently appear in pairs separated by 2 unit cells along the [0001] direction. When these occur on the same side, the original stacking sequence is restored, and such a fault is sometimes denoted I_3 (see § 1.1.2.2 on page 5). Discontinuities along the length of a BSF were also often found, where the BSF continued along a different basal plane also separated by 2-3 unit cells (figure 5.24).

The B-layer sublattice remains intact across an I_1-type BSF; only the alternating layers are changed from the A-position to the C-position across the boundary (figure 5.25a). This happens abruptly moving in the [0002] direction across the BSF, but a smooth transition is observed moving parallel to the $[1\bar{1}00]$ direction horizontally

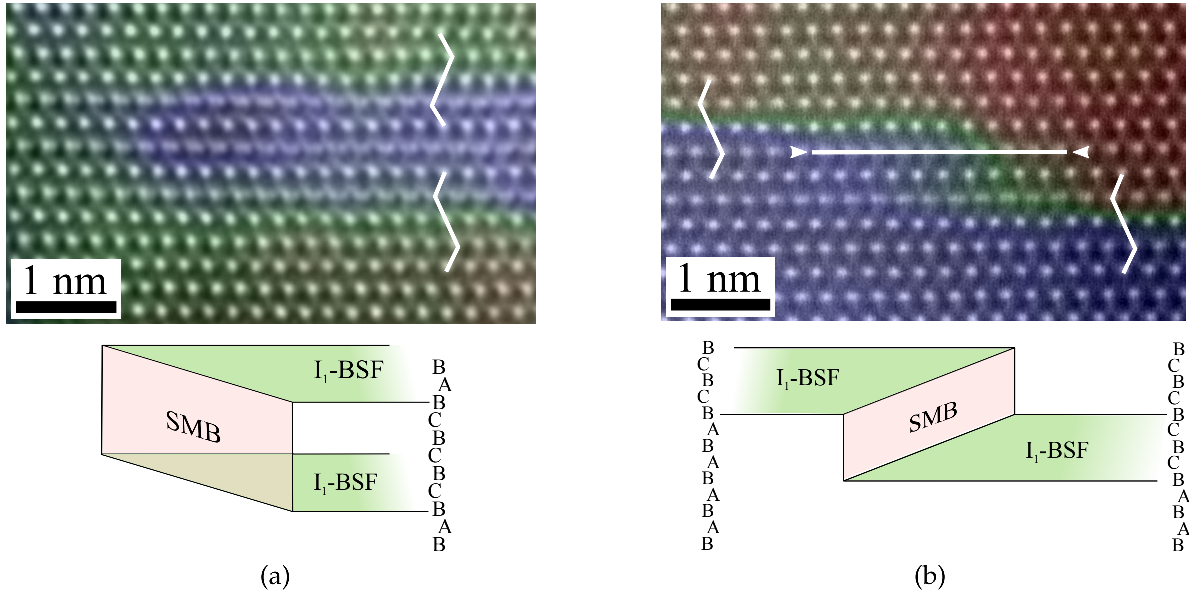

Figure 5.24: STEM image along the $[11\bar{2}0]$ zone axis with phase information from the $1\bar{1}00$ reflection superimposed. Changes in the phase correspond to the presence of I_1-type BSFs. Panel (a) shows the two I_1-type BSFs occurring on the same side (also known as an I_3-type BSF) and in (b) the BSF continues on the opposite side of the SMB.

across the BSF step (see 5.25b). The figure shows two rows in the (0002) which have blurred atomic columns with respect to the surrounding lattice. The two alternating rows of atomic columns appeared blurred across the double step due to the presence of a stacking mismatch boundary (SMB) at an angle to the viewing direction [23, 24]. By taking a line profile of the STEM-HAADF intensity across such an (0002) row, it is even possible to distinguish double peaks corresponding to the two different stacking positions 5.25c. If we treat the intensity to follow the following relation:

$$I \propto \sin^2\{(kx + \phi)\}$$

with the phase shifts, ϕ_i, of the three possible stacking positions given by:

$$\begin{aligned} \phi_A &= \quad n\pi \\ \phi_B &= \quad (n + \tfrac{1}{3}\pi) \\ \phi_C &= \quad (n + \tfrac{2}{3}\pi) \end{aligned}$$

where k corresponds to the atomic column spacing in the (0001), i.e. $k \approx \frac{\pi}{a}$ Å^{-1}.

Thus a phase change of $\frac{2}{3}\pi$ rad is expected across a I_1-type BSF; this is in close agreement with the experimental values of 2.20 ± 0.26 rad.

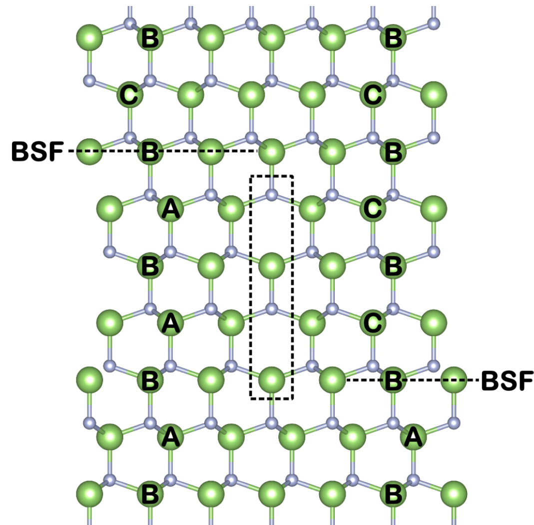

(a) Atomic configuration of a SMB linked by two I_1-type BSFs either side [170].

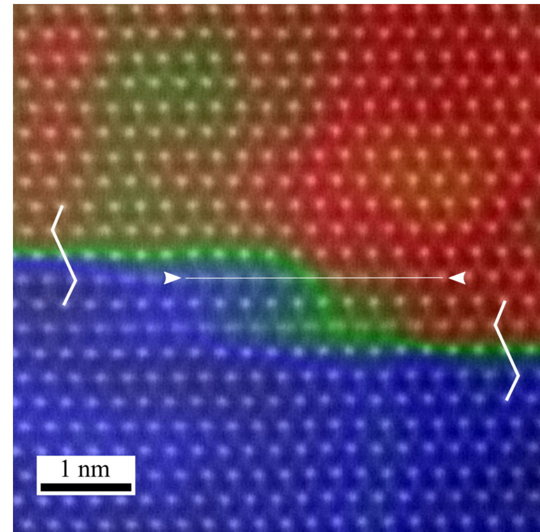

(b) STEM image with superimposed phase image from the $1\bar{1}00$ reflection. The step in the I_1-type BSF is visible in the centre of the image.

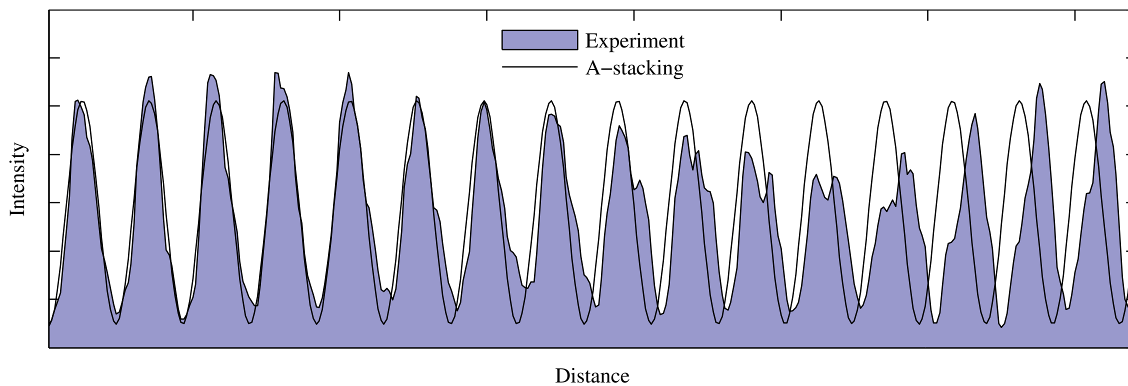

(c) STEM-HAADF line profile across blurred (0002) line, where atomic columns are displaced from the A to the C-stacking position. The theoretical phase shift from A to C-stacking is $\frac{2}{3}\pi$.

Figure 5.25

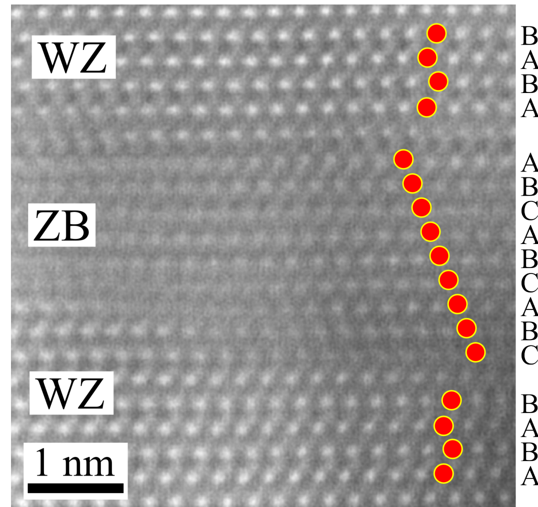

Figure 5.26: Aberration-corrected STEM micrograph of a zinc-blende inclusion in a wurtzite ScGaN matrix. The image was taken along the $[11\bar{2}0]$ zone axis with the stacking sequence labelled in the figure.

5.6.2.2 Cubic inclusions

As can be seen in figure 5.26, the second type of planar defect observed in ScGaN films are coherent lamellar inclusions with an interplanar spacing of 2.61 ± 0.03 Å, compared to the wurtzite (0001) planes which were measured to have an interplanar spacing of d_{0001} = 2.60 ± 0.01 Å. The lamellae appear to include (111) planes of either rock-salt or zinc-blende material, with thicknesses varying between 2 and 4 cubic unit cells. In both structures the metal cations are arranged in a face centred cubic sublattice, with only the positions of the N atoms being different. However, the spatial resolution is insufficient to distinguish changes in the positions of the N atoms from these micrographs. The measured interplanar spacing in the inclusion was found to be consistent with the (111) planar spacing of the zinc-blende phase of ScGaN ($d_{111}(zb)$ = 2.60 ± 0.01 Å), but significantly different from the (111) spacing of the rock-salt phase ($d_{111}(rs)$ = 2.47 Å). Thus the inclusions are of the zinc-blende polymorph of ScGaN, with an epitaxial relationship of $(111)_{zb} \parallel (0001)_{wz}$ and $[1\bar{1}0]_{zb} \parallel [11\bar{2}0]_{wz}$.

EDX scans over the zinc-blende inclusions revealed no detectable differences in the Sc content compared to the surrounding wurtzite material. The formation energy of *zb*-GaN is only 0.015 eV/formula unit higher than that of *wz*-GaN, and is not expected to change significantly with the introduction of low concentrations of Sc.

5.7 Synopsis

This chapter investigated the microstructural properties of dilute $Sc_xGa_{1-x}N$ films with Sc contents of up to $x = 0.059$. The Sc contents were determined via the X-ray absorption intensity, normalised with respect to a ScN film grown by NH_3-MBE which was assumed to be stoichiometric. In addition, a method which could determine the Sc content and strain state of the films using HRXRD was devised.

It was found that the growth rates of ScGaN films were lower than comparable GaN films by about a factor of 2. Similar observations have been made for other TM-doped GaN films, and were found to result from the formation of a metallic floating layer on the growth surface. Although the Sc content increased at higher Sc fluxes, the overall growth rate of these films was found to decrease. The growth rate was found to be independent with respect to the substrate temperature over a temperature range of 650 − 900 °C [159].

The $Sc_xGa_{1-x}N$ films were found to remain single-crystal with an epitaxial relationship of $(0001)_{ScGaN} \,||\, (0001)_{GaN}$ and $[11\bar{2}0]_{ScGaN} \,||\, [11\bar{2}0]_{GaN}$ to the underlying GaN substrate. The ScGaN films showed a high density of planar defects, including I_1-type BSFs and lamellar inclusions of the zinc-blende phase [170]. EDX scans showed no detectable compositional variations in the film, in agreement with the prediction that ScGaN films should form complete solid solutions at these Sc contents [95].

Chapter 6

ScGaN: X-ray absorption spectroscopy

"The doer alone learneth"

-Friedrich Nietzsche

Contents

6.1 Introduction 121
6.2 EXAFS 123
6.3 XANES 129

6.1 Introduction

X-ray absorption spectroscopy (XAS) is a chemically sensitive technique that can probe the local electronic structure and geometrical bonding of selected elements within a material. The previous chapter looked at the microstructural properties of dilute $Sc_xGa_{1-x}N$ alloys grown heteroepitaxially on GaN. A marked increase in defect concentration was found in ScGaN compared to the GaN pseudosubstrate, most notably in the form of the introduction of basal plane and prismatic stacking faults. At Sc contents of $x = 0.059$, a number of lamellar zinc-blende inclusions embedded in the wurtzite matrix was also observed. However, no evidence of compositional fluctuations were found, strengthening the theoretical studies that predict complete solid solutions of ScGaN [95, 101]. These studies also predict a local distortion to occur in the bonding around the substitutional Sc atoms, which increases with Sc content. In

	GaN		$Sc_1Ga_{15}N_{16}$		Distortion	
	$\perp c$	$\parallel c$	$\perp c$	$\parallel c$	$\perp c$	$\parallel c$
N-shell	1.96628	1.97951	2.02315	2.05290	+2.9%	+3.7%
Ga-shell	3.2209	3.21155	3.20803	3.22545	-0.4%	+0.4%
N-(Ga/Sc)-N	109.98°	108.96°	109.73°	109.21°	-0.2%	+0.2%

Table 6.1: Bond lengths for GaN and the $Sc_1Ga_{15}N_{16}$ structure from [95]

addition to the stable rock-salt structure, ScN is predicted to be metastable in a hexagonal non-polar structure as in hexagonal BN [76]. Moving across the composition range, the bonding around Sc is predicted to deviate from a four-fold coordination of the ideal wurtzite structure, B4, towards a near five-fold coordinated structure, B_k (see figure 1.10).

Although the expected distortions at these Sc contents (x = 0.0625) are up to $\sim$ 4% in the metal-nitrogen bond lengths (see table 6.1) [95], they will not be directly observable using high-resolution STEM. Primarily this is because imaging by TEM is an average through the thickness of the specimen. As the ScGaN is very dilute, any distortions occurring around a single Sc atom will be obscured by the number of Ga atoms sitting in the same atomic column. Secondly, the contrast in STEM-HAADF varies as a function of Z^2; thus while both Sc and Ga atoms produce strong contrast, light elements such as N cannot be observed using this technique. Unfortunately, the most significant distortions around Sc are expected in the Sc-N bonding, while the position of the neighbouring Ga atoms is not expected to change by more than 0.5% [95]. XAS techniques, however, are both sensitive enough to be able to detect such subtle changes in bond lengths and element specific.

This chapter presents the use of synchrotron based X-ray absorption techniques, such as X-ray absorption fine-structure spectroscopy (EXAFS) and X-ray absorption near-edge spectroscopy (XANES), to investigate the local coordination environment, bonding and electronic structure of Sc in $Sc_xGa_{1-x}N$. The experimental findings are then compared to theoretical models predicted by density functional theory (DFT). In the first section, the EXAFS measurements were used to accurately detect a distortion in the bonding occurring around the Sc atoms, confirming the theoretical predictions. The measured distortions were found to increase at higher Sc contents. In the second section, the XANES measurements were compared to projected density of states (PDOS) calculations and simulated XANES spectra.

For a description of the theory of XAS please refer to § 3.7 on page 55. All experi-

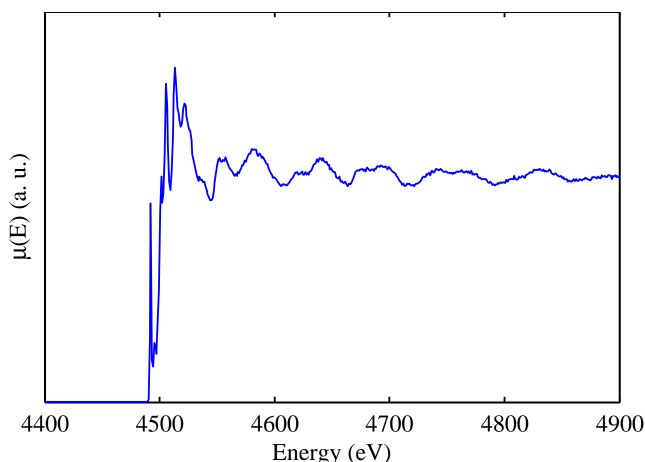

Figure 6.1: Raw absorption signal for $Sc_xGa_{1\text{-}x}N$ film with $x = 0.012$ at the Sc K-edge.

ments were performed on the ID26 beamline at the European Synchrotron Radiation Facility, Grenoble, France, working in collaboration with Dr. Mauro Rovezzi. Theoretical models of the ScGaN supercells were performed by Dr. Siyuan Zhang using DFT as implemented by `Wien2k` [171]. Details on the experimental setup and theoretical framework can be found in [147].

6.2 EXAFS

The local coordination environment of Sc in $Sc_xGa_{1\text{-}x}N$ alloy films was investigated using EXAFS performed at the Sc K-edge. Three samples of increasing Sc content were investigated to study potential variations in the bonding geometry with composition. An example of an EXAFS scan for the lowest Sc content sample, $x = 0.012$, is shown in figure 6.1. Before analysis with the EXAFS equation, the raw data is reduced according to the procedure outlined in § 3.7.1 on page 56, employing a smoothing spline to fit the absorption edge (μ_0) and setting the energy edge value E_0 to the maximum of the derivative.

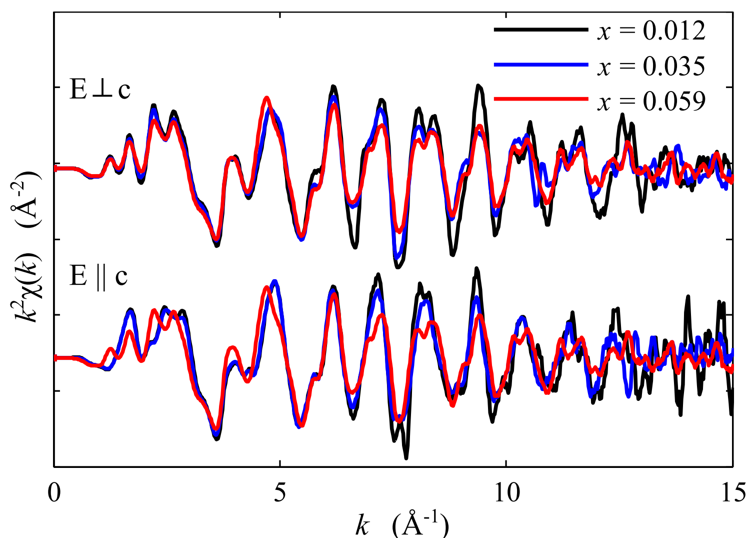

Figure 6.2: Variation of k^2-weighted EXAFS data with Sc content in k-space.

6.2.1 Data extraction

A plot of the k^2-weighted EXAFS data, with the polarisation perpendicular and parallel to the wurtzite c-axis is shown in figure 6.2. Resolving the EXAFS signal into two perpendicular components allows the analysis of the in-plane and out-of-plane bonding around Sc, and can thus be used to identify potential distortions in the bonding as the Sc content increases. Qualitatively there are no observable differences between the spectra, except for a visible increase in the damping at higher Sc contents. This indicates that the majority of Sc atoms remain in the same coordination environment, with greater structural disorder in the crystal at higher Sc contents (as observable by TEM) leading to a reduction in the EXAFS signal.

The Fourier-transformed spectra are shown in figure 6.3, averaged to eliminate dichroic effects.[1] The FT signal can be treated in simple terms as a radial distribution function (RDF) around the absorbing atom, although the distances will not be accurate due to a loss in phase. Unlike a RDF, the intensities of the peaks in the FT are also dependent on the chemical species of the scattered atom, as well as their number. EXAFS is especially sensitive to changes in the bonding close to the absorbing atom. At larger scattering paths, crystal disorder and increased scattering path lengths lead to decreased EXAFS signal intensity and requires heavier computing power to analyse. The first two coordination shells visible in figure 6.3 correspond to the Sc-N

[1] For hexagonal crystals, the spectrum is given as a weighted average of the two polarised spectra: $[2 \times (E \perp c) + (E \parallel c)]/3$

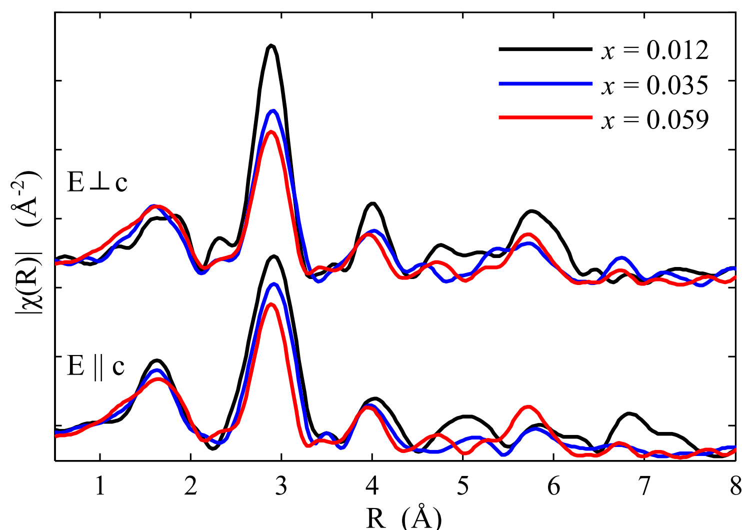

Figure 6.3: Fourier-transformed EXAFS data and in R-space, shown for two perpendicular orientations.

and the Sc-Ga shell, which have 4 and 12 nearest-neighbours in a wurtzite crystal, respectively. An illustration of the bonding environment of a Sc_{Ga} in a *wz*-ScGaN is shown in figure 6.4. The indicated bond lengths correspond to those calculated for a $Sc_xGa_{1-x}N$ supercell with $x = 0.0625$ [147].

6.2.2 EXAFS fits

Quantitative analysis was carried out using the `IFEFFIT-ARTEMIS` programs [140, 145] employing the `FEFF9.6` code [143]. The fitting was performed in R-space over the

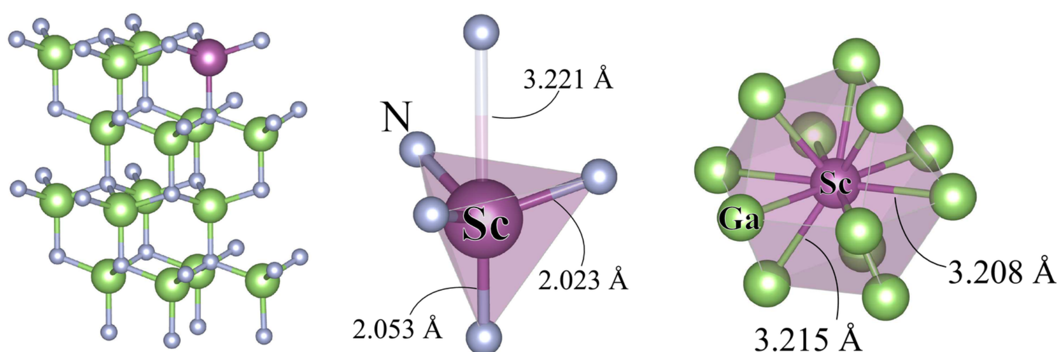

Figure 6.4: Local bonding around the Sc atoms in a wurtzite structure, showing the 4-fold coordination of Sc by N (1st shell) and the 12-fold coordination of Sc by Ga (2nd shell).

range R = 1 − 3.6 Å, using the k^2-weighted EXAFS data in the range of k = 3 − 11 Å. Forward and reverse FT over these ranges were performed using Hanning-type [138] windows, with slope parameters of dk = 1 and dR = 0.5, respectively.

6.2.2.1 Fitting parameters

A conventional two-shell model was used in the fitting, as it is commonly used for Mn_{Ga} [55] and Fe_{Ga} systems [54]. However, to be able to identify distortions in the tetrahedral bonding around Sc, the Sc-N (R_N) and Sc-Ga (R_{Ga}) interatomic distances were separated into components parallel and perpendicular to the wurtzite c-axis. To reproduce damping in the EXAFS signal due to thermal and crystalline disorder in the sample, a Debye-Waller factor for the cation shell (σ^2_{Ga}) was also introduced (σ_{N} was constrained to σ_{Ga}). To keep the fitting variables to a minimum, the common amplitude reduction factor was fixed at $S_0^2 = 0.935$ and the threshold energy shift was also kept constant at $\Delta E_0 = 0 \pm 1$ eV.

6.2.3 Results and discussion

The fitted EXAFS spectrum and associated FT of the highest Sc content film is shown in figure 6.5, with the fitting parameters and their associated errors reported in table 6.2. For reference, the Ga-N and Ga-Ga interatomic distances in binary GaN are also listed.

The results confirm that Sc substitutes for Ga on the cation sites for all three Sc contents. As can be seen in table 6.2, the introduction of Sc introduces a significant distortion in the Sc-N shell, with increases in the bond lengths of $5.3 \pm 0.1\%$ and $6.4 \pm 0.5\%$ perpendicular and parallel to the wurtzite c-axis. The deformation lengths in the Sc-Ga are considerably lower, with bond elongations of $0.78 \pm 0.01\%$ ($E \perp c$) and $1.42 \pm 0.01\%$ ($E \parallel c$). These results are consistent with a local increase in the internal parameter u occurring around the Sc atoms, leading to a local 'flattening' of the wurtzite structure as predicted by theory (and thus deviating from the ideal tetrahedral (T_d) bonding environment around Sc). Similar observations have also been made in other studies where Ga has been substituted by other transition metals (*e.g.* Mn doped GaN [55]). The amplitude damping in the EXAFS signal was successfully fitted by the increasing σ_{Ga}, which is consistent with the expected increase in random alloy disorder. The good fit quality of the model is reflected in the low R-factors, which for the intermediate Sc content spectra was only 3.2%.

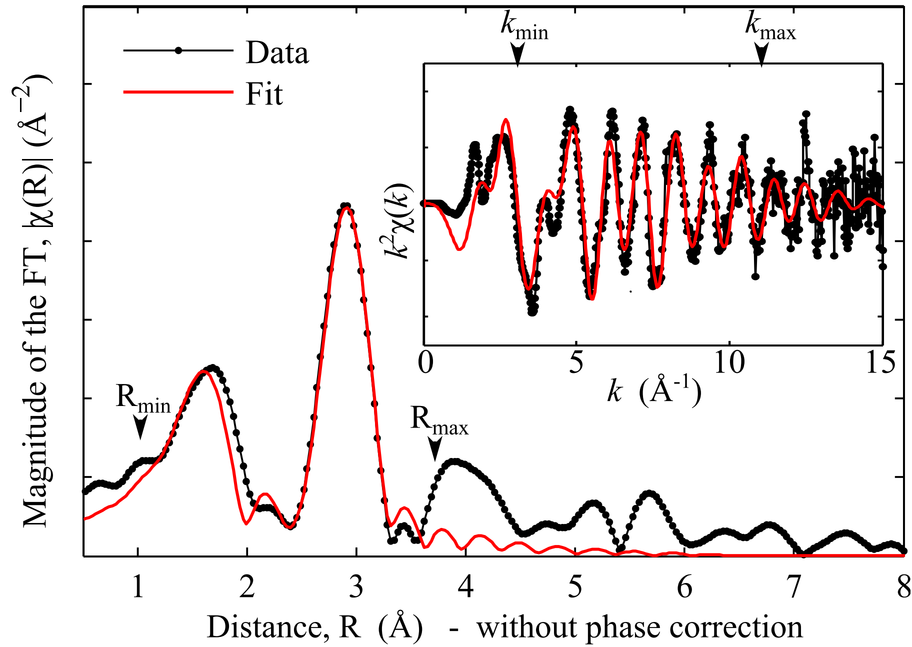

Figure 6.5: EXAFS data and relative fit for $Sc_xGa_{1-x}N$ with x = 0.059, shown in R-space and in k-space (inset). The fitting was performed in R-space, between the limits indicated on the diagram.

Sc content (x)	R_N (Å)		R_{Ga} (Å)		σ_{Ga} (Å^{-2})
	E ⊥ c	E ∥ c	E ⊥ c	E ∥ c	
0	1.947	1.960	3.189	3.180	-
0.012	2.046(9)	2.075(9)	3.206(3)	3.218(3)	0.0058(4)
0.035	2.043(7)	2.073(3)	3.214(3)	3.225(3)	0.0072(4)
0.059	2.05(1)	2.08(1)	3.209(4)	3.220(4)	0.0085(5)

Table 6.2: Summary of fitting parameters used to model the EXAFS spectra, compared to the interatomic distances for pure GaN (x = 0). Uncertainties in the final digit are indicated in brackets.

	$E \perp c$		$E \parallel c$	
Sc content (x)	$Sc_1Ga_{15}N_{16}$	ScN	$Sc_1Ga_{15}N_{16}$	ScN
0.012	1	0	0.96(3)	0.04(3)
0.035	1	0	0.92(2)	0.08(2)
0.059	0.94(3)	0.06(3)	0.87(3)	0.13(3)

Table 6.3: Results of linear combination of fits between simulated *wz*-$Sc_1Ga_{15}N_{16}$ and *rs*-ScN spectra, with uncertainties given in the last digit given in brackets.

6.2.4 EXAFS simulations

To explore the possibility of more than one coordination environment, the analysis of the EXAFS data needs to be extended into higher coordination shells not considered in the EXAFS fits. In addition to the T_d coordination, it is possible that a minority fraction of the Sc atoms are incorporated in an octahedral (O_h) bonding environment such as that found in *rs*-ScN. As the large number of scattering paths and multiple phases considerably increase the number of free parameters for EXAFS fits, simulations of the EXAFS spectra were performed instead. This method has been demonstrated to work well in similar material systems [172].

The input crystal structures of *rs*-ScN and $Sc_1Ga_{15}N_{16}$ were calculated previously by DFT [95, 147]. For each structure, model EXAFS spectra were simulated using the `FEFF9.6` code using single and multiple scattering paths up to a maximum path length of R = 10 Å. The observable damping in the experimental signal was accounted for by introducing a Debye-Waller factor (σ_{Ga}) to reproduce the effects of structural disorder. The simulated EXAFS spectra are then fitted to the experimental data over a k-range of $k = 2.5 - 10.5$ Å^{-1}, using the least-squares approach as employed in the `IFEFFIT-ATHENA` program. To obtain a quantitative measure of the fraction of Sc atoms in each coordination environment, a linear combination of fits between the simulated $Sc_1Ga_{15}N_{16}$ and ScN spectra was performed to obtain the best match to the experimental data. Numerical results of the fits are provided in table 6.3.

The simulated spectra were found to be in good agreement with the experiment for the most dilute case (x = 0.012), for both $E \parallel c$ and $E \perp c$ (figure 6.6). As with the EXAFS fits, the σ_{Ga} factor was successfully able to reproduce the observable decrease in experimental amplitude with Sc content, attesting to the increased structural disorder. Averaging to eliminate dichroism, the results indicate that for the lowest Sc content of x = 0.012, at least $95 \pm 5\%$ of the Sc atoms exist in a T_d coordination environment, with this value slightly decreasing to about $90 \pm 10\%$ for the highest Sc

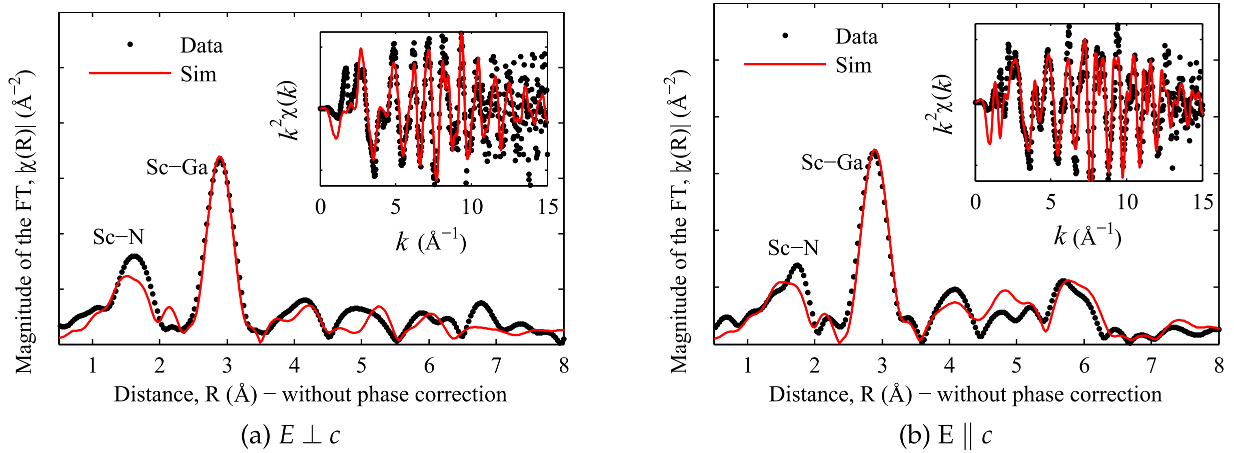

Figure 6.6: Experimental and simulated FT-EXAFS spectra for the x = 0.012 sample, for both polarisations. The k^2 weighted EXAFS data is shown in the insets.

content of $x = 0.059$. It is shown that this decrease is mainly due to the change in coordination of Sc along to the wurtzite c-axis. For $E \parallel c$, a statistically significant increase in the ScN mole fraction is observed with Sc content, from $3.9 \pm 2.6\%$ to $13.1 \pm 2.6\%$. However, no such trend was observed for $E \perp c$ polarisation. These results show that although there are no detectable differences in the basal-plane coordination of Sc, the coordination along the c-axis changes with increasing Sc content. Along this direction, the coordination of Sc is progressing from the T_d configuration (with one atom along c) towards an O_h configuration (with two atoms along c), leading to a local increase in the internal parameter u around the Sc atoms.. This can be thus interpreted as moving from four-fold to a five-fold coordinated structure, with Sc in a trigonal-bipyramidal coordination as found in B_k-ScN (see figure 6.7). This local increase in u at the Sc atom, accompanied by an increase in the metal-nitrogen bond lengths, had been predicted by DFT calculations of relaxed $Sc_1Ga_{15}N_{16}$ supercells [95].

6.3 XANES

The local electronic structure of Sc in ScGaN was investigated by X-ray near-edge spectroscopy (XANES). Compared to the EXAFS, the features in the XANES spectrum can be related to the electronic band structure of the absorbing atom. As these experiments were conducted on the Sc K-edge, corresponding to the Sc $1s \rightarrow 4p$ transitions. It has been shown that XANES spectra can be directly interpreted using calculated projected density of states (PDOS) calculations [173].

Figure 6.8 shows the XANES spectra for three different Sc contents, with the main spectral features labelled for discussion. The spectra were obtained by averaging the spectra taken at both polarisations to eliminate dichroic effects. Normalisation was performed using the `Viper` [142] software package, with the average post-edge function set to unity.

All three spectra show similar features, with two distinct peaks before the main absorption edge (labelled A_1 and A_2) and several peaks in the fine-structure region (B-D). The fine-structure region is predominantly sensitive to the bonding geometry around the absorbing atom, and to a lesser extent to the chemical species of the coordinating atoms. For this reason, the XANES spectrum of Sc in ScGaN shows similarities to other transition metal doped wurtzite materials, such as Mn-doped GaN [55] and Mn doped ZnO [174]. The number and position of the peaks remain unchanged with Sc content, indicating that the average electronic and bonding environments of Sc remain similar. However an overall loss in oscillation amplitude is observed in the post-edge region, which can be attributed to the increased degree of crystallographic disorder at higher Sc contents, as observed previously by TEM (§ 5.6 on page 107) and EXAFS (§ 6.2.2 on page 125). The most striking feature of the XANES spectra are the intense A_1 and A_2 pre-edge peaks, shown in more detail in the inset of figure 6.8. A decrease in intensity of the A_1 peak is observed with increasing Sc content, while the A_2 peak remains unchanged. The quantification of the changes is summarised in table 6.4 on the facing page. The pre-edge peak intensity and position were determined by fitting two Gaussian functions to A_1 and A_2, after removal of the absorption edge using a cumulative Boltzmann function as outlined in § A.6 on page 152.

In summary, two main trends can be identified from the experimental XANES:

1. Decrease in the A_1 pre-edge peak intensity with Sc content

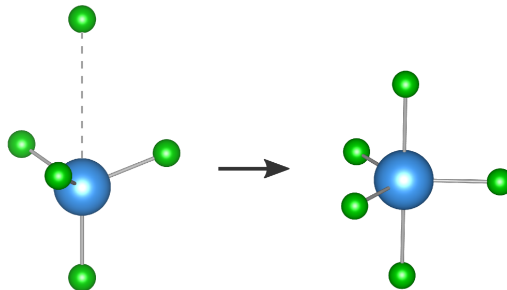

Figure 6.7: Schematic representation of bonding around Sc, progressing from four-fold (tetrahedral) to five-fold (trigonal-bipyramidal) coordination.

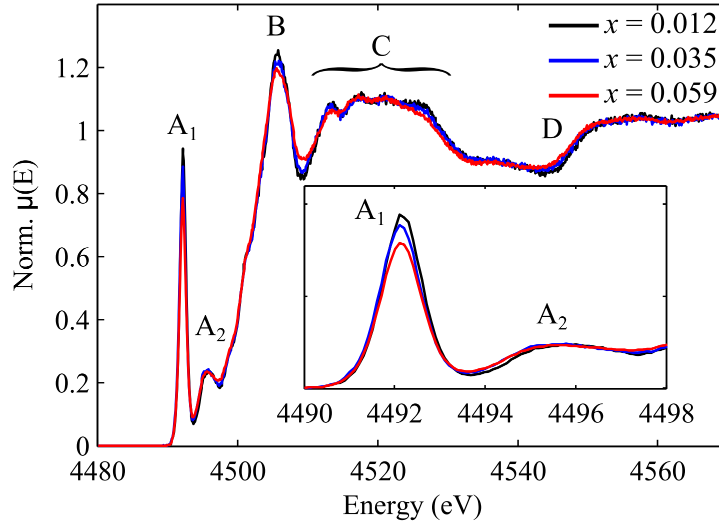

Figure 6.8: XANES spectra from $Sc_xGa_{1-x}N$ films, averaged to eliminate dichroic effects.

Sc content (x)	A_1 Energy (eV)	A_1 Area (eV)	A_2 Energy (eV)	A_2 Area (eV)
0.012	4492.2(9)	0.971(9)	4495.7(9)	0.40(2)
0.035	4492.1(9)	0.933(9)	4495.6(9)	0.46(2)
0.059	4492.1(9)	0.906(8)	4495.60(9)	0.52(2)

Table 6.4: Pre-edge absorption peak positions and integrated areas. Uncertainties in the final digit are given in brackets.

2. Decrease in oscillation amplitude in the fine-structure region with Sc content

6.3.1 Discussion

The experimental XANES spectra were compared to simulated spectra using the `FDMNES` code [175], for both $E \perp c$ and $E \parallel c$ polarisations (figure 6.9) and using the relaxed $Sc_1Ga_{15}N_{16}$ cell as structural input. The main experimental features (A-D) are reproduced well for both polarisations by `FDMNES`, with both A_1 and A_2 peaks in particular showing a good match to the experiment. The presence of a strong pre-edge absorption peak is characteristic of transition metals in a T_d coordination environment. A thorough investigation by Yamamoto *et al.* [156] showed that the pre-edge peaks arise from electric dipole transitions to the *p*-component of *d*-*p* mixed orbitals. This is strong evidence that the majority fraction of Sc atoms exist in a T_d co-ordination environment, in agreement with the EXAFS results presented previously.

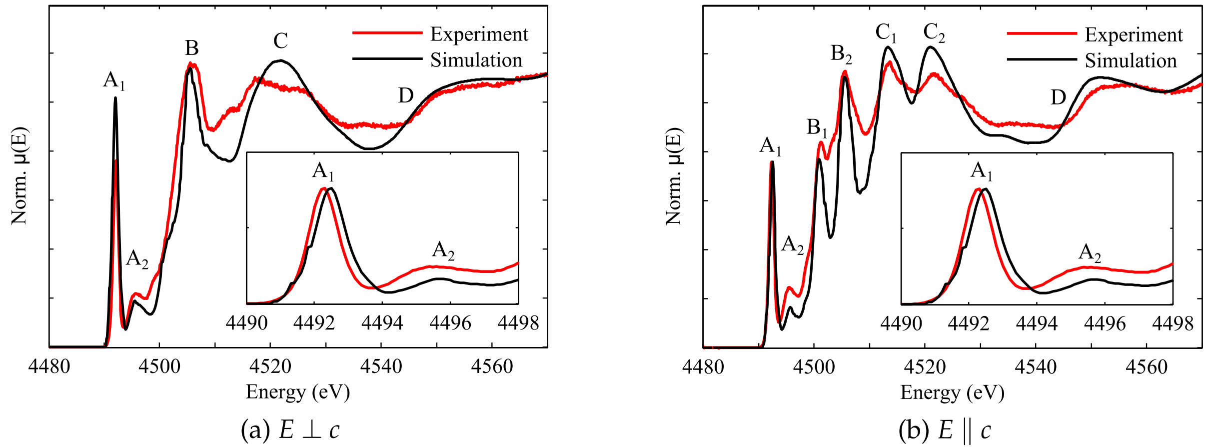

(a) $E \perp c$ (b) $E \parallel c$

Figure 6.9: Comparison of experimental XANES spectrum of $Sc_{0.059}Ga_{0.941}N$ sample and simulated spectrum of the $Sc_1Ga_{15}N$ supercell, shown for (a) E $\perp$ c and (b) E $\parallel$ c.

To further support this argument, the PDOS have been calculated for Sc existing in three different local coordination environments, namely:

1. O_h, as found in the rock-salt structure (B1, six-fold coordination)

2. trigonal-bipyramidal, as observed in hexagonal BN (B_k structure, five-fold coordination) [93]

3. T_d, as found in the wurtzite structure (B4, four-fold coordination)

The PDOS calculations were performed by `Wien2k` as outlined in [147], and subsequently broadened by convoluting with a Gaussian curve with an energy-dependent FWHM. The results of the PDOS calculations are shown in figure 6.10. As expected, the PDOS calculations for the O_h symmetry clearly show the absence of any pre-edge peaks, whereas the calculations for the five-fold coordinated trigonal-bipyramidal coordination show only very weak features in the pre-edge region. The A_1 peak is clearly visible in the T_d coordinated PDOS. The A_1 peak intensity can thus serve as an indicator regarding the coordination number around Sc. Experimentally a decrease in A1 peak intensity is observed with increasing Sc content. This can be understood to be due to the increasing deviation from the ideal T_d coordination, as observed in the EXAFS analysis and predicted by theoretical studies. A quantitative measure, however, is not possible at present due to limitations in the theory involved as well as the empirical broadening parameters used.

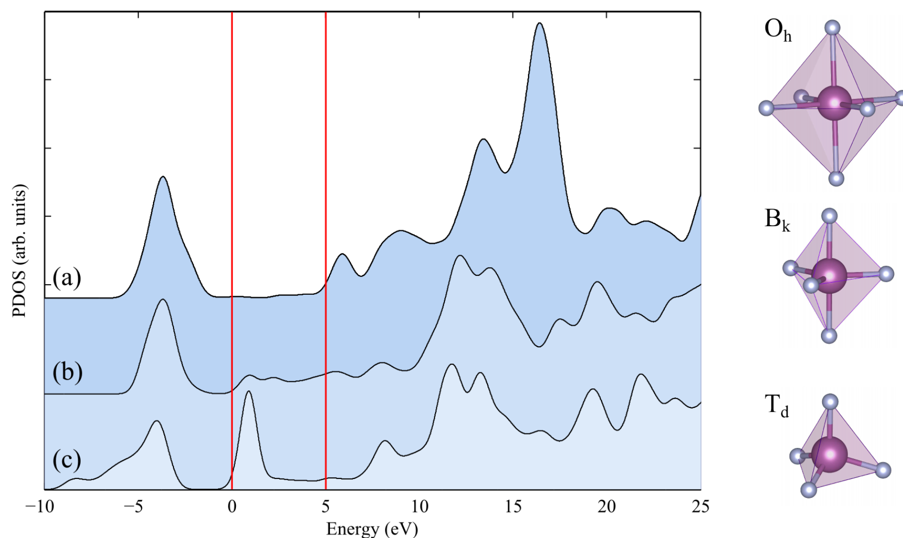

Figure 6.10: Broadened calculated unoccupied *p* PDOS for Sc bonded to N in different local coordination environments: (a) octahedral (O_h), (b) trigonal-bipyramidal (B_k) and (c) slightly distorted tetrahedral (T_d), as in $Sc_1Ga_{15}N_{16}$. The pre-edge region is indicated by the solid red lines. Adapted from [147].

6.3.2 X-ray linear dichroism

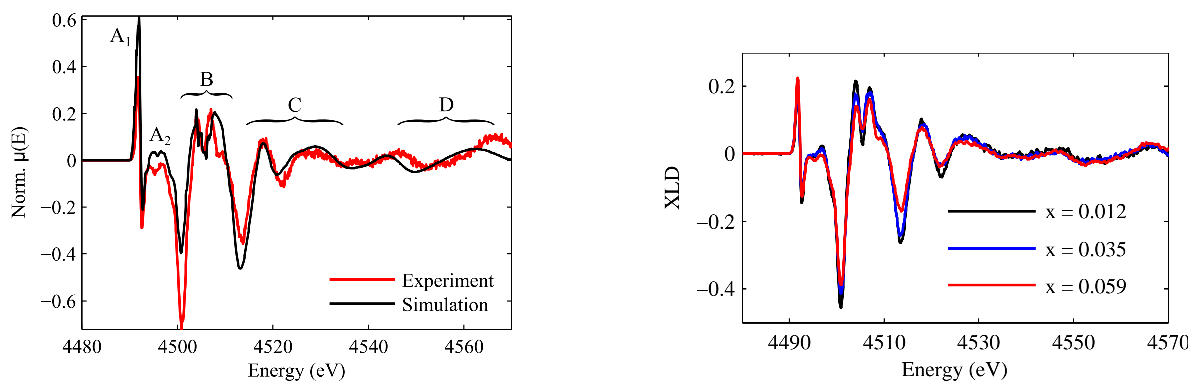

(a) Comparison of experimental XLD for $Sc_{0.059}Ga_{0.941}N$ and theoretical XLD from $Sc_1Ga_{15}N_{16}$ supercell.

(b) Compositional variation of experimental XLD plots for $Sc_xGa_{1-x}N$ samples with increasing x.

Figure 6.11: XLD spectra for $Sc_xGa_{1-x}N$ alloys.

X-ray natural linear dichroism (XLD) [144] is defined as the difference between the normalised XANES spectra polarised perpendicular and parallel to the crystallographic *c*-axis:

$$\text{XLD} = \mu(E \perp c) - \mu(E \parallel c)$$

By comparison with the theoretical calculation, a quality parameter (Q) can be extracted which can be used as a quantitative measure of the degree of substitutional inclusion [155]. The quality parameter is defined as:

$$Q = \text{XLD}_{\text{max}} - \text{XLD}_{\text{min}}$$

Figure 6.11a shows the experimental and calculated XLD spectra for $Sc_xGa_{1-x}N$ with x = 0.059 and x = 0.0625, respectively. Using the dichroism for the strongest absorption feature (B), a quality factor of above $Q \geq 95\%$ was obtained for all three Sc contents, in agreement with EXAFS results. The decrease in XLD amplitude with increasing Sc content is shown in figure 6.11b, which illustrates the increasing fraction of Sc not incorporated in an ideal T_d bonding environment.

Chapter 7

Conclusions and suggestions for future work

Contents

7.1 Conclusions 137
7.2 Suggestions for future work 139

7.1 Conclusions

This thesis is an account of an in-depth investigation into the microstructure and electronic structure of scandium nitride and scandium gallium nitride thin films grown heteroepitaxially by molecular beam epitaxy. The material properties have been extensively characterised, using AFM for the surface topography; TEM and related techniques for microstructure and diffraction; XRD and XAS for chemical analysis; Hall probe for resistivity measurements; PL and UV-Vis spectroscopy for investigation of optical properties; and EXAFS and XANES for local geometric and electronic structure measurements.

In Chapter 4, the properties of epitaxial ScN films were investigated. To enable optimisation of the growth conditions for ScGaN, it was necessary to have an understanding of the MBE system for binary ScN growth alone. For films grown on GaN, an epitaxial relationship of $(111)_{\mathrm{ScN}} \,||\, (0001)_{\mathrm{GaN}}$ and $\langle 1\bar{1}0\rangle_{\mathrm{ScN}} \,||\, [11\bar{2}0]_{\mathrm{GaN}}$ was observed, with a high degree of twinning parallel to (111) along $[11\bar{2}]$. The lowest defect densities and smoothest film surfaces were obtained for MBE grown samples using

NH_3 as a nitrogen source. For the PA-MBE grown samples, it was found that the growth rates for ScN increase monotonically with increasing Sc flux, also indicating nitrogen-rich growth conditions. However, the microstructure deteriorates significantly at higher Sc fluxes, which was also found for XANES measurements of these films. In conclusion, the optimum growth conditions for ScN are in the nitrogen-rich regime, unlike GaN which is commonly ideally grown under Ga-rich conditions to achieve step-flow growth.

Chapter 5 investigates the microstructural properties of single-crystal epitaxial ScGaN films grown by MBE. The films were found to maintain an epitaxial relationship of $(0001)_{ScGaN} \parallel (0001)_{GaN}$ and $[11\bar{2}0]_{ScGaN} \parallel [11\bar{2}0]_{GaN}$, as established by SADP and XRD analysis. The Sc content was found to remain below $x = 0.059$ for all samples [170].

Determination of the Sc content for $Sc_xGa_{1\text{-}x}N$ films is a non-trivial task. In this chapter, three different methods of obtaining good estimates of the Sc content are presented. The most accurate method used relied on using the XAS absorption intensity and comparing to a reference ScN sample, which was assumed to be stoichiometric. As the XAS absorption intensity is directly proportional to the number of Sc atoms sampled, by correcting for film thickness and density, a relatively accurate estimate of the Sc content could be obtained. The second method relies on using Vegard's law applied to low Sc contents. By extrapolation of the calculated variation of lattice parameters to a Sc content of $x = 1$, the lattice parameters and Poisson ratio for a hypothetical *wz*-ScN were obtained ($a = 3.517$ Å, $c = 5.379$ Å and $\nu = 0.610$). It is important to realise although these values do not correspond to any real material, they serve as input parameters to allow Vegard's law to be used for low Sc content wurtzite $Sc_xGa_{1\text{-}x}N$ alloys. Thirdly, a method was developed which allows both Sc content and film strain state to be directly measured using a pair of symmetric and asymmetric reciprocal space maps.

Investigation of the growth rates and surface topographies indicate the likely presence of a Sc-rich surface 'floating layer' during growth, as has also been observed for the growth of other transition metal doped nitrides, such as MnGaN, FeGaN and CrGaN [159]. Microstructural investigations of the ScGaN films showed a high density of I_1-type basal plane stacking faults, which were found to increase with Sc content. The stacking faults were imaged using a combination of WBDF and high-resolution STEM, which revealed that many appear in pairs (sometimes termed an I_3-BSF) and were linked by stacking mismatch boundaries. In addition to the BSFs, a high den-

sity of thin lamellar inclusions of the cubic zinc-blende phase were observed. These inclusions have an epitaxial relationship of $(111)_{zb} \parallel (0001)_{wz}$ and $[1\bar{1}0]_{zb} \parallel [11\bar{2}0]_{wz}$ and vary between 2-4 stacking repeats of the zinc-blende phase in thickness [170].

Chapter 6 investigates the local bonding and electronic structure of Sc in ScGaN films. In conclusion, the XAS results have shown that at least $90 \pm 10\%$ of Sc atoms substitute for Ga in a distorted T_d environment, with the remaining fraction likely to be located at defects or cubic inclusions, where the local coordination environment around Sc is different. A local increase in the internal parameter u was observed at the Sc atoms, with a strong distortion in the Sc-N coordination shell. An intense pre-edge peak in the XANES spectra is characteristic of transition metals in T_d bonding environments, and was successfully reproduced by theoretical calculations [147].

7.2 Suggestions for future work

There are several areas which are worth further investigation:

Although indirect evidence of a Sc-rich floating layer has been presented in this thesis, it is was not possible to verify this suggestion experimentally during growth. For future growth of ScGaN films by PA-MBE, it will be possible to perform *in-situ* characterisation of the growth surface using RHEED. These investigations will provide greater insight into the growth process of ScGaN and allow better optimisation of the growth parameters.

The measurement of Sc content by XAS absorption intensity provides an accurate measure of composition, but is a very impractical measurement technique. It is worthwhile to establish an empirical model of relative elemental EDX emission intensities, which would allow rapid quantification of the Sc content in the STEM. This would require specimens of a known thickness and Sc content to establish reference spectra. In the same vein, the exact stoichiometries of the ScN epilayers would enable a more complete understanding of the XANES features to be obtained. In both cases such quantification could be achieved using Rutherford backscattering spectroscopy (RBS).

The cubic inclusions in STEM were identified as possessing the zinc-blende structure based on the spacing of the (111) planes. Both zinc-blende and rock-salt crystal structures possess the face-centred cubic lattice. However, they differ in the location of the N sublattice, which cannot be imaged by STEM-HAADF. The defect structure of can be investigated in further detail by using annular bright-field (ABF) HR-STEM

imaging, which would allow the direct detection of lighter elements such as N. This information could then be used to compare to existing XAS investigations.

All the investigations conducted in this thesis were performed on $Sc_xGa_{1-x}N$ alloys with Sc contents below $x = 0.059$. In order to assess the possibility of integration of Sc-based III-nitride alloys into existing III-nitride technology, it is necessary to synthesize and characterise higher Sc content films and achieve device-quality films. In addition to $Sc_xGa_{1-x}N$ alloys, it will also be important to extend the investigation into $Sc_xAl_{1-x}N$ materials. Therefore, I recommend at least two further growth series:

1. Grow a series of $Sc_xGa_{1-x}N$ and $Sc_xAl_{1-x}N$ films with increasing Sc content on both GaN and AlN substrates, to determine the influence of growth conditions on the film microstructure.

2. Grow a series of $Sc_xGa_{1-x}N$ quantum wells and multi quantum well heterostructures to assess the efficacy of light emission from these materials.

Appendix A

Analysis and TEM sample preparation techniques

Contents

A.1 Statistical analysis in the AFM 143

A.2 TEM specimen preparation 145

A.3 Monte Carlo simulation 147

A.4 X-ray analysis 147

A.5 Broadening of spectral lines 151

A.6 XAS pre-edge peak quantification 152

A.1 Statistical analysis in the AFM

Most current semiconductor devices have a 2D layered heterostructure design. Many require compositionally abrupt and structurally coherent interfaces between layers, such as the InGaN/GaN interface in LED structures. This requires an in-depth understanding of the properties of the growth surface. AFM is a powerful tool with the ability to quantitatively detect height differences of 1 Å or less. However, most experimentalists still only interpret the measured data qualitatively, or using 1-dimensional characterisation parameters such as RMS roughness (commonly denoted R_q). These first-order parameters only describe the properties of individual points *i.e.* the z-heights, and are as such insufficient to fully characterise surface topography. To give a

more detailed description of the surface, the analysis needs to be extended to second-order functions such as the autocorrelation and the power spectral density functions. These functions also take into account the lateral relationship between two points on the surface. A brief discussion of the different analysis tools used in the AFM study is given below.

First-order parameters RMS roughness is given in equation A.1, where z is the pixel height and M and N are the total number of pixels in the fast (x-axis) and slow (y-axis) scanning directions, respectively.

$$R_q = \sqrt{\frac{1}{N}\sum_{i=1}^{N} z_i^2} \tag{A.1}$$

Complementary to this there is the area RMS roughness (S_q), given by:

$$S_q = \sqrt{\frac{1}{MN}\sum_{i=1}^{M}\sum_{j=1}^{N} z_{i,j}^2} \tag{A.2}$$

AFM scans are usually taken line by line, the horizontal axis is the fast-scan direction, and will generally be more accurate as it does not suffer from thermal drift etc. It is thus better to use the one-dimensional data, with a possible further averaging over all scan lines. Note that this procedure is only appropriate for isotropic surfaces.

Second-order parameters As mentioned before R_q will only provide a measure of the distribution of z-heights in the image, but not how two points are related laterally. This can be quantified by using the autocorrelation function, shown in equation A.3.

$$G\left(\tau_x, \tau_y\right) = \int_{-\infty}^{\infty} z_1 z_2 w\left(z_1, z_2, \tau_x, \tau_y\right) dz_1 dz_2 \tag{A.3}$$

For discrete AFM data along the x-axis this can be reformulated as:

$$G_x = \frac{1}{(M-k)}\sum_{i=1}^{M-k} z_i z_{i+k} \tag{A.4}$$

The 1D autocorrelation function can be treated as a Gaussian curve, *i.e.* charac-

terised by relation A.5:

$$G_x(\tau_x) = \sigma^2 \exp\left\{-\frac{\tau_x^2}{T^2}\right\} \tag{A.5}$$

where σ = R_q and T is the autocorrelation length. For very rough surfaces one would expect to find a small value of T, whereas smooth surfaces give larger values of T. The advantage of using the autocorrelation function is that the resultant roughness parameters are invariant of sample size.

A.2 TEM specimen preparation

Optimum TEM specimens need to be thinned down to ideally below ~200 nm to become electron transparent, although the ideal specimen thickness is dependent on the TEM technique used. This can range from anywhere below 500 nm for BF/DF to below 50 nm for HRTEM [131]. Two methods of specimen preparation are introduced here, known as cross-sectional (XS) and plan-view (PV) geometries [133, 135].

A.2.1 Cross-sectional specimens

1. The wafer is cleaved into two 3 × 3 mm squares from the region of interest, taking precaution to avoid damaging the surface. After cleaning in acetone and ethanol solutions, the pieces are inspected for scratches under the optical microscope. The two pieces are rotated by 90° and glued together film-on-film using commercial *Araldite* epoxy resin. This sandwich geometry allows the inspection of two zone axes, $[11\bar{2}0]$ and $[1\bar{1}00]$, using the same specimen. Pressure and heat are applied while the epoxy sets in order to make the glue line as thin as possible.

2. The sides of the structure are ground using SiC paper to be square. One of the sides of the structure is then mechanically polished using a tripod polisher and diamond lapping films to be specular. The particle sizes are decreased stepwise from 30 µm, 15 µm, 6 µm, 3 µm and 1 µm.

3. Using the epoxy resin, the polished side is glued onto a copper TEM grid commercially available. The specimen is then turned upside down and its rough side is ground to a thickness of about 100 µm using progressively finer SiC paper.

4. At this point, the Gatan Dimple grinder using lubricated 3 µm diamond paste is used to produce a dimple in the centre of the structure, leaving a section of the specimen with a thickness of 25 µm.

5. The final stage of the specimen preparation is milling with argon ions using the *Gatan* Precision Ion Polishing System (PIPS). The specimen is milled at 5 keV at ±7° from both sides until interference fringes are observed under the optical microscope (figure A.1). To avoid milling the cross-sectional specimen holder, milling is performed in the double-modulation mode. At this point the gun energy is dropped first to 2.5 keV and finally to 1.8 keV until a hole is observed, to reduce beam damage and argon ion implantation.

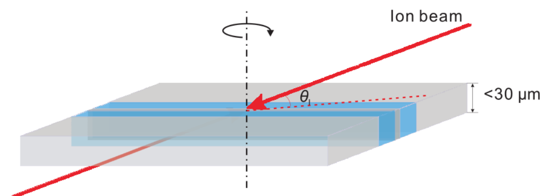

Figure A.1: Schematic of PIPS geometry for XS TEM. From [135].

A.2.2 Plan-view specimens

1. A small 2 × 2 mm section is cleaved from the region of interest using a diamond scribe. After cleaning in acetone and ethanol solutions, the surface is inspected for scratches and glued face-down onto a copper TEM grid using *Araldite* epoxy resin. The specimen needs to be large enough to fully cover the hole in the TEM grid in order to avoid beam damage in the ion-milling stage.

2. The specimen is ground from the substrate side (Al_2O_3) down to a thickness of about 100 µm, using progressively finer SiC paper. The film should be fully protected from mechanical damage. At this stage, the specimen is mounted onto a tripod polisher and polishing is continued using diamond lapping films to a thickness of about 50 µm.

3. The centre of the specimen is dimpled to a thickness of 25 µm using the *Gatan* Dimple grinder, using lubricated 3 µm diamond paste.

4. After dimpling the specimen is mounted on a plan-view sample holder and inserted into the PIPS (figure A.2). Milling is performed at +6° from both sides with single modulation until interference fringes appear. As with the cross-sectional specimen, the final milling is performed at low energies of 2.5 keV and 1.8 keV in order to minimise beam damage.

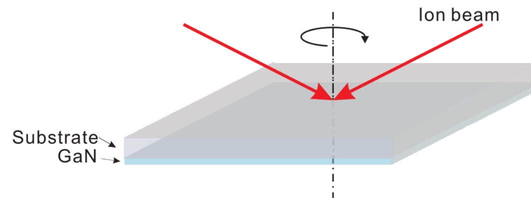

Figure A.2: Schematic for PIPS of PV TEM sample. From [135].

A.3 Monte Carlo simulation

Simulations were performed using the commercially available `Casino v2` software [158]. For the simulation in figure 5.1 on page 87, multiple energies were simulated from 1 keV to 20 keV, in 1 keV steps. At each energy, 10^5 electron trajectories were simulated, using a vertically incident beam of 20 nm in diameter. The interaction volume depends strongly on the material properties defined in the simulation, in particular on the material density and the average atomic number. A film thickness of 250 nm was assumed, which corresponds to an average of the ScGaN film thicknesses grown by NH_3-MBE, as measured by TEM experiments. The Sc content was set to x = 0.1, with a density of $\rho = 6.15$ g/cm^3 corresponding to the density of wurtzite GaN at room temperature [26]. Electron interaction volumes at acceleration voltages of 1, 5, 10 and 15 kV are shown in figure A.3.

A.4 X-ray analysis

A.4.1 Symmetric $\omega - 2\theta$ diffractogram simulations

Diffractogram simulations were performed using the *Philips* `X'Pert Epitaxy 4.0` software. To keep the fitting parameters to a minimum, a simple 2-layer input sample

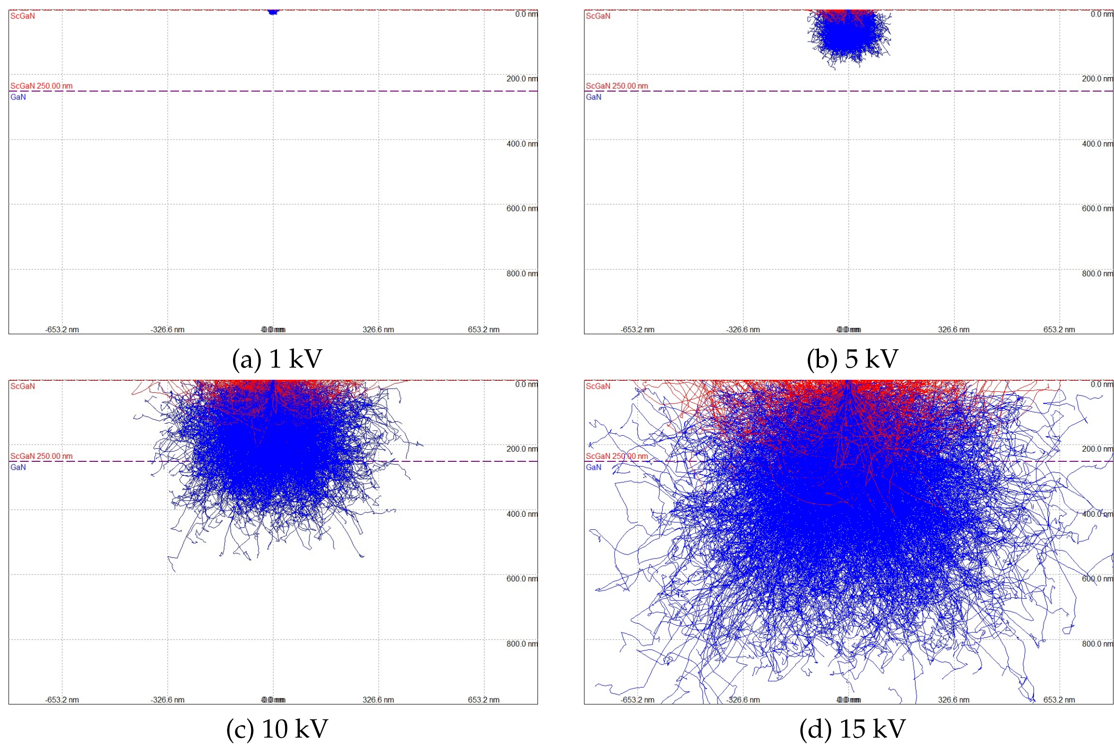

(a) 1 kV

(b) 5 kV

(c) 10 kV

(d) 15 kV

Figure A.3: MC simulations for 10^5 electron trajectories in a 250 nm ScGaN film, with composition of x = 0.1. Re-exiting trajectories are marked in red.

was used:

1. GaN substrate layer, 500 µm thickness

2. $Sc_xGa_{1-x}N$ epilayer

The films were assumed to be fully strained to the GaN substrate and retain the wurtzite structure, with the *wz*-ScN lattice parameters taken as a = 3.517 Å and c = 5.379 Å (see table 5.1 on page 89). The variable parameters included ScGaN film thickness and Sc content, x.

A.4.2 RSM calculations

This analysis is based on the assumption that the position in reciprocal space of an asymmetric reflection such as the $10\bar{1}5$ in *wz*-ScGaN can be used to simultaneously determine the composition and strain state of the film with respect to the underlying GaN pseudosubstrate. The experimental values are compared to DFT calculations from the literature [95]. Table 5.2 provides a list of lattice parameters for $Sc_xGa_{1-x}N$ across the composition range as well as values for the Poisson ratio of the $Sc_xGa_{1-x}N$ alloys in the wurtzite phase. The method assumes a slab model for film and substrate and does not take into account mechanisms for strain relaxation.

A.4.2.1 Method

Step 1: Calculating lattice parameters The in-plane biaxial strain state of the $Sc_xGa_{1-x}N$ film is first calculated with respect to the underlying GaN substrate using the corrected lattice parameters for each Sc content.

$$\varepsilon_{xy} = \frac{a_{\text{ScGaN}} - a_{\text{GaN}}}{a_{\text{ScGaN}}}$$

Partially relaxed in-plane lattice parameters are then determined as a fraction of the maximum in-plane strain, where R corresponds to the degree of strain relaxation:

$$a(R) = \left[1 - (1 - R)\varepsilon_{xy}\right] \times a_{R=0}$$

The out-of-plane strain (ε_z) is calculated assuming planar biaxial strain and using the composition dependent Poisson ratio given in table 5.2 (up to a maximum Sc content of x = 0.375).

$$\varepsilon_z = -\frac{2\nu}{(1 - \nu)}(\varepsilon_{xy})$$

The out-of-plane lattice parameter c_{ScGaN} are then determined using these values.

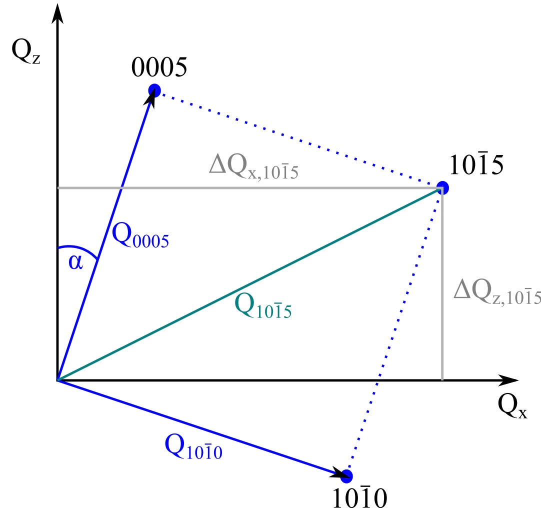

Figure A.4: The effect of tilt on the position of a reflection in reciprocal space. Here the position of the $10\bar{1}5$ reflection is shown, with the x and z coordinates determined by $\mathbf{Q}_{10\bar{1}0}$ and $\mathbf{Q}_{0005}$. To correct for tilt a rotation by α about the y-axis needs to be performed.

$$c = [1 - (1 - R)\varepsilon_z] \times c_{R=0}$$

Thus we obtain a $m \times n$ matrix for both the in-plane and out-of-plane lattice parameters, with each element corresponding to a particular Sc content and strain state.

$$e.g.\ a_{\mathrm{ScGaN}} = \begin{bmatrix} a_{x=0,R=0} & a_{x=0,R=0.1} & a_{x=0,R=0.2} & . \\ a_{x=0.0625,R=0} & . & . & . \\ a_{x=0.1250,R=0} & . & . & . \\ . & . & . & . \end{bmatrix}$$

Step 2: Creating a RSM The coordinates in reciprocal space for any asymmetric reflection can be theoretically established by considering a symmetric reflection and an in-plane reflection. Thus for the $10\bar{1}5$ reflection, the $\mathbf{Q}_z$ coordinate will be given by the magnitude of $\mathbf{Q}_{0005}$ and the $\mathbf{Q}_x$ coordinate by that of $\mathbf{Q}_{10\bar{1}0}$ (see figure A.4). Note that as only the coordinates are necessary, it is irrelevant whether or not the particular reflection is systematically absent or not (as is the case with 0005). The magnitudes of the reciprocal space vectors $\mathbf{Q}$ were taken as the inverse of the interplanar spacing: $d_{hkl} = \frac{1}{\mathbf{Q}_{hkl}}$.

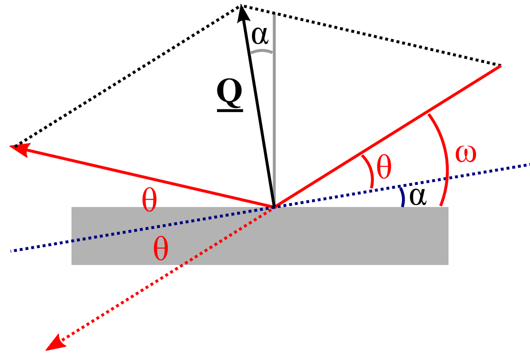

Figure A.5: Tilt can be measured by considering the difference between ω and θ for a symmetrical reflection, by what is commonly called an offset scan.

Step 3: Correcting for tilt Accurate analysis requires measurement of two RSMs: around a symmetric peak (*e.g.* 0004) and an asymmetric peak (*e.g.* $10\bar{1}5$), noting the $\mathbf{Q}_x$ and $\mathbf{Q}_z$ coordinates for each material.

Film tilt is measured from a symmetric reflection, where $\alpha = \omega - \theta$ (see figure A.5). Although measurement of a simple $\omega - 2\theta$ line scan will give a measurement of tilt of the GaN film, a full RSM is necessary to correct for relative tilt between the GaN substrate and the ScGaN film. By correcting for tilt, one is essentially rotating in reciprocal space to line up the symmetrical reflections along the $\mathbf{Q}_z$ axis.

Step 4: Comparing to experimental data The position of the calculated GaN $10\bar{1}5$ peak is adjusted to match the tilt corrected experimental values. By plotting the position of the ScGaN film the strain and Sc content can then be read off directly. Figure A.6 shows two plots displaying the relative position of a ScGaN film as a function of Sc content (figure A.6a) and as a function of strain relaxation in the ScGaN film (figure A.6b).

A.5 Broadening of spectral lines

All plots of the PDOS and `FDMNES` [175] calculations shown in this thesis were preprocessed to simulate the effects of spectral broadening, allowing a better comparison to the experimental data to be made. Here, a linear convolution was performed with the use of a Gaussian function with a constant full-width at half-maximum (FWHM) of 0.5 eV and a second Gaussian with a linearly increasing FWHM of $E \times 0.03$ eV. The choice of broadening parameters were made to best match the experimental data.

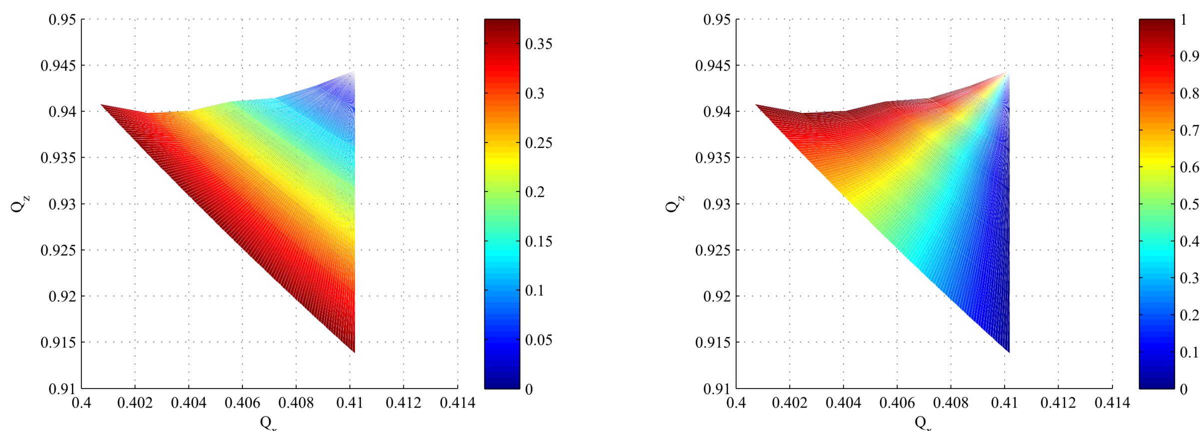

(a) Position of ScGaN $10\bar{1}5$ reflection as a function of Sc content (indicated in colour bar)

(b) Position of ScGaN $10\bar{1}5$ reflection as a function of strain relaxation, *R* (indicated in colour bar)

Figure A.6: Calculated positions of the ScGaN $10\bar{1}5$ reflection as a function of Sc content and strain relaxation.

A.6 XAS pre-edge peak quantification

A two-step method was used to quantify the peak positions:

1. Removal of the baseline by fitting a Boltzmann function to the absorption edge (excluding the pre-edge peaks)

2. Fitting of two Gaussian functions to the pre-edge peaks

An example of the baseline removal and fitting applied to a XANES spectrum of a $Sc_xGa_{1-x}N$ (x = 0.012) sample is shown in figure A.7, and a description of the two fitting functions used can be seen in figure A.8.

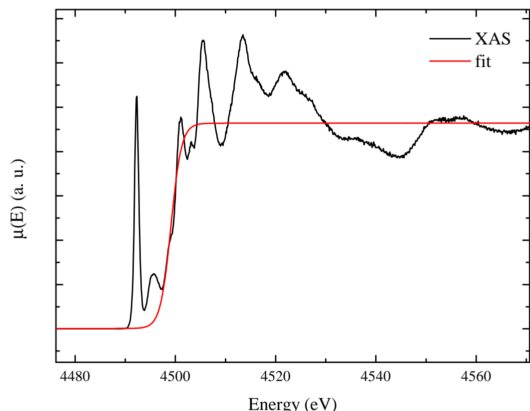

(a) Baseline removal by fitting of a Boltzmann function to the absorption edge.

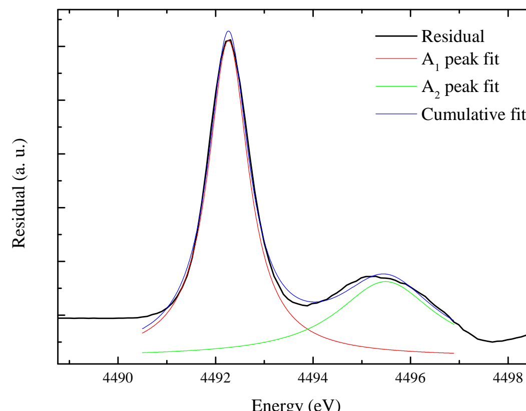

(b) Fitting of the pre-edge peaks using two Gaussian functions.

Figure A.7: Steps for pre-edge peak quantification in a typical XANES spectrum.

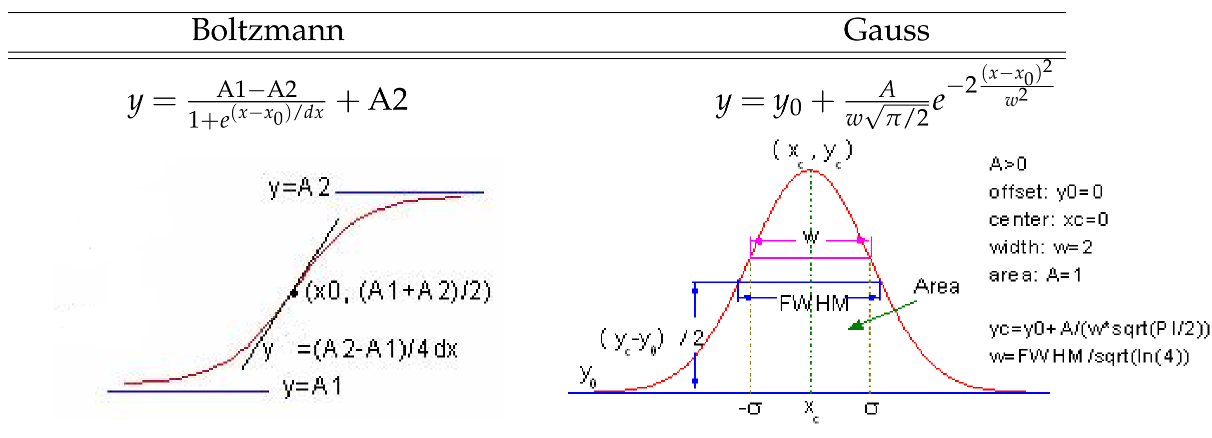

Figure A.8: Description of functions used in the fitting procedure. The Boltzmann function was used to fit to the absorption edge and the pre-edge peaks were fitted using Gaussian functions. Figures reproduced from [176].

Appendix B

Growth parameters

The samples investigated in this work were grown in two separate batches, both using MOVPE grown GaN-on-sapphire pseudosubstrates:

B.1 Ammonia MBE growth

ScN and low Sc-content ScGaN epilayers were grown by NH_3-MBE by Dr. Michelle Moram and co-workers using a custom-built MBE reactor at the University of Liverpool. An average base pressure of 1×10^{-8} Pa was measured inside the reaction chamber prior to growth. The back-surface of the sapphire wafer was sputtered with molybdenum prior to growth to improve thermal homogeneity and to assist substrate temperature measurements performed using an optical pyrometer. Growth temperatures varied from 650 - 900 °C, as measured by a Mo-calibrated pyrometer. To improve compositional and surface uniformity, the substrates were continuously rotated at 60 revolutions per minute (rpm) during growth. To minimise contamination very high purity sources were used, *viz.* 99.995% Sc metal, 99.999% Ga metal and 99.999% NH_3. The composition was changed by varying the effusion cell temperatures, with the Sc cell temperature ranging from 1370 - 1400 °C and the Ga cell temperature from 930 - 1000 °C. The temperature stability of the effusion cells were $\pm$2.5 °C and $\pm$0.5 °C for the Sc and Ga cells, respectively. The ammonia flow rate was kept constant at 40 standard cubic centimeters per minute (sccm), resulting in a NH_3 partial pressure of $\sim 8 \times 10^{-5}$ Torr ($\approx 10^{-2}$ Pa).

B.2 Plasma-assisted MBE growth

Binary ScN and ternary ScGaN samples were grown by PA-MBE using a custom-built MBE reactor at the Cavendish Laboratory in the University of Cambridge. Growth was performed by Dr. Michelle Moram and Dr. Harvey Beere. Again, samples were back-coated with Mo prior to growth. To obtain higher growth temperatures, growth was performed on 1/4−pieces of 2-inch wafers, held in position by specialised sample holders. Substrate temperatures ranged from 600 °C to over 880 °C as monitored using an Mo-calibrated pyrometer. Elemental flux ratios were determined by a retractable ion gauge positioned in front of the substrate holder. The effusion cells used had purities of 99.995% Sc metal, 99.9999% Ga metal and 99.9999% Al metal. The nitrogen source was provided by an RF plasma source using 99.9999% pure N_2 gas.

Sample #	T_{growth} (°C)	T_{Sc} (°C)	Sc flux (nA)	Ammonia flux (sccm)	Growth time (min)	thickness (nm)
MBE 21	800	1320	no data	40	131	195 ± 5

(a) ScN grown by NH_3-MBE on GaN-on-sapphire presudosubstrates.

Sample #	T_{growth} (°C)	T_{Sc} (°C)	Sc flux, J_{Sc} (nA)	P_{N_2}(mbar)	Growth time (min)	Thickness (nm)
AMBE 103	no data	1264	1.6	5×10^{-5}	60	139 ± 5
AMBE 105	no data	1305	2.4	5×10^{-5}	60	157 ± 15
AMBE 104	no data	1288	3.2	5×10^{-5}	60	230 ± 5
AMBE 106	no data	1320	4.0	5×10^{-5}	60	390 ± 27

(b) PA-MBE grown ScN. A $In_{0.18}Al_{0.82}N$ on GaN-on-sapphire pseudosubstrate was used for all four films.

Table B.1: Growth parameters for ScN samples.

Sample #	T_{growth} (°C)	T_{Sc} (°C)	T_{Ga} (°C)	NH_3 flux (sccm)	Growth time (min)	Thickness (nm)	Sc content
MBE 51	650	1400	940	40	24	267	$<0.1\%$
MBE 52	725	1400	940	40	90	260	$<0.1\%$
MBE 45	800	1400	940	40	135	265	3.5%
MBE 50	900	1400	940	40	130	267	2.3%

(a) Ammonia MBE grown ScGaN. Growth temperature series.

Sample #	T_{growth} (°C)	T_{Sc} (°C)	T_{Ga} (°C)	NH_3 flux (sccm)	Growth time (min)	Thickness (nm)	Sc content
MBE 48	800	1370	955	40	120	341	0.1%
MBE 47	800	1380	950	40	120	289	0.1%
MBE 46	800	1390	950	40	120	258	2.3%

(b) Ammonia MBE grown ScGaN. J_{Sc} series.

Sample #	T_{growth} (°C)	T_{Sc} (°C)	T_{Ga} (°C)	NH_3 flux (sccm)	Growth time (min)	Thickness (nm)	Sc content
MBE 49	800	1400	935	40	120	133	0.1%
MBE 45	800	1400	940	40	135	265	3.5%
MBE 34	800	1400	970	40	90	457	5.9%
MBE 36	800	1400	1000	40	120	457	2.3%

(c) Ammonia MBE grown ScGaN. J_{Ga} series.

Table B.2: Growth parameters for ScGaN samples grown on GaN-on-sapphire pseudosubstrates.

Appendix C

Preliminary PL data

This appendix presents preliminary photoluminescence spectra of the $Sc_xGa_{1-x}N$ films grown by NH_3-MBE, together with 1×1 μm AFM topography scans for reference. The three sample series investigated are:

1. Growth temperature series (see figure C.1)

2. Scandium cell series (see figure C.2)

3. Gallium cell series (see figure C.3)

The main absorption edge was found to remain constant at 3.41 ± 0.01 eV for all films investigated. These data were included as a reference for future investigations into the PL spectra of $Sc_xGa_{1-x}N$ alloy systems.

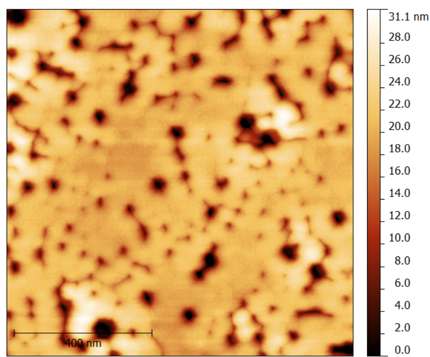

(a) T_g = 650 °C

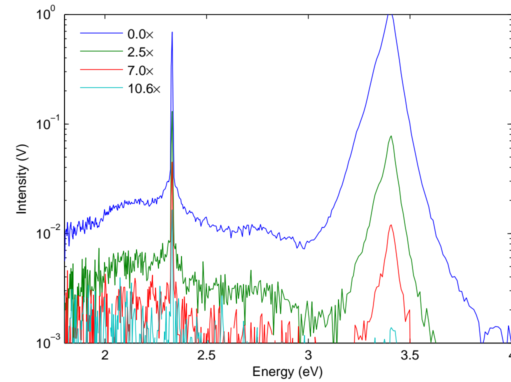

(b) PL power series of sample (a)

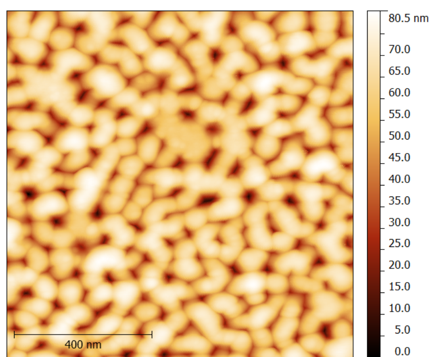

(c) T_g= 725 °C

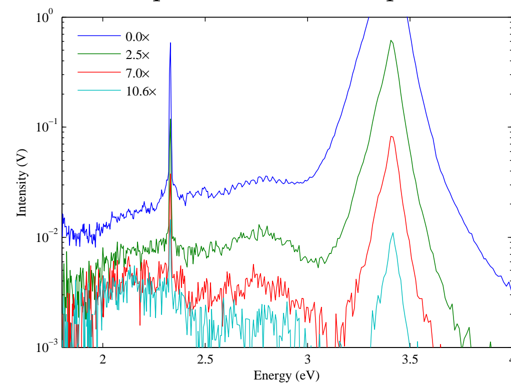

(d) PL power series of sample (c)

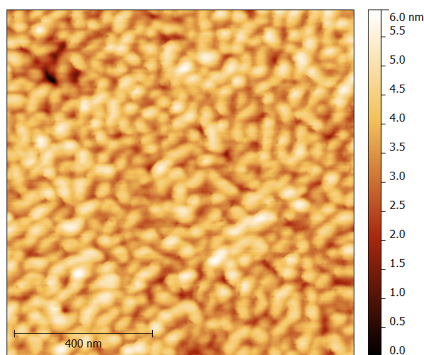

(e) T_g= 800 °C

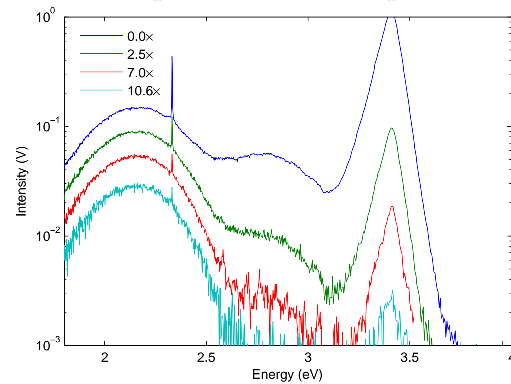

(f) PL power series of sample (e)

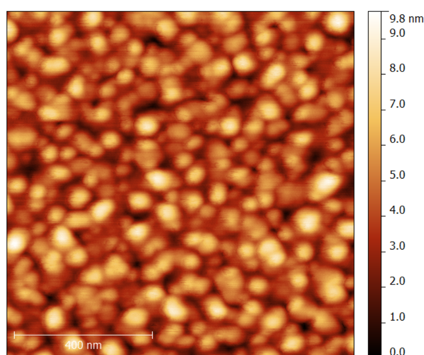

(g) T_g= 900 °C

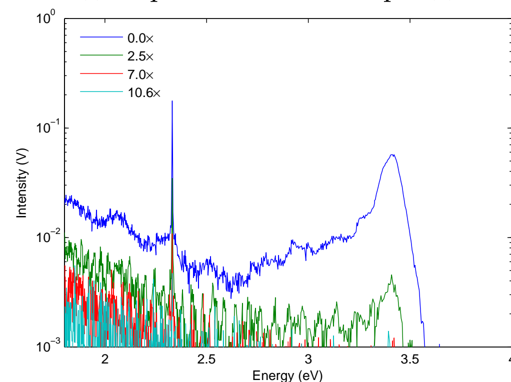

(h) PL power series of sample (g)

Figure C.1: Left: 1 × 1 μm AFM topography scans of ScGaN films grown on GaN-on-sapphire substrates by NH_3-MBE. Right: Corresponding room-temperature photoluminescence power series. The four samples represent a series with increasing substrate temperature.

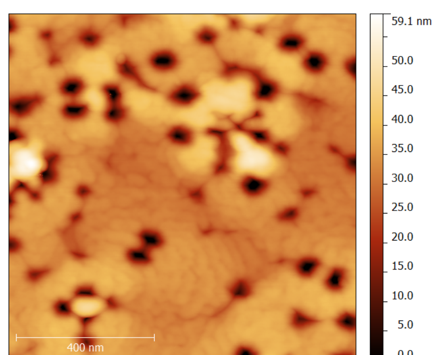

(a) T_{Sc} = 1370 °C

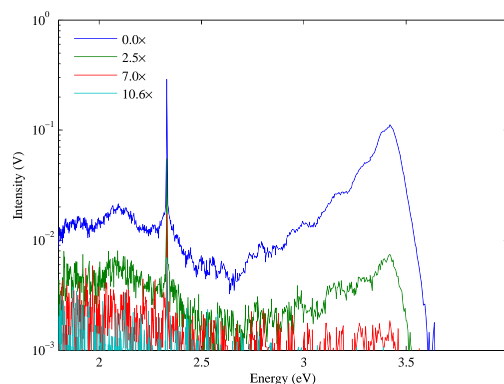

(b) PL power series of sample (a)

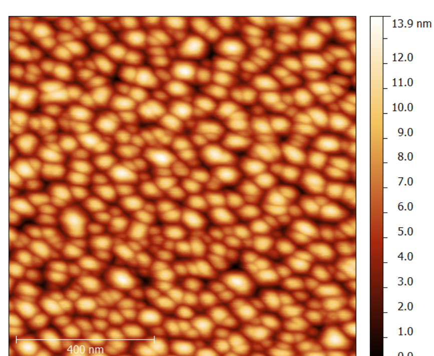

(c) T_{Sc}= 1380 °C

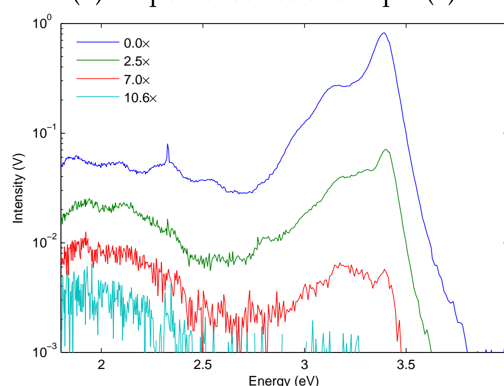

(d) PL power series of sample (c)

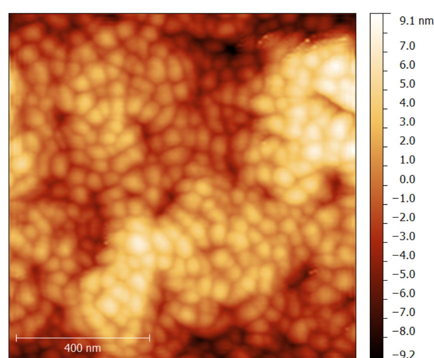

(e) T_{Sc}= 1390 °C

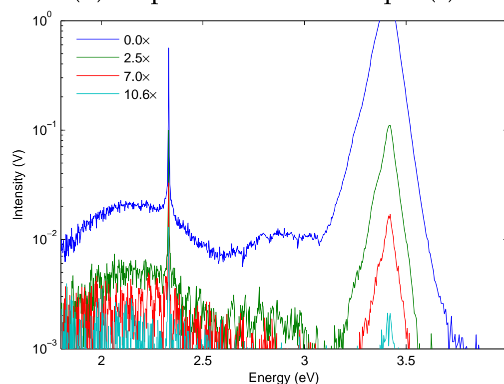

(f) PL power series of sample (e)

Figure C.2: Left: 1 × 1 μm AFM topography scans of ScGaN films grown on GaN-on-sapphire substrates by NH_3-MBE. Right: Corresponding room-temperature photoluminescence power series. The four samples represent a series with increasing scandium cell temperature.

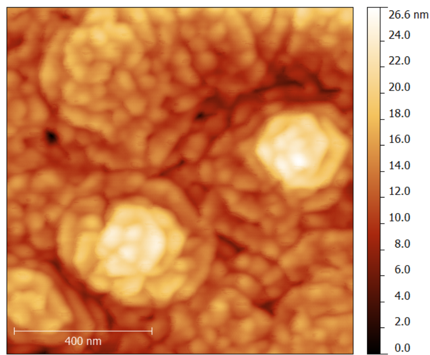

(a) T_{Ga} = 935 °C

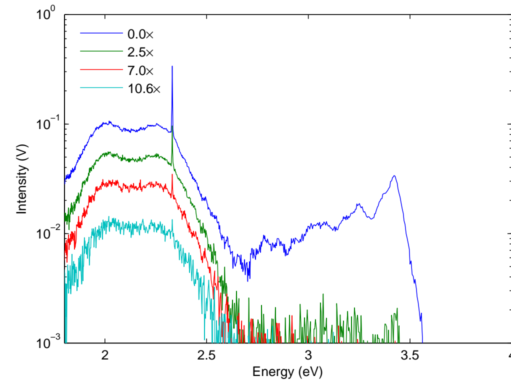

(b) PL power series of sample (a)

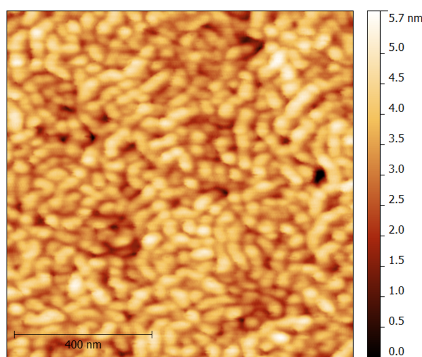

(c) T_{Ga}= 970 °C

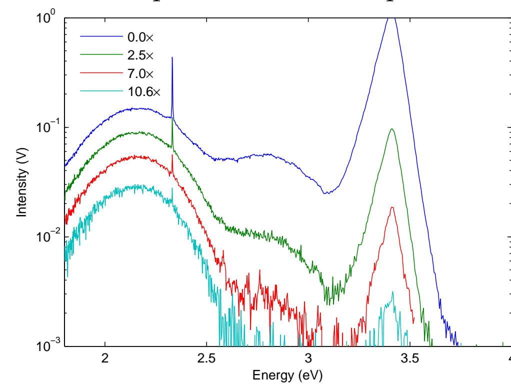

(d) PL power series of sample (c)

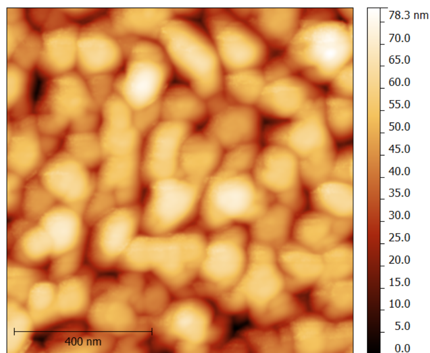

(e) T_{Ga}= 970 °C

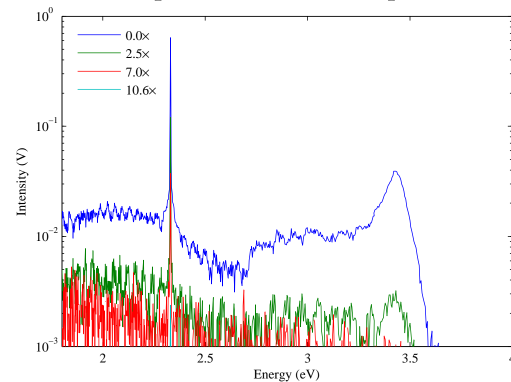

(f) PL power series of sample (e)

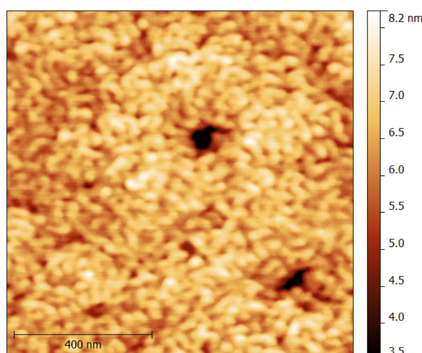

(g) T_{Ga}= 1000 °C

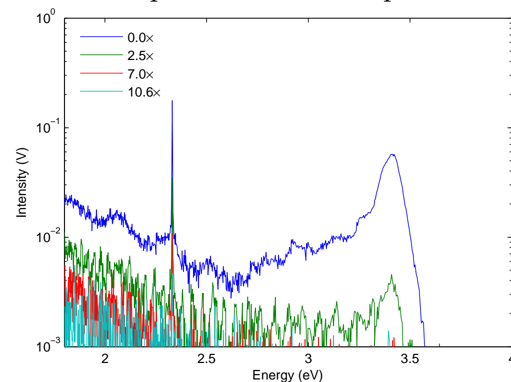

(h) PL power series of sample (g)

Figure C.3: Left: 1 × 1 μm AFM topography scans of ScGaN films grown on GaN-on-sapphire substrates by NH_3-MBE. Right: Corresponding room-temperature photoluminescence power series. The four samples represent a series with increasing gallium cell temperature.

References

[1] T. MATSUOKA *et al.* *Applied Physics Letters*, **81(7)**, 1246 (2002). doi:10.1063/1.1499753.

[2] J. WU *et al.* *Applied Physics Letters*, **80(21)**, 3967 (2002). doi:10.1063/1.1482786.

[3] I. VURGAFTMAN and J. R. MEYER. *Journal of Applied Physics*, **94(6)**, 3675 (2003). doi:10.1063/1.1600519.

[4] J. SINGH. *Electronic and optoelectronic properties of semiconductor structures*, volume 54, (Cambridge Univ Pr2003). ISBN 9780521823791.

[5] J. W. ORTON and C. T. FOXON. *Reports on Progress in Physics*, **61(1)**, 1–75 (1998). doi:10.1088/0034-4885/61/1/001.

[6] I. VURGAFTMAN *et al.* *Journal of Applied Physics*, **89(11)**, 5815 (2001). doi:10.1063/1.1368156.

[7] J. I. PANKOVE and T. D. MOUSTAKAS. *Gallium Nitride (GaN) II*, volume 57, (Academic Press, San Diego1999). ISBN 0127521666.

[8] S. STRITE and H. MORKOÇ. *Journal of Vacuum Science & Technology B: Microelectronics and Nanometer Structures*, **10**, 1237–1266 (1992).

[9] R. PEOPLE and J. C. BEAN. *Applied Physics Letters*, **47(3)**, 1–3 (1985). doi:10.1063/1.96206.

[10] D. HOLEC *et al.* *Journal of Crystal Growth*, **303(1)**, 314–317 (2007). doi:10.1016/j.jcrysgro.2006.12.054.

[11] W. Y. FU *et al.* *(private communication)* (2014).

[12] R. A. OLIVER *et al.* *Applied Physics Letters*, **89(1)**, 011914 (2006). doi:10.1063/1.2219747.

[13] M. A. MORAM *et al.* *Journal of Applied Physics*, **106(7)**, 073513 (2009). doi:10.1063/1.3225920.

[14] T. SUGAHARA *et al.* *Japanese Journal of Applied Physics*, **37(2)**, 398–400 (1998). doi:10.1143/JJAP.37.L398.

[15] F. A. PONCE *et al.* *Applied Physics Letters*, **69(6)**, 770 (1996). doi:10.1063/1.117886.

[16] M. KAPPERS *et al.* *Physica B: Condensed Matter*, **401-402(1)**, 296–301 (2007). doi:10.1016/j.physb.2007.08.170.

[17] M. A. MORAM *et al.* *Applied Physics Letters*, **91(15)**, 152101 (2007). doi:10.1063/1.2794009.

[18] P. GIBART. *Reports on Progress in Physics*, **67(5)**, 667–715 (2004). doi:10.1088/0034-4885/67/5/R02.

[19] V. POTIN *et al.* *Journal of Physics: Condensed Matter*, **12(49)**, 10301–10306 (2000). doi:10.1088/0953-8984/12/49/332.

[20] D. N. ZAKHAROV *et al.* *Physical Review B*, **71(23)**, 235334 (2005). doi:10.1103/PhysRevB.71.235334.

[21] C. STAMPFL and C. G. VAN DE WALLE. *Physical Review B*, **57(24)**, R15052–R15055 (1998). doi:10.1103/PhysRevB.57.R15052.

[22] C. M. DRUM. *Philosophical Magazine*, **11(110)**, 313–334 (1965). doi:10.1080/14786436508221859.

[23] H. BLANK *et al.* *Physica Status Solidi (B)*, **7(3)**, 747–764 (1964). doi:10.1002/pssb.19640070304.

[24] J. E. NORTHRUP *et al.* *Physical Review Letters*, **77(1)**, 103–106 (1996). doi:10.1103/PhysRevLett.77.103.

[25] P. VERMAUT *et al.* *Philosophical Magazine A*, **75(1)**, 239–259 (1997). doi:10.1080/01418619708210293.

[26] H. MORKOÇ. *Handbook of Nitride Semiconductors and Devices*, (Wiley-VCH2008), 1st edition. ISBN 978-3527407972. doi:10.1002/9783527628438.

[27] S. NAKAMURA *et al.* *Japanese Journal of Applied Physics Part 2-Letters*, **30(12A)**, 1998–2001 (1991).

[28] P. CHERNS. "A Transmission Electron Microscopy Study of AlGaN/GaN Heterostructures". Ph.D. thesis, University of Cambridge (2007).

[29] M. R. KRAMES *et al.* *Journal of Display Technology*, **3(2)**, 160–175 (2007). doi:10.1109/JDT.2007.895339.

[30] J. M. PHILLIPS *et al.* *Laser & Photonics Review*, **1(4)**, 307–333 (2007). doi:10.1002/lpor.200710019.

[31] G. HARBERS *et al.* *Journal of Display Technology*, **3(2)**, 98–109 (2007). doi:10.1109/JDT.2007.894384.

[32] C. J. HUMPHREYS. *MRS Bulletin*, **33**, 459 (2008). doi:10.1109/JLT.2008.927128.

[33] M. LEROUX *et al.* *Physical Review B*, **58(20)**, 13371–13374 (1998). doi:10.1103/PhysRevB.58.R13371.

[34] M. KNEISSL *et al.* *Semiconductor Science and Technology*, **26(1)**, 014036 (2011). doi:10.1088/0268-1242/26/1/014036.

[35] M. KNEISSL. "External Quantum Efficiency of UV LEDs - State of the Art, http://www.ifkp.tu-berlin.de/fileadmin/i1/Kneissl/" (2013).

[36] P. VENNÉGUÈS *et al.* *Physica Status Solidi (C)*, **3(6)**, 1658–1661 (2006). doi:10.1002/pssc.200565292.

[37] K.-C. KIM *et al.* *Physica Status Solidi (RRL)*, **1(3)**, 125–127 (2007). doi:10.1002/pssr.200701061.

[38] V. VEZIN *et al.* *Japanese Journal of Applied Physics*, **36(Part 2, No. 11B)**, L1483–L1485 (1997). doi:10.1143/JJAP.36.L1483.

[39] L. K. TELES *et al.* *Applied Physics Letters*, **80(7)**, 1177 (2002). doi:10.1063/1.1450261.

[40] G. FOX-RABINOVICH *et al.* *Surface and Coatings Technology*, **200(20-21)**, 5738–5742 (2006). doi:10.1016/j.surfcoat.2005.08.132.

[41] S. ZHANG and W. ZHU. *Journal of Materials Processing Technology*, **39**, 165–177 (1993). doi:10.1016/0924-0136(93)90016-Y.

[42] L. PORTE. *Journal of Physics C: Solid State Physics*, **18(36)**, 6701–6709 (1985). doi:10.1088/0022-3719/18/36/024.

[43] D. HOLEC *et al. Journal of Physics D: Applied Physics*, **43(14)**, 145403 (2010). doi:10.1088/0022-3727/43/14/145403.

[44] M. A. MORAM and S. ZHANG. *Journal of Materials Chemistry A* (2014). doi:10.1039/c3ta14189f.

[45] S. A. WOLF *et al. Science (New York, N.Y.)*, **294(5546)**, 1488–95 (2001). doi:10.1126/science.1065389.

[46] T. DIETL. *Physical Review B*, **63(19)** (2001). doi:10.1103/PhysRevB.63.195205.

[47] C. LIU *et al. Journal of Materials Science: Materials in Electronics*, **16(9)**, 555–597 (2005). doi:10.1007/s10854-005-3232-1.

[48] A. BONANNI. *Semiconductor Science and Technology*, **22(9)**, 41–56 (2007). doi:10.1088/0268-1242/22/9/R01.

[49] K. SATO *et al. Reviews of Modern Physics*, **82(2)**, 1633–1690 (2010). doi:10.1103/RevModPhys.82.1633.

[50] V. AVRUTIN *et al. Proceedings of the IEEE*, **98(7)**, 1288–1301 (2010). doi:10.1109/JPROC.2010.2044966.

[51] A. BONANNI *et al. Physical Review B*, **75(12)**, 1–18 (2007). doi:10.1103/PhysRevB.75.125210.

[52] P. CHEN. *Journal of Crystal Growth*, **251(1-4)**, 331–336 (2003). doi:10.1016/S0022-0248(02)02204-2.

[53] K. SATO *et al. Japanese Journal of Applied Physics*, **44(30)**, 948–951 (2005). doi:10.1143/JJAP.44.L948.

[54] M. ROVEZZI *et al. Physical Review B*, **79(19)**, 195209 (2009). doi:10.1103/PhysRevB.79.195209.

[55] W. STEFANOWICZ *et al.* *Physical Review B*, **81(23)**, 235210 (2010). doi:10.1103/PhysRevB.81.235210.

[56] M. E. OVERBERG *et al.* *Applied Physics Letters*, **79(9)**, 1312 (2001). doi:10.1063/1.1397763.

[57] S. SONODA *et al.* *IEEE Transactions on Magnetics*, **38(5)**, 2859–2862 (2002). doi:10.1109/TMAG.2002.803147.

[58] P. RUTERANA *et al.* *Nitride Semiconductors: Handbook on Materials and Devices*, (Wiley-VCH, Weinheim2003), 1st edition. ISBN 3-527-40387-6.

[59] S. DHAR *et al.* *Physical Review B*, **67(16)**, 1–7 (2003). doi:10.1103/PhysRevB.67.165205.

[60] S. HEIKMAN *et al.* *Journal of Crystal Growth*, **248**, 513–517 (2003). doi:10.1016/S0022-0248(02)01926-7.

[61] A. CORRION *et al.* *Journal of Crystal Growth*, **289(2)**, 587–595 (2006). doi:10.1016/j.jcrysgro.2005.12.084.

[62] A. BONANNI *et al.* *Physical Review Letters*, **101(13)**, 1–4 (2008). doi:10.1103/PhysRevLett.101.135502.

[63] K. H. PLOOG *et al.* *Journal of Vacuum Science & Technology B: Microelectronics and Nanometer Structures*, **21(4)**, 1756 (2003). doi:10.1116/1.1588649.

[64] Y. CUI and L. LI. *Applied Physics Letters*, **80(22)**, 4139 (2002). doi:10.1063/1.1483387.

[65] M. A. MORAM *et al.* *Journal of Applied Physics*, **100(2)**, 023514 (2006). doi:10.1063/1.2217106.

[66] J. DISMUKES *et al.* *Journal of Crystal Growth*, **13-14**, 365–370 (1972). doi:10.1016/0022-0248(72)90185-6.

[67] A. R. SMITH *et al.* *Journal of Applied Physics*, **90(4)**, 1809 (2001). doi:10.1063/1.1388161.

[68] D. GALL *et al.* *Physical Review B*, **63(12)**, 1–9 (2001). doi:10.1103/PhysRevB.63.125119.

[69] M. A. MORAM *et al. Journal of Crystal Growth*, **298**, 268–271 (2007). doi:10.1016/j.jcrysgro.2006.10.027.

[70] R. MONNIER *et al. Physical Review B*, **31(8)**, 5554–5556 (1985). doi:10.1103/PhysRevB.31.5554.

[71] G. TRAVAGLINI *et al. Physical Review B*, **34(6)**, 3876–3882 (1986). doi:10.1103/PhysRevB.34.3876.

[72] N. TAKEUCHI. *Physical Review B*, **65(4)**, 3–6 (2002). doi:10.1103/PhysRevB.65.045204.

[73] C. STAMPFL *et al. Physical Review B*, **63(15)**, 155106 (2001). doi:10.1103/PhysRevB.63.155106.

[74] W. LAMBRECHT. *Physical Review B*, **62(20)**, 13538–13545 (2000). doi:10.1103/PhysRevB.62.13538.

[75] C. KITTEL. *Introduction to Solid State Physics*, (Wiley-VCH, New York2005), 8th edition. ISBN 978-0-471-41526-8.

[76] N. FARRER and L. BELLAICHE. *Physical Review B*, **66(20)**, 4–7 (2002). doi:10.1103/PhysRevB.66.201203.

[77] M. MORENO-ARMENTA and G. SOTO. *Computational Materials Science*, **40(2)**, 275–281 (2007). doi:10.1016/j.commatsci.2006.12.009.

[78] R. SMITH. *Titanium and titanium alloys*, volume 258, (Rheinhold Publishing Corp., New York1954). ISBN 9783527605200. doi:10.1016/0016-0032(54)90914-X.

[79] M. A. MORAM *et al. Thin Solid Films*, **516(23)**, 8569–8572 (2008). doi:10.1016/j.tsf.2008.05.050.

[80] P. V. BURMISTROVA *et al. Journal of Applied Physics*, **113(15)**, 153704 (2013). doi:10.1063/1.4801886.

[81] W. LENGAUER. *Journal of Solid State Chemistry*, **76(2)**, 412–415 (1988). doi:10.1016/0022-4596(88)90236-8.

[82] R. NIEWA *et al. Chemistry of Materials*, **16(25)**, 5445–5451 (2004). doi:10.1021/cm048667y.

[83] Z. Gu *et al.* *Journal of Materials Science: Materials in Electronics*, **15(8)**, 555–559 (2004). doi:10.1023/B:JMSE.0000032591.54107.2c.

[84] X. Bai and M. E. Kordesch. *Applied Surface Science*, **175-176**, 499–504 (2001). doi:10.1016/S0169-4332(01)00165-9.

[85] D. Gall *et al.* *Journal of Applied Physics*, **86(10)**, 5524 (1999). doi:10.1063/1.371555.

[86] J. M. Gregoire *et al.* *Journal of Applied Physics*, **104(7)**, 074913 (2008). doi:10.1063/1.2996006.

[87] M. Karl *et al.* *Zeitschrift für anorganische und allgemeine Chemie*, **625(3)**, 375–376 (1999). doi:10.1002/(SICI)1521-3749(199903)625:3<375::AID-ZAAC375>3.0.CO;2-T.

[88] H. Al-Brithen and A. R. Smith. *Applied Physics Letters*, **77(16)**, 2485 (2000). doi:10.1063/1.1318227.

[89] M. A. Moram *et al.* *Applied Surface Science*, **252(24)**, 8385–8387 (2006). doi:10.1016/j.apsusc.2005.11.069.

[90] T. Ohgaki *et al.* *Journal of Applied Physics*, **114(9)**, 93704 (2013). doi:10.1063/1.4820391.

[91] J. Edgar *et al.* *Journal of Crystal Growth*, **310(6)**, 1075–1080 (2008). doi:10.1016/j.jcrysgro.2007.12.053.

[92] K. A. Fleeting *et al.* *Chemical Vapor Deposition*, **5(6)**, 261–264 (1999). doi:10.1002/(SICI)1521-3862(199912)5:6<261::AID-CVDE261>3.0.CO;2-2.

[93] V. Ranjan *et al.* *Physical Review Letters*, **90(25)**, 25–28 (2003). doi:10.1103/PhysRevLett.90.257602.

[94] V. Ranjan *et al.* *Physical Review B*, **72(8)**, 1–9 (2005). doi:10.1103/PhysRevB.72.085315.

[95] S. Zhang *et al.* *Journal of Applied Physics*, **114(13)**, 133510 (2013). doi:10.1063/1.4824179.

[96] M. Akiyama *et al.* *Advanced Materials*, **21(5)**, 593–596 (2009). doi:10.1002/adma.200802611.

[97] M. MOREIRA *et al.* *Vacuum*, **86(1)**, 23–26 (2011). doi:10.1016/j.vacuum.2011.03.026.

[98] M. AKIYAMA *et al.* *Journal of the Ceramic Society of Japan*, **118(1384)**, 1166–1169 (2010).

[99] C. HÖGLUND *et al.* *Journal of Applied Physics*, **105(11)**, 113517 (2009). doi:10.1063/1.3132862.

[100] C. CONSTANTIN *et al.* *Physical Review B*, **70(19)**, 1–4 (2004). doi:10.1103/PhysRevB.70.193309.

[101] C. CONSTANTIN *et al.* *Journal of Applied Physics*, **98(12)**, 123501 (2005). doi:10.1063/1.2140889.

[102] R. DENG *et al.* *Applied Physics Letters*, **102(11)**, 112103 (2013). doi:10.1063/1.4795784.

[103] M. E. LITTLE and M. E. KORDESCH. *Applied Physics Letters*, **78(19)**, 2891 (2001). doi:10.1063/1.1370548.

[104] C. CONSTANTIN *et al.* *Materials Research Society Symposium Proceedings*, **799**, 1–6 (2004).

[105] M. A. MORAM *et al.* *Journal of Applied Physics*, **106(11)**, 113533 (2009). doi:10.1063/1.3268466.

[106] AIXTRON. "CRIUS II-L Product Specification" (2014).

[107] G. B. STRINGFELLOW. *Organometallic Vapor-Phase Epitaxy: Theory and Practice*, (Academic Press1999). ISBN 0080538185.

[108] G. B. STRINGFELLOW. *Materials Science and Engineering: B*, **87(2)**, 97–116 (2001). doi:http://dx.doi.org/10.1016/S0921-5107(01)00712-7.

[109] T. WEBB. *Thomas Swan Scientific Equipment CCS-MOCVD Reactor System Manual - CS12171*, (Thomas Swan Scientific Equipment LTD1999).

[110] M. A. MORAM *et al.* *Journal of Applied Physics*, **109(7)**, 73507–73509 (2011). doi:doi:10.1063/1.3553841.

[111] M. A. MORAM *et al.* *Applied Physics Letters*, **97(26)**, 261907 (2010). doi:10.1063/1.3532965.

[112] C. T. FOXON and O. H. HUGHES. *Journal of Materials Science: Materials in Electronics*, **9**, 227–230 (1998). doi:10.1023/A:1008834426133.

[113] E. J. TARSA *et al.* *Journal of Applied Physics*, **82(11)**, 5472 (1997). doi:10.1063/1.365575.

[114] B. HEYING *et al.* *Journal of Applied Physics*, **88(4)**, 1855 (2000). doi:10.1063/1.1305830.

[115] B. HEYING *et al.* *Applied Physics Letters*, **77(18)**, 2885 (2000). doi:10.1063/1.1322370.

[116] W. C. HUGHES. *Journal of Vacuum Science & Technology B: Microelectronics and Nanometer Structures*, **13(4)**, 1571 (1995). doi:10.1116/1.588189.

[117] T. OHACHI *et al.* *Journal of Crystal Growth*, **311(10)**, 2987–2991 (2009). doi:10.1016/j.jcrysgro.2009.01.069.

[118] N. GRANDJEAN *et al.* *Applied Physics Letters*, **74(13)**, 1854 (1999). doi:10.1063/1.123691.

[119] A. R. SMITH *et al.* *Applied Physics Letters*, **72(17)**, 2114 (1998). doi:10.1063/1.121293.

[120] AGILENT. "Standard oq test specifications for uv-visible spectrophotometers, http://tinyurl.com/n85szrd" (2014).

[121] S. SOUSA. "Fundamentals of modern UV-Visible spectroscopy". Technical report, Agilent Technologies (2009).

[122] J. TAUC *et al.* *Physica Status Solidi (B)*, **15(2)**, 627–637 (1966). doi:10.1002/pssb.19660150224.

[123] M. MEINERT and G. REISS. *Journal of Physics: Condensed Matter*, **26(11)**, 115503 (2014).

[124] B.-C. CHUNG and M. GERSHENZON. *Journal of Applied Physics*, **72(2)**, 651 (1992). doi:10.1063/1.351848.

[125] R. DINGLE and M. ILEGEMS. *Solid State Communications*, **9(3)**, 175–180 (1971). doi:10.1016/0038-1098(71)90112-8.

[126] T. ZHU *et al.* *Journal of Applied Physics*, **107(2)**, 023503 (2010). doi:10.1063/1.3284944.

[127] V. L. MIRINOV. *Fundamentals of scanning probe microscopy*, (ND-MDT, Nizhny Novgorod2004).

[128] H. WENHAO and C. YUHANG. *Journal of Physics: Conference Series*, **13**, 44–50 (2005). doi:10.1088/1742-6596/13/1/011.

[129] P. F. FEWSTER. *X-ray Scattering from Semiconductors*, (Imperial College Press, London2003), 2nd editio edition. ISBN 1860941591.

[130] M. A. MORAM and M. E. VICKERS. *Reports on Progress in Physics*, **72(3)**, 036502 (2009). doi:10.1088/0034-4885/72/3/036502.

[131] D. B. WILLAMS and C. B. CARTER. *Transmission Electron Microscopy*, (Plenum Press, New York1996), 1st edition. ISBN 0-306-45247-2.

[132] M. E. VICKERS *et al.* *Journal of Applied Physics*, **94(3)**, 1565 (2003). doi:10.1063/1.1587251.

[133] T. SMEETON. "The nanostructures of InGaN quantum wells". Ph.D. thesis, University of Cambridge (2005).

[134] B. FULTZ and J. M. HOWE. *Transmission Electron Microscopy and Diffractometry of Materials*, (Springer, Berlin2002), 2nd edition. ISBN 3-540-43764-9.

[135] Y. ZHANG. "Characterisation of GaN Using Transmission Electron Microscopy". Ph.D. thesis, University of Cambridge (2008).

[136] J. P. HIRTH and J. LOTHE. *Theory of Dislocations*, (John Wiley & Sons, New York1982).

[137] S. J. PENNYCOOK and P. D. NELLIST. *Scanning Transmission Electron Microscopy*, (Springer, Heidelberg2011), 7 edition. ISBN 978-1-4419-7200-2.

[138] M. NEWVILLE. *Reviews in Mineralogy and Geochemistry*, **78(1)**, 33–74 (2014). doi:10.2138/rmg.2014.78.2.

[139] G. BUNKER. *Introduction to XAFS: A Practical Guide to X-ray Absorption Fine Structure Spectroscopy*, (Cambridge University Press, Cambridge2010). ISBN 052176775X.

[140] B. RAVEL and M. NEWVILLE. *Journal of synchrotron radiation*, **12(Pt 4)**, 537–41 (2005). doi:10.1107/S0909049505012719.

[141] S. KELLY. "Basics of EXAFS data analysis". Technical report, Argonne National Laboratory, Argonne (2004).

[142] K. KLEMENTEV. *Nuclear Instruments and Methods in Physics Research Section A: Accelerators, Spectrometers, Detectors and Associated Equipment*, **448(1-2)**, 299–301 (2000). doi:10.1016/S0168-9002(99)00710-X.

[143] J. J. REHR *et al.* *Physical Chemistry Chemical Physics*, **12(21)**, 5503 (2010). doi: 10.1039/b926434e.

[144] C. BROUDER. *Journal of Physics: Condensed Matter*, **2(3)**, 701 (1990). doi:10.1088/0953-8984/2/3/018.

[145] M. NEWVILLE. *Journal of Synchrotron Radiation*, **8(2)**, 322–324 (2001). doi:10.1107/S0909049500016964.

[146] M. NEWVILLE. *Consortium for Advanced Radiation Sources, University of Chicago (USA)* (2004).

[147] S. M. KNOLL *et al.* *Journal of Physics: Condensed Matter*, **26(22)**, 225801 (2014). doi:10.1088/0953-8984/26/22/225801.

[148] P. GLATZEL and U. BERGMANN. *Coordination Chemistry Reviews*, **249(2)**, 65–95 (2005). doi:10.1016/j.ccr.2004.04.011.

[149] H. AL-BRITHEN. *Journal of Crystal Growth*, **242(3-4)**, 345–354 (2002). doi:10.1016/S0022-0248(02)01447-1.

[150] R. KRSMANOVIĆ *et al.* *Nanotechnology*, **17(11)**, 2805–2812 (2006). doi:10.1088/0957-4484/17/11/013.

[151] H. AL-BRITHEN *et al.* *Journal of Applied Physics*, **96(7)**, 3787 (2004). doi:10.1063/1.1788842.

[152] D. GALL *et al.* *Journal of Vacuum Science & Technology A: Vacuum, Surfaces, and Films*, **16(4)**, 2411–2417 (1998). doi:10.1116/1.581360.

[153] S. KERDSONGPANYA *et al.* *PHYSICAL REVIEW B*, **86(19)** (2012). doi:{10.1103/PhysRevB.86.195140}.

[154] R. PASSLER. *Journal of Applied Physics*, **101(9)**, 93512–93513 (2007). doi:10.1063/1.2721749.

[155] A. NEY *et al.* *New Journal of Physics*, **12(1)**, 13020 (2010). doi:10.1088/1367-2630/12/1/013020.

[156] T. YAMAMOTO. *X-Ray Spectrometry*, **37(6)**, 572–584 (2008). doi:10.1002/xrs.1103.

[157] K. KANAYA and S. OKAYAMA. *Journal of Physics D: Applied Physics*, **5(1)**, 43 (1972). doi:10.1088/0022-3727/5/1/308.

[158] D. DROUIN *et al.* *Scanning*, **29(3)**, 92–101 (2007). doi:10.1002/sca.20000.

[159] S. M. KNOLL *et al.* *Physica Status Solidi (a)*, **209(1)**, 33–40 (2012). doi:10.1002/pssa.201100158.

[160] T. BÖTTCHER *et al.* *Applied Physics Letters*, **73(22)**, 3232 (1998). doi:10.1063/1.122728.

[161] S. KURODA *et al.* *Applied Physics Letters*, **83(22)**, 4580 (2003). doi:10.1063/1.1629791.

[162] M. B. HAIDER *et al.* *Journal of Applied Physics*, **93(9)**, 5274 (2003). doi:10.1063/1.1565511.

[163] M. B. HAIDER *et al.* *Journal of Crystal Growth*, **285(3)**, 300–311 (2005). doi:10.1016/j.jcrysgro.2005.08.047.

[164] M. MESRINE *et al.* *Applied Physics Letters*, **72(3)**, 350 (1998). doi:10.1063/1.120733.

[165] W. M. TONG and R. S. WILLIAMS. *Annual Review of Physical Chemistry*, **45(1)**, 401–438 (1994). doi:10.1146/annurev.pc.45.100194.002153.

[166] H. GAO and W. D. NIX. *Annual Review of Materials Science*, **29(1)**, 173–209 (1999). doi:10.1146/annurev.matsci.29.1.173.

[167] M. PRISTOVSEK *et al.* *Physica Status Solidi (C)*, **6(S2)**, S565–S569 (2009). doi:10.1002/pssc.200880915.

[168] S. ZHANG *et al.* *Journal of Applied Physics*, **114(24)**, 243516 (2013). doi:10.1063/1.4848036.

[169] L. Z.-Y. LIU. "Advanced Transmission Electron Microscopy of GaN-based Materials and Devices". Ph.D. thesis, University of Cambridge (2011).

[170] S. M. KNOLL *et al.* *Applied Physics Letters*, **104(10)**, 101906 (2014). doi:10.1063/1.4868538.

[171] P. BLAHA *et al.* "WIEN2k, An Augmented Plane Wave + Local Orbitals Program for Calculating Crystal Properties". Technical report, Karlheinz Schwarz, Techn. Universität Wien, Austria (2001).

[172] T. DEVILLERS *et al.* *Scientific reports*, **2**, 722 (2012). doi:10.1038/srep00722.

[173] J. P. PERDEW *et al.* *Physical Review Letters*, **77(18)**, 3865–3868 (1996). doi:10.1103/PhysRevLett.77.3865.

[174] A. A. GUDA *et al.* *Journal of Analytical Atomic Spectrometry*, **28(10)**, 1629 (2013). doi:10.1039/c3ja50153a.

[175] Y. JOLY. *Physical Review B*, **63(12)**, 125120 (2001). doi:10.1103/PhysRevB.63.125120.

[176] *OriginPro* (OriginLab, Northampton, MA), 9.0 edition.